UNIVERSITY OF SOUTHAMPTON

The Mechanics of an Unbonded Locked Sand at Low Effective Stresses

by

Athma Ram Bhandari

A thesis submitted in fulfillment for the
degree of Doctor of Philosophy

in the
Faculty of Engineering, Science & Mathematics
School of Civil Engineering and the Environment

June 2009

Declaration of Authorship

I, Athma Ram Bhandari, declare that this thesis titled, 'The Mechanics of an Unbonded Locked Sand at Low Effective Stresses' and the work presented in it are my own. I confirm that:

- This work was done wholly or mainly while in candidature for a research degree at this University.
- Where any part of this thesis has previously been submitted for a degree or any other qualification at this University or any other institution, this has been clearly stated.
- Where I have consulted the published work of others, this is always clearly attributed.
- Where I have quoted from the work of others, the source is always given. With the exception of such quotations, this thesis is entirely my own work.
- I have acknowledged all main sources of help.
- Where the thesis is based on work done by myself jointly with others, I have made clear exactly what was done by others and what I have contributed myself.

Signed: _____

Date: _____

"We must learn to distinguish between what we understand and what we don't understand."

- Socrates

UNIVERSITY OF SOUTHAMPTON

Abstract

Faculty of Engineering, Science & Mathematics
School of Civil Engineering and the Environment

Doctor of Philosophy

by Athma Ram Bhandari

Natural soil deposits are likely to have a structure resulting from particle bonding or interlocking or both. Recent research on natural sand having a predominantly locked structure with very little cement bonding has shown that, at low stresses, this material tended to mobilise its peak strength at or slightly before the onset of dilation. The intact material also displayed peak strengths very significantly greater than for comparable reconstituted samples. A fall and recovery in the stiffness of the material was observed prior to the onset of dilation. Dilation was associated with destructurisation, localisation and a loss of strength.

Understanding the behaviour before and after the start of dilation, and the role of destructurisation and localisation is essential to the development of reliable quantitative descriptions of the engineering behaviour of locked sands. This cannot be done in a conventional triaxial test with conventional instrumentation alone. To address this shortcoming, a digital image-based deformation measurement technique has been developed. Three digital cameras placed on radii at intervals of 120 degrees viewed on plan outside a transparent triaxial cell are used to capture images of the deforming samples at various instants. A suitable digital image correlation program has been written to analyse the captured images, using ray tracing to take account of image distortion due to refraction.

Linear Variable Differential Transformers (LVDTs) together with volume change measurement are used to characterise the behaviour of the material at small strains. The digital image-based technique has been used to determine the instant of onset of localisation, and the distribution of localisations within the sample as deformation progresses in a naturally locked sand. The implications of deformation localisation on the strength and mechanical behaviour of the material are studied. The effect of changing the confining pressure on the transition of deformation characteristics is also examined.

Acknowledgements

I would like to acknowledge and thank all people for their help and support that make this thesis possible.

Firstly, I am deeply indebted to my supervisor, Prof. William Powrie, for providing the opportunity to join this research project and for providing clear direction, motivation, guidance and constructive criticisms during this research.

I am very much thankful to Richard Harkness. He has always shown great interest in my work and has been a great source of inspiration. I have learnt a lot from him when discussing about image-based measurement techniques. I am also thankful to Dr. Andrew Cresswell for providing initial laboratory inductions, accompanying me on visits to the sand quarry and teaching me the time consuming but interesting field and laboratory sampling techniques with great efforts.

I would like to thank Harvey Skinner for helping during visits to the sand quarry, in setting up instruments and in troubleshooting various technical problems in the lab. Dr. John Harkness provided technical help on many occasions. Technicians Ken Yates, Earl Peters and Dave Lynock at the School's Workshop provided great help converting my drawings into tools. Graham Tucker allowed block sampling of Reigate silver sand at Park Pit, Reigate so I would like to acknowledge his help and support for this research. I am grateful to Dr. Veerle Huvenne (National Oceanography Centre, Southampton) for her help with the laser diffraction testing.

I would like to thank Dr. Antonis Zervos for evaluating and providing critical suggestions on the transfer report and Prof. Chris Clayton for evaluating and providing helpful suggestions on the nine month report.

The financial support for this study was provided by the Engineering and Physical Sciences Research Council (EPSRC), the University of Southampton - School of Civil Engineering and the Environment, and the ORSAS (Overseas Research Student Award Scheme) Award and is gratefully acknowledged.

I thank all my colleagues for their friendly help and for the pleasant years working together. My Nepalese friends living in Southampton provided environment similar to that back in Nepal in several occasions and at celebrations held during festivals, which are always memorable.

My wife Laxmi & my daughter Alisha are always a great source of inspiration for me and provided great accompany and support. I am very grateful to all my family members for their continuous love, care and support throughout my life.

Contents

List of Figures

List of Tables

Abbreviations

BS	**B**ritish **S**tandards
CCD	**C**harge **C**ouple **D**evice
CMOS	**C**omplementary **M**etal **O**xide **S**emiconductor
CT	**C**omputed **T**omography
CV	**C**omputer **V**ision
DIC	**D**igital **I**mage **C**orrelation
DLL	**D**ynamic **L**ink **L**ibrary
ISO	**I**nternational **O**rganization for **S**tandardization
JPEG	**J**oint **P**hotographic **E**xperts **G**roup
LBS	**L**eighton **B**uzzard **s**and
LVDT	**L**inear **V**ariable **D**ifferential **T**ransformer
MEX	**M**atlab **Ex**ecuteable
PVA	**P**oly**v**inyl **A**cetate
RSS	**R**eigate **s**ilver **s**and

Symbols

d	rate of dilation
e	void ratio
e_{max}	maximum void ratio
e_{min}	minimum void ratio
m_s	dry mass of sample
n_a	refractive index of air
n_p	refractive index of perspex
n_w	refractive index of water
p'	mean effective stress ($p' = \frac{\sigma'_1 + 2\sigma'_3}{3}$)
q	deviator stress ($q = \sigma'_1 - \sigma'_3$)
t_m	membrane thickness
v	specific volume ($v = 1 + e$)
v_c	specific volume at critical state
A_{eff}	effective cross-sectional area of sample
$C(u, v)$	cross-correlation function
$C_n(u, v)$	normalised cross-correlation coefficient
C_u	coefficient of uniformity
D	distance of imaginary plane from the apparent focus
D_0	initial diameter of sample
D_{50}	50 % particles pass a sieve size of this diameter (diameter)
E_m	Young's modulus
G	tangent shear modulus ($G = \frac{\delta q}{2(\delta\varepsilon_1 - \delta\varepsilon_3)}$)
G_s	specific gravity

H_0	initial height of sample
I_D	relative density index ($I_D = \frac{e_{max}-e}{e_{max}-e_{min}}$)
I_R	relative dilatancy index ($I_R = I_D(10 - \ln p') - 1$)(Bolton, 1986)
L	distance of centre of sample from the apparent focus
M	critical state friction parameter
Q	ram load
R	radius of sample
R_1	outer radius of the cell
R_2	inner radius of the cell
U	domain
V_0	initial volume of sample
V_t	volume of sample at the current stage of shearing
ΔW_{struc}	work dissipated in disrupting soil fabric
ε_1	axial local axial strain
ε_3	local radial strain
ε_a	global axial strain
ε_r	average radial strain
ε_s	deviatoric strain ($\varepsilon_s = \frac{2(\varepsilon_a-\varepsilon_r)}{3}$)
ε_{vol}	average volumetric strain
ε_s^p	plastic part of deviatoric strain
ε_v^p	plastic part of volumetric strain
η	stress ratio ($\eta = \frac{q}{p'}$)
Ψ	state parameter ($\Psi = v - v_c$)(Been & Jefferies, 1985)
ψ	dilation angle
ϕ'_{cv}	critical state friction angle
ϕ'_{mob}	mobilized angle of internal friction
ϕ'_p	peak friction angle
ϕ_μ	inter-particle friction angle
ρ_w	mass density of water
σ'_1	effective vertical stress

σ'_3	effective all around horizontal stress
σ_c	cell pressure
σ'_c	effective cell pressure
σ_u	pore water pressure

Dedicated to my...

Parents, brothers Krishna and Bishwo, wife Laxmi and daugther Alisha

Chapter 1

Introduction

Natural soil deposits are likely to have a structure resulting from bonding or interlocking of the particles or both. Recent research on natural sands that have a predominantly locked structure with very little cement bonding has shown that, at low stresses, these materials tend to mobilise their peak strength at or slightly before the onset of dilation (Cresswell & Powrie, 2004). They also display peak strengths that are very significantly greater than for comparable reconstituted samples. A fall and recovery of shear stiffness was observed prior to the onset of dilation. Dilation is associated with destructurisation, localisation and a loss of strength.

This study utilises sampling and sample preparation techniques that allow the laboratory testing of intact locked sands with negligible grain bonding. Image analysis based displacement measurement technique suitable for triaxial tests is developed, together with local strain measurement methods using LVDTs (Linear variable differential transformers) for close observation of the deformation of samples under test.

The proper understanding of the effect of interlocked fabric is necessary before the development of any new engineering design models to exploit with confidence the high peak strength and stiffness of this material in design. In addition, many natural deposits are locked to at least some extent. But current methods of characterization and design do not specifically take into account "locked" fabric behaviour.

Aims and objectives

The main aim of this research is to develop an improved understanding of the stress-strain-strength behaviour of a locked sand and the microstructural mechanisms that underlie it, by carrying out experimental studies on intact samples of a locked sand at low effective stresses.

The objectives of this research are to:

- investigate the influence of an interlocked fabric on small strain behaviour
- clarify the apparent ability to sustain stress ratios close to peak without dilation
- understand the role and significance of dilation
- investigate the formation of shear bands and the role of localisation in subsequent deformation
- explore the dip in shear modulus that occurs prior to yield
- understand the behaviour of intact and pluviated samples at large strain

Organisation of this thesis

This thesis consists of six chapters, as follows:

1. Chapter 1 summarises the context, methodology, contributions, and defines the aims and objectives of this research work.
2. Chapter 2 presents the background of this research in detail.
3. Chapter 3 examines the strength and deformation characteristics of intact and pluviated samples of Reigate silver sand in conventional triaxial compression at effective cell pressures from 12.5 to 100 kPa with LVDT based local strain measurement. This chapter describes the first series of test (Test Series B1) carried out with particular focus on understanding the small strain behaviour. New insights regarding the influence of fabric structure on strength and deformation characteristics at low effective stresses are presented. The

difficulty associated with identifying the onset of localisation by relying on the visual evidence of the divergence of LVDTs was highlighted. The shortcomings of the LVDTs in characterising localised deformation and post-peak deformation were highlighted.

4. Chapter 4 presents the development of a new image-based surface deformations measurement system for triaxial samples for the detailed monitoring of cylindrical triaxial samples to understand the local phenomena occurring at a particle scale which in fact determine the global response of the samples.

5. Chapter 5 uses the image-based deformation monitoring system developed in chapter 4 to study the surface deformation characteristics of intact samples of Reigate silver sand tested at different confining pressures, 100 kPa or below. This chapter describes the second series of test (Test Series B2) to study the initial deformation, initiation of onset of localisation, evolution of deformation from onset of localisation to shear banding (i.e. formation of persistent shear band), and development of rigid body movement mechanisms outside the shear band. The effect of confining pressure in developing different kinematic mechanisms, and their impacts on global stress-strain relations, are studied.

6. Chapter 6 presents the conclusions and recommendations for future work.

Chapter 2

Background

2.1 Influence of structure on the engineering behaviour of natural sands

The geometrical arrangement of soils particles and the voids between them, *i.e. soil structure*, is a subject which has evoked interest over a long period in soil mechanics. The effect of structure on the engineering behaviour of clays has long been recognised due to the significant difference in behaviour between intact and remoulded samples (Burland, 1990). However, for sands the in situ structure is usually assumed to be replicable by preparing samples in the laboratory at a similar relative density. Owing to the importance of the behaviour of natural sand deposits and the development of new sampling and sample preparation techniques which enables undisturbed testing of sands, the influence of structure on the stress-strain behaviour of sands has recently become a key topic of research (for example, Leroueil & Vaughan, 1990; Cuccovillo & Coop, 1997; Cuccovillo & Coop, 1999; Kavvadas & Amorosi, 2000; Cresswell & Powrie, 2004; Shuttle, 2006; Guo & Su, 2007). Structure in natural sands may be classified into bonded structure or fabric structure or both. Due to the relative ease of extracting samples from the field and preparing samples (natural or artificial) in the laboratory, the effect of bonded structure in sands is comparatively well studied (for example, Clough et al., 1981; Coop & Atkinson, 1993; Malandraki & Toll, 2000). However, fabric structure is difficult to be created artificially and so intact samples must be tested. Fabric structure is very prone to disturbance, which poses a serious obstacle to studies focusing purely on its effect.

2.1.1 Effects of bonded structure

At low effective stresses, the bonding between grains dominates the behaviour of a cemented sand and it exhibits brittle failure. Peak strengths are achieved without dilation (Clough et al., 1981). At high effective stresses, the bonding between grains is broken during the application of the cell pressure, so that inter-particle friction dominates and behaviour at failure is ductile (Clough et al., 1981; Cuccovillo & Coop, 1999). In other words, the bonding component of strength controls the overall behaviour at low confining pressures and the frictional component (as in unstructured soils) at higher confining pressures. In addition, the behaviour of cemented sand is strongly influenced by the amount of cementing agent, relative density and grain size distribution. Also, failure modes are found to vary with level of cementation, and relative density. The peak strength increases with the degree of cementation. The strain at peak strength mobilization decreases as the degree of cementation is increased. The volume increase during shear is concentrated over a smaller strain range and occurs at a smaller strain as the degree of cementation increases. The stress-strain response becomes more brittle as the relative density is increased.

The effect of cementation is usually assessed by comparing the behaviour of cemented sands with uncemented or destructured sands. However, Coop & Atkinson (1993) have shown that an important effect of cementing is a reduction in specific volume resulting from the increase in fines content, which influences both the stress-strain behaviour and the peak strengths at strains beyond those required to fracture the cement bonding. Therefore, they have emphasized the importance of comparison between the behaviour of cemented and uncemented soils with the same gradings.

2.1.2 Effects of fabric structure

Locked sands, defined by Dusseault & Morgenstern (1979), are an ideal material for the study of this component of structure. Due to the exceptionally low porosities of locked sands, samples of these materials cannot be created artificially (Cresswell & Powrie, 2004). Previous research at Southampton has focused on: identification of locked sand in English Tertiary sand beds as introduced by Dusseault & Morgenstern (1979) in North American sands (Barton et al., 1986), classification

of locked sand as a transitional material between sands and sandstones (Barton, 1993), studies on Folkestone bed sands (Richards & Barton, 1999), and development of sampling and strength testing of unbonded locked sand (Cresswell, 1999; Cresswell & Barton, 2003). More recently, the triaxial tests on purely locked sand by Cresswell & Powrie (2004) have provided an opportunity to investigate particularly the effect of fabric structure.

Triaxial tests on intact and reconstituted Reigate silver sand (a locked sand with virtually no cement bonding) by Cresswell & Powrie (2004) have demonstrated that:

1. intact locked sand exhibits three stress ratio envelopes, corresponding to the start of dilation, peak and critical state strengths (Figure 2.1)

2. at moderate cell pressures ($\leq 100kPa$), intact locked sands mobilise stress ratios close to peak strengths before the onset of dilation (Figure 2.2). This type of behaviour was noted by Cuccovillo & Coop (1999) for a sandstone but was attributed by them to the cement bonding which was significant in their case

3. very significant increases in peak strength of intact locked sand with respect to reconstituted sand samples over the range of cell pressure investigated (50-800 kPa)

4. the behaviour of an intact locked sand at very small strains is complex, with a fall and recovery in the slope of the stress-strain curve occurring consistently as revealed by the variation of shear modulus prior to the onset of dilation (Figure 2.3).

2.2 Conventional soil mechanics and the lack of a measure for structure of natural sands

In conventional soil mechanics, which has developed primarily on the basis of the behaviour of reconstituted or unstructured soils, either the void ratio, e, or specific volume, $v(= 1 + e)$, is commonly used to represent the volumetric state of a soil. Maximum and minimum void ratios, e_{max} and e_{min} respectively, depend

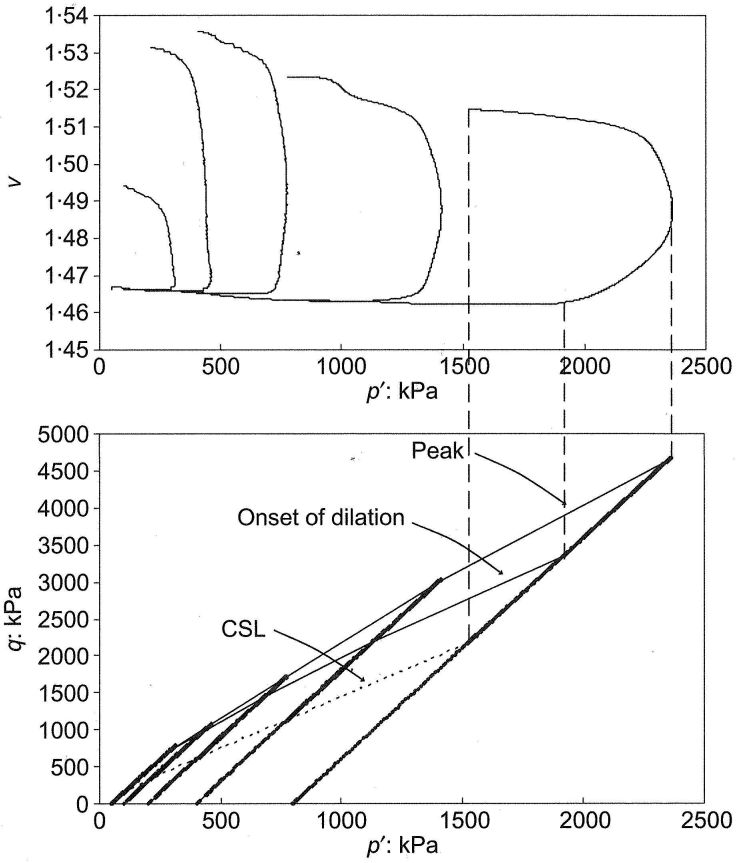

FIGURE 2.1: State states (deviator stress q against average effective stress $p^{'}$ and specific volume v plotted against $p^{'}$) followed by samples of intact Reigate silver sand in conventional triaxial compression tests. Peak, onset of dilation and possible critical state envelopes are marked (Cresswell & Powrie, 2004)

on mineralogy, particle shape and grading of soil particles. The relative density index I_D, which is derived from e or v and defined as $I_D = \frac{e_{max}-e}{e_{max}-e_{min}}$, is used as an estimate of the state of soil relative to its densest and loosest conditions. Been & Jefferies (1985) proposed the use of a parameter $\Psi = v - v_c$ to describe the state of a sand, where v_c is the specific volume at the critical state under the current average effective stress p'. This is more satisfactory than the relative density because it takes into account the effect of the stress level. Bolton (1986) proposed a scalar parameter I_R defined as $I_R = I_D(10 - \ln p') - 1$, called the *relative dilatancy index*, which also combines the influence of density and confining pressure. However, the state of a natural sand cannot be defined by the above parameters alone since the processes experienced in the ground during its geological history are not taken into consideration. These processes are reflected in the soil structure, which should be considered as an additional element of the soil nature (Leroueil & Vaughan, 1990). Between e or v (which is the simplest possible partial description of the

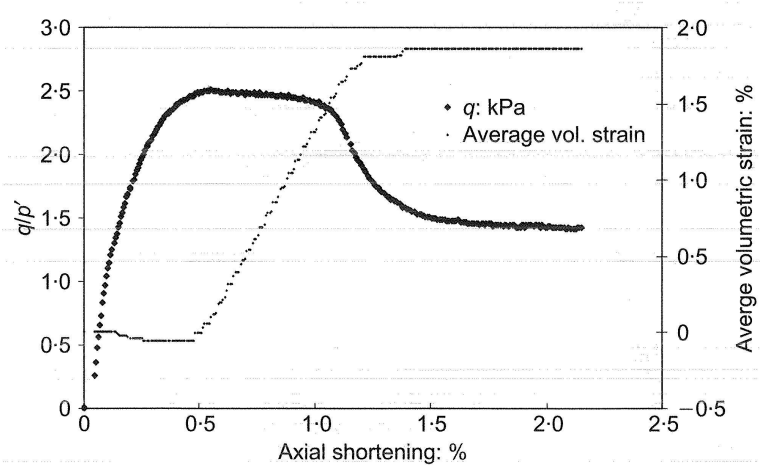

FIGURE 2.2: Typical stress-strain behaviour of an intact sample of Reigate silver sand at an effective cell pressure of 50 *kPa* (Cresswell & Powrie, 2004)

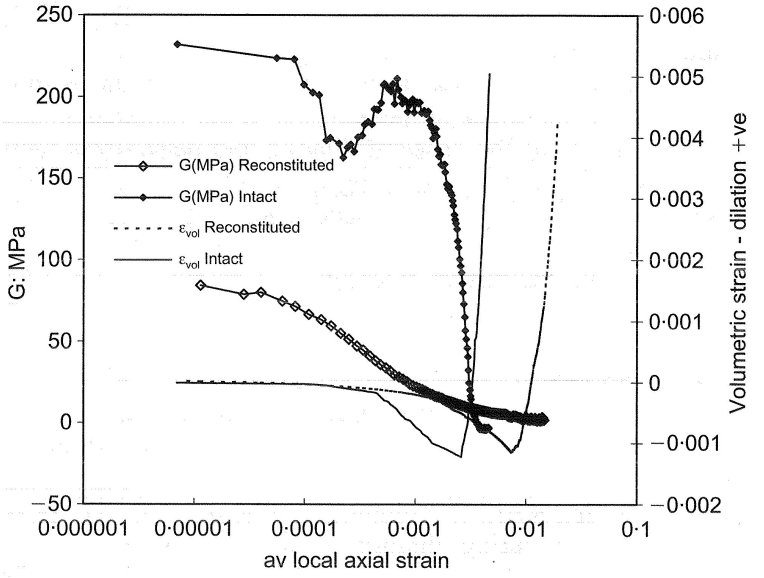

FIGURE 2.3: Shear modulus G and average volumetric strain against average local axial strain for intact and pluviated samples of Reigate silver sand tested in triaxial compression tests (Cresswell & Powrie, 2004)

soil; Muir Wood, 1990), I_D and Ψ (derived from e or v), and I_R, there is a clear lack of a single proper measure to describe satisfactorily the state of a structured soil. It is therefore difficult to describe the state and behaviour of structured sands within the conventional framework.

2.3 Peak strength, dilatancy and critical state strength

It is now widely accepted that the strength of cohesionless soils and volume changes during shear are interrelated. It has been consistently observed in triaxial tests that, subjected to shear under drained conditions, loose sand contracts accompanied by strain hardening while dense sand dilates accompanied by strain softening. Furthermore, for a sand that is initially in either the loose or dense state, there is an ultimate state of failure at which the volumetric strain rate is zero. This ultimate state is the well-known critical state (Roscoe et al., 1958). In critical state soil mechanics (Schofield & Wroth, 1968), a loose or dense state is defined in terms of not only the density but also the confining pressure. This is because such a definition (dense or loose) is relative to the critical state line in e versus p' space. For a given e, for example, the sand may behave like a dense material at a low p' and like a loose material at a high p'. In this context, the density and pressure dependence of shear strength, an important feature of behaviour of sands, has attracted many researchers. Laboratory investigations have studied extensively the influence of density, confining pressure, stress paths and boundary conditions on shear strengths of sands (for example, Cornforth, 1964; Been & Jefferies, 1985; Been et al., 1991; Vaid & Sasitharan, 1992; Schanz & Vermeer, 1996).

Any strength mobilised in excess of the critical state strength is conventionally associated with dilation (Taylor, 1948; Schofield & Wroth, 1968; Bolton, 1991). Mathematically, $\eta = M + d$; where η is the mobilised stress ratio, M is the stress ratio at the critical state and d represents the component due to dilation. The strength of sand is usually characterised by the peak friction angle ($\phi_p^{'}$) and the critical state friction angle ($\phi_{cv}^{'}$). Bolton (1986) presented a comprehensive review of the experimental data and correlated the difference between the peak and critical state friction angles of a dense soil to its rate of dilation and thence to its relative density and mean effective stress (p'), combined in a relative density index (I_D);

$$\phi_p^{'} - \phi_{cv}^{'} = 3\left[I_D\left(10 - \ln p^{'}\right) - 1\right] \tag{2.1}$$

Stress dilatancy theories (Rowe, 1962; Newland & Allely, 1957) back up these ideas in that the maximum stress ratio is mobilized when the sample is exhibiting its maximum rate of dilation (Equation 2.2).

$$\frac{\sigma_1^{'}}{\sigma_3^{'}(1+\frac{d\dot{V}}{V\dot{\varepsilon}_1})} = \tan^2(45^\circ + \frac{\phi_\mu}{2}) \tag{2.2}$$

The results reported by Cresswell & Powrie (2004), i.e. the attainment of strengths in excess of critical in the absence of dilation at low confining stress as stated in the previous section, are not consistent with the concept that dilatancy alone is responsible for mobilizing strengths in excess of the critical state value.

Recently, some studies (for example, Cuccovillo & Coop, 1999; Guo & Su, 2007) have highlighted the necessity of including the constraints imposed by an interlocking structure to describe properly the stress-dilation behaviour. The concept is that any microscopic constraints might increase the rate of internal energy dissipated and thus tend to decrease the overall dilatancy. Using the energy balance principle, Cuccovillo & Coop (1999) proposed the following expression:

$$\frac{q}{p^{'}} = M - \frac{\delta\varepsilon_v^p}{\delta\varepsilon_s^p} + \frac{\Delta W_{struc}}{p'\delta\varepsilon_s^p} \tag{2.3}$$

where q is the deviator stress, p' is the mean effective stress, M is critical state stress ratio, $\delta\varepsilon_v^p$ is the plastic volumetric strain increment, $\delta\varepsilon_s^p$ is the plastic triaxial shear strain increment and ΔW_{struc} is the additional work spent in degrading the bonding and disrupting the soil fabric. A similar expression was recently proposed by Guo & Su (2007) to describe the dilatancy characteristics of a granular material with strong interparticle locking associated with particle angularity. The total energy dissipation was partly related to interparticle friction and partly to disrupting interparticle locking.

In this context, at low effective stresses ($\leq 100kPa$) where the peak strength of a locked sand is controlled by the interlocked structure, experimental investigations of load-deformation behaviour with detailed observations and identification of the grain-scale processes are required to understand properly the stress-dilatancy behaviour of locked sands.

Chapter 3

Conventional triaxial compression tests at low effective stresses with LVDTs based local strain measurement

3.1 Introduction

The study of the behaviour of sand in triaxial compression tests at low effective stresses has received comparatively little attention. Only a few studies have been carried out in the past, especially below 100 kPa on reconstituted and intact samples (for example, Ponce & Bell, 1971; Fukushima & Tatsuoka, 1984; Sture et al., 1998; Lancelot et al., 2003; Cresswell & Powrie, 2004; Lancelot et al., 2006).

Triaxial tests performed by Ponce & Bell (1971) on uniform, clean, rounded to subrounded quartz sand ($e_{max} = 0.72$; $e_{min} = 0.46$) showed that a decrease in the cell pressure led to a strong increase in both peak friction and dilatancy angles (Figure 3.1). They concluded that more dilatant deformation behaviour during shear at extremely low pressures produces an increase in the principal stress ratio at failure as a result of the energy required for expansion (dilation). Fukushima & Tatsuoka (1984) observed a small variation in peak friction angle and deformation characteristics for cell pressures below 50 kPa in Toyoura sand, which is a fine, angular sand ($D_{50} = 0.16$; $C_u = 1.46$; $e_{max} = 0.977$; $e_{min} = 0.605$), especially lower

than about 10 *kPa* (Figure 3.2). Lancelot et al. (2006) studied the behaviour of Hostun sand, which is a subangular medium sand (D_{50} = 0.471; C_u = 2.26; e_{max} = 0.943; e_{min} = 0.575), at cell pressures 20 to 50 *kPa*. They found that both the peak friction and dilatancy angles at low stresses are stress dependent (Figure 3.3). Relationships between failure and dilatancy angles (such as Rowe's or Bolton's) were shown to be in good agreement with experimental data. In all of these studies, the degree to which a sample undergoes volumetric deformation during shear has been shown to have a significant bearing on the measured peak strength. An inter-relationship between mobilisation of peak strength and the achievement of maximum dilation rate has been apparent.

It seems that no, or very few, triaxial tests have previously been carried out on intact undisturbed sands at low effective stresses except for Cresswell & Powrie (2004). Recently, undisturbed sand samples from an ancient riverbed in the Haifa Bay area was studied by Frydman et al. (2007) over a range of confining pressure of 100 to 260 *kPa*. They found the stress-dilation behaviour to obey a similar stress-strain relation as for reconstituted sands (Figure 3.4).

This chapter examines the strength and deformation characteristics of intact and pluviated samples of Reigate silver sand in conventional triaxial compression at effective cell pressures from 12.5 to 100 *kPa* with LVDTs based local strain measurement. The focus is particularly on understanding the small strain behaviour using a strain controlled triaxial apparatus comprising a modified Wykeham Farrance cell. Results from second series of tests which are described in more detail in Chapter 5, where focus is on understanding localisation, dilation and the post-peak response using the new image-based measurement system described in chapter 4, are included in the discussion section at the end of this chapter. The deformation behaviour over the range 50 to 800 *kPa* was investigated by Cresswell & Powrie (2004). For comparison purposes, the deformation characteristics of pluviated samples of Leighton Buzzard sand prepared at maximum density are also presented. New insights regarding the influence of fabric structure on strength and deformation characteristics at low effective stresses are discussed.

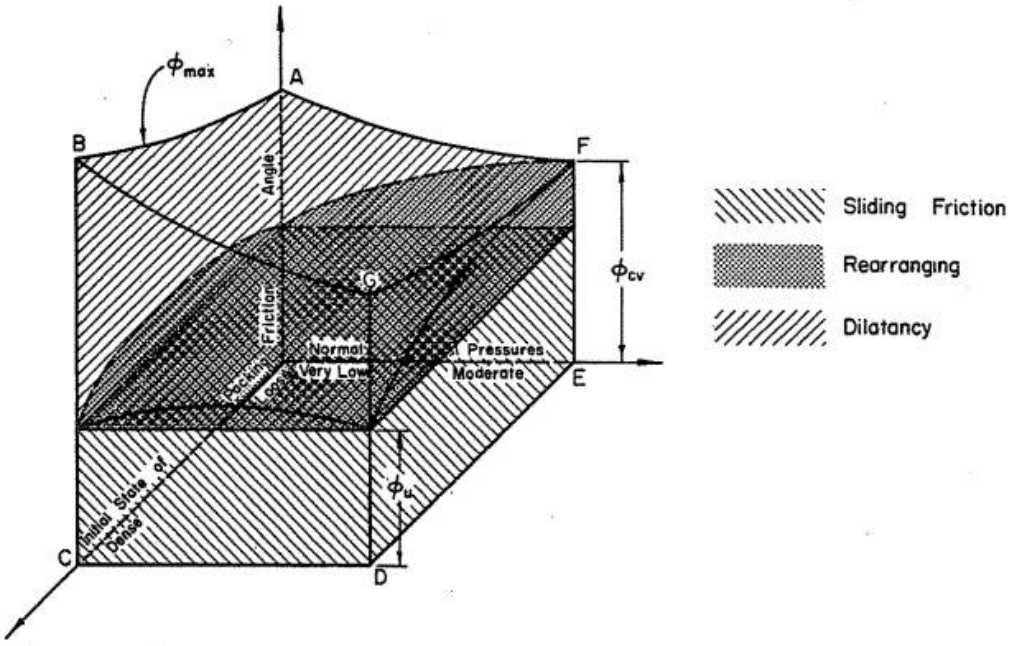

FIGURE 3.1: Tri-dimensional geometrical model of components of shear strength of sand as function of normal pressure range and initial state of packing (Ponce & Bell, 1971)

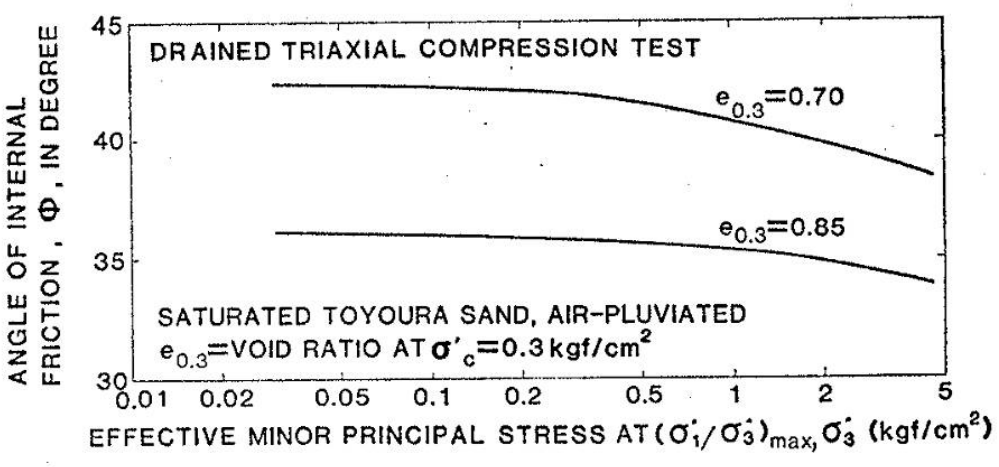

FIGURE 3.2: Relationships between angle of internal friction at peak, ϕ, in degree and effective minor principal stress (Fukushima & Tatsuoka, 1984)

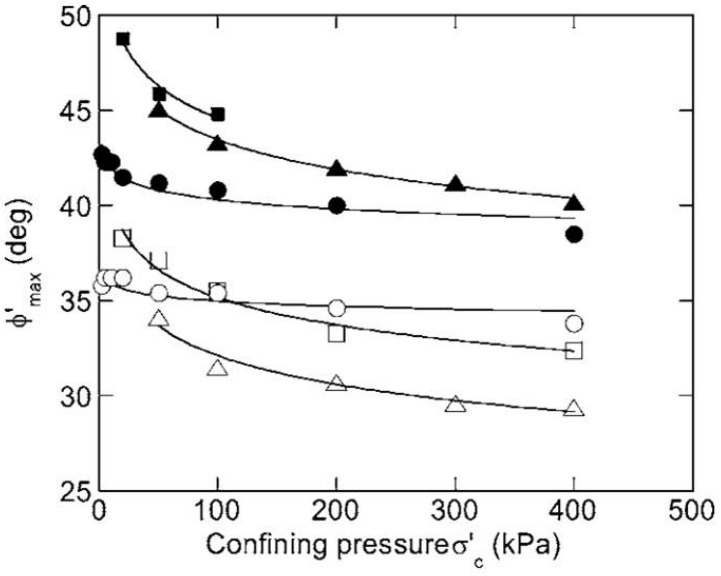

(a)

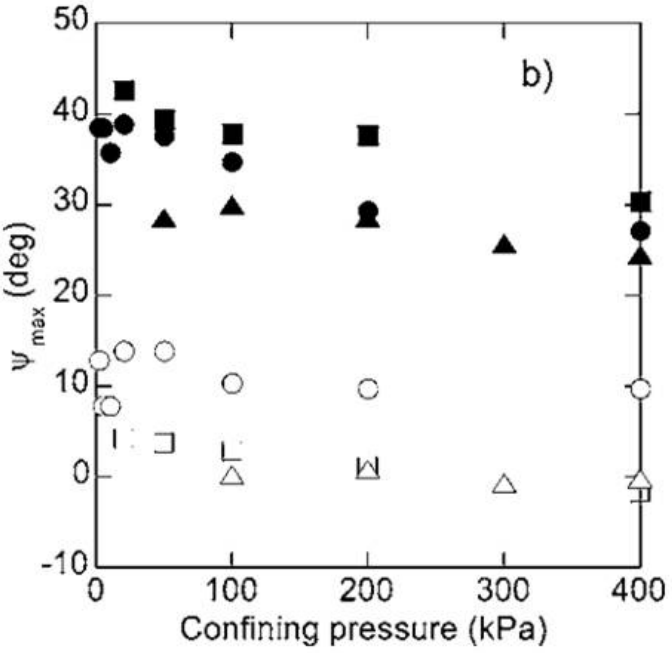

(b)

FIGURE 3.3: (a) Influence of confining pressure on maximum friction angle for different sands: Hostun (open square = loose, closed square = dense), Karlsruhe (open triangle = loose, closed triangle = dense), and Toyoura (open circle = loose, closed circle = dense) (b) Influence of confining pressure on ψ_{max} for Hostun sand (open square = loose, closed square = dense), Karlsruhe (open triangle = loose, closed triangle = dense), and Toyoura (open circle = loose, closed circle = dense) (Lancelot et al., 2006)

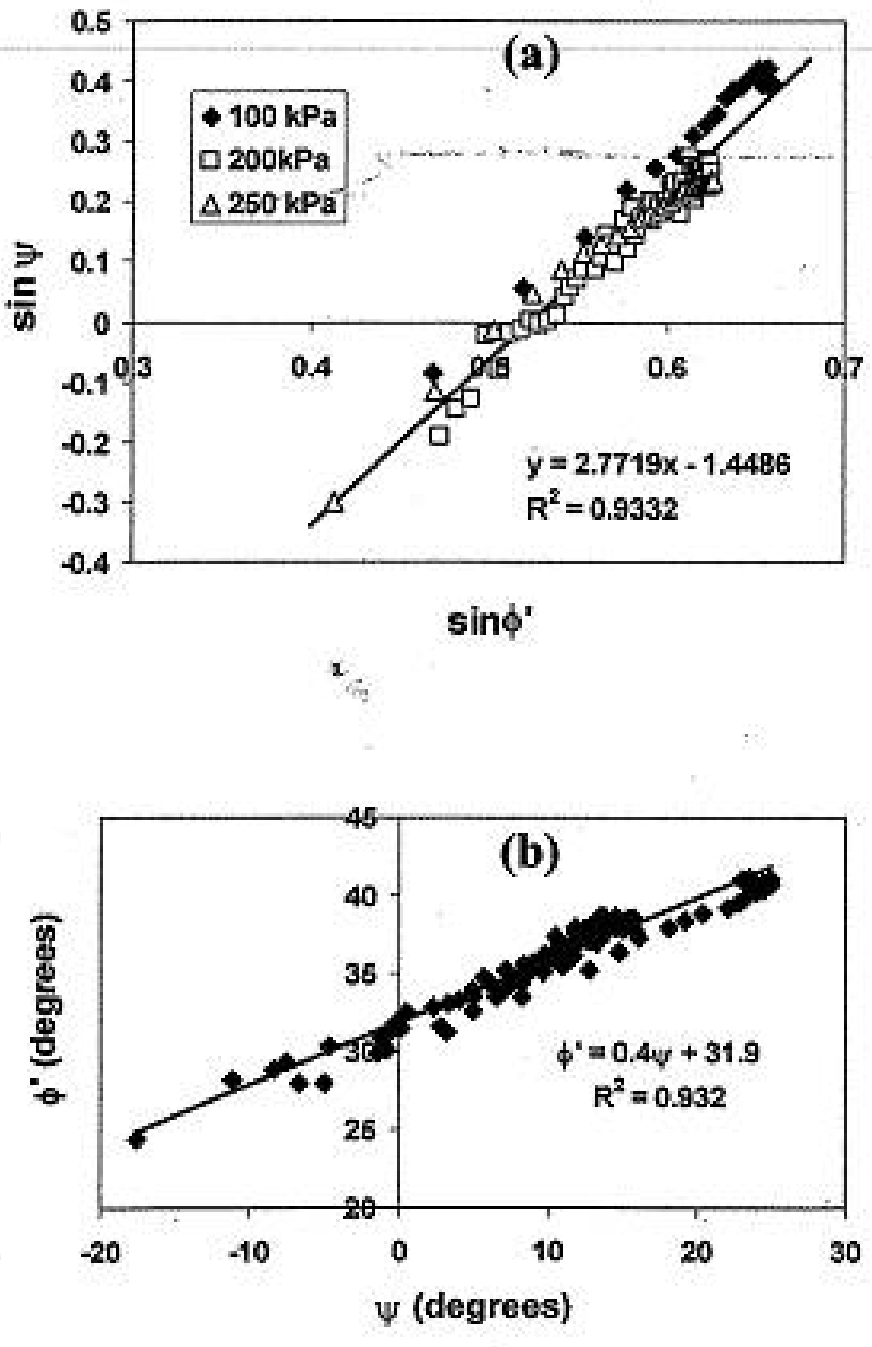

FIGURE 3.4: Stress-dilation relationship obtained from triaxial tests on undisturbed specimens (Frydman et al., 2007)

3.2 Materials

3.2.1 Reigate silver sand

To study the effect of interlocking structure in particular, Reigate silver sand from the same quarry as studied previously by Cresswell & Powrie (2004), was used in this study. Reigate silver sand is from the Folkestone Sand formation (Cretaceous, Lower Greensand age) of the southeast of England. Folkestone Sand is mainly a poorly cemented, quartzose fine, medium and coarse sand with considerable local variations in grading and cement contents (Richards & Barton, 1999). The silver sand itself is also variable, with some parts containing very small quantities of either clay or iron oxide cement (Cresswell & Barton, 2003).

Earlier thin sections of intact Reigate silver sand are shown in Figure 3.5. Computed Tomography (CT) images of intact Reigate silver sand are shown in Figure 3.6. The few white spots in the CT slices are the traces of iron oxide. In these figures, in comparison with the point contacts the existence of plenty of long straight and concavo-convex contacts can be seen. As reported by Cresswell & Barton (2003), the tangential index (the proportion of tangential contacts to all other types) is only 26% and the relative density is 136%. Figure 3.7 shows a Scanning Electron Microscope (SEM) image of the disaggregated grains. Grain morphology varies from well rounded to angular. Some few highly angular grains are also present.

3.2.2 Leighton Buzzard sand (Fraction B)

Leighton Buzzard sand (Fraction B) is quartzose, subrounded and uniformly graded sand. Figure 3.8 shows the SEM image. Grain size distributions for Leigthon Buzzard sand and disaggregated Reigate silver sand are shown in Figure 3.9. With significant differences primarily in grain shape, size and void ratio, and thence the resulting fabric structure, comparison with the test results on Leighton Buzzard sand provides an opportunity to identify dissimilarities of behaviour between the two sands.

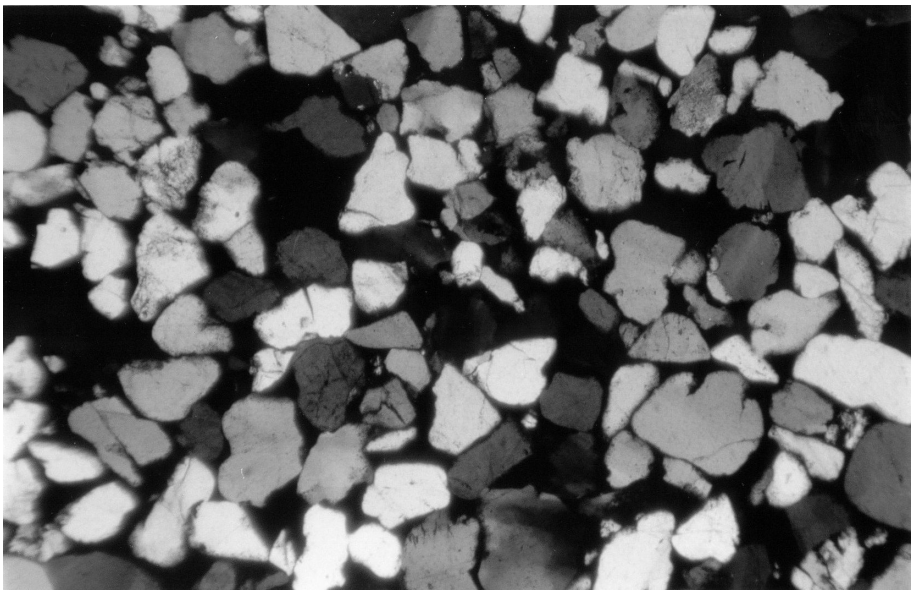

(a)

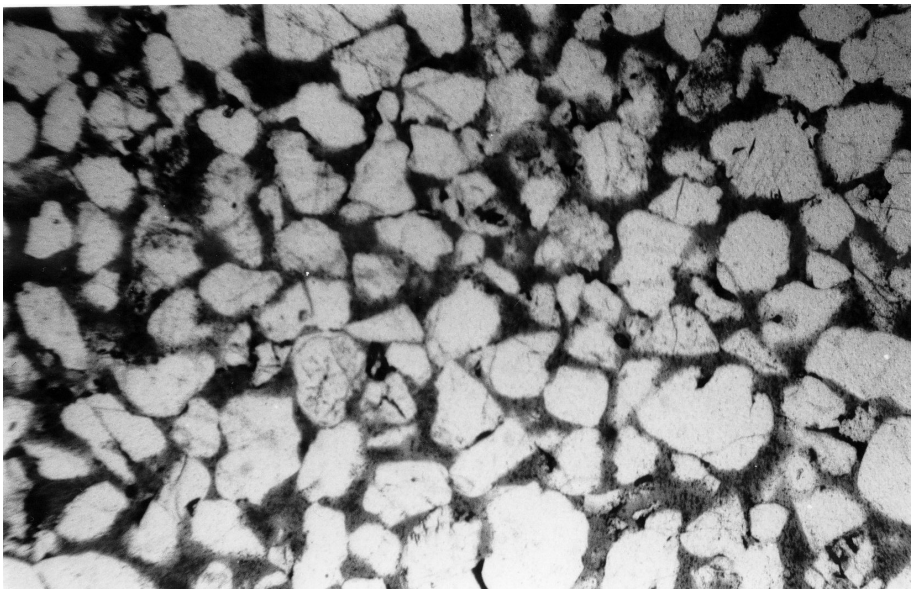

(b)

FIGURE 3.5: Reigate silver sand A4: (a) cross-polarised light, emphasising the grain contacts; (b) plane-polarised light, differentiating the quartz grains that are visible in (a) from the impregnating resin. Field of view 3mm. (Cresswell & Powrie, 2004)

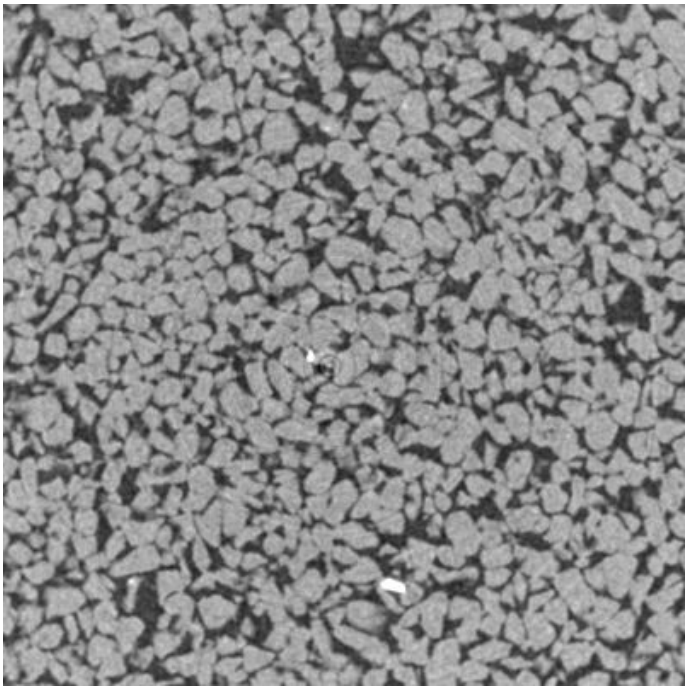

(a)

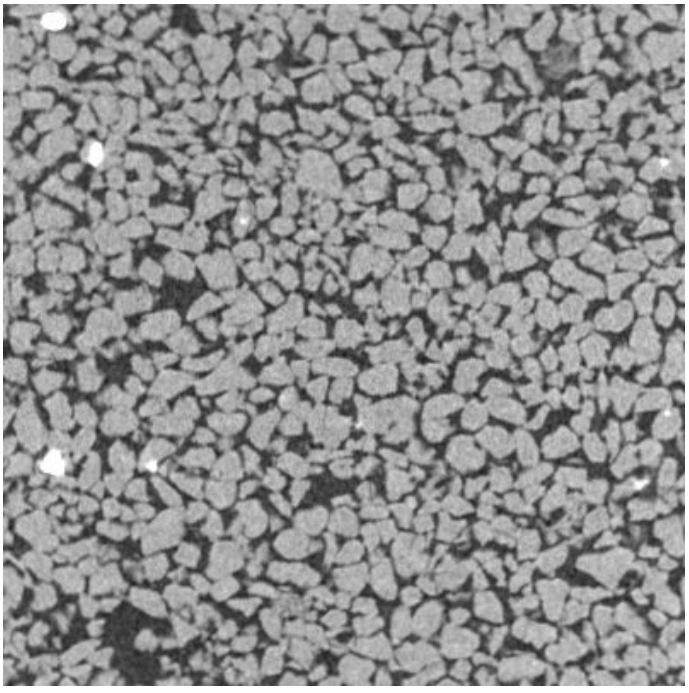

(b)

FIGURE 3.6: Intact Reigate silver sand CT images (a) Horizontal slice (i.e. on the horizontal plane or the bedding plane), and (b) Vertical slice. Field of view width is 3.68 mm and the resolution of CT scan is 9.62 μm. Few white spots are the traces of iron oxide. (See Appendix D for details about the *Computed Tomography (CT) Technology*) and the sample details

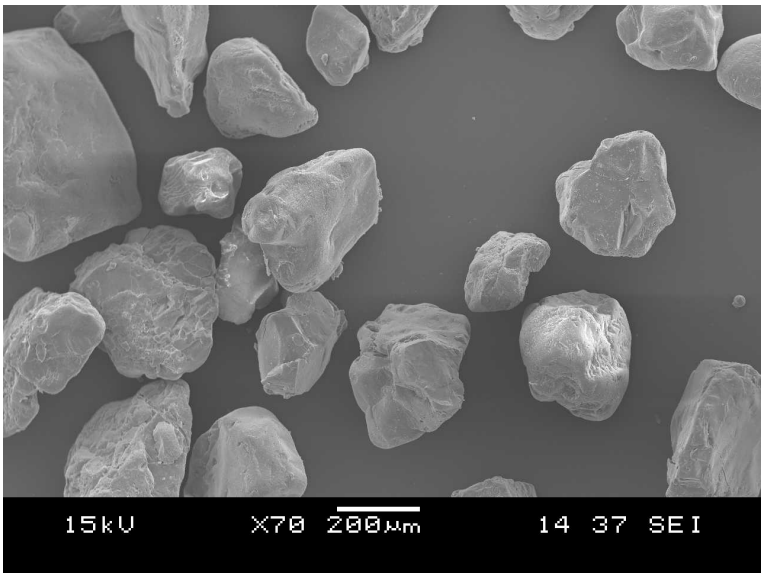

FIGURE 3.7: SEM image of disaggregated Reigate silver sand

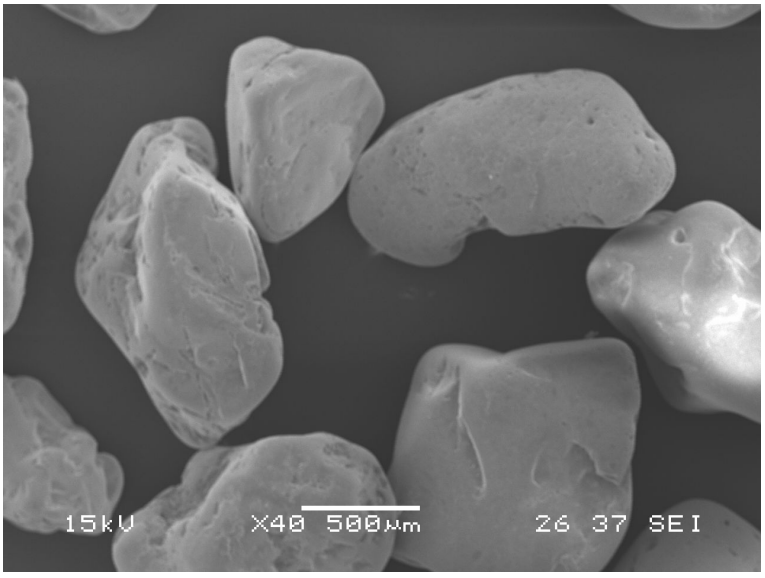

FIGURE 3.8: SEM image of Leighton Buzzard sand

3.3 Conventional triaxial compression test

3.3.1 Intact samples

3.3.1.1 Block sampling

The block samples of Reigate Silver sand used in this study were extracted from Park Pit Quarry, Tapwood, Buckland, Reigate, the same location as Cresswell

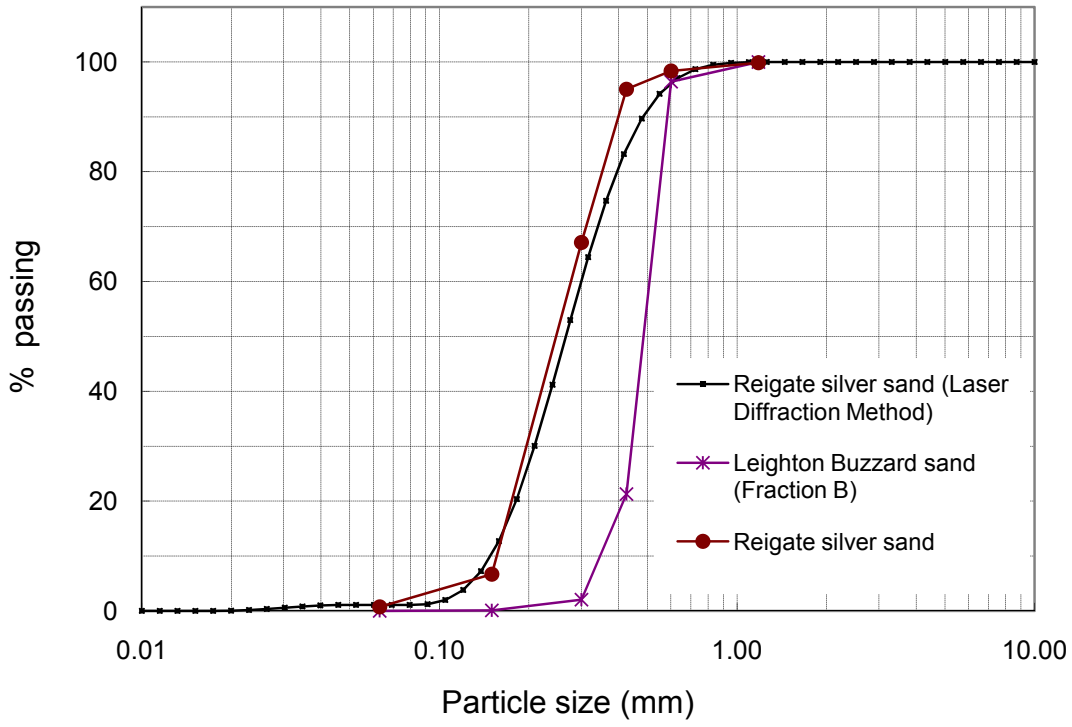

FIGURE 3.9: Particle size distribution curves for Reigate silver sand and Leighton Buzzard sand

& Powrie (2004). Block samples were taken very carefully by sawing using tools specially designed for this material. Cresswell (2001) described in detail the tools and methods of block sampling. During this research, when the field condition was wet, some attempts of block sampling were unsuccessful. The block samples were found to collapse easily while they were being placed in the plastic storage crates after cutting them from the ground. On the other hand, in dry conditions the sand blocks were found to be more stable and could be easily handled and placed in the plastic storage crates. Therefore, the additional strength produced by the matrix suction in the dry field condition could be responsible for the increased stability of the sand blocks. Some improvement of the method of Cresswell (2001) was made to enable sampling even in wet field conditions. Elasticated tubular support bandage was used to provide additional support. Figure 3.10 shows the procedure used to place the bandage around the block sample. After the sides of the block had been cut with the wide scraper saw, the stretcher was used to stretch the bandage and they were placed around the block. The bandage was pulled downwards from the bottom corners while holding and pulling the stretcher upwards. After the bandage had been placed around the sample, the base of the block was cut with the cord saw. The support provided by the bandage was sufficient to prevent any

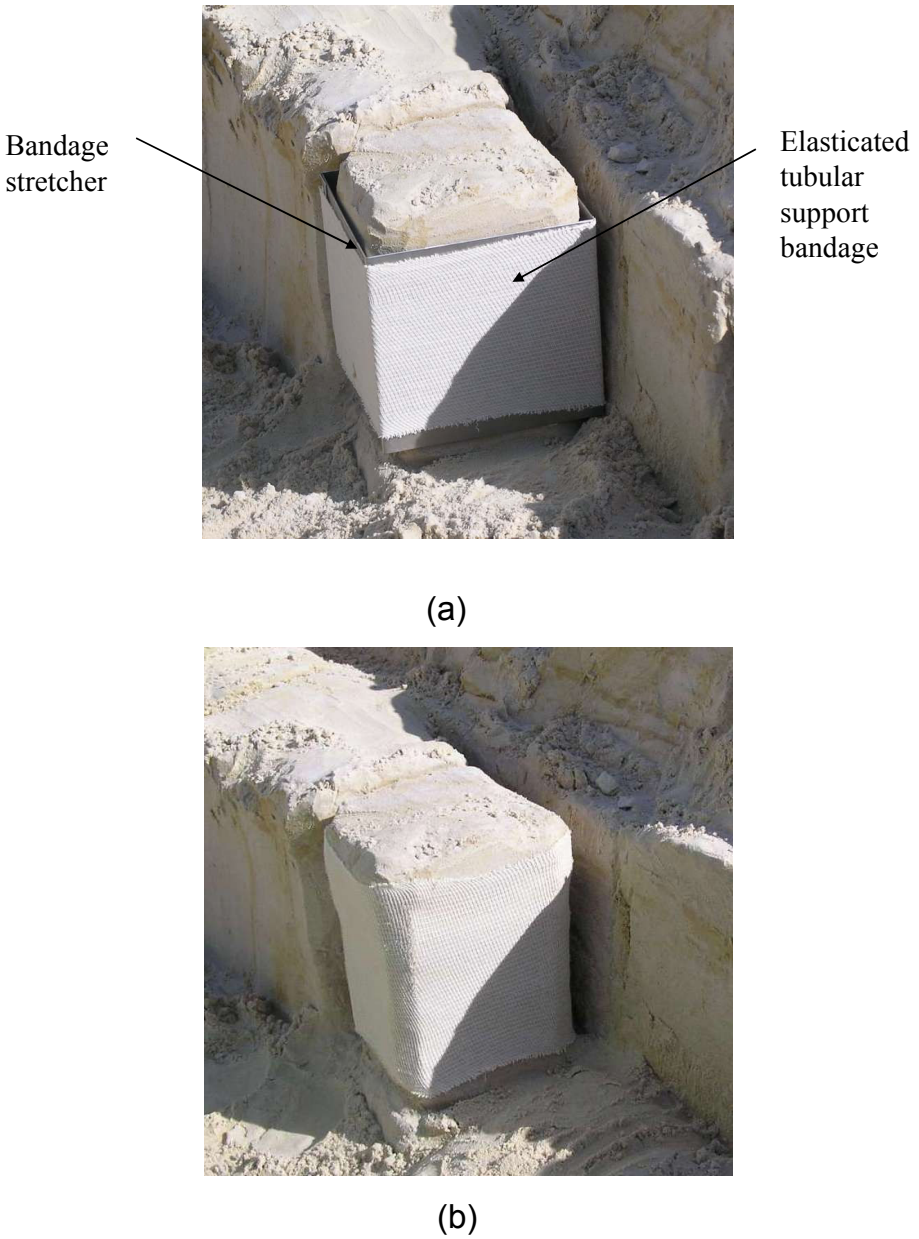

FIGURE 3.10: Procedure to place an elasticated tubular support bandage around the block sample (a) bandage stretched with the stretcher (b) bandage around the block sample

local cracking and also enabled easy handling and transportation of block samples. The blocks were transported from the quarry to the laboratory in plastic storage crates surrounded by firmly packed disaggregated sand.

3.3.1.2 Test sample preparation from a block sample

A considerable amount of time and effort is needed to prepare a cylindrical sample from a block of intact sand. Locked sands are cut or reduced in size by a process of grain plucking. This can be achieved by abrasion or a scraping action (Cresswell, 2001). The procedure for preparing a 70 mm diameter triaxial test sample is as follows:

1. The elasticated tubular support bandage was removed after transporting the samples to the laboratory. The samples were left for a few days to dry in air. Then the whole block sample was hairsprayed. It consists of two stages: first the exposed upper surfaces and then the underside after the top and the side faces were hardened and the sample was turned over.

2. The block sample was cut into smaller blocks using a surface-set tungsten carbide hacksaw blade on a glass plate. After each cut the new surface was hair-sprayed to maintain a continuous shell.

3. One end of the block was ground flat on the glass plate using abrasive, sprayed, and placed on a 70 mm platen.

4. The prism was filed down using grade 80 abrasive paper stuck to a right-angled wooden block. Figure 3.11 shows diagrammatic cross-sections of the sample at various stages of preparation. The hatched portions were removed at each stage. To maintain the circular cross-section, initially only one-eighth of the emerging cylinder was exposed at a time. A set square was used to check constantly for a right angle between the sample and the glass plate.

5. Step 4 was repeated until the cross-section of the cylinder was reduced almost to the required diameter. Then while preparing the final surface, to keep the surface perfectly cylindrical as far as possible, only one-sixteenth of the emerging cylinder was prepared at a time. Only the prepared areas were lightly hair-sprayed.

6. Next the top end of the sample was made flat. To keep the edge perfect when finished special care was taken while flattening the top. After cutting the top, the edge was chamfered as shown in Figure 3.12 and then made flat using the abrasive side of the wooden block. To check that the top end was parallel to the glass plate, a platen was placed on the top of the sample and

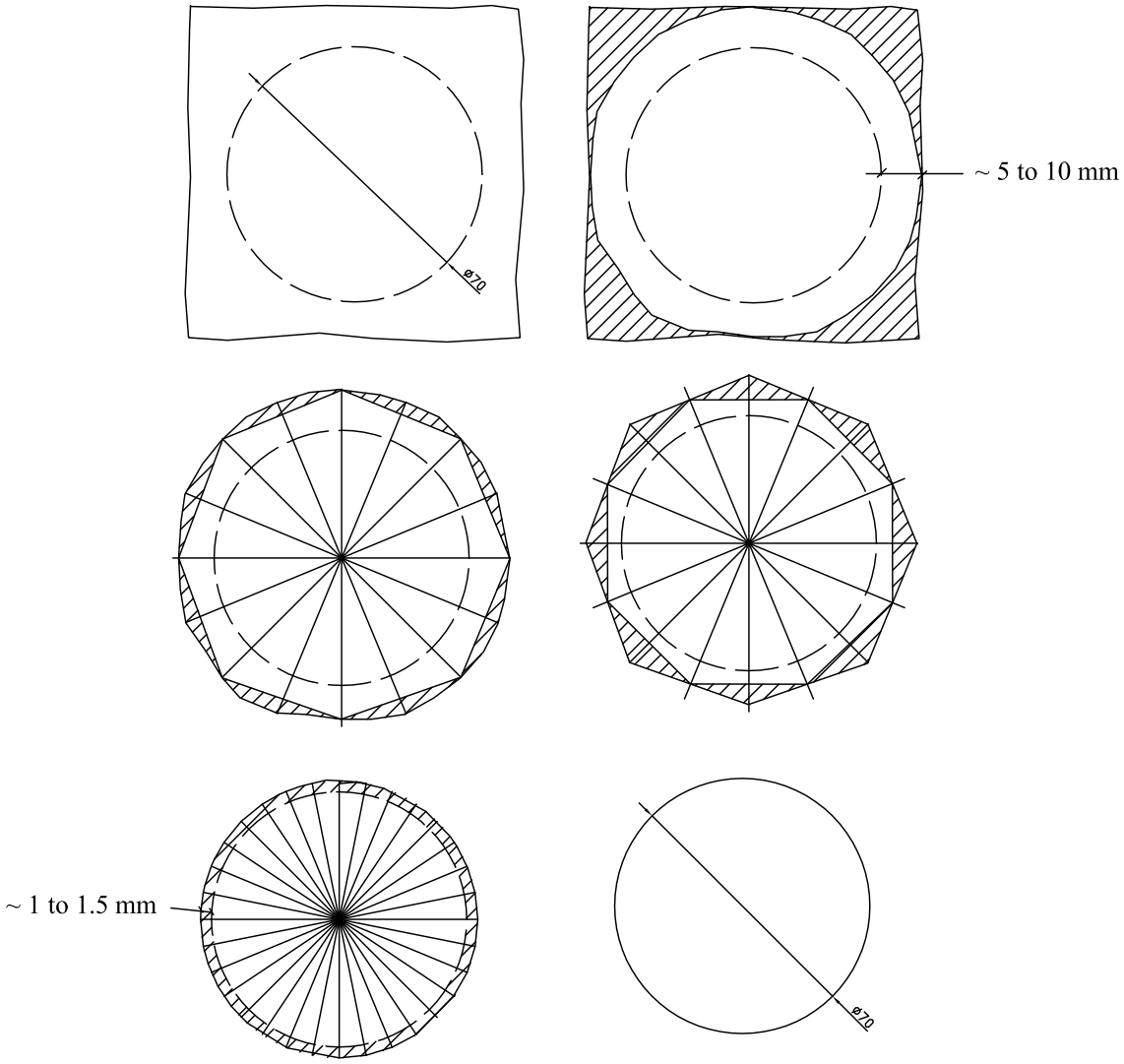

FIGURE 3.11: Diagrammatic illustration of the sample cross-sections during preparation:(a) initially, (b) corners (hatched portions) to be filed down, (c) and (d) one-eighth portion (hatched portions) to be filed down, (e) cross-section when reduced to almost required diameter (f) the sample cross-section when prepared.

a 300 mm straight edge placed on this. Measurements between the ends of the straightedge and the glass plate were taken. These were kept within 2 mm of each other, giving a tolerance on the sample ends of 0.24 mm or 0.368 degrees (Cresswell, 2001). In addition, a bubble level was also used to check the level of top end.

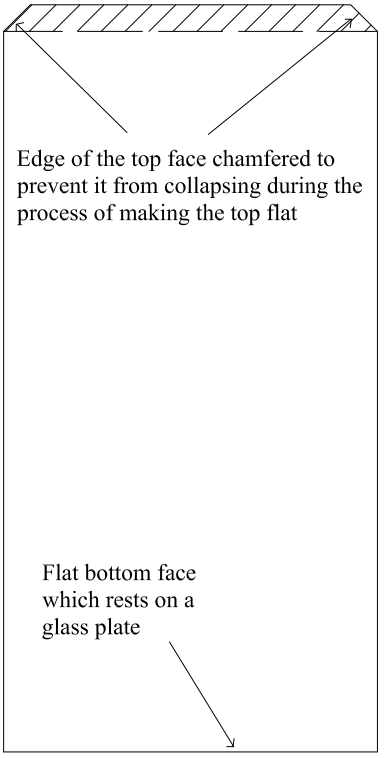

FIGURE 3.12: Preparation of the top face of a sample

3.3.2 Pluviated samples

Pluviation is a widely used method for the preparation of sand samples for laboratory testing. The samples are easily reproducible and uniform. High dry density can also be achieved. The maximum dry density can be achieved by controlling the depositional density, uniformity of sand rain, and the height of the drop (Cresswell et al., 1999). Since the purpose is to compare the behaviour of pluviated samples with intact Reigate silver sand, pluviated samples of Leighton Buzzard sand and Reigate silver sand were prepared at the maximum possible dry density. The apparatus used for preparation of samples by pluviation is shown in Figure 3.13. Height of the drop, measured from the delivery funnel bottom opening to the mid-height of the sample, was 700 mm. The depositional density can be varied by controlling the diameter of the delivery funnel bottom opening. For pluviated samples of Leighton Buzzard sand, the opening diameter was kept 4.5 mm wide. For pluviated samples of Reigate silver sand, the opening diameter was kept 11.5 mm wide. The dry density and minimum average void ratio of pluviated samples of Leighton Buzzard sand prepared in the laboratory were about 1.477 Mg/m^3 and 0.48, respectively. In pluviated samples of Reigate silver sand, the dry density

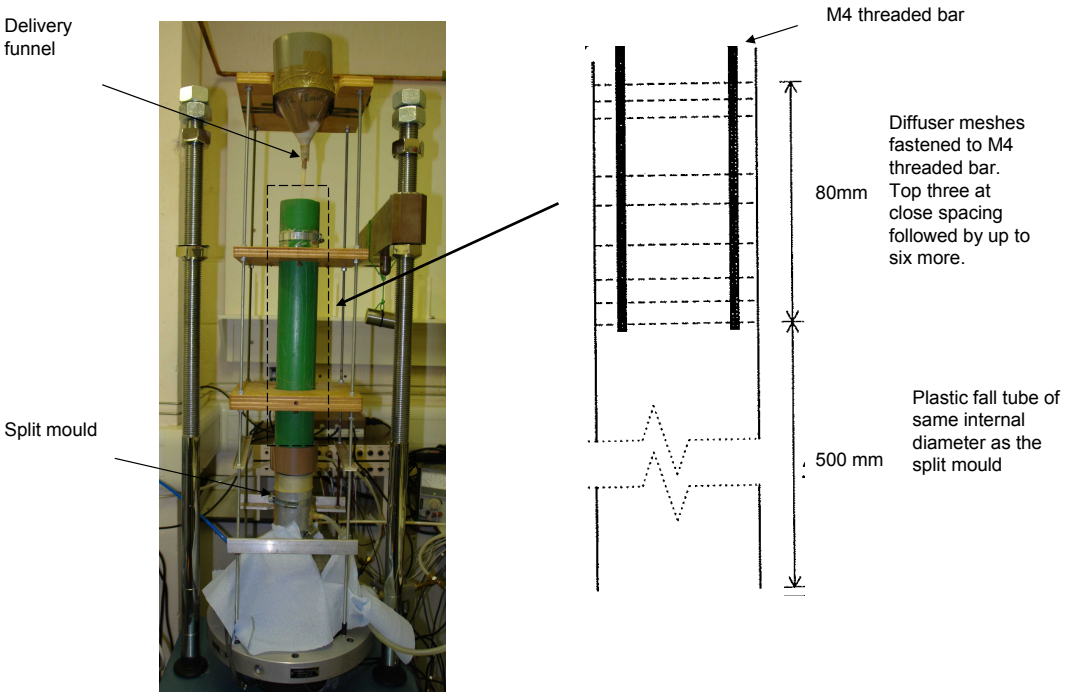

FIGURE 3.13: Pluviation apparatus (after Cresswell et al., 1999)

and minimum average void ratio were about 1.650 Mg/m^3 and 0.60, respectively. The average void ratio of intact samples of Reigate silver sand is about 0.44. The average void ratios of intact and pluviated samples of Reigate silver sand tested by Cresswell & Powrie (2004) were about 0.46 and 0.66, respectively.

3.3.3 Description of triaxial cell and local instrumentation

The first set of tests (Series B1) was carried out on 70 mm diameter × 140 to 150 mm high samples in a strain-controlled triaxial apparatus comprising a modified Wykeham Farrance cell (Figure 3.14). This cell (internal diameter 230 mm) provided enough room for local instrumentation (including radial strain calliper) within the cell. Local instrumentation consisted of an internal load cell to measure the axial force; four LVDTs (*RDP Electronics*) to determine local axial strains, mounted vertically at 90 degree intervals on plan over the middle 40 mm of the sample; and an LVDT monitored radial strain calliper (Figure 3.15).

The second set of tests (Series B2) was carried out on 70 mm diameter × 148 to 178 mm high samples in a strain-controlled triaxial apparatus comprising a transparent triaxial cell, three digital cameras, uniform light source, and light reflecting surface

(Figure 4.3, Chapter 4). Local instrumentation consisted of an internal load cell (same as in the above test series); three LVDTs (*RDP Electronics*) in some of the tests to determine local axial strains and to compare with the new image-based measurement technique (will be described in Chapter 4). The results from this test series are described in detail in chapter 5. In this chapter, the test results from series B2 are included in the discussion section for the purpose of comparison.

The above tests were carried out with the top cap arrangement modified by (Cresswell & Powrie, 2004) on the axial loading system (Figure 3.15). This arrangement ensures the applied axial load to transmit vertically through the centre of the top platen. It also allows for any misalignment of the sample during docking.

3.3.4 Challenges involved in low pressure triaxial testing

Because of low effective cell pressures involved, careful considerations are required for the several factors that normally would be expected to have a negligible effect on the test results. These factors include the stability of the cell and pore pressure application system, the additional strength contributed by the rubber membrane enclosing the sample, and the effect of the stiffness of LVDT cable.

3.3.4.1 Control of cell and pore pressure

When two standard GDS controllers were used to control cell and pore pressures independently, hunting was observed as the sample started to dilate. This was evident from the fluctuations of the cell and pore pressures and as a consequence the non-smoothness of stress-strain curve in Figure 3.16. To eliminate this effect and for better control of the cell and pore pressures in low pressure tests, a new arrangement for applying the cell pressure and the pore pressure was developed. Cell pressure was applied through a pipe connected to a cylinder with an air/water interface inside it (Figure 3.14(c)). A constant air pressure was maintained (measured by a pressure gauge) in the air chamber. A new high resolution pressure/volume controller (with 0.01 kPa resolution supplied by GDS Ltd.) was used to control pore pressure.

Figure 3.17 shows cell pressure (σ_c), pore water pressure (σ_u) and effective cell pressure ($\sigma_c^{'}$) plotted against global axial strain during a drained triaxial compression

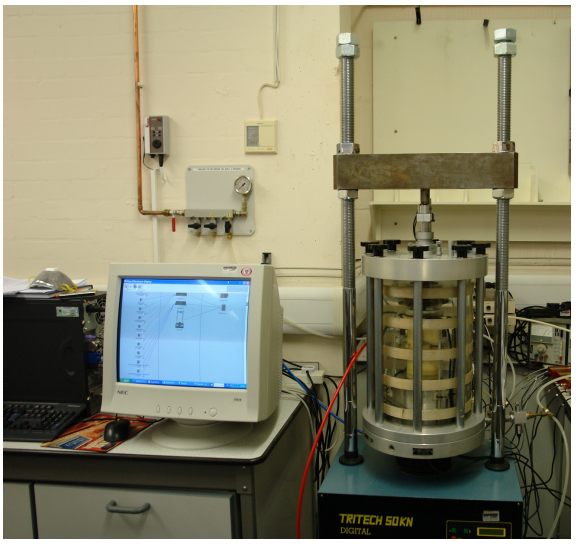

(a)

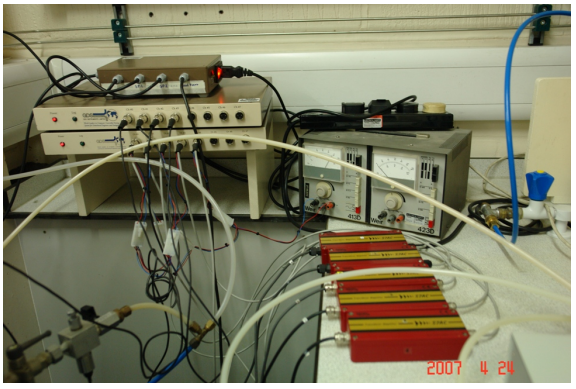

(b)

(c)

FIGURE 3.14: (a) The triaxial cell and computer (b) GDS datalogger, voltage supplier and transducer amplifiers (c) cell pressure and vacuum application system

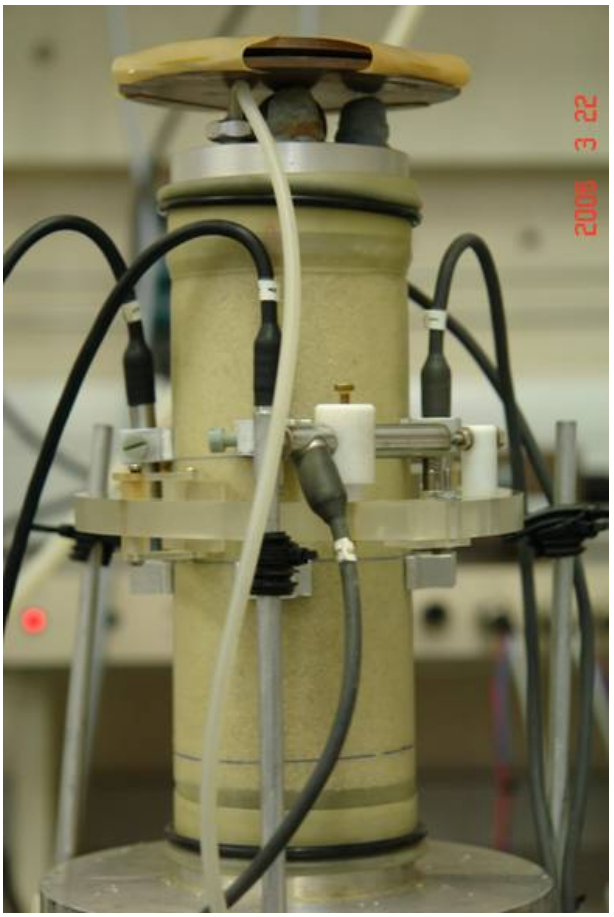

FIGURE 3.15: Sample with all instrumentation for local strain measurement and the top cap arrangement

test. σ_c and σ_u, remained approximately constant at 62.5 and 50 kPa respectively, even while the sample was dilating, and therefore effective cell pressure of 12.5 kPa remained constant throughout the test.

3.3.4.2 Additional strength contributed by the rubber membrane

Due to the very rough surfaces of the sand samples and also as the buckling of membrane can occur at a larger strain, it is difficult to find an exact method of stress corrections for membrane forces (Fukushima & Tatsuoka, 1984). In their study, they compared three different methods, all based on elasticity theories:

- Method I assumed that a membrane has a shape of perfect thin-wall cylindrical shell. This method was called *Compression shell theory* by Henkel & Gilbert (1952).

- Method II assumed that in a membrane the axial deformation occurs independently of the radial and circumferential deformations.
- Method III assumed that the resistance of membrane against axial deformation is negligible due to buckling and there is resistance only in the radial and circumferential directions. This method was called *Hoop tension theory* by Henkel & Gilbert (1952).

Their main findings about methods I, II and III are summarised below:

- Both Method I and Method III can be considered appropriate for the membrane force correction at peak stress conditions (Figure 3.18).
- In physical terms, Method III is more reasonable than Method I at larger axial strains while Method I was considered more reasonable than Method III at small axial strains.
- Method II is unrealistic from the viewpoint of elasticity theory.

Method III will be used to correct for the membrane forces in this study (see Section 3.5, Equation 3.3).

3.3.4.3 Effect of the stiffness of LVDT cable

The shakiness of the LVDT holders increases with decreasing effective cell pressure. Since the tests were required to run at low effective stresses, the effect of the stiffness of LVDT cable on the measured displacement requires consideration. An LVDT was set up on a vacuum (20 kPa) confined sample. The LVDT cable was then pushed upward by lifting the plug through which LVDT cables were passed to the cell by about 2mm as shown in Figure 3.19. No difference in LVDT reading was observed. This test confirms that LVDT measurements up to at least 5% local axial strain were not affected by the stiffness of the cable. LVDT readings after peak, at which a shear band has already started to form or the sample started to bulge, are of little relevance; the present LVDT setup therefore serves its purpose.

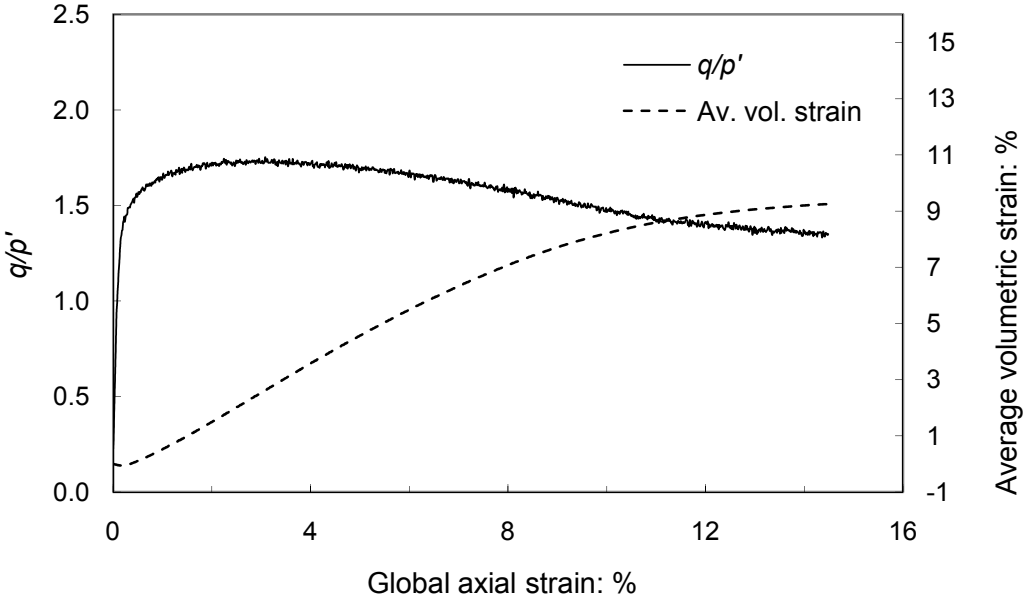

(a)

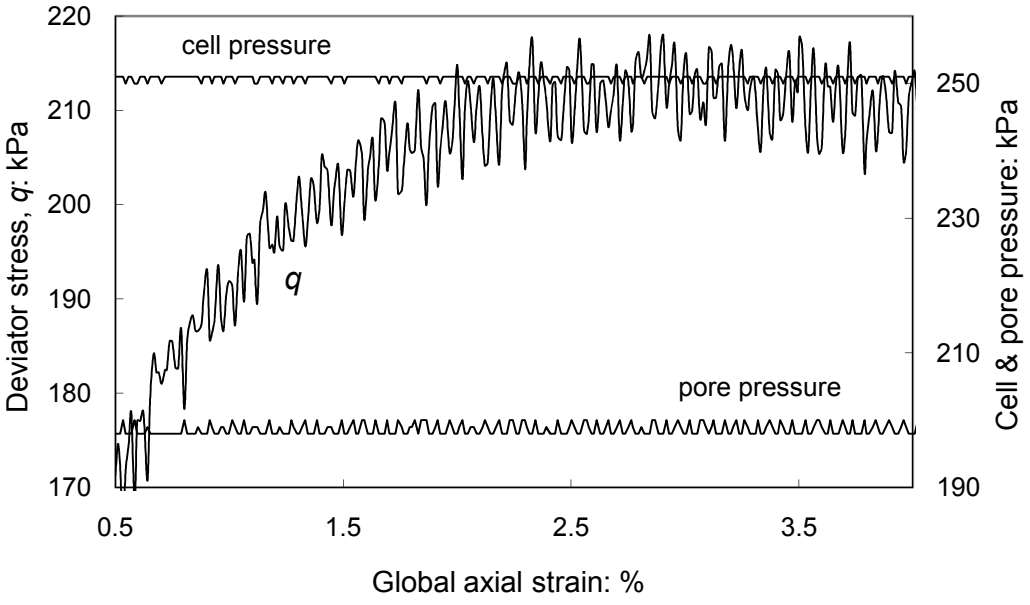

(b)

FIGURE 3.16: The hunting effect: (a) Stress-ratio and volumetric strain plotted against global axial strain; (b) deviatoric stress (q), cell pressure (σ_c) and pore water pressure (σ_u) plotted against global axial strain. Note the fluctuations of σ_c and σ_u, which are intended to remain constant at 250 kPa and 200 kPa respectively, even while the sample is dilating.

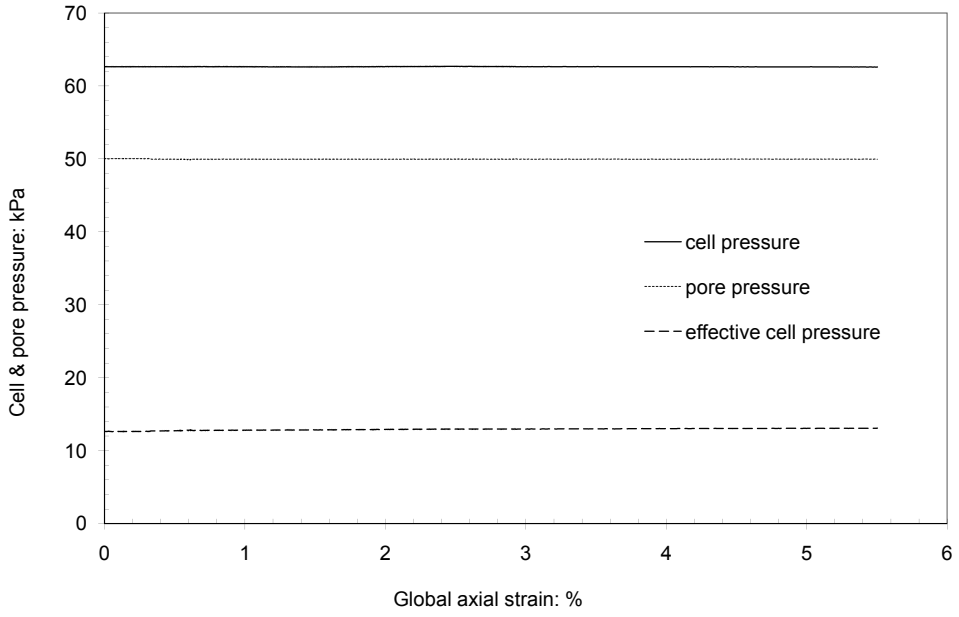

FIGURE 3.17: Cell pressure (σ_c), pore water pressure (σ_u) and effective cell pressure ($\sigma_c^{'}$) plotted against global axial strain. σ_c and σ_u, remained approximately constant at 62.5 kPa and 50 kPa respectively, even while the sample was dilating thus effective cell pressure of 12.5 kPa remained constant throughout the test.

3.3.5 Calibration and datalogging system

The load cell and the pressure transducers were calibrated using a dead-weight calibration system (DH Budenberg Ltd., 580-series hydraulic dead-weight tester). The LVDTs were calibrated with a micrometer (Mitutoyo series 152-348), which has a range of 25 mm and a resolution of $\pm 1 \mu m$. Pressure readings of the advanced GDS pressure/volume controller with water columns (10 mm diameter, therefore any capillary effect can be neglected) of various heights at its entrance/outlet were recorded and compared. The maximum error was found to be $\pm$ 0.06 kPa. Cell and pore pressure transducers were also checked by the advanced controller in the range of 10 to 110 kPa. A maximum discrepancy of 1.15 kPa was observed at 110 kPa. All of the instruments were logged using a personal computer using the GDSLAB software and a GDS Ltd datalogging system (16 *bit* data acquisition).

The details and calibration results for the load cell, pressure transducers, and LVDTs; the results of a check of the advanced GDS controller reading against water columns, and check of cell and pore pressure transducers by the advanced controller are shown in Appendix A.

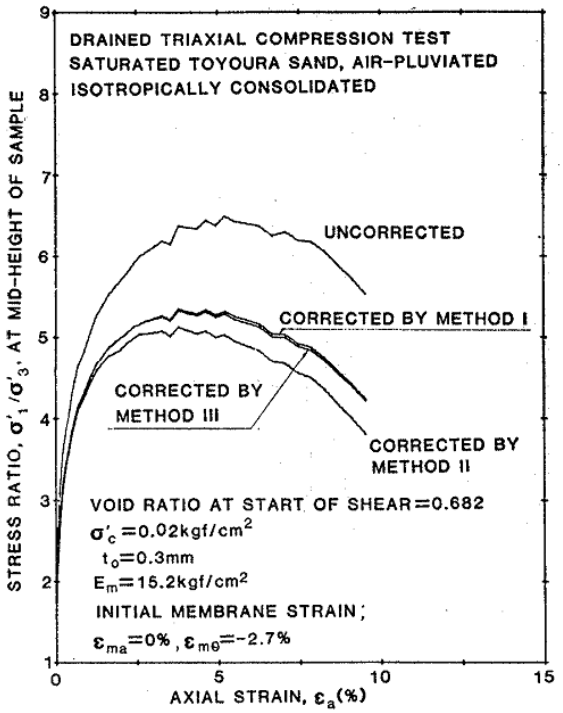

(a)

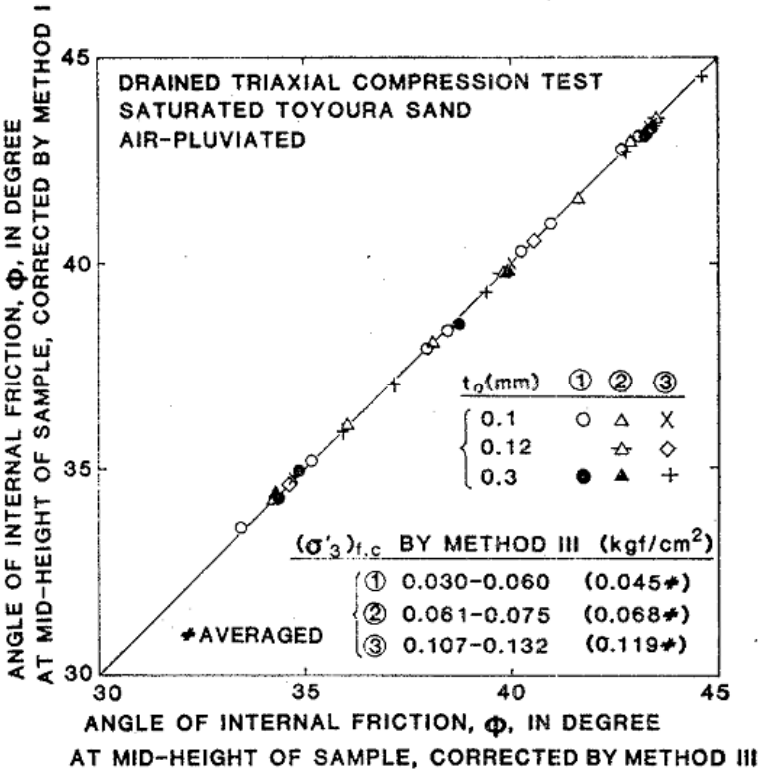

(b)

FIGURE 3.18: (a) Stress-strain relationships for stresses corrected or uncorrected for membrane forces ($1kgf/cm^2 = 98kN/m^2$), (b) Angle of internal friction at peak corrected by Method I versus by Method III for $\sigma_c^{'}$ equal to or less than $0.1kgf/cm^2$ ($9.8kN/m^2$) (after Fukushima & Tatsuoka (1984))

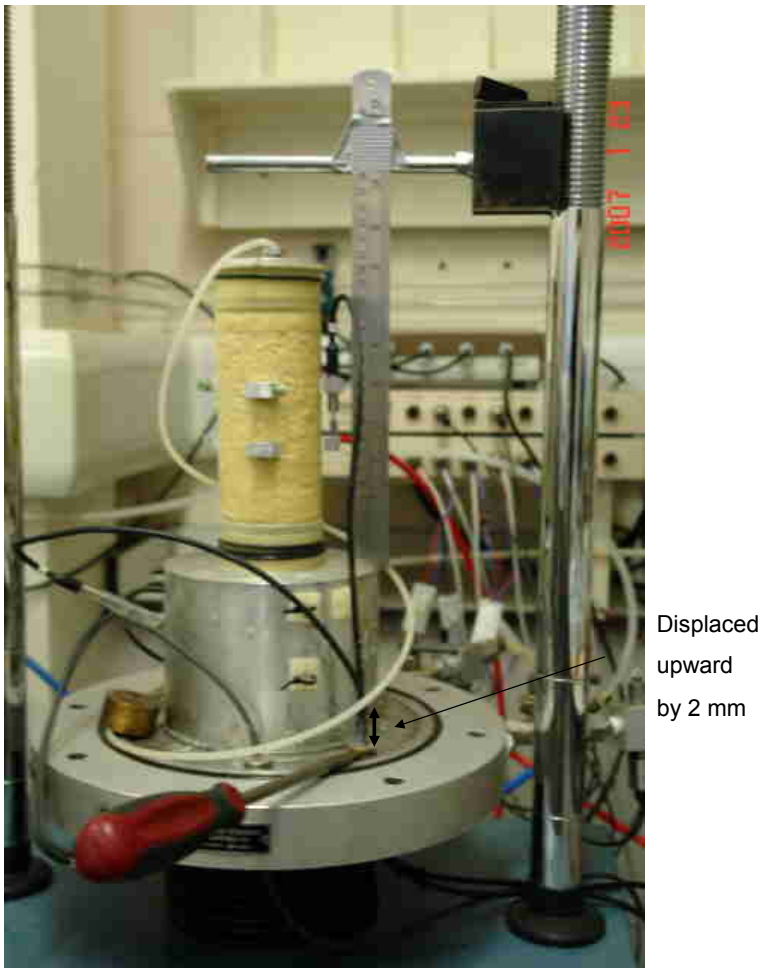

FIGURE 3.19: Examination of effect of stiffness of cable on recorded readings

3.4 Test procedure

3.4.1 Saturation and consolidation

The procedures for preparing cylindrical samples from an intact block of Reigate silver sand and by pluviation were explained in the previous section. Here, the procedures for setting up the sample in triaxial cell, its saturation and consolidation before shearing at a desired cell pressure are described. Keeping the sample under a vacuum of about 15 *kPa*, LVDT holders were stuck to the membrane using super glue and the LVDTs were set up to lie at one end of the calibration range. The cell was then filled with de-aired water and pressurised to about 20 *kPa*. Before passing de-aired water through the sample, carbon dioxide gas was flushed through the sample for about 5 minutes at a pressure not exceeding 10 *kPa*. More than 2000 *ml* of de-aired water was passed through the sample. In case

of the intact samples, it was important to flush out the hair spray. The sample was left overnight at a back pressure of 50 kPa. The cell pressure was kept 15 kPa higher than the back pressure. When checked the following day, the B value was usually found to be in the range of 0.92-0.96. Although, it is difficult to estimate the degree of saturation from the B value, in view of the stiffness of the material a B value in the range of 0.92-0.96 indicates that the sample is adequately saturated (Bishop, 1973; Black & Lee, 1973; Lade & Boer, 1997). All the tests were conducted in drained conditions, with nonlubricated end platens.

3.4.2 Shear deformation

Samples were sheared at a constant axial strain rate of 0.018 %/minute (in the case of an intact sample) or 0.036 %/minute (for a pluviated sample). These strain rates enabled control of the pore pressure during shearing, even when the sample was dilating at its maximum rate. The tests were carried out at 1 % per hour or 0.017 %/minute by Cresswell & Powrie (2004). The process of shearing was continued until the load reached an approximately constant value and the rate of volume change of the sample became negligible. The test data were recorded typically every 10 seconds in the case of intact samples and every 20 seconds for pluviated samples.

3.5 Description of parameters

3.5.1 Stress parameters

The effective vertical (axial) stress is calculated (in kPa) as

$$\sigma_1^{'} = \frac{Q}{A_{eff}} + (\sigma_c - \sigma_u) \tag{3.1}$$

where Q is ram load (in kN), A_{eff} was the effective cross-sectional area of the sample during shearing (in square metres), σ_c is the cell pressure (in kPa) and σ_u is the pore water pressure (in kPa).

The effective cross-sectional area of the sample, A_{eff}, was calculated assuming that the sample remains a right circular cylinder during shearing. Thus, $A_{eff} = \frac{V_0 - \triangle V_{tf}}{H_o - \triangle H}$, where V_0 and H_0 are the volume and height of the sample at the start of shearing, and $\triangle V_{tf}$ and $\triangle H$ are the changes in volume and height of the sample during shearing.

The effective horizontal (radial) stress is given by

$$\sigma_3^{'} = (\sigma_c - \sigma_u) + \delta\sigma_3 \tag{3.2}$$

where $\delta\sigma_3$ is the additional radial stress due to membrane deformation. Considering the membrane as a thin elastic tube undergoing the same deformations as the sample, the average radial extra stress due to the deforming membrane can be calculated as (Fukushima & Tatsuoka, 1984; Bishop & Henkel, 1962)

$$\delta\sigma_3 = \frac{2\, t_m\, \varepsilon_r\, E_m}{d} \tag{3.3}$$

where E_m is the membrane Young's modulus (1.3 MPa (Lancelot et al., 2006)), t_m is the membrane thickness (0.3 mm), d is the current sample diameter (which varies during the test) calculated using A_{eff} and ε_r is the sample radial strain. For an intact sample tested at 12.5 kPa effective cell pressure, the additional radial stress exerted by the membrane at the end of shearing process (i.e. at large strain) was found to be less than 4.0 % of the applied effective cell pressure. For a pluviated sample tested at 12.5 kPa effective cell pressure, it was found to be about 12.0 % of the applied effective cell pressure.

For studying the stress:strain behaviour of soils in triaxial stress conditions, the pair of stress parameters, mean effective stress, p', and deviator stress, q , are defined as follows (Muir Wood, 1984):

$$p^{'} = \frac{\sigma_1^{'} + 2\sigma_3^{'}}{3} \tag{3.4}$$

$$q = \sigma_1^{'} - \sigma_3^{'} \tag{3.5}$$

3.5.2 Strain parameters

Global axial strain (ε_a): calculated as the change in height of the sample in the axial direction divided by the initial height of the sample.

Average local axial strain (ε_1) : the arithmetic mean of the local strains measured by the four LVDTs. The local strain measured by each LVDT is obtained by dividing the recorded displacement with the gauge length, i.e. the spacing of pedestals holding the LVDT (40 *mm*).

Average local radial strain (ε_3): the change in the sample diameter measured by the local radial strain gauge (half the recorded displacement since it is measured at one end only (Bishop & Henkel, 1962)) divided by the initial diameter of the sample.

Average volumetric strain (ε_{vol}): the change in volume of the sample, as measured by the GDS advanced pressure/volume controller which measures the volume of pore water in and out of the sample while maintaining a constant pore pressure, divided by the initial volume of the sample. During shearing in which deformation localises into a narrow band, this does not represent the true volumetric response of the sample after rupture.

Specific volume:

$$v = 1 + e = \frac{V_t G_s \rho_w}{m_s} \tag{3.6}$$

where, V_t is the volume of the sample at the current stage of shearing, G_s is the grain specific gravity (taken as 2.64; (Powrie, 2004)), ρ_w is the mass density of water, m_s is the dry mass of sand on the sample.

3.5.3 Other parameters

Tangent Shear Modulus (G):

The deviatoric stress increment divided by the corresponding shear strain increment calculated over an interval of 100 seconds (The test data were recorded typically every 10 seconds in the case of intact samples and every 20 seconds for pluviated samples).

$$G = \frac{\delta q}{2\left(\delta\varepsilon_1 - \delta\varepsilon_3\right)} \tag{3.7}$$

Mobilised friction angle (ϕ'_{mob}):

Considering the Mohr-Coulomb Criterion, the mobilised friction angle at any stage of shearing for a material with zero cohesion can be calculated as

$$\phi'_{mob} = \frac{\sigma'_1 - \sigma'_3}{\sigma'_1 + \sigma'_3} \tag{3.8}$$

Rate of dilation (d):

$$\mathsf{d} = \frac{\delta\varepsilon^p_{vol}}{\delta\varepsilon^p_s} = \frac{2 \times \delta\varepsilon^p_{vol}}{(3 \times \delta\varepsilon^p_a + \delta\varepsilon^p_{vol})} \tag{3.9}$$

where, $\delta\varepsilon^p_{vol}$ is the plastic volumetric strain increment and $\delta\varepsilon^p_s$ is the plastic triaxial shear strain increment defined as $\delta\varepsilon^p_s = 2/3(\delta\varepsilon_a - \delta\varepsilon_r)$. The changes in elastic strain components are assumed to be negligible.

Dilation angle (ψ) (Houlsby, 1991; Vaid & Sasitharan, 1992):

$$\psi = sin^{-1}\left(-\frac{\delta\varepsilon^p_a + 2\delta\varepsilon^p_r}{\delta\varepsilon^p_a - \delta\varepsilon^p_r}\right) \tag{3.10}$$

3.6 Test results

3.6.1 Small strain behaviour

For intact Reigate silver sand (RSS) samples, initial shear moduli during shearing were found to depend on the applied cell pressures (Figure 3.20(a)). As can be seen, initially the shear modulus decreased quite gradually with strain. The sample starts to compress, at first as stiffness decreases but then accelerates suddenly as the stiffness starts to recover to the initial value. The initial compression may be due to the elastic deformation of grains and initial contacts sliding. As more flat contacts slip into place, the fabric becomes more locked resulting in the increase in stiffness. The onset of yielding, evident by the sharp reduction of stiffness and the development of relatively large strains, corresponds to 0.1 % average local axial strain. As can be seen in Figure 3.20(b), the onset of yielding also coincides with the onset of volumetric dilation.

In the case of pluviated RSS samples, the dependence of the initial moduli on the applied cell pressure can be seen in Figure 3.21. However, the magnitudes of shear moduli in general are much smaller than for the intact samples tested at same cell pressures (cf. Figure 3.20(a)). A relatively smooth variation in the shear moduli with no well-defined yield points can be seen. The onset of volumetric dilation does not coincide with the onset of yielding (Figure 3.21(b)). As shown in Figure 3.22(a), the Leighton Buzzard sand (LBS) samples show high initial shear moduli. Again, the onset of volumetric dilation of these samples does not coincide with the onset of yielding (Figure 3.22(b)).

Figure 3.23(a) compares the tangent shear moduli for intact RSS, pluviated RSS and pluviated LBS at an effective cell pressure of 100 kPa. The initial shear moduli for the intact RSS and pluviated LBS were almost equal. With increasing strain, the shear modulus of intact sample of RSS decreased initially then increased again to equal the initial stiffness and thereafter decreased more rapidly with strain. However, the pluviated LBS and pluviated RSS samples showed a steady decrease in shear modulus with increasing strain. The onset of yielding corresponds to the onset of volumetric dilation in intact samples, while in pluviated samples no such correspondence was observed (Figure 3.23(b)). Figures 3.24- 3.26 compare the shear modulus of the test materials as a function of effective stress at three different average local axial strains.

Figure 3.27 shows the unloading-reloading response of an intact RSS sample tested at effective cell pressure of 50 kPa. It shows hysteresis and irreversible strains. It can be interpreted as the start of fabric destructurisation developing in the sample.

3.6.2 Peak strength and volumetric behaviour at peak

Figure 3.28 shows the stress ratio, q/p', and average volumetric strain plotted against global axial strain measured in drained triaxial compression tests at effective cell pressures of 12.5, 25, 50 and 100 kPa, respectively, for intact samples of RSS. Peak friction angles, $\phi_p^{'}$, were found to be 59.7, 59.4, 53.2 and 52.5 degrees, respectively (Figure 3.29). The peak stress ratios, $(q/p')_{max}$ or η_{max}, were mobilised at the early stage of dilation and occurred before the maximum dilation rate was achieved (Figure 3.30 and Figure 3.31). At 50 kPa, the average volumetric strain - global axial strain curve (Figure 3.28(b)) and the rate of dilation - global axial strain curve (Figure 3.31 (a)) both show that the rate of dilation is maintained for an axial strain of about 2 % after the peak stress. In contrast to the intact samples, the peak stress ratios, $(q/p')_{max}$, in tests on pluviated samples of RSS and LBS were mobilized at about the maximum rate of dilation (Figure 3.32 to Figure 3.35). For pluviated samples of RSS, $\phi_p^{'}$ at 12.5, 50 and 100 kPa were found to be 46.1, 42.1 and 41.8 degrees, respectively. Pluviated samples of LBS mobilised 43.2, 43.5, 42.2 degrees of $\phi_p^{'}$ at 12.5, 50 and 100 kPa, respectively.

Figure 3.36 shows the stress ratio, $q/p^{'}$, plotted against rate of dilation, d, measured in drained triaxial compression tests at effective cell pressures of 12.5, 25, 50 and 100 kPa, respectively, for intact samples of RSS. At the start of dilation, achievement of stress ratios very close to peak can be clearly seen. These stress ratios are significantly higher than the stresses mobilised at the probable critical state. The maximum rate of dilation decreases with increasing confining pressure. Figure 3.37 and Figure 3.38 show the stress ratio, $q/p^{'}$, plotted against rate of dilation, d, measured in drained triaxial compression tests at effective cell pressures of 12.5, 50 and 100 kPa, respectively, for pluviated samples of RSS and LBS. The peak stress ratios were achieved when the maximum dilation rates were observed.

Figure 3.39 - Figure 3.41 compare stress ratio, $q/p^{'}$ or η, plotted against rate of dilation, d, for intact and pluviated samples of RSS measured in drained triaxial compression tests at effective cell pressures of 12.5, 50 and 100 kPa, respectively.

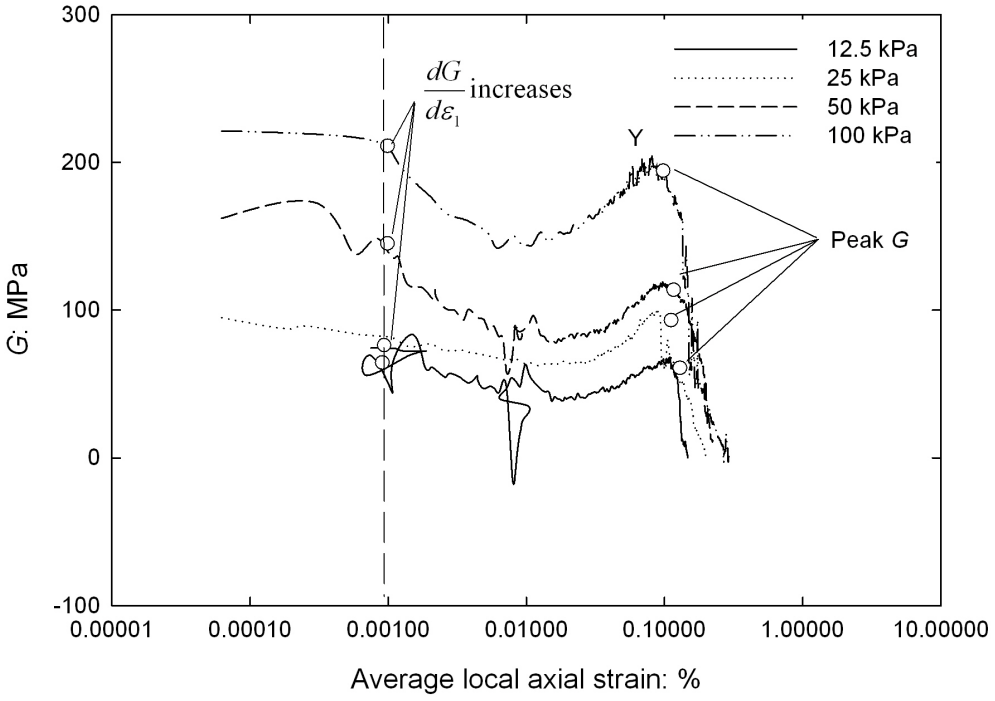

(a)

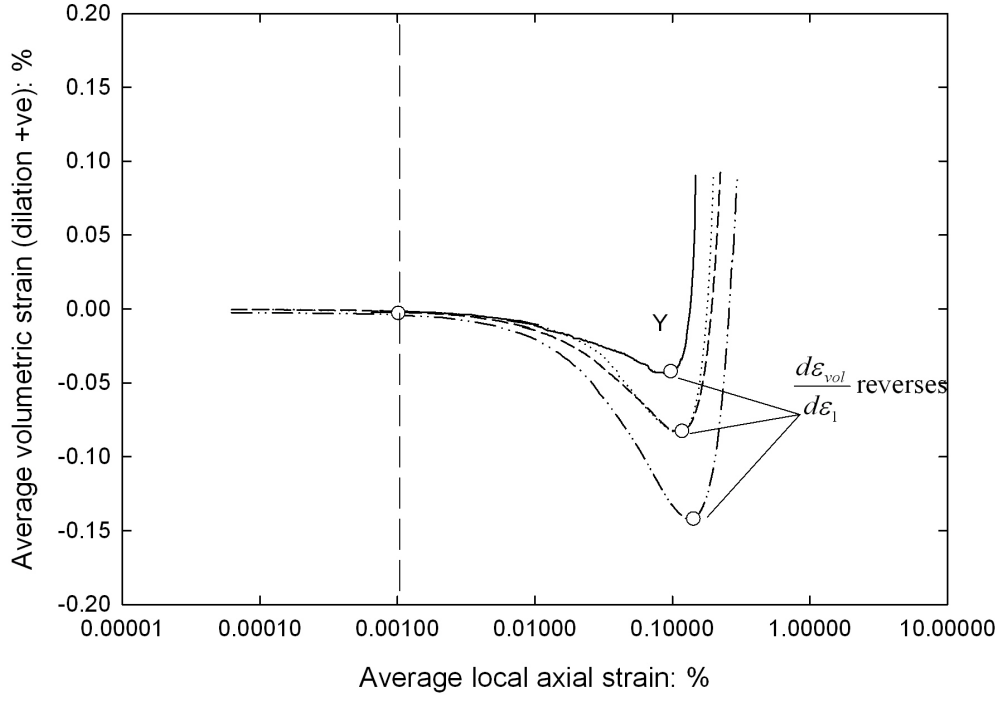

(b)

FIGURE 3.20: Intact RSS samples: (a) Shear modulus degradation curves (b) Evolution of average volumetric strain with average local axial strain during initial stage of shearing

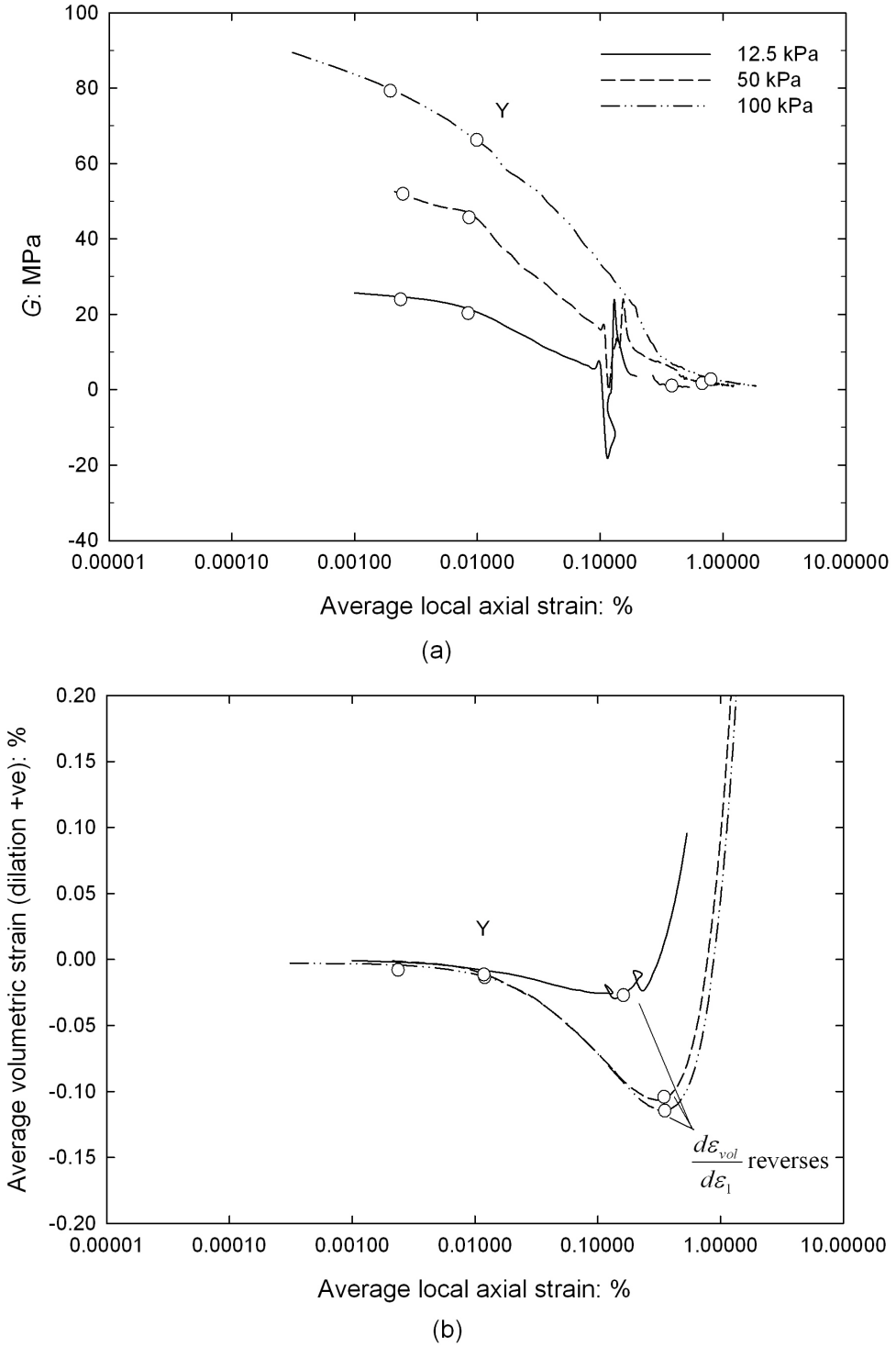

FIGURE 3.21: Pluviated RSS samples: (a) Shear modulus degradation curves (b) Evolution of average volumetric strain with average local axial strain during initial stage of shearing

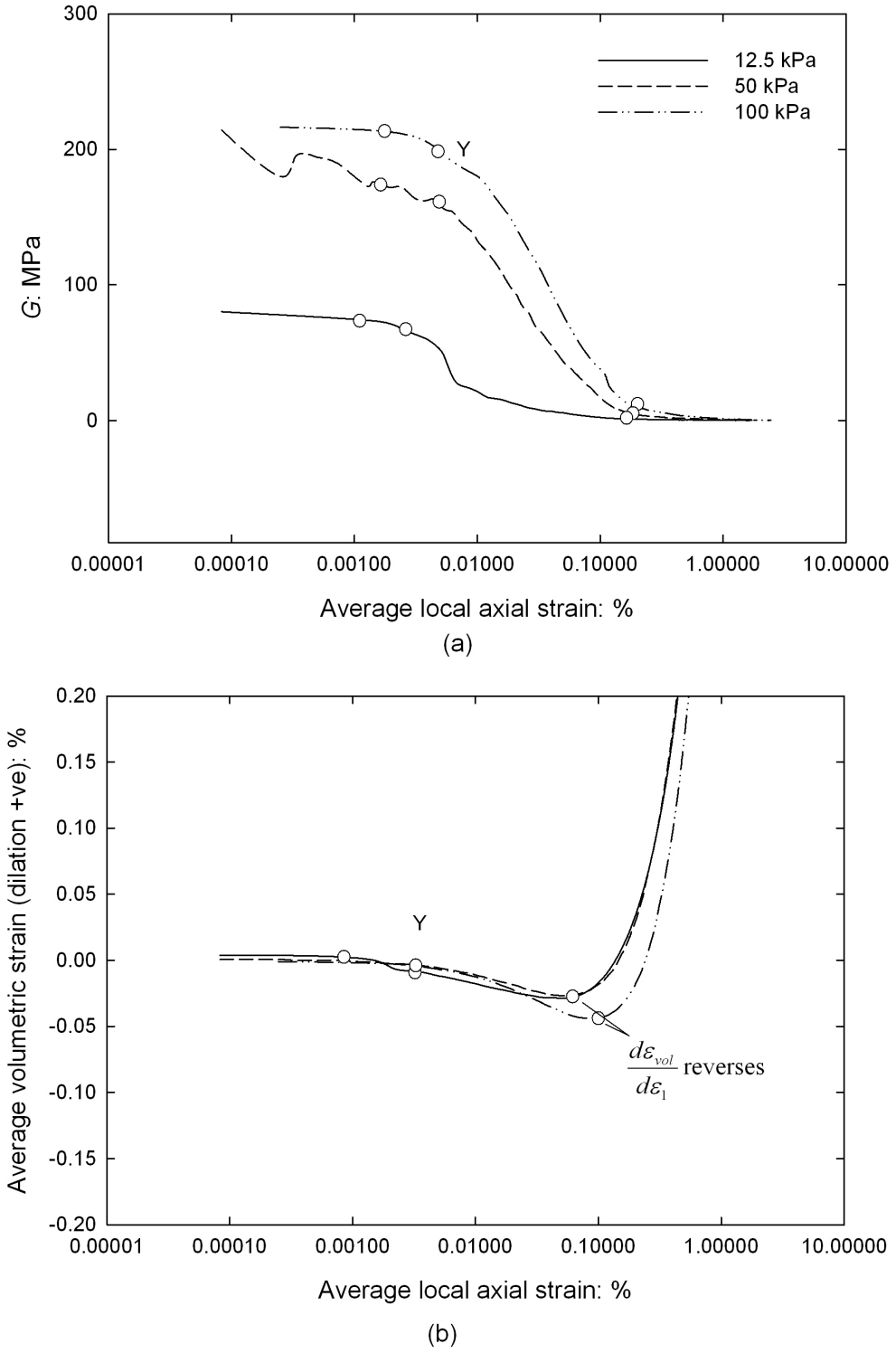

FIGURE 3.22: Pluviated LBS samples: (a) Shear modulus degradation curves (b) Evolution of average volumetric strain with average local axial strain during initial stage of shearing

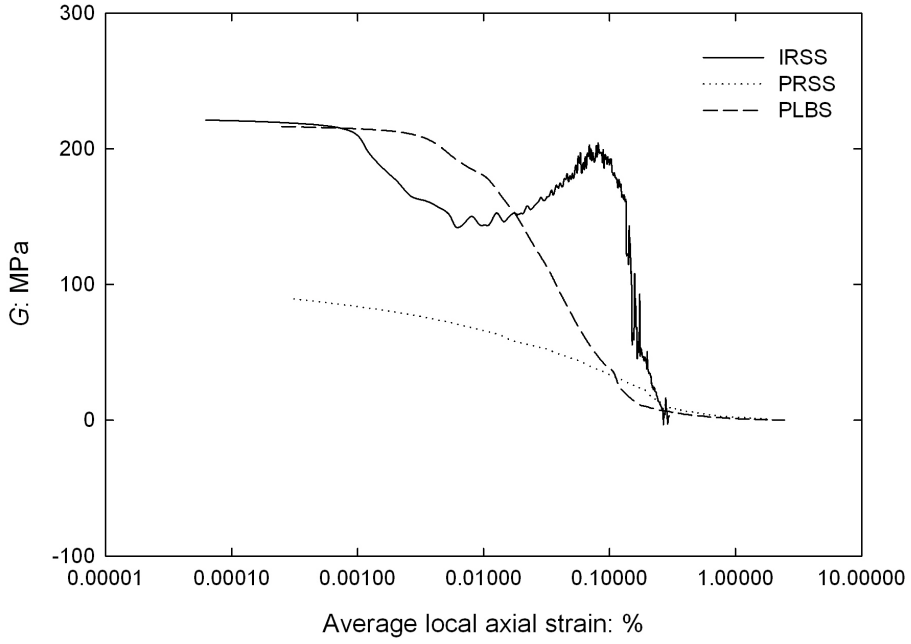

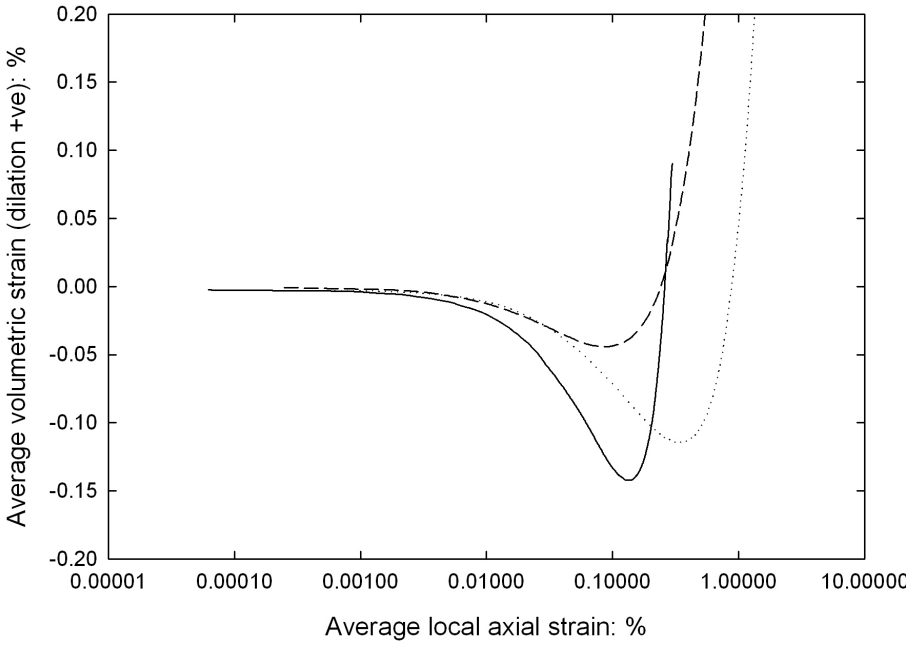

FIGURE 3.23: Shear modulus, G, and volumetric strain plotted against average local axial strain for intact RSS, pluviated LBS and pluviated RSS at an effective cell pressure of 100 kPa

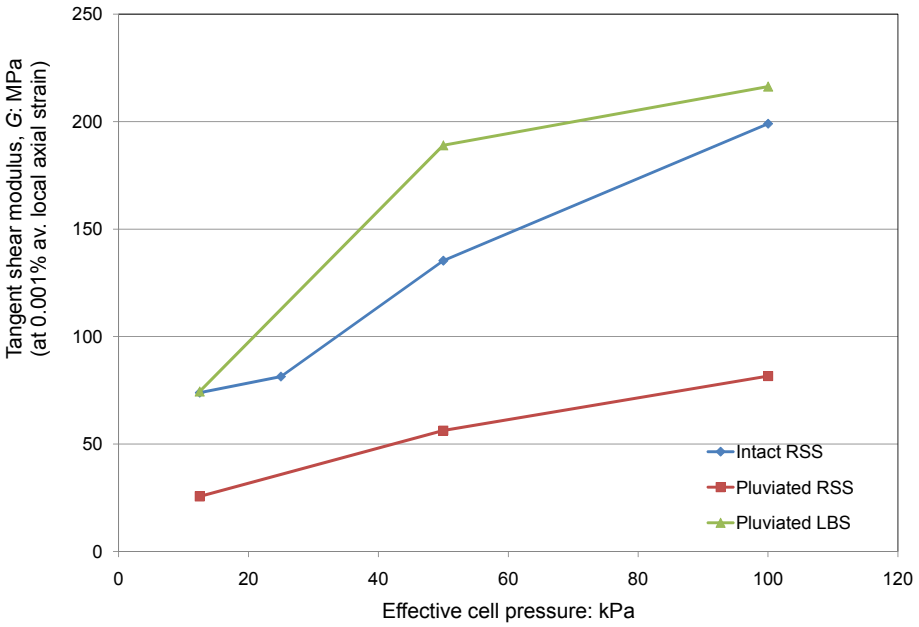

FIGURE 3.24: Shear modulus at 0.001% average local axial strain of the test materials (intact RSS, pluviated LBS and pluviated RSS) as a function of effective cell pressure

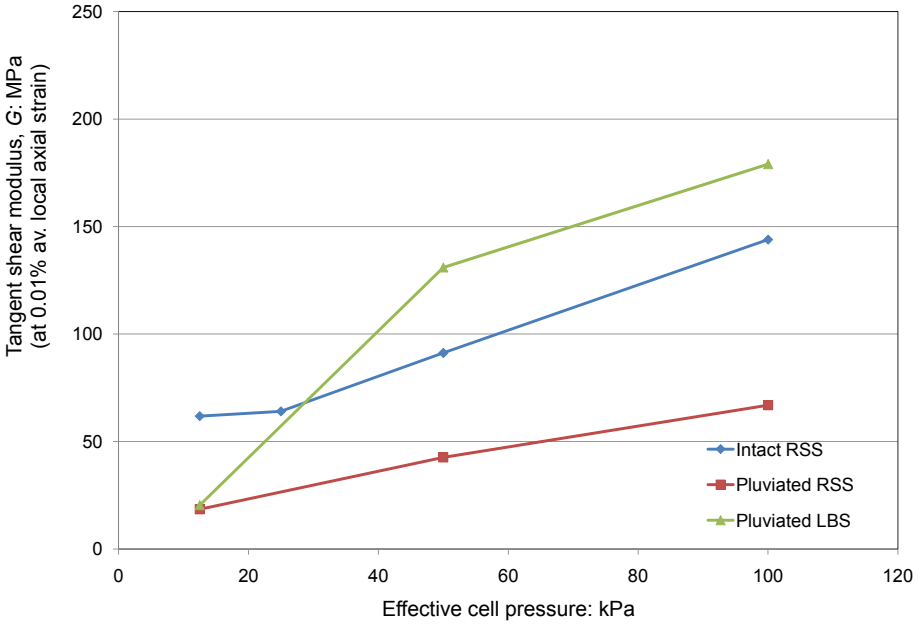

FIGURE 3.25: Shear modulus at 0.01% average local axial strain of the test materials (intact RSS, pluviated LBS and pluviated RSS) as a function of effective cell pressure

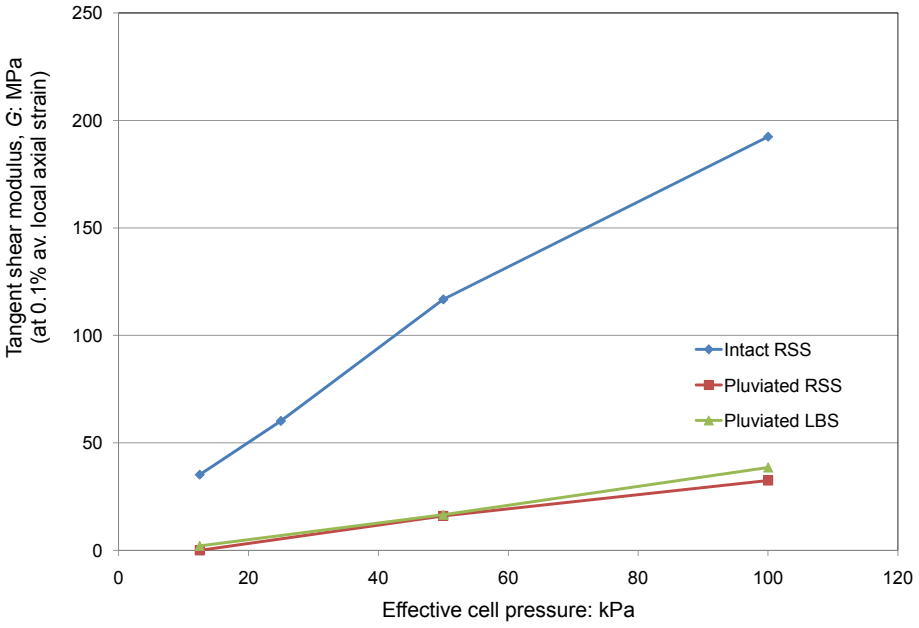

FIGURE 3.26: Shear modulus at 0.1% average local axial strain of the test materials (intact RSS, pluviated LBS and pluviated RSS) as a function of effective cell pressure

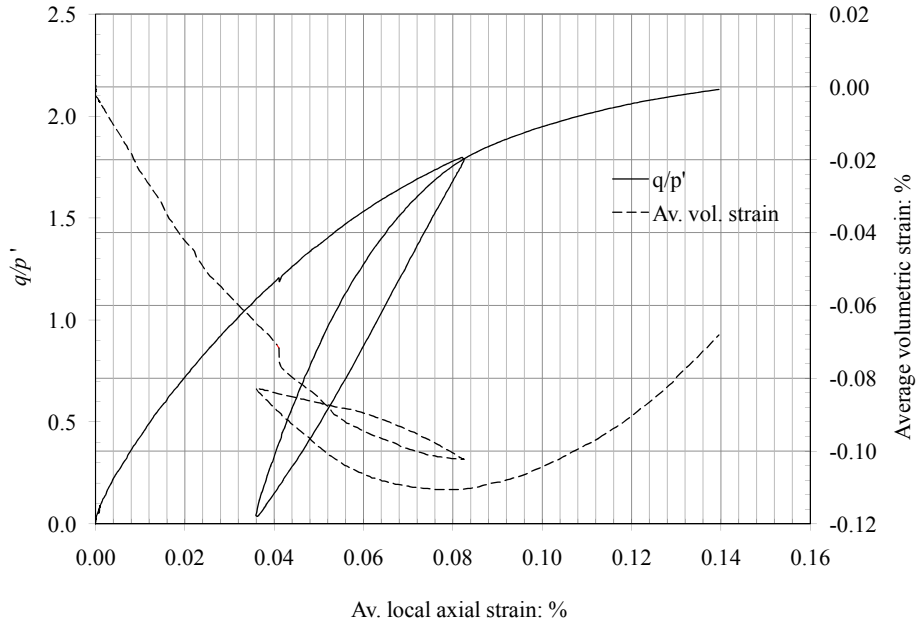

FIGURE 3.27: Unloading-reloading response of an intact RSS sample tested at effective cell pressure of 50 kPa just before onset of dilation

For the purpose of comparison, the original Cam clay and the Rowe's stress-dilatancy relations are also shown (both with $M = 1.24$ (Cresswell & Powrie, 2004); since reliable estimation of M could not be obtained from the low pressure tests presented in this chapter, the reasons will be discussed later in this chapter and in a greater detail in chapter 5).

Table 3.1 presents detailed information concerning the location of the peak stress ratio, the onset of dilation, maximum dilation rate and probable critical state with respect to the corresponding global and/or local axial strains.

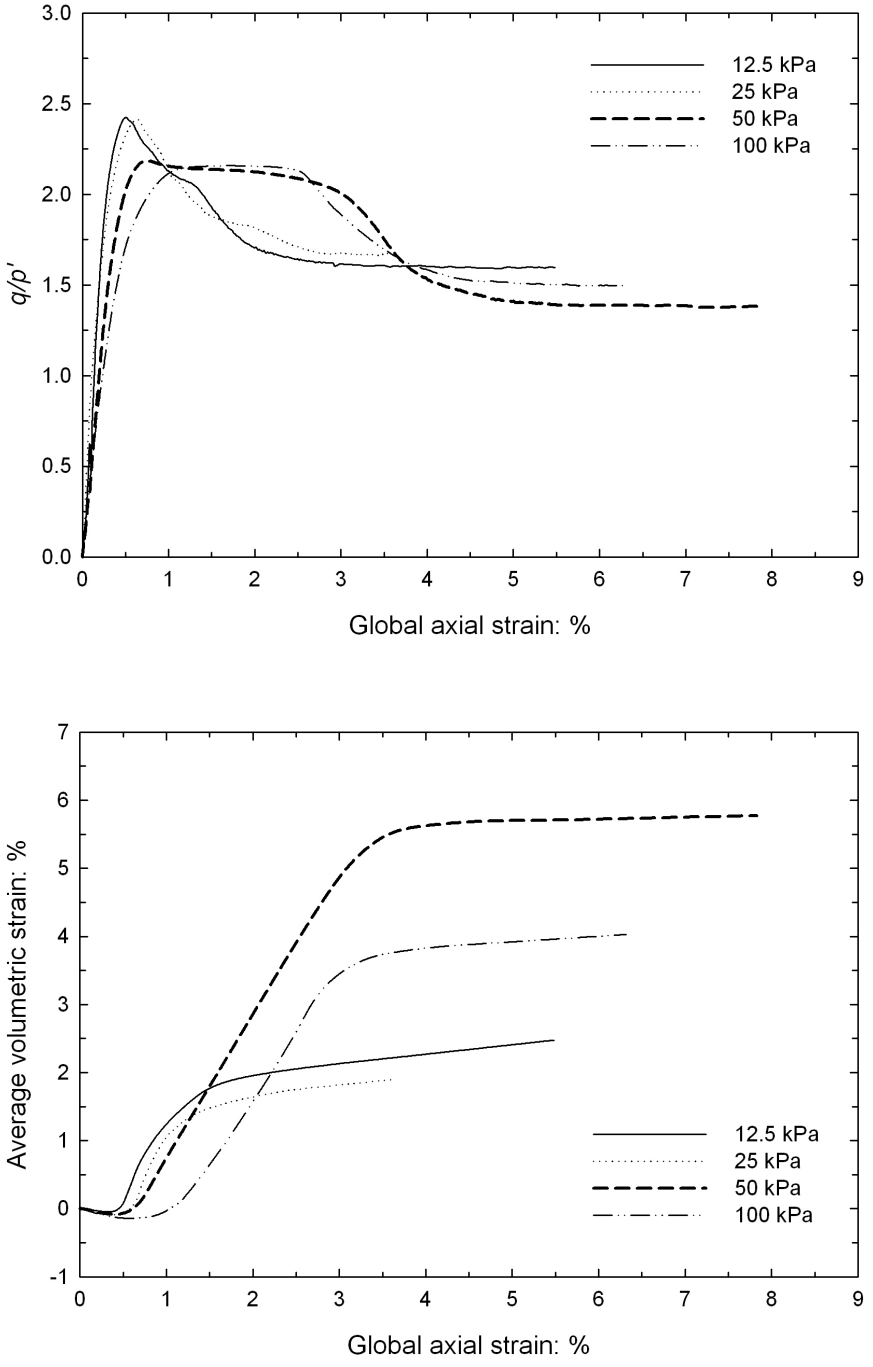

FIGURE 3.28: Stress ratio, $q/p^{'}$, and average volumetric strain plotted against global axial strain measured in drained triaxial compression tests at effective cell pressures of 12.5, 25, 50 and 100 *kPa*, respectively, for intact samples of RSS

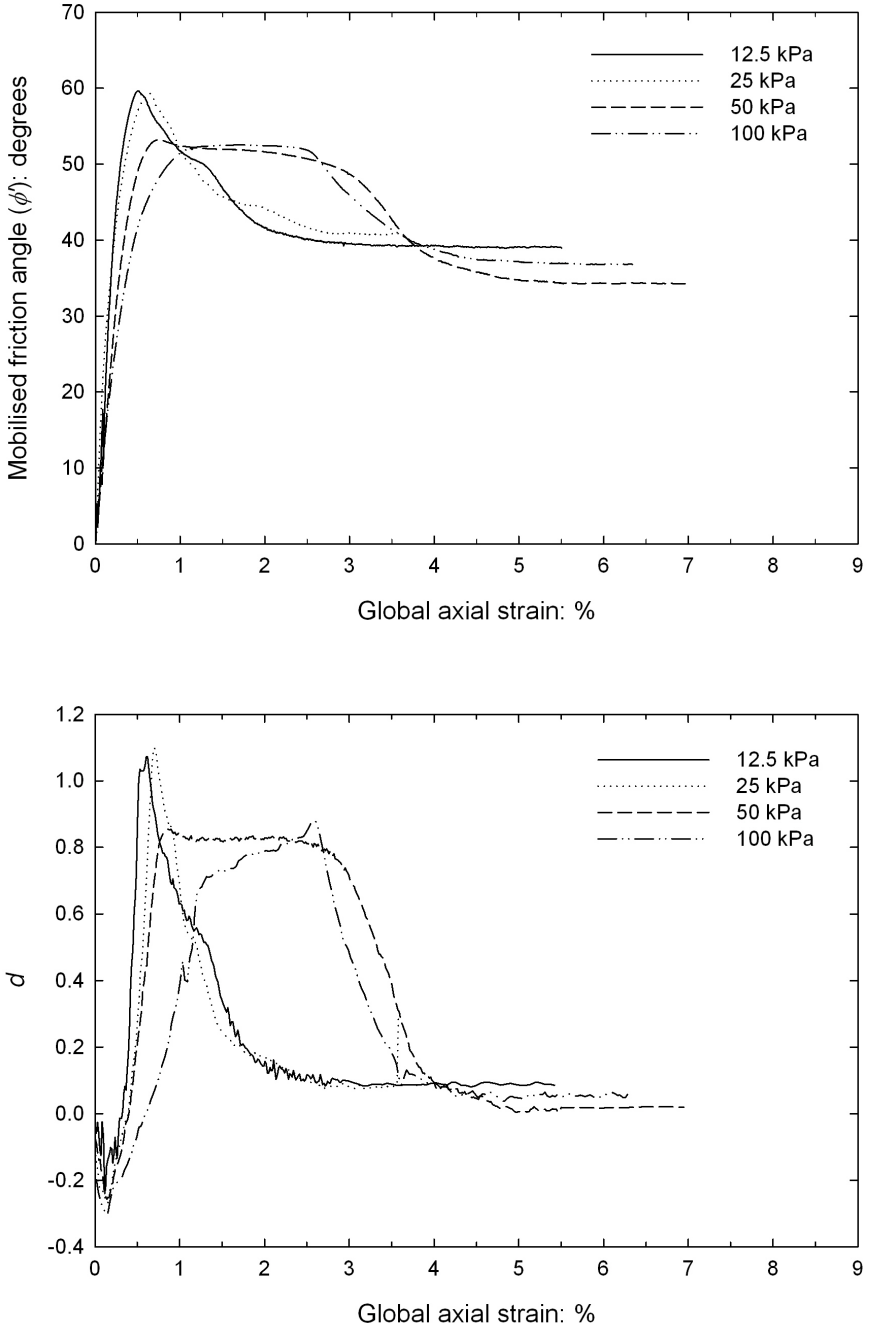

FIGURE 3.29: Mobilised friction angle, $\phi^{'}$, and rate of dilation, d, plotted against global axial strain measured in drained triaxial compression tests at effective cell pressures of 12.5, 25, 50 and 100 kPa, respectively, for intact samples of RSS

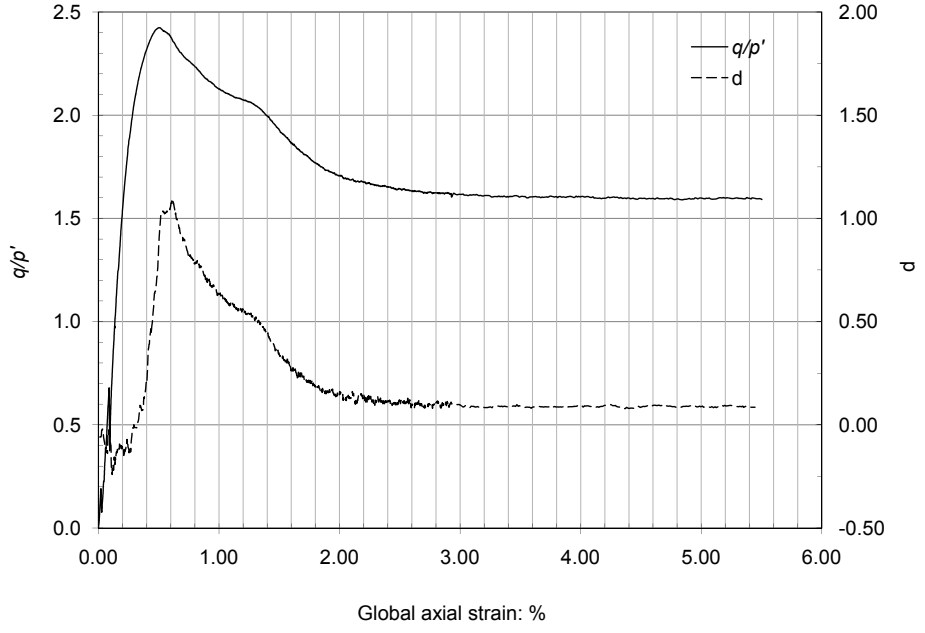

(a)

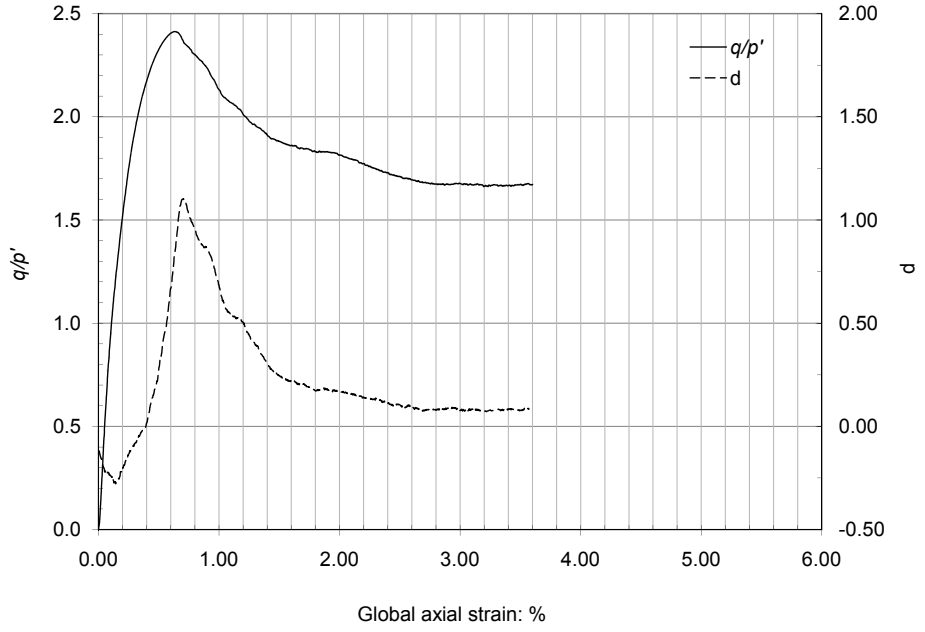

(b)

FIGURE 3.30: Stress ratio, $q/p^{'}$, and rate of dilation, d, plotted against global axial strain measured in drained triaxial compression tests at effective cell pressures of (a) 12.5 and (b) 25 kPa, respectively, for intact samples of RSS

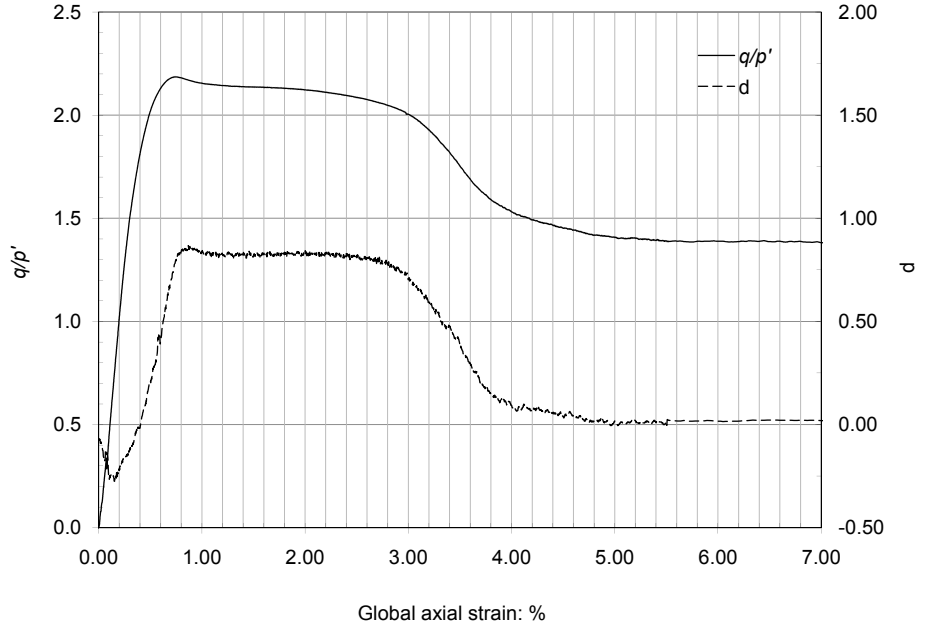

(a)

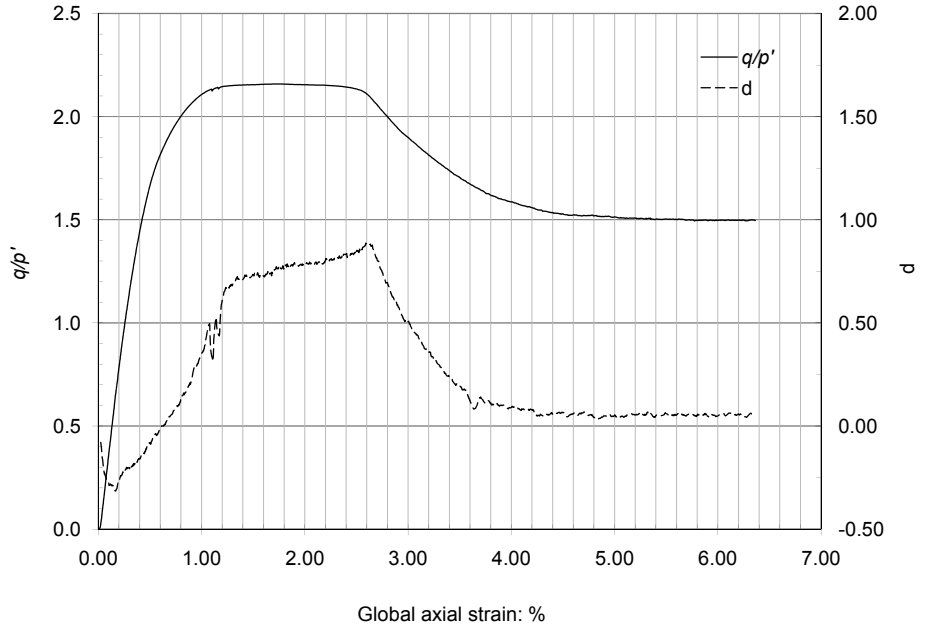

(b)

FIGURE 3.31: Stress ratio, $q/p^{'}$, and rate of dilation, d, plotted against global axial strain measured in drained triaxial compression tests at effective cell pressures of (a) 50 and (b) 100 kPa, respectively, for intact samples of RSS

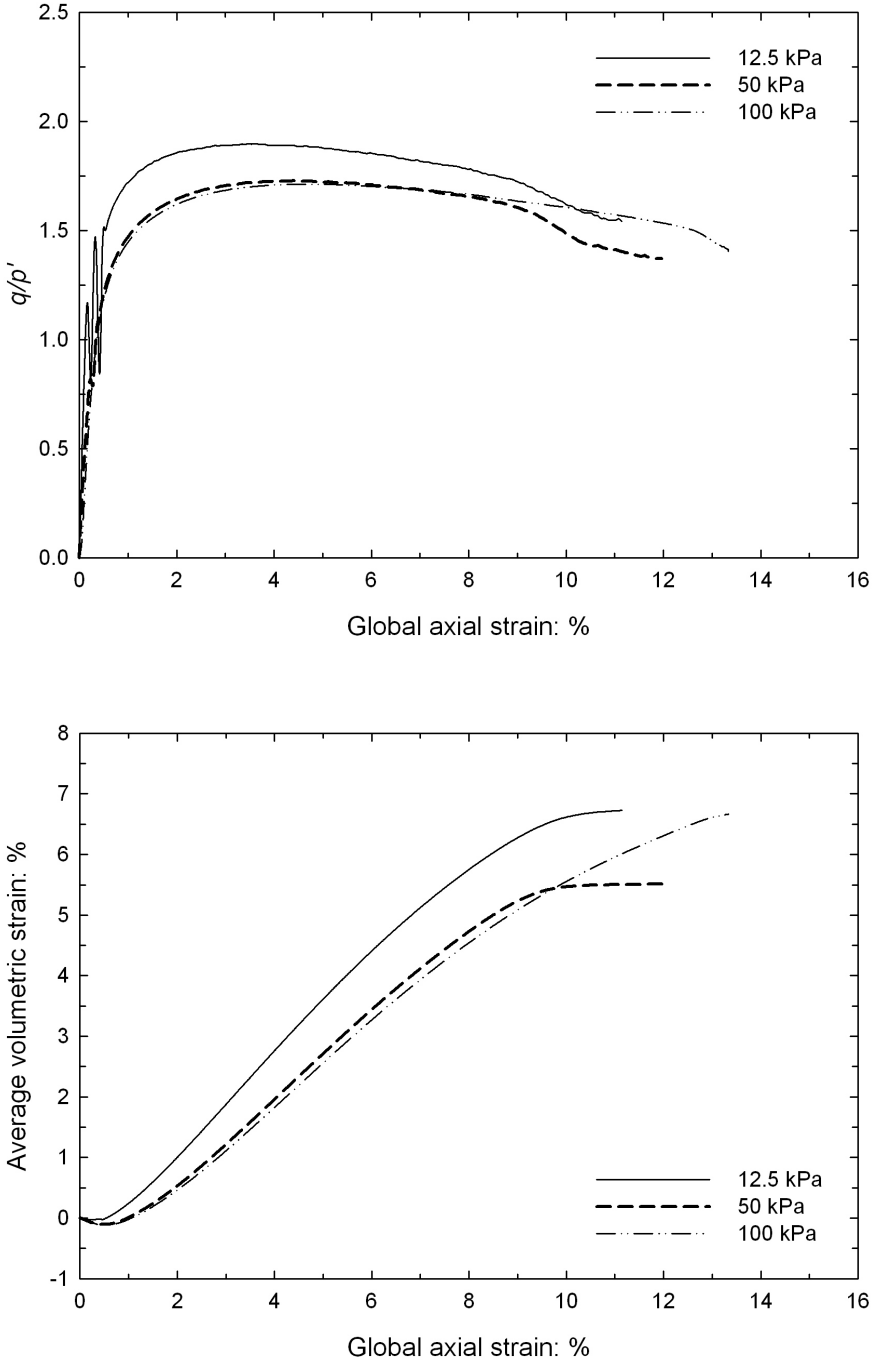

FIGURE 3.32: Stress ratio, $q/p^{'}$, and average volumetric strain plotted against global axial strain measured in drained triaxial compression tests at effective cell pressures of 12.5, 50 and 100 kPa, respectively, for the pluviated samples of RSS

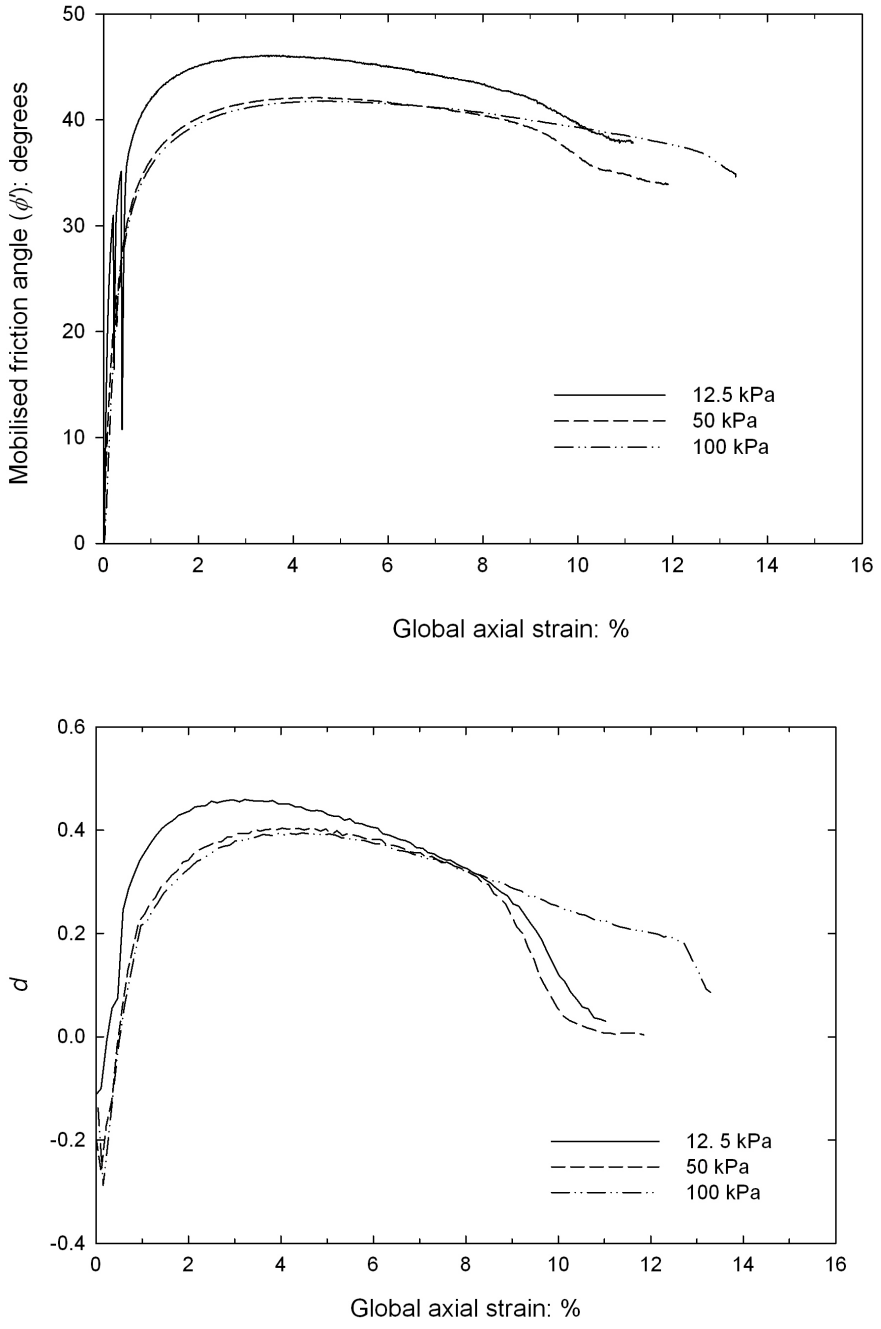

FIGURE 3.33: Mobilised friction angle, ϕ', and rate of dilation, d, plotted against global axial strain measured in drained triaxial compression tests at effective cell pressures of 12.5, 50 and 100 kPa, respectively, for pluviated samples of RSS

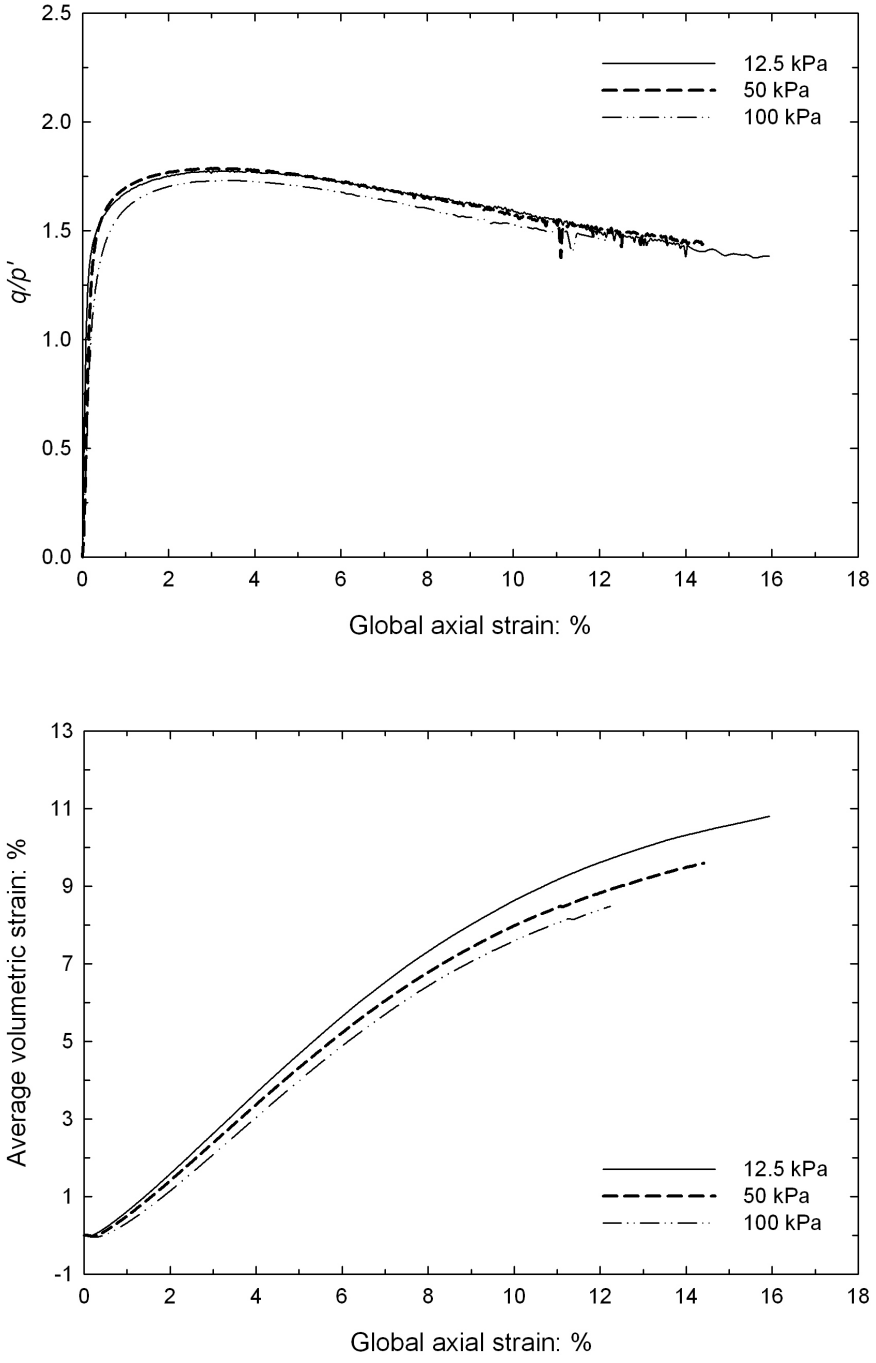

FIGURE 3.34: Stress ratio, $q/p^{'}$, and average volumetric strain plotted against global axial strain measured in drained triaxial compression tests at effective cell pressures of 12.5, 50 and 100 kPa, respectively, for the pluviated samples of LBS

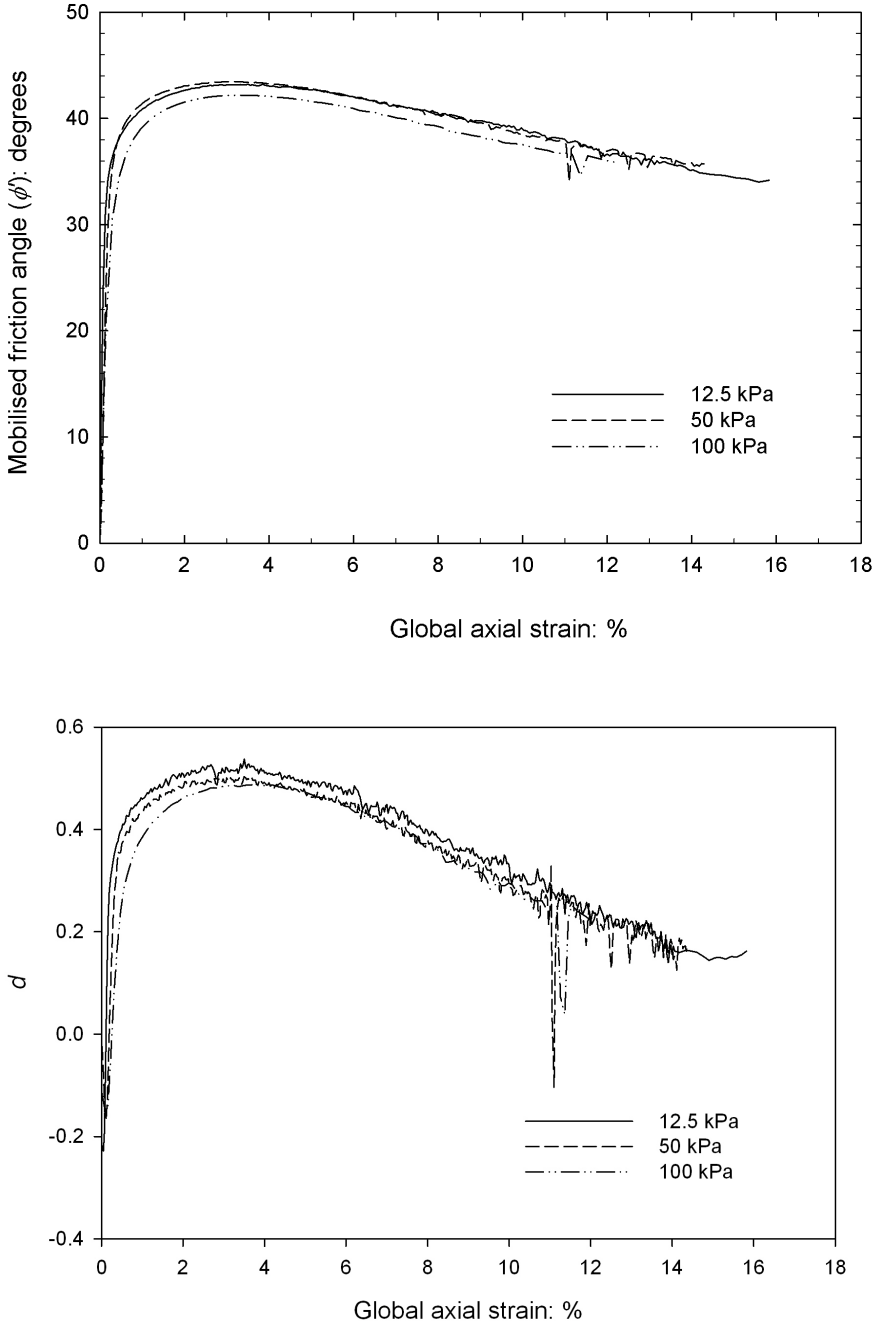

FIGURE 3.35: Mobilised friction angle, ϕ', and rate of dilation, d, plotted against global axial strain measured in drained triaxial compression tests at effective cell pressures of 12.5, 50 and 100 kPa, respectively, for pluviated samples of LBS

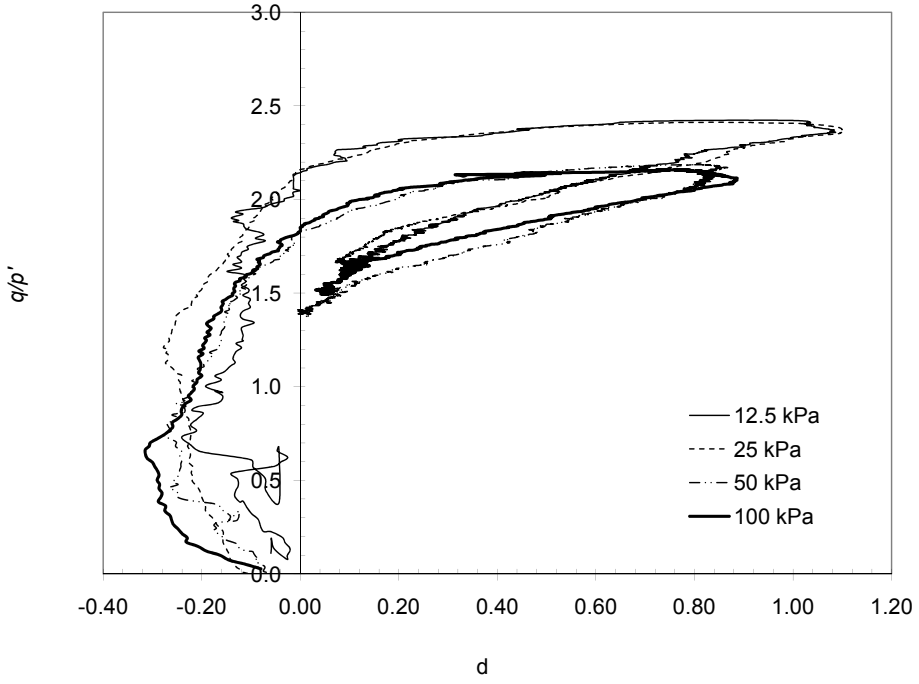

FIGURE 3.36: Stress ratio, $q/p^{'}$, plotted against rate of dilation, d, measured in drained triaxial compression tests at effective cell pressures of 12.5, 25, 50 and 100 kPa, respectively, for intact samples of RSS

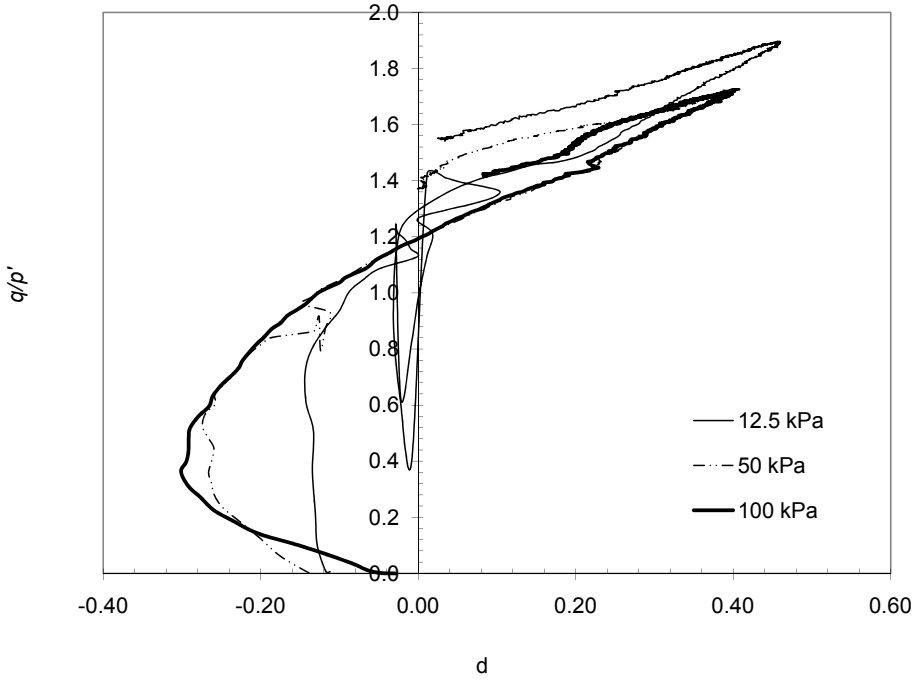

FIGURE 3.37: Stress ratio, $q/p^{'}$, plotted against rate of dilation, d, measured in drained triaxial compression tests at effective cell pressures of 12.5, 50 and 100 kPa, respectively, for pluviated samples of RSS

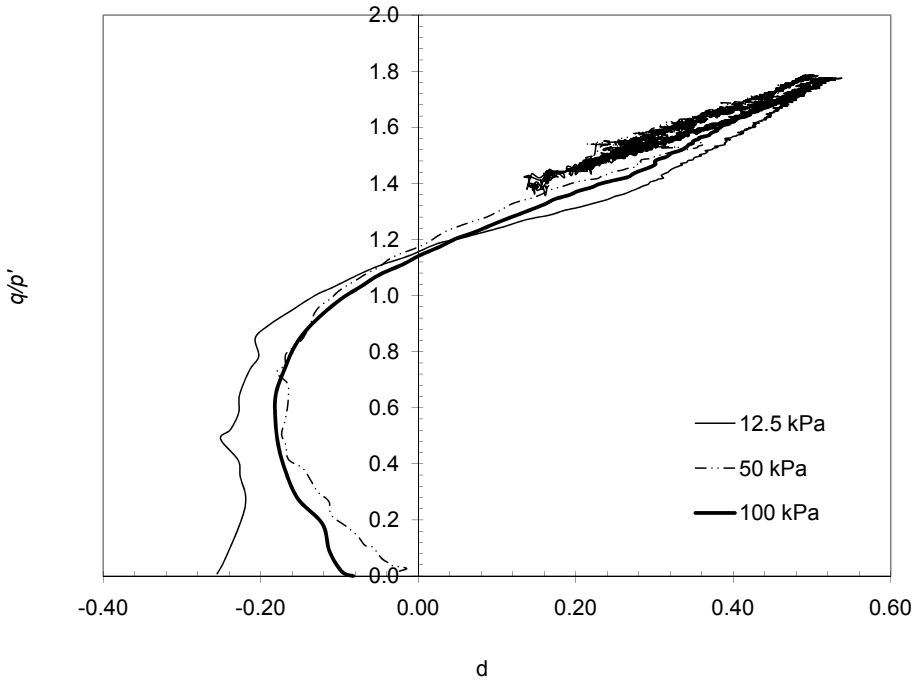

FIGURE 3.38: Stress ratio, $q/p^{'}$, plotted against rate of dilation, d, measured in drained triaxial compression tests at effective cell pressures of 12.5, 50 and 100 kPa, respectively, for pluviated samples of LBS

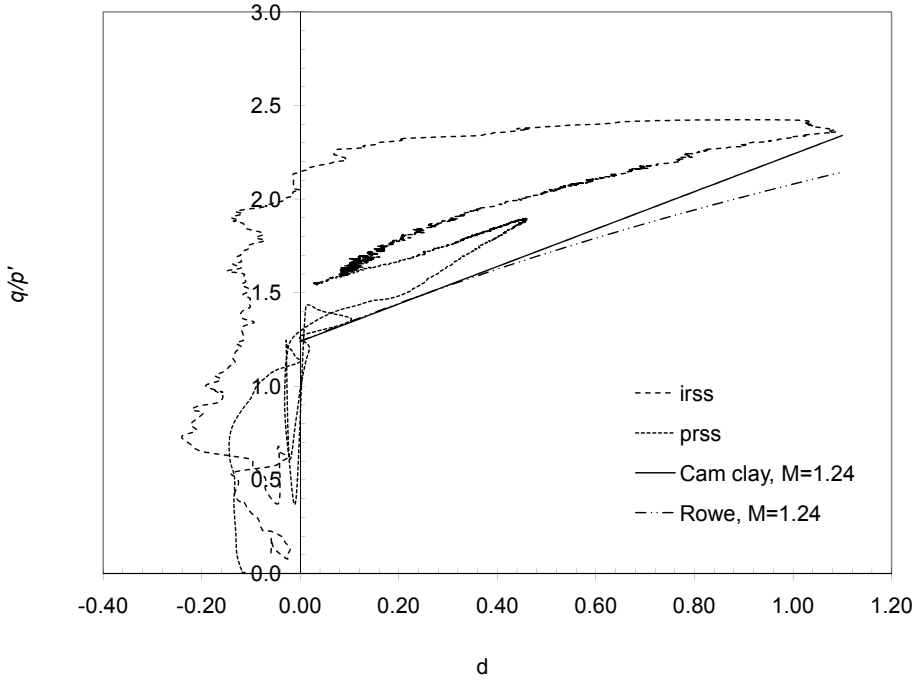

FIGURE 3.39: Stress ratio, $q/p^{'}$, plotted against rate of dilation, d, measured in drained triaxial compression tests at effective cell pressure of 12.5 kPa, respectively, for intact and pluviated samples of RSS

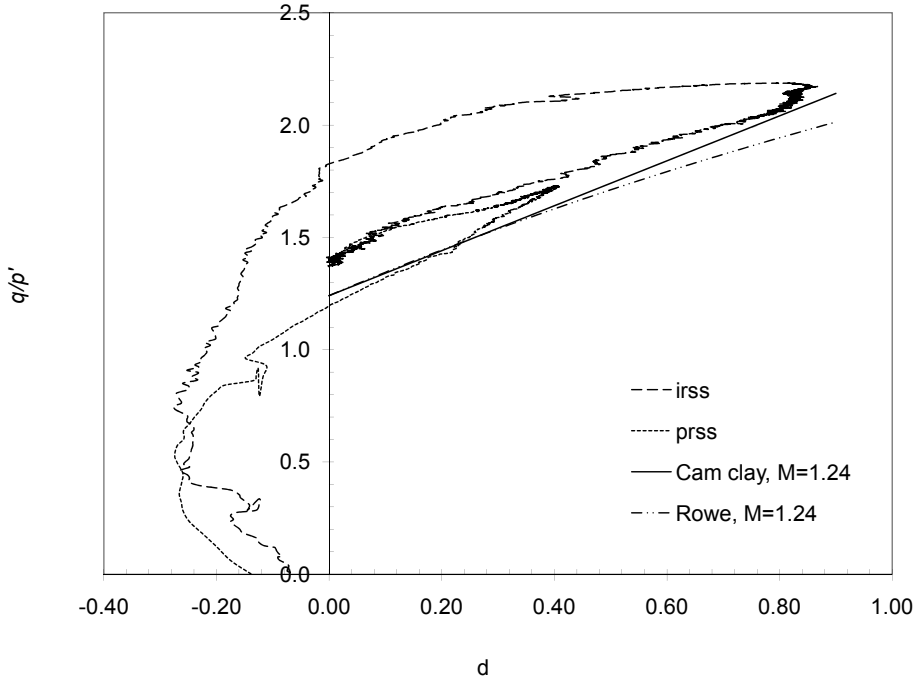

FIGURE 3.40: Stress ratio, $q/p^{'}$, plotted against rate of dilation, d, measured in drained triaxial compression tests at effective cell pressure of 50 kPa, respectively, for intact and pluviated samples of RSS

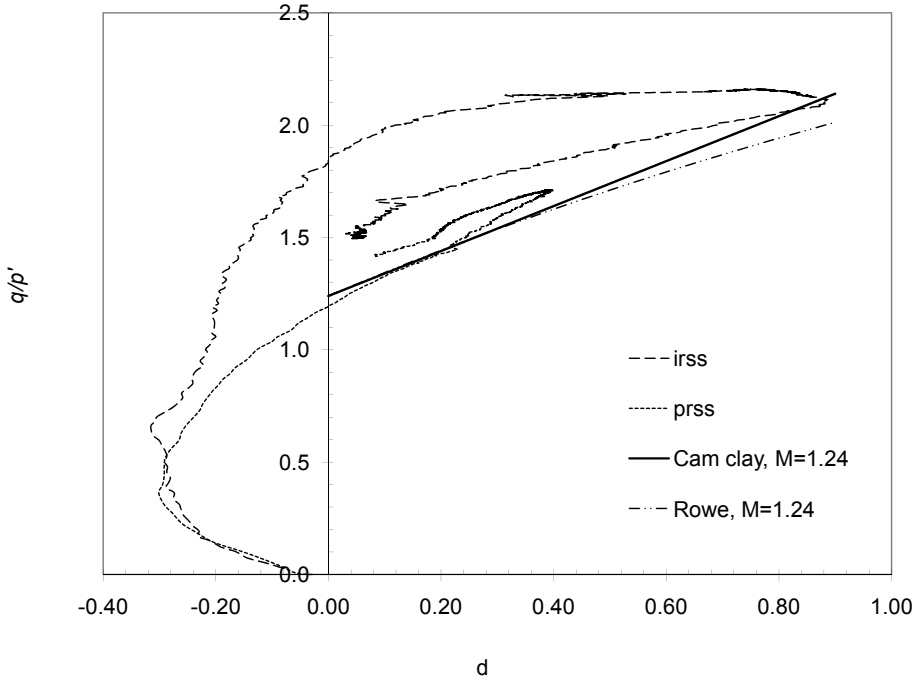

FIGURE 3.41: Stress ratio, $q/p^{'}$, plotted against rate of dilation, d, measured in drained triaxial compression tests at effective cell pressure of 100 kPa, respectively, for intact and pluviated samples of RSS

TABLE 3.1: Maximum stress ratio, onset of dilation, maximum dilatancy rate and critical state for intact RSS, pluviated RSS and pluviated LBS samples

Test	Effective cell pressure	$\frac{H_0}{D_0}$	At $(q/p^{'})_{max}$						At onset of dilation			At d_{max}			At critical state
Series B1	*kPa*		η	Global axial strain: %	Av. local axial strain:%	Vol. change, dilation +ve		d	η	Global axial strain: %	Av. local axial strain:%	η	Global axial strain: %	Av. local axial strain:%	η
	Intact RSS					mm^3	%								
IRSS-1	12.5	2.04	2.42	0.50	0.147	452	0.08	0.88	2.18	0.34	0.10	2.36	0.62	0.149	1.59
IRSS-2	25	2.06	2.41	0.63	0.198	472	0.09	0.84	2.20	0.41	0.12	2.36	0.71	0.203	1.67
IRSS-3	50	2.04	2.19	0.74	0.244	1002	0.18	0.78	1.83	0.41	0.12	2.17	0.86	0.290	1.38
IRSS-4	100	1.99	2.16	1.69	0.547	5502	0.99	0.76	1.87	0.62	0.14	2.11	2.59	1.016	1.50
	Pluviated RSS														
PRSS-1	12.5	1.98	1.90	3.46	2.994	11895	2.29	0.46	1.21	0.26	0.14	1.90	3.33	2.885	1.54
PRSS-2	50	1.98	1.73	4.40	3.803	11751	2.26	0.40	1.20	0.49	0.32	1.73	4.28	3.709	1.37
PRSS-3	100	1.96	1.71	4.54	3.887	11583	2.22	0.40	1.18	0.49	0.32	1.71	4.76	1.020	1.41
	Pluviated LBS														
PLBS-1	12.5	1.99	1.78	3.89	3.414	18598	3.55	0.52	1.19	0.12	0.05	1.77	3.50	3.119	1.39
PLBS-2	50	1.96	1.79	3.04	2.449	12397	2.42	0.50	1.19	0.19	0.05	1.78	3.05	2.458	1.45
PLBS-3	100	2.01	1.73	3.45	2.688	13063	2.51	0.49	1.14	0.26	0.09	1.72	4.11	3.186	1.45

3.6.3 State envelopes

State paths (q against p' and v against p') followed during the tests on the samples of intact RSS, pluviated RSS and pluviated LBS are shown in Figures 3.42, 3.43 and 3.44. These state paths enable onset of dilation and peak strength envelopes to be determined in the $q : p'$ plane as shown. A probable critical state is also identified; although the criterion of the attainment of a constant volume condition was not yet satisfied in the pluviated samples at the end of the tests. In the case of intact samples, the ability to mobilise strengths above that at the critical state before dilation was identified.

3.6.4 Strain localisation & shear band development

At all cell pressures, shear bands were found to develop in intact samples during the shearing process (Figure 3.45). The post peak behaviour was found to be predominantly determined by shear band behaviour. At 12.5 and 25 kPa cell pressures, shear bands formed near the peak and thereafter deformation was mainly focused on the shear band. In contrast, at 50 and 100 kPa cell pressures, shear bands developed only after the samples had experienced significant dilation at almost constant stress ratio, before the stress ratio dropped to the ultimate value with the formation of the clearly visible slip plane. The volumetric strains experienced by the samples were also found to depend on the post peak behaviour. The change in deformation characteristics with the change of cell pressure from 25 to 12.5 kPa was rather small. The deformation characteristics change from brittle to ductile between 25 and 50 kPa.

Pluviated samples of RSS tested at 12.5, 50 and 100 kPa were found to barrel in the post-peak deformation regime, although clear shear bands were visible at the end of tests (Figure 3.46). LBS samples tested at 12.5, 50 and 100 kPa were found to barrel in the post-peak deformation regime (Figure 3.47). The average volumetric strain at ultimate failure was found to decrease with elevated cell pressures.

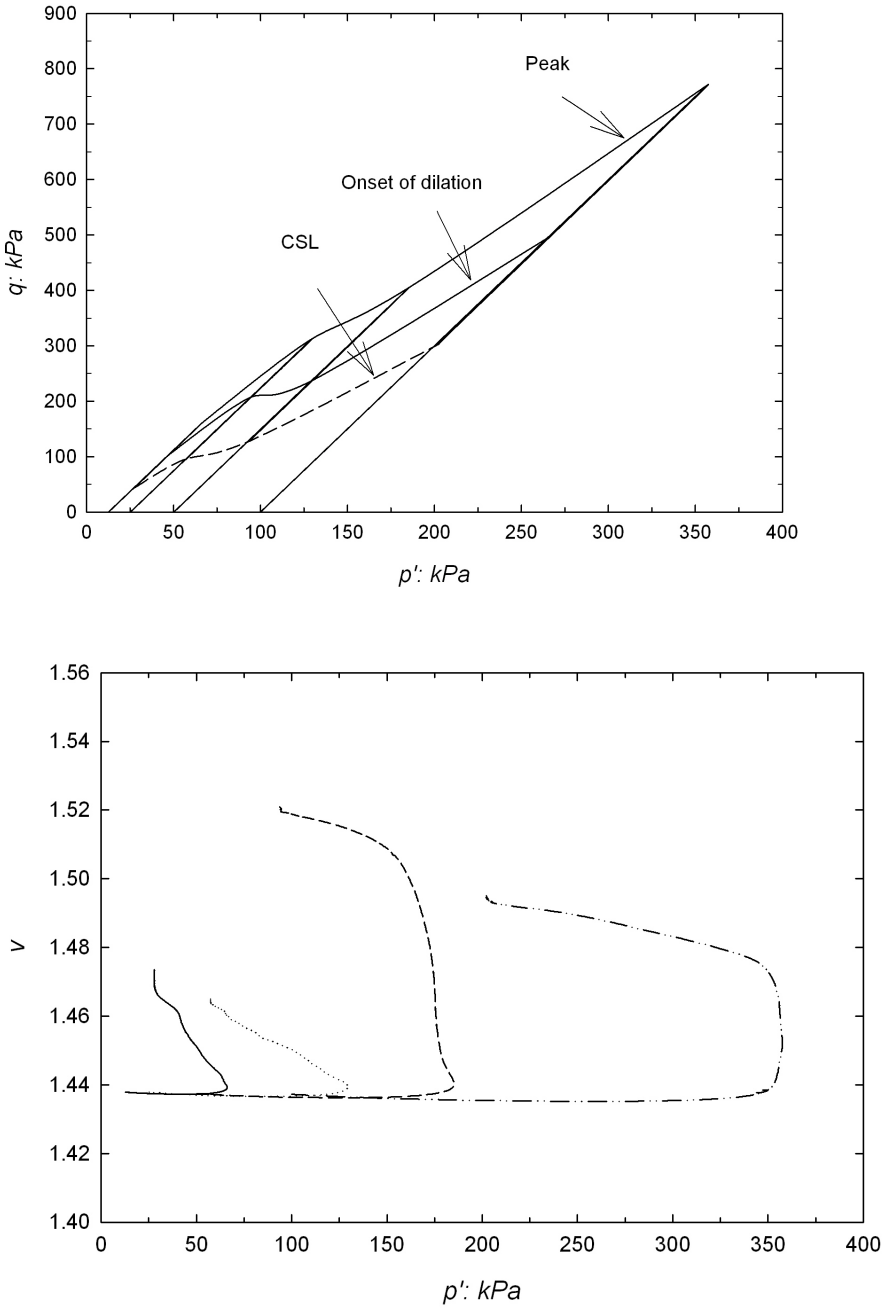

FIGURE 3.42: Deviator stress, q, and specific volume, v, plotted against mean effective stress, p', measured in drained triaxial compression tests at effective cell pressures of 12.5, 25, 50 and 100 kPa, respectively, for the intact samples of RSS. Peak, onset of dilation and possible critical state envelopes are shown.

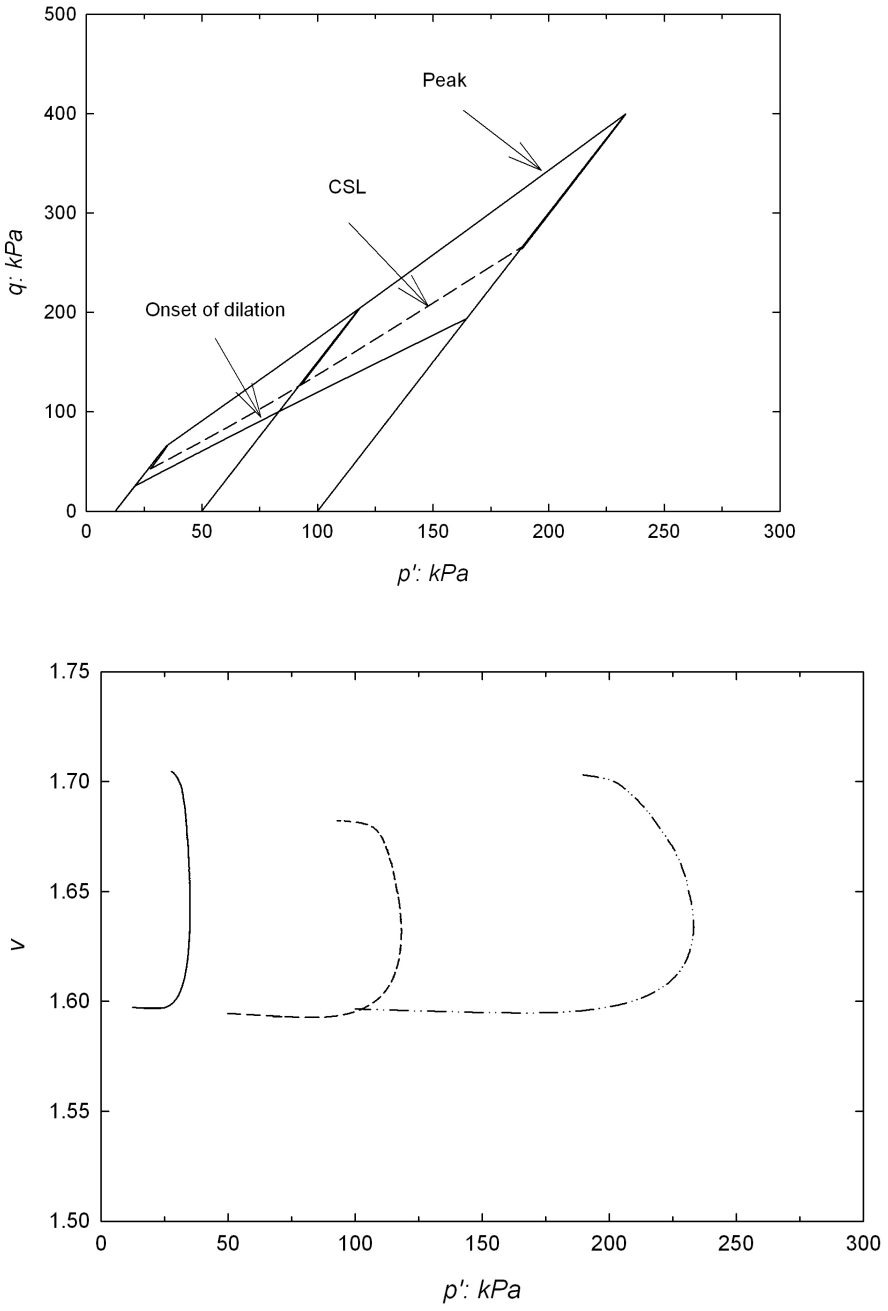

FIGURE 3.43: Deviator stress, q, and specific volume, v, plotted against mean effective stress, p', measured in drained triaxial compression tests at effective cell pressures of 12.5, 50 and 100 kPa, respectively, for the pluviated samples of RSS. Peak, onset of dilation and possible critical state envelopes are shown.

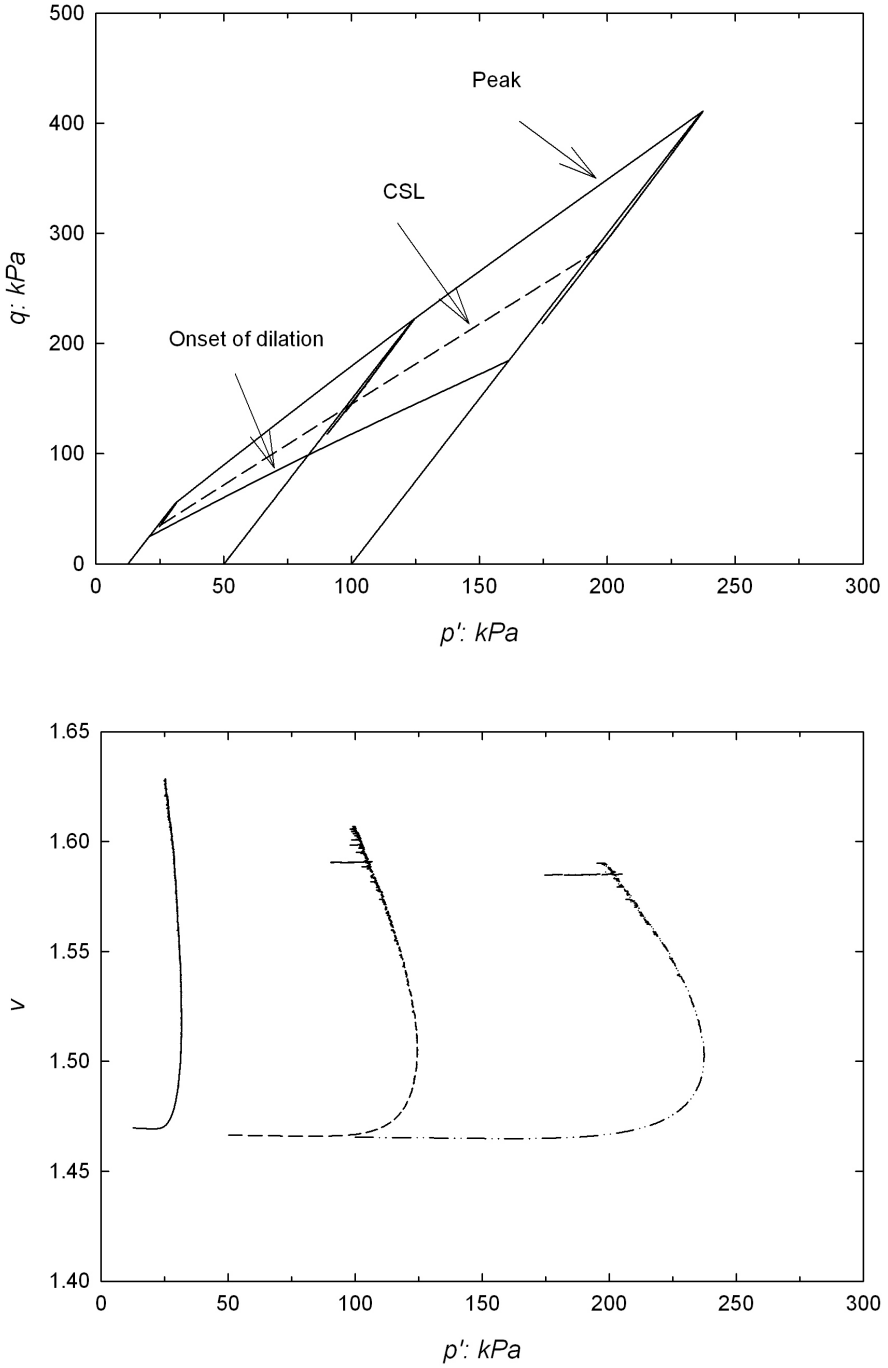

FIGURE 3.44: Deviator stress, q , and specific volume, v , plotted against mean effective stress, p', measured in drained triaxial compression tests at effective cell pressures of 12.5, 50 and 100 kPa, respectively, for the pluviated samples of LBS. Peak, onset of dilation and possible critical state envelopes are shown.

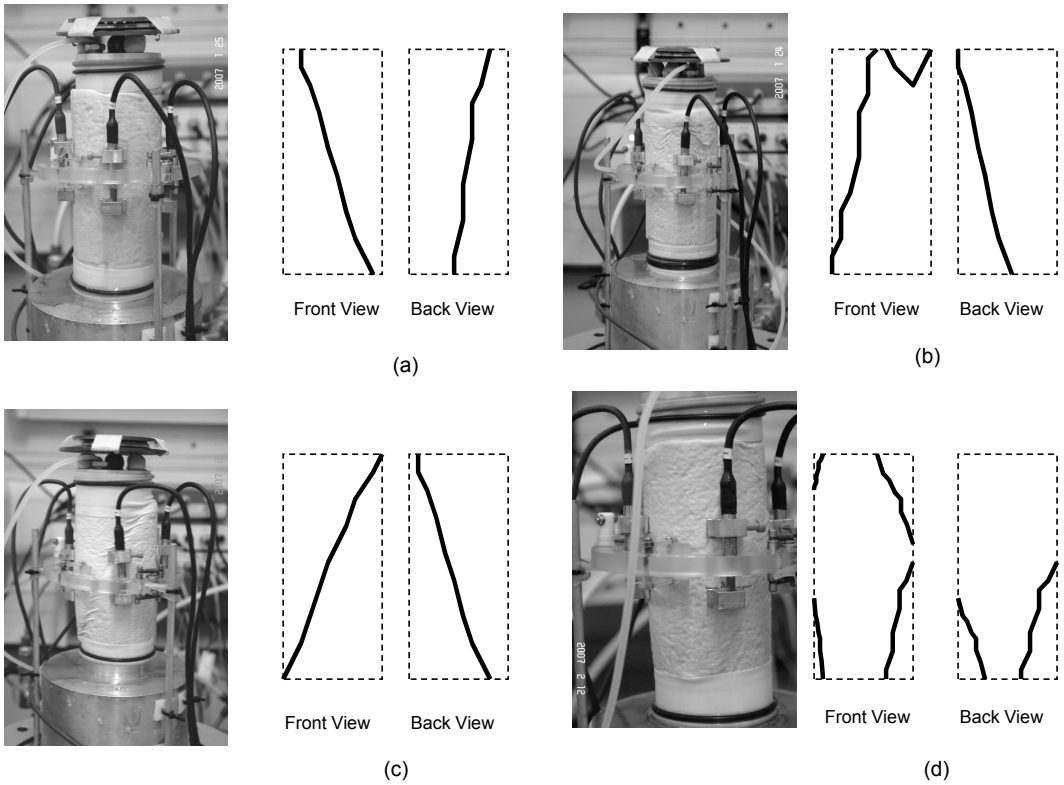

FIGURE 3.45: Photographs of the samples taken after drained triaxial compression tests at effective cell pressures of (a) 12.5 *kPa*, (b) 25 *kPa*, (c) 50 *kPa* and (d) 100 *kPa*, respectively, for intact RSS. The sketches show the positions of slip surfaces.

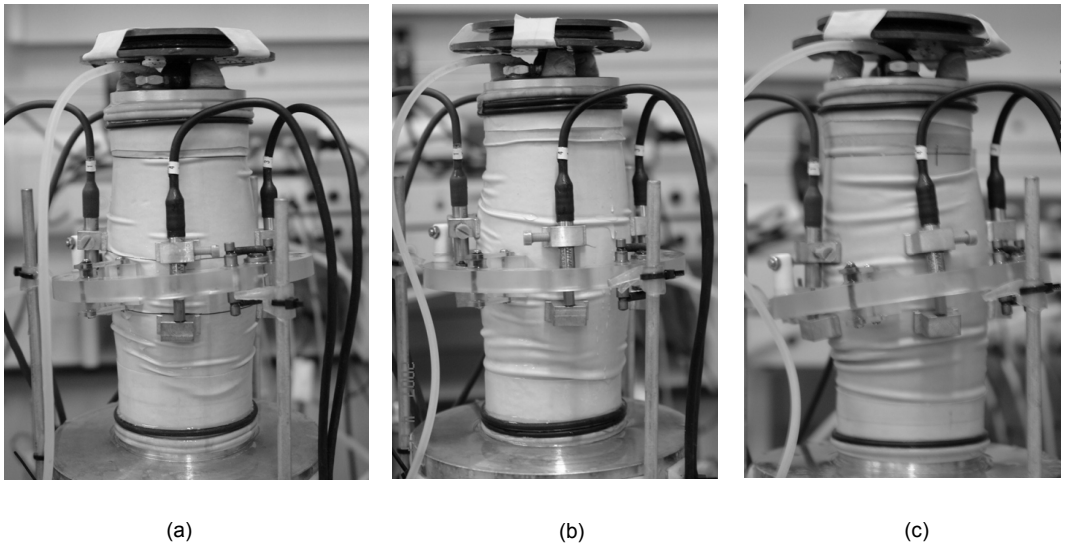

FIGURE 3.46: Photographs of the samples taken after drained triaxial compression tests at effective cell pressures of (a) 12.5 *kPa*, (b) 50 *kPa* and (c) 100 *kPa*, respectively, for the pluviated samples of RSS

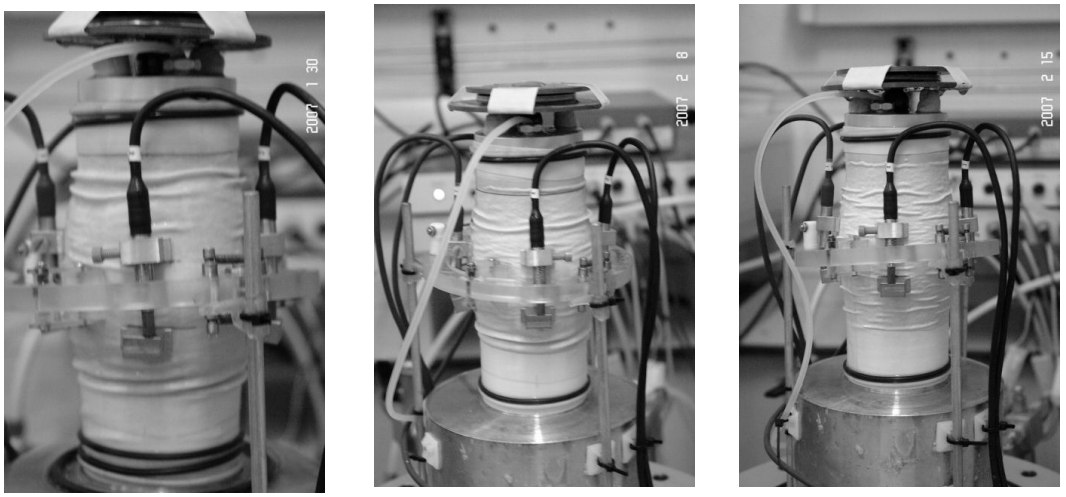

(a) (b) (c)

FIGURE 3.47: Photographs of the samples taken after drained triaxial compression tests at effective cell pressures of (a) 12.5 kPa, (b) 50 kPa and (c) 100 kPa, respectively, for the pluviated samples of LBS

3.6.5 Particle breakage

Particle breakage suppresses dilatancy (Hardin, 1985). To identify and quantify particle breakage during the shearing process, if any, sieve analysis and Laser Diffraction Analysis were carried out (see Appendix B for details about the *Laser Diffraction Technology*).

Figure 3.48 shows the particle size distribution(PSD) curves determined using sieve analysis of disaggregated RSS before and after a test at 50 kPa effective cell pressure. No difference in the curves was observed with this analysis so there is no clear indication of grain crushing during the shearing process.

A Mastersizer 2000 (Malvern Instruments Ltd., Worcestershire, UK), at the National Oceanography Centre, Southampton, was used to analyse the samples of Reigate Silver sand taken before and after the shearing test. As shown in Figure 3.49 and Figure 3.50 no significant change in particle size distribution curves were observed except samples #15 and #16 in which cases very slight changes were observed.

No significant difference observed in the percentage of fines between the curves of samples before and after testing confirmed that the grain breakage during the shearing process, if any, is very minimal.

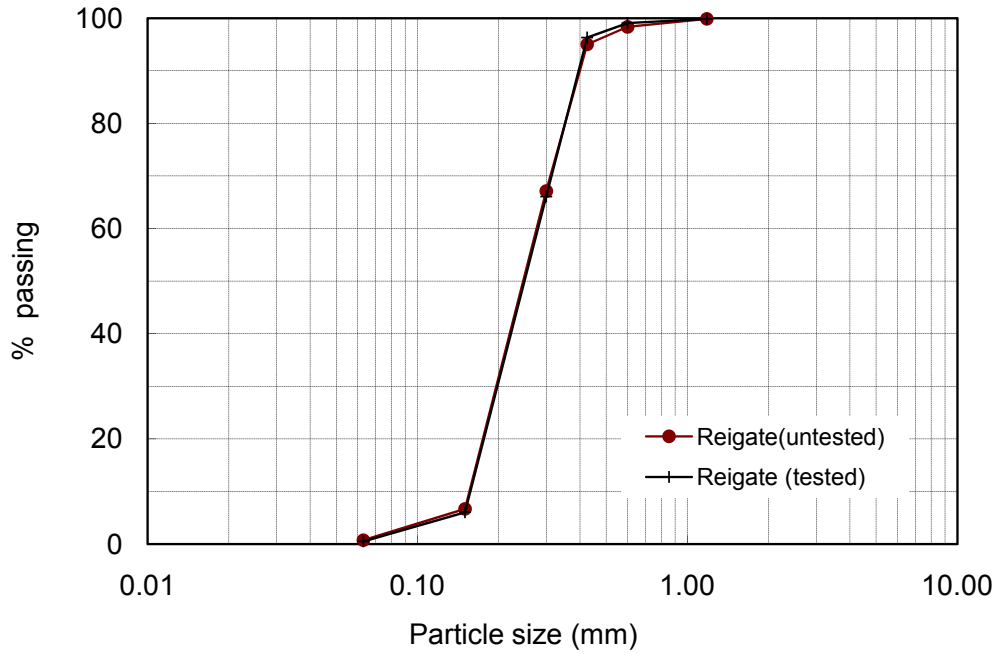

FIGURE 3.48: Particle size distribution curves determined by Sieve Analysis for untested and tested (at effective cell pressure of 50 kPa) RSS.

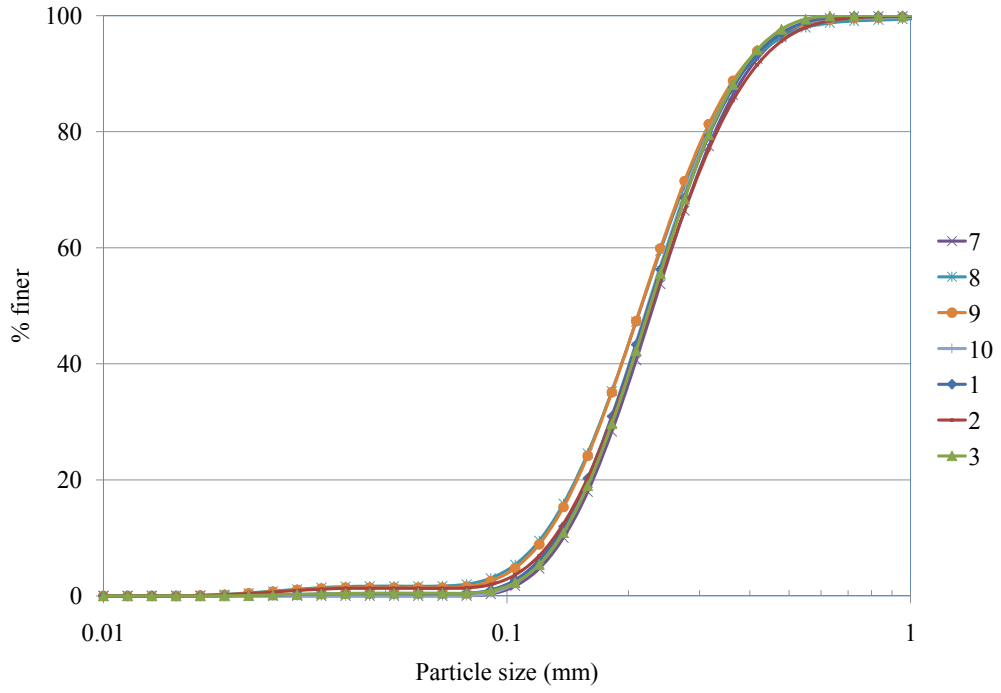

FIGURE 3.49: Particle size distribution curves of RSS determined by Laser Diffraction Method before and after shearing at effective cell pressure of 100 kPa . Samples #1, #2, and #3 were taken before shearing, samples #9, and #10 were taken from the shear band and samples #7, and #8 were taken from elsewhere after shearing

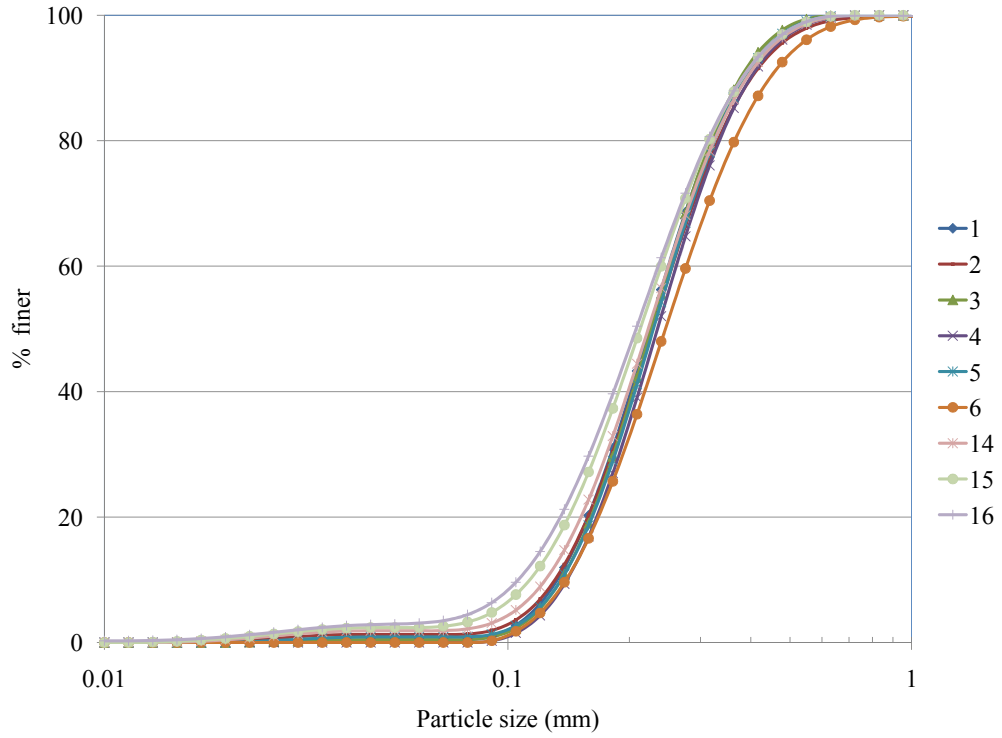

FIGURE 3.50: Particle size distribution curves of RSS determined by Laser Diffraction Method before and after shearing at effective cell pressure of 50 kPa . Samples #1, #2, and #3 were taken before shearing, samples #4, #5, and #6 were taken from the shear band and samples #14, #15, and #16 were taken from elsewhere of the sample after shearing

3.7 Discussion

It is now widely accepted that the shear modulus of a soil at small strain is influenced significantly by the void ratio and the applied stress. In the results presented (Figure 3.20 - 3.26), the initial shear modulus for all the three different materials showed a clear dependence on the applied cell pressure. The effect of the interlocked fabric on the initial stiffness of the intact material was also quite significant. This is evident from the relatively high initial stiffness of the intact material compared with the pluviated samples. The intact Reigate silver sand also exhibited a stiffness comparable with the pluviated samples of Leighton Buzzard sand. The initial shear moduli for pluviated samples of Reigate silver sand were significantly smaller than for pluviated Leighton Buzzard sand. This was likely due to the differences in void ratio, particle size and particle shape. A decrease in particle size increases the number of contacts per unit solid volume, decreasing the sample stiffness. Similarly, an increase in angularity (an effect of particle shape) increases the number of contacts per unit solid volume and hence decreases sample stiffness (Bui, 2009). The effect of the interlocked fabric on the shear modulus degradation of the intact material was found to be quite significant. This is evident from the relatively high stiffness of the material, even at 0.1 % average local axial strain, compared with the pluviated samples.

In some tests (especially at 12.5 kPa effective cell pressure), before the achievement of the peak strength, sudden jumps were observed on the q/p' and ϕ'_{mob} curves (for example, see Figures 3.30, 3.32, 3.33). There are two possible explanations for this observation: (i) closing of micro-cracks within the sample, and (ii) collapse of surface irregularities at the interfaces between the sample and the porous stones tend platens to achieve a proper fit . In tests carried out at relatively high cell pressures, the micro-cracks within the sample and the surface irregularities at the interfaces, if any, are more likely to close during the application of cell pressure, before the start of shear.

At the onset of dilation, no divergence of the LVDTs was observed in intact samples (Figure 3.51 and Figure 3.52). As shown in Figure 3.53, Cresswell & Powrie (2004) observed significant divergence in the displacements recorded by LVDTs at onset of dilation and used it as an indicator of strain localisation. In the intact samples tested at 50 and 100 kPa by Cresswell & Powrie (2004), the peak strengths were achieved immediately after the onset of dilation. In the current

tests, divergence was only observed near the peak. The divergence of LVDTs was commonly used as an indicator of the initiation of strain localisation in a sample (for example, Besuelle et al., 2000; Georgiannou & Burland, 2006; Abdelaziz et al., 2008). Although it is without doubt a function of where LVDTs are positioned relative to the location of localisation, with the use of four LVDTs chances of picking up any nonuniformity of deformation should be high. It is therefore not clear whether in the current tests the strain localisation started at the onset of dilation or around the peak.

The stress-strain responses of intact samples from the series B1 and the series B2 were similar (Figure 3.28(a), Figure 3.54(a)). This suggests that the observed behaviour of the intact material is reproducible.

As shown in Figure 3.55, the stress ratios, $q/p_0^{'}$, at peak for tests carried out at 50 and 100 kPa effective cell pressures ($q/p_0^{'}$ at 50 kPa = 8.06 and $q/p_0^{'}$ at 100 kPa = 7.71) were found to be significantly lower than those measured by Cresswell & Powrie (2004) ($q/p_0^{'}$ at 50 $kPa \approx$ 15.50 and $q/p_0^{'}$ at 100 $kPa \approx$ 10.50). The shape of q/p' curves at 50 and 100 kPa, however, showed significant similarities with this study (cf. Figure 3.54(b) with Figure 3.28(a) and Figure 3.54(a)). Figure 3.56 and Figure 3.57 indicate the friction angles mobilised (at the onset of dilation and at the pea), and the maximum dilation angles observed for the intact samples from series B1, series B2 and Cresswell & Powrie (2004) at different cell pressures. Significantly higher values of friction angles were mobilised by the intact samples of Cresswell & Powrie (2004), both at the onset of dilation and at the peak, than in the intact samples tested in this study. The maximum dilation angles observed (at similar cell pressures) were however almost similar. Cresswell and Powrie's pluviated samples exhibited peak friction angles similar to those observed in the pluviated samples tested in this study (at similar cell pressures), but higher values of friction angle at the onset of dilation. Similarly, Cresswell and Powrie's pluviated samples exhibited maximum dilation angles similar to those observed in the pluviated samples tested in this study (at similar cell pressures).

The peak friction angles for intact samples tested in series B1 and series B2 were similar, except at 12.5 kPa where a variation of nearly 3 degrees was observed. The friction angles at the onset of dilation were found to be similar for intact samples tested in series B1 and series B2, expect at 25 kPa where a variation of nearly 4 degrees was observed.

Possible explanations for the difference in behaviour are (i) the difference in void ratio, (ii) the amount of cement content, and (iii) the degree of saturation of the samples. There is no significant difference in void ratio between the intact samples tested in this study and by Cresswell & Powrie (2004). A comparison between the earlier thin-section examination by Cresswell & Powrie (2004) (Figure 3.5) and CT images (Figure 3.6) also shows no obvious difference in the interlocked structure of these materials. Only a few traces of cement were reported by Cresswell & Powrie (2004), and the same was observed in this study. There is however some difference in the B-value of the samples measured after saturation. The B-values of the samples tested in this study were all above 0.90 (in the range of 0.92 - 0.96). The B-value observed by Cresswell & Powrie (2004) were below 0.90 (in the range of 0.80-0.90)[1]. All the tests in this study and those by Cresswell & Powrie (2004) were carried out drained while maintaining a constant pore pressure of 50 kPa. A notable difference between the initial volumetric response before the achievement of the peak strength was identified. The initial volumetric response observed in this study for the intact samples was quite smooth. The onset of dilation was distinct and corresponded to an obvious yield point at which the stiffness of the sample started to reduce dramatically. The volumetric response observed by Cresswell & Powrie (2004) was almost flat until the onset of dilation, and then changed abruptly after onset of dilation (Figure 3.53 and Figure 2.3). No correspondence can be found in Cresswell & Powrie (2004) between the onset of dilation and the onset of yielding (as evident by the sharp reduction of stiffness and the development of relatively large strains).

In intact samples, the stress ratio mobilised at peak is not solely a function of rate of dilation. A plot like Figure 3.58 looks only at what is going on at the instant of peak strength. It does not reflect the fact that there are significant parts of the stress-strain curve at or near peak strength during which near-peak strengths are mobilised with comparatively small dilation rates and these near-peak strengths arise because of the interlocked structure. In other words, it obscures the significant role played by the interlocked structure in an intact sample on the mobilised strength over most of the strain range. To appreciate this, plots of mobilised stress ratio, q/p', versus rate of dilation in the intact samples were plotted in Figure 3.36 for the whole of each test. This figure show that high strengths are mobilised at comparatively lower dilation rates in the lead-up to the final peak strength. This is evidenced by the stress-dilation curve lying substantially above the relationships

[1]Private communication with Dr. A. Cresswell

given by Cam Clay and Rowe (Figure 3.39 to Figure 3.41). Once the peak has been passed, the effect of the locked structure is lost and the stress-dilation relationship is much closer to that for a pluviated sand or the relationships given by Rowe and Cam Clay. Figure 3.58 relates to what has happened after the benefit of the locked structure has been used up. Thus the stress-dilatancy relationship of the intact sand seems similar or even below that for the pluviated material. The only possible distinguishing factor is that the dilation rates (and hence the peak strengths) are greater for the intact material - but the plot shows that this is explained completely by their higher initial density, and is not an effect of the locked structure as such.

The stress ratios mobilised at the critical state in the intact samples were mostly slightly higher than in the pluviated samples of RSS tested at the same effective cell pressures as given in Table 3.1(cf. Cresswell & Powrie (2004): M (intact) = 1.41, M (pluviated) =1.24) except at 50 kPa cell pressure in which case the same stress ratio was mobilised. They were also generally found to increase with a decrease in confining pressure. This raises an important question of how the intact and pluviated samples with the same intrinsic material properties can have different critical state strengths? The difference might be an artefact of the apparatus that arose from the significant difference in deformation modes between intact and pluviated samples and different deformation mechanisms developed on the post-peak regime on intact samples depending on confining pressures applied. Furthermore, as the shear band intercepts both the top and bottom platens at low effective stresses (as shown in Figure 3.45(a)), for $H_0/D_0 \approx 2$ intact sample, we can not ignore the platen interference. The overall effect might be the apparent mobilisation of higher critical state strength in intact samples (Wong, 1999).

The above result highlights the shortcoming of an interpretation of stress-strain behaviour based on the assumption of homogeneous deformation, especially in the post-peak regime. Therefore, the constitutive responses and critical state of intact samples should be determined based on the synthesis of global behaviour prior to peak and shear band (local) behaviour following peak, or more rigorously before/after the onset of localisation, as highlighted by Finno & Rechenmacher (2003) and Mooney et al. (1998) in plane strain tests of dense sands.

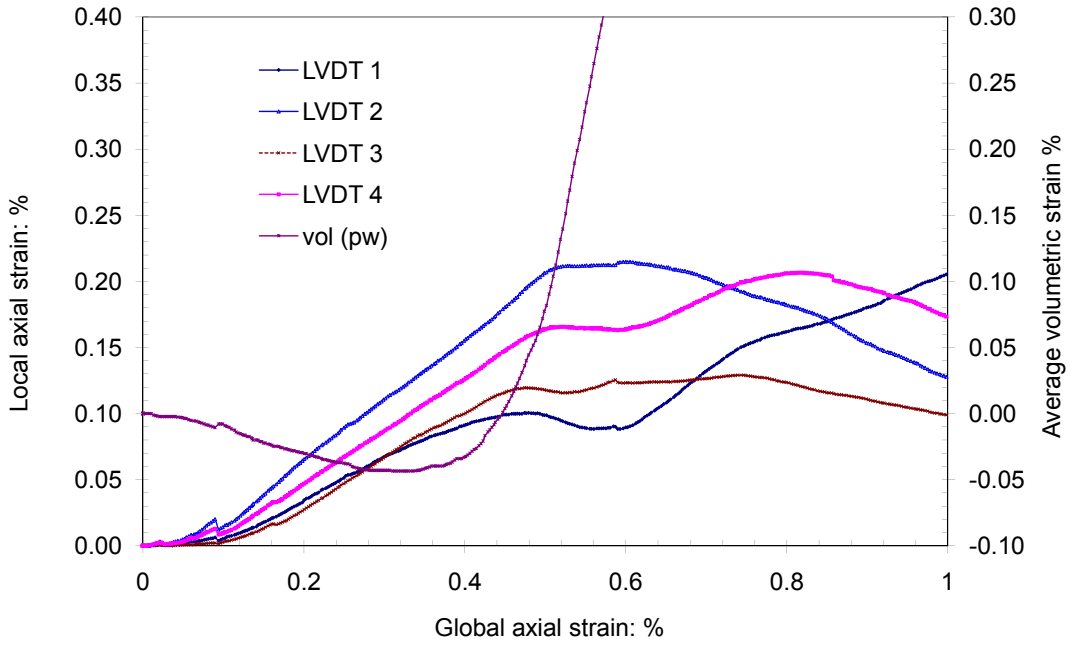

(a)

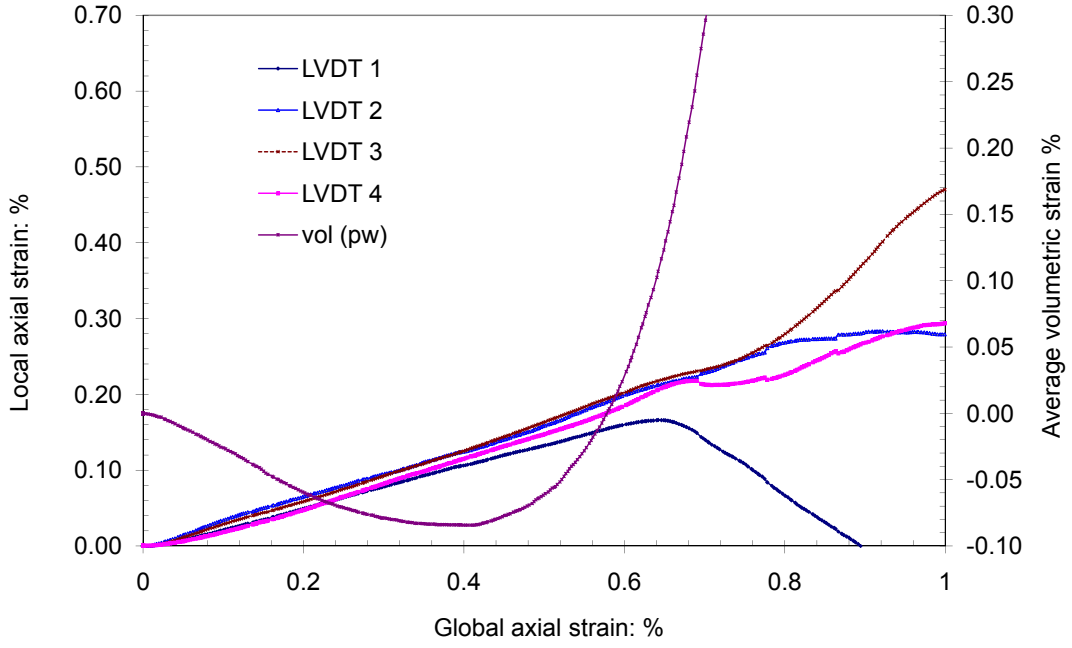

(b)

FIGURE 3.51: Local axial strain and volumetric strain plotted against global axial strain for intact RSS tested at effective cell pressure (a) 12.5 and (b) 25 *kPa*

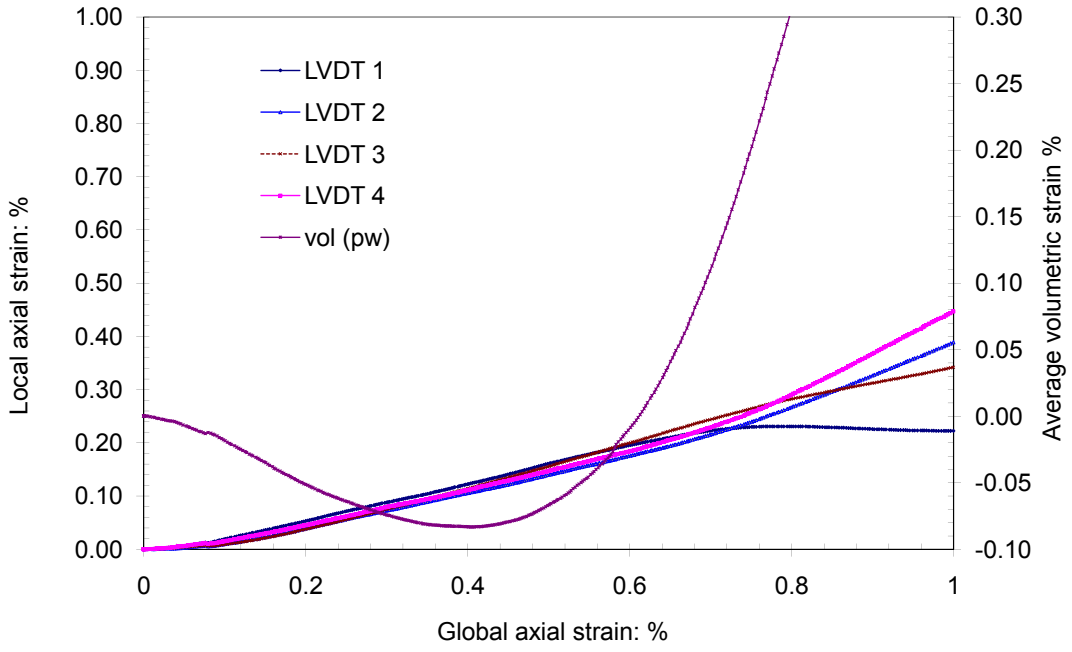

(a)

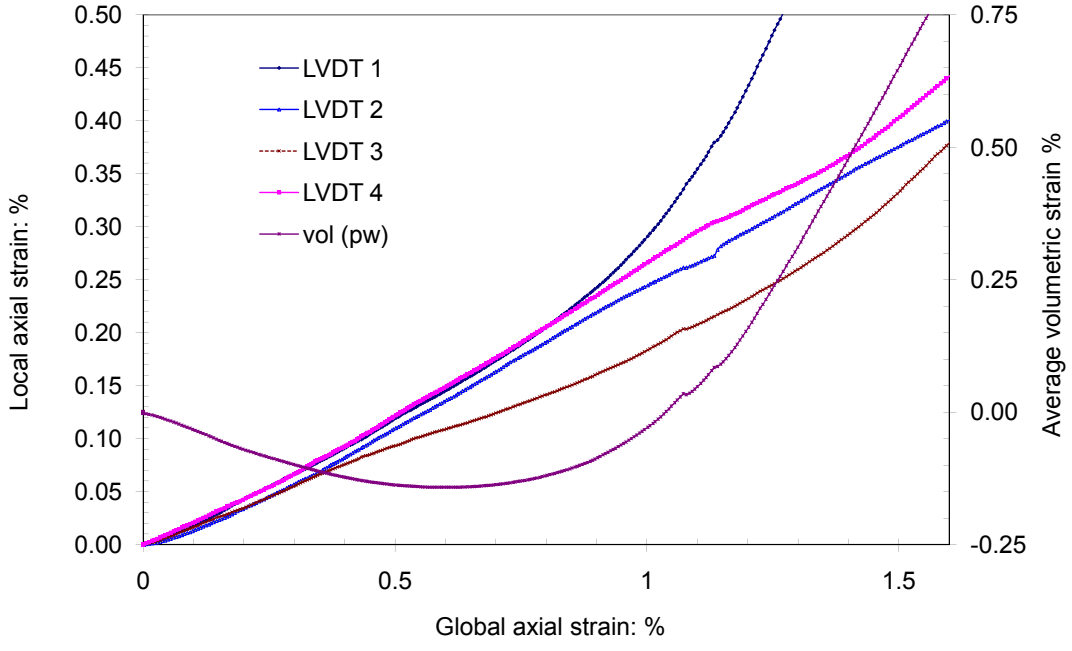

(b)

FIGURE 3.52: Local axial strain and volumetric strain plotted against global axial strain for intact RSS tested at effective cell pressure (a) 50 and (b) 100 *kPa*

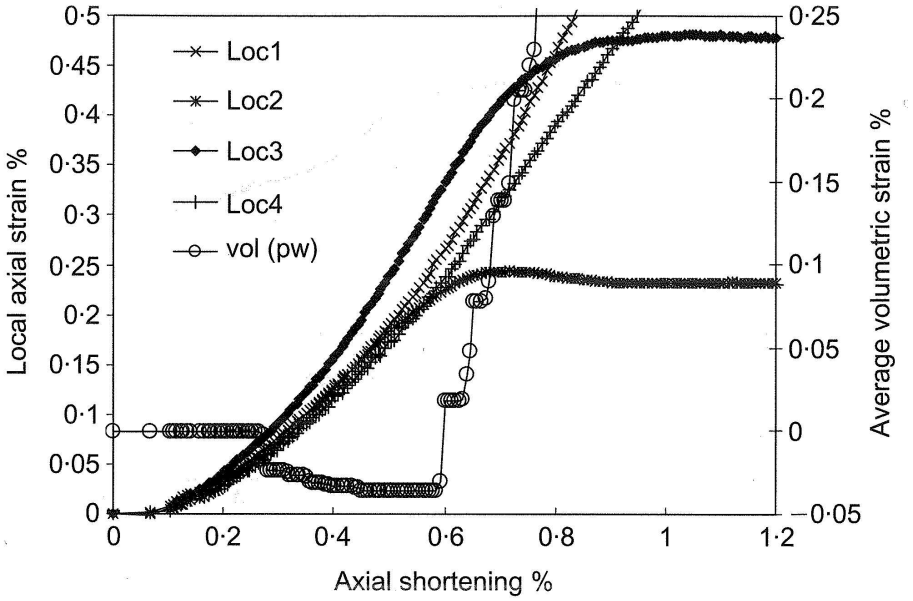

FIGURE 3.53: Local axial strain and average volumetric strain plotted against percentage axial shortening for intact A4 from block p (effective cell pressure 100 kPa) (Cresswell & Powrie, 2004).

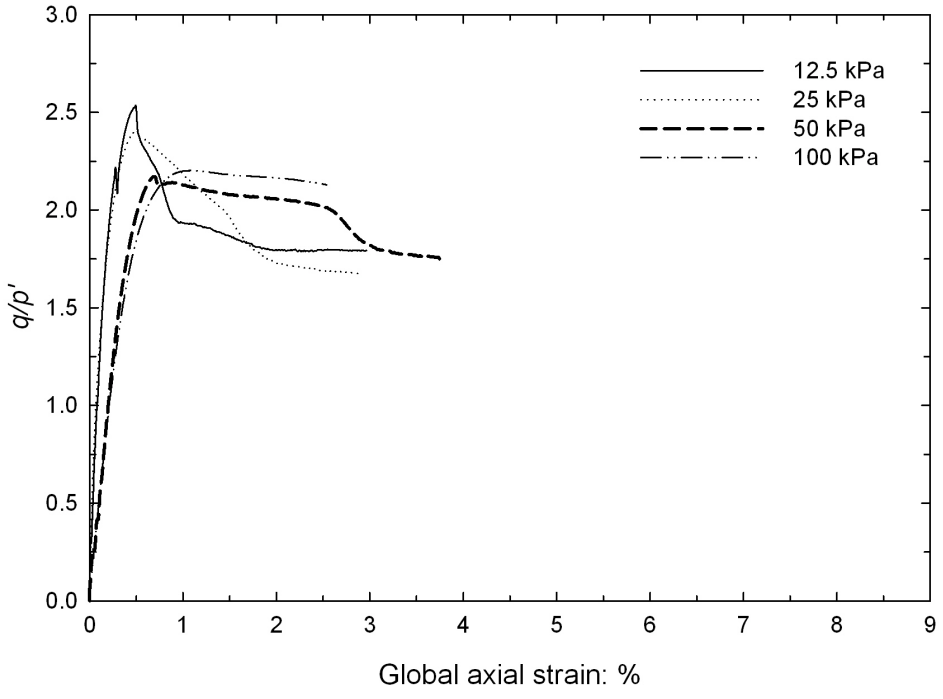

(a)

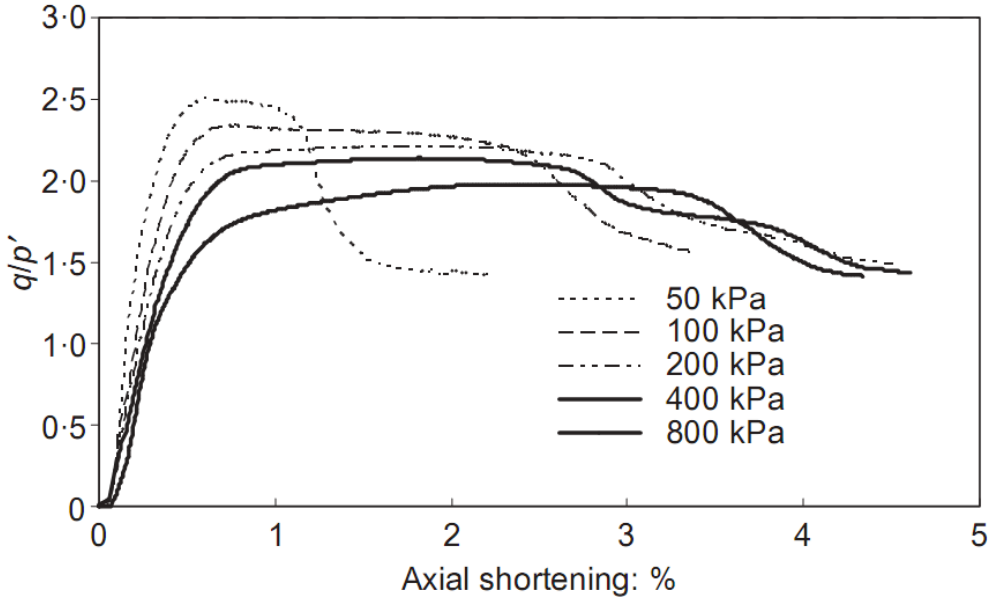

(b)

FIGURE 3.54: (a) Stress ratio, q/p', plotted against global axial strain, measured in drained triaxial compression tests at effective cell pressures of 12.5, 25, 50 and 100 *kPa*, respectively, for the intact samples of RSS (series B2). (b) Stress ratio, q/p', plotted against axial shortening, for tests on intact samples of A4 from block, p, at effective cell pressures of 50, 100, 200, 400 and 800 *kPa*, respectively (Cresswell & Powrie, 2004).

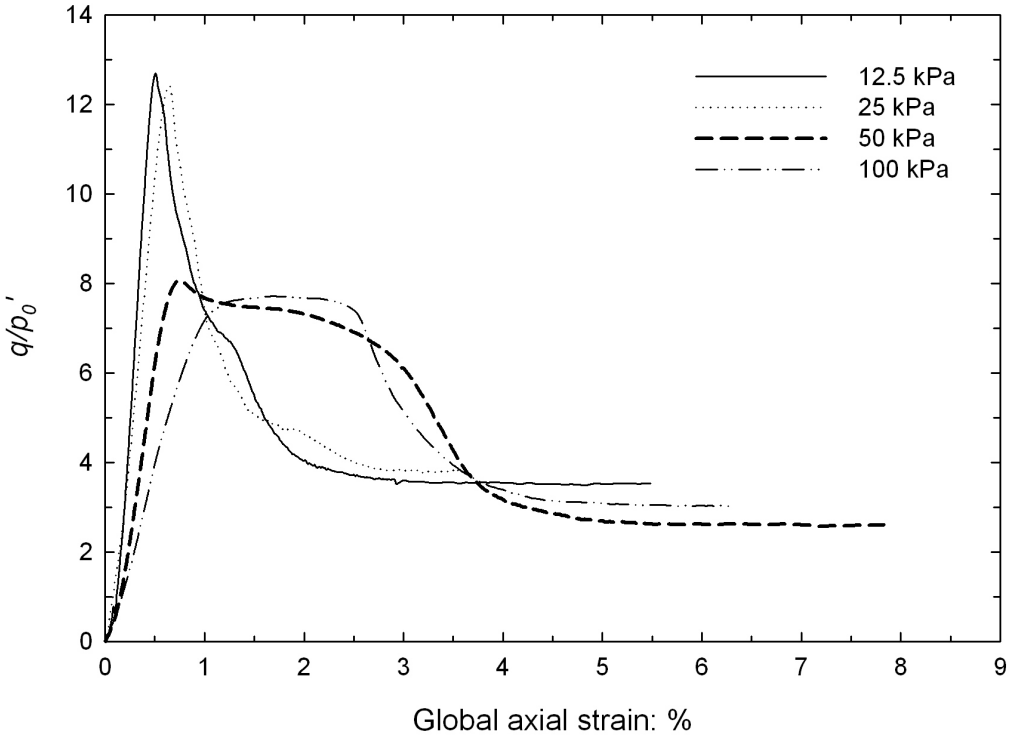

(a)

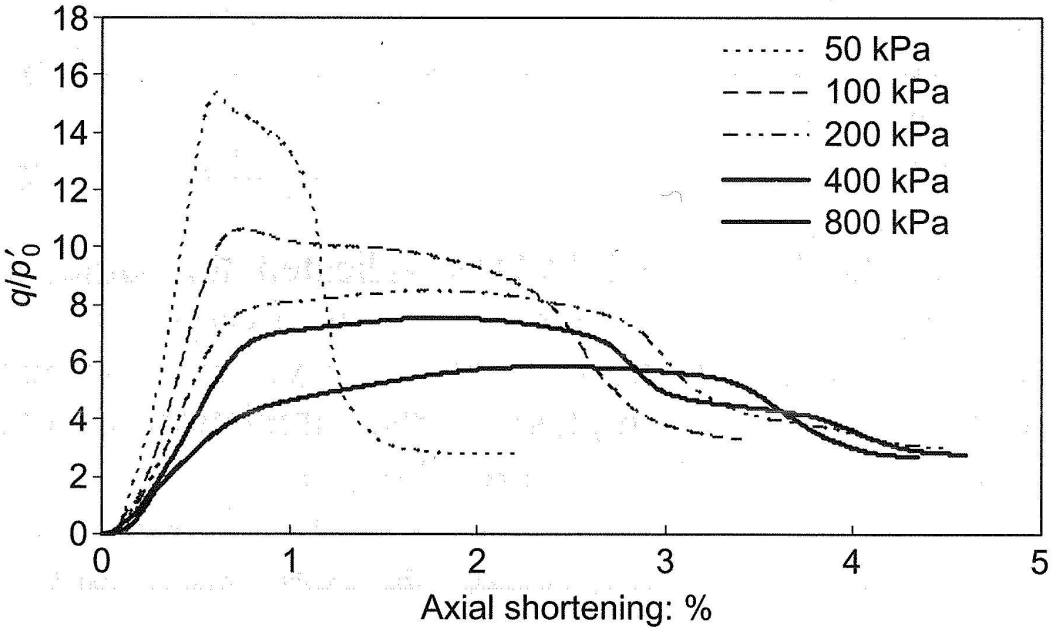

(b)

FIGURE 3.55: (a) Stress ratio, $q/p_0^{'}$, plotted against global axial strain, measured in drained triaxial compression tests at effective cell pressures of 12.5, 25, 50 and 100 *kPa*, respectively, for the intact samples of RSS. (b) Cresswell & Powrie (2004).

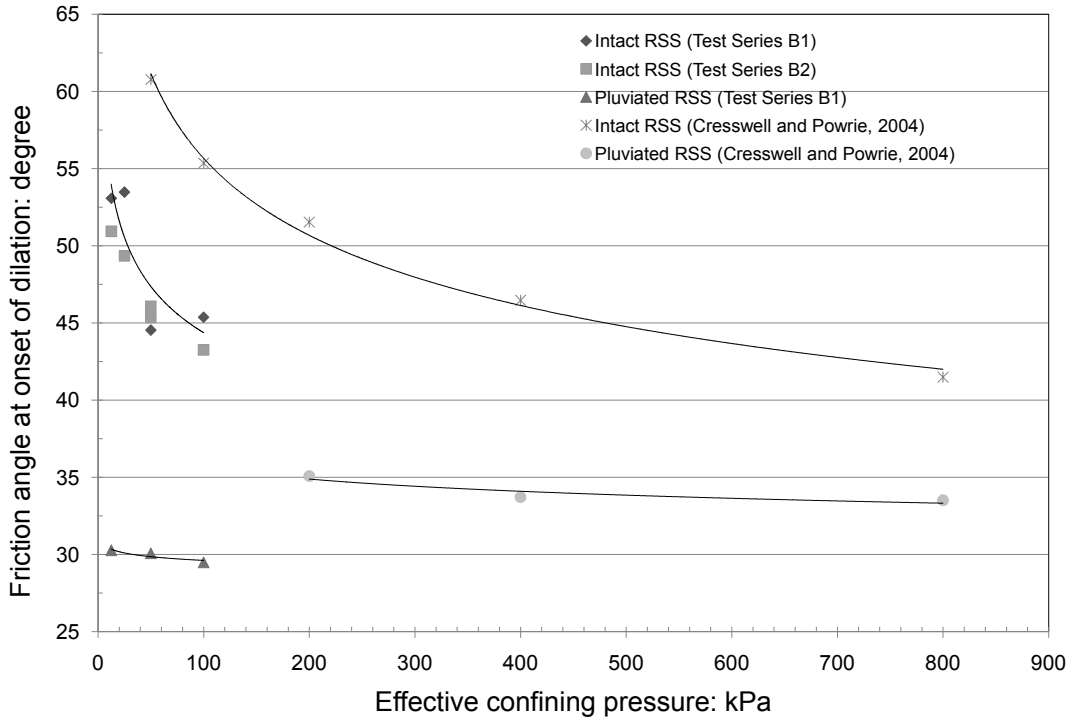

(a)

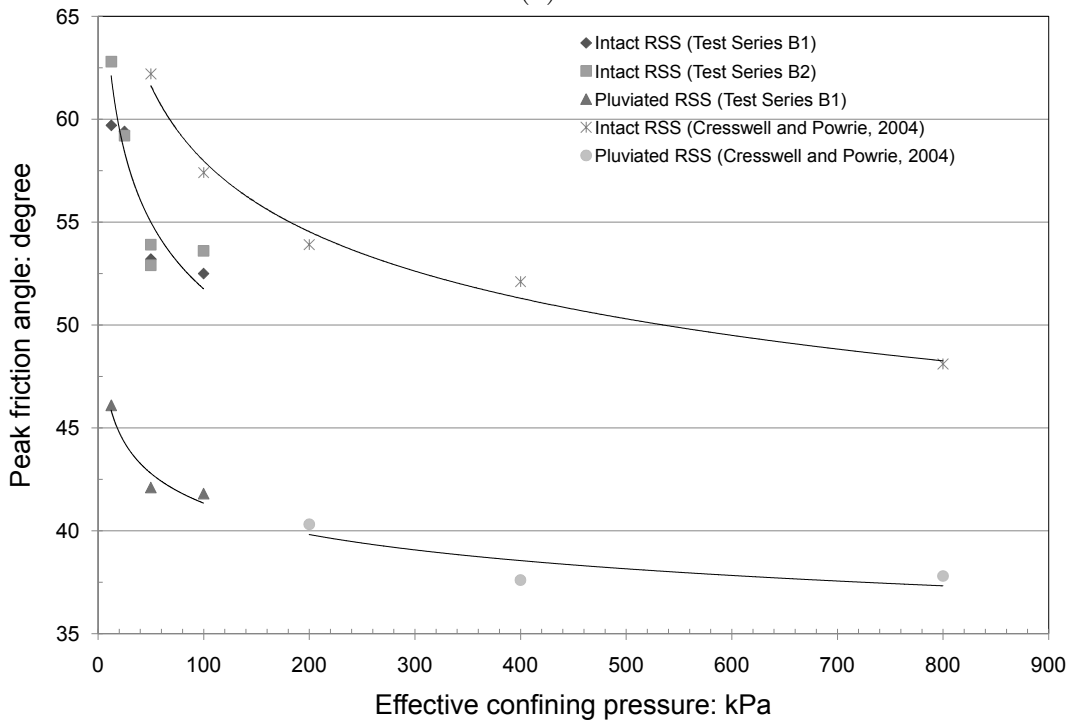

(b)

FIGURE 3.56: (a) Mobilised friction angle at onset of dilation for tests from series B1, series B2 and Cresswell and Powrie (2004). (b) Mobilised friction angle at peak for tests from series B1, series B2 and Cresswell and Powrie (2004).

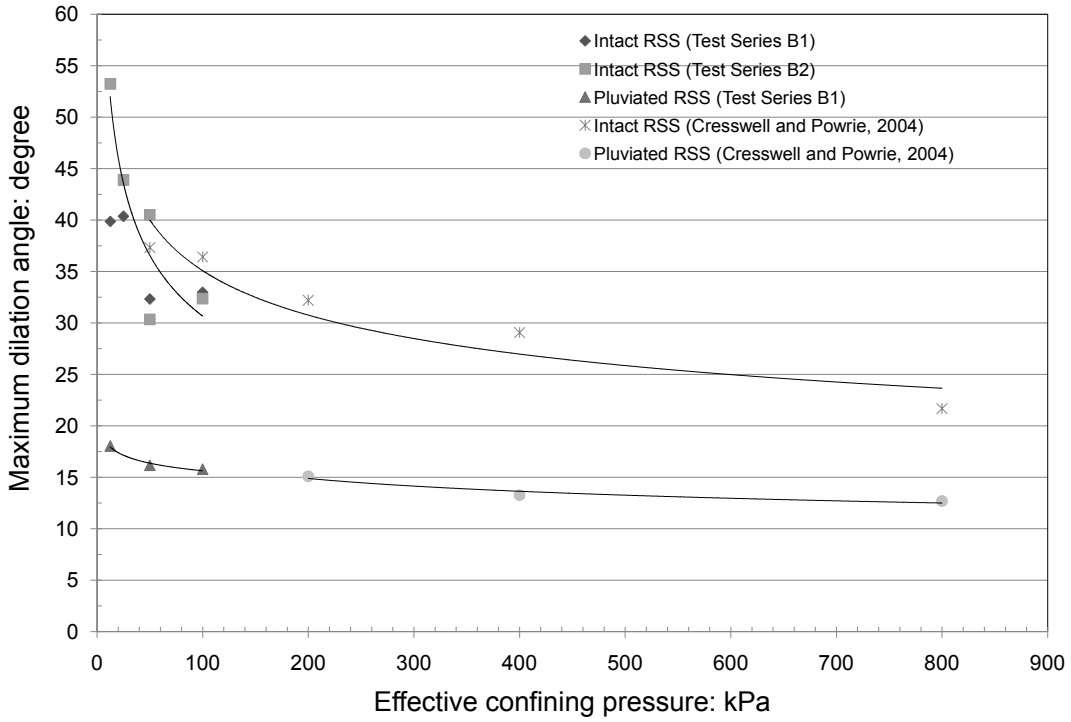

FIGURE 3.57: Maximum dilation angle for tests from series B1, series B2 and Cresswell and Powrie (2004)

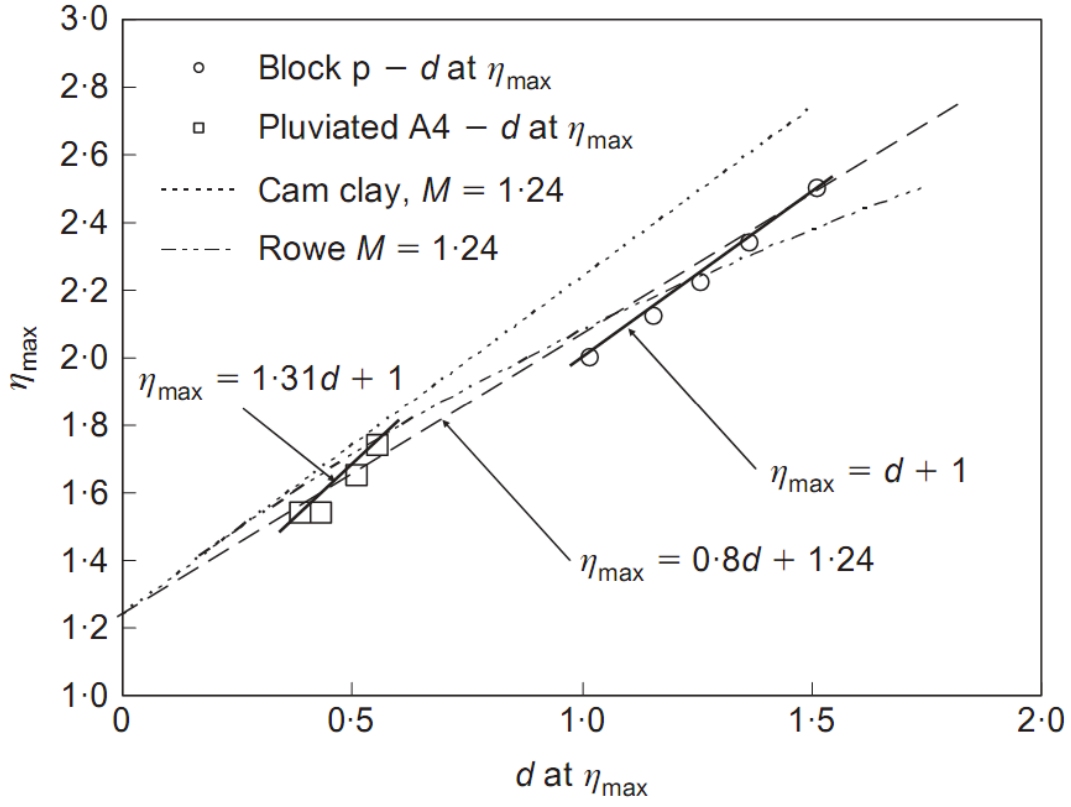

FIGURE 3.58: Rate of dilation, d, at maximum stress ratio, η_{max}, for tests on both intact and pluviated A4 at different cell pressures (after Cresswell & Powrie (2004)).

3.8 Conclusions

From the experimental results presented in this chapter, the following conclusions can be drawn:

1. At low effective stresses, intact samples can sustain stress ratios close to peak before the onset of dilation. It highlights the significant effect of the interlocked fabric on the strength deformation behaviour.

2. At very low strain, as the shear modulus decreases gradually the sample exhibits compression. Compression continues slowly accompanied by a reduction in stiffness, but an acceleration of the rate of compression is associated with a recovery of stiffness back to its initial value. The dip in shear modulus observed at very low strain is linked to the compression of the sample. An obvious yield point can be defined at which (a) the sample stiffness starts to reduce dramatically and (b) dilation starts.

3. In the intact samples, the peak stress achieved does not correspond to the instant at which the dilation rate is a maximum. Until the onset of dilation, significant contribution is made by the interlocked structure on the mobilised strength, and starts to fall thereafter. From the onset of dilation to the achievement of peak strength, dilation plays an important role in additional strength mobilisation. During this regime, although the dilation makes the contribution of interlocked fabric weaker, the work required to overcome the resistant against it mobilises some additional strength.

4. In the pluviated samples, however, the peak strength corresponds to the instant at which maximum dilation rate is achieved by the samples as in conventional soil mechanics.

5. In the intact samples, peak friction angle was found to decrease by more than 7 degrees when the cell pressure was changed from 12.5 to 100 kPa. Friction angle and rate of dilation at peak were found to strongly depend on stress level.

Chapter 4

Development of a new image-based surface deformation measurement system for cylindrical triaxial samples

4.1 Introduction

In recent years, there has been a rapid increase in the use of digital cameras to monitor the deformation of soils in centrifuge and laboratory element tests. The popularity of the method is mainly due to the fact that no contact with the soil sample is needed, and the availability of inexpensive digital cameras. By employing suitable digital image analysis techniques, the method has the potential to provide effectively continuous information at both the full field and local microscale. The triaxial test is the most commonly used laboratory element test in soil mechanics. The deformation of a triaxial sample is complex as the soil is free to move in all directions, unlike a plane strain test in which deformation takes place within a defined plane. The study of deformation using digital cameras in triaxial tests is further complicated by the distortion of the image of the sample by refraction due to the cell fluid, cell wall and air between the sample and the camera.

To develop a measurement system based on images, captured from outside the triaxial cell, it is necessary to understand properly the optics of the triaxial cell.

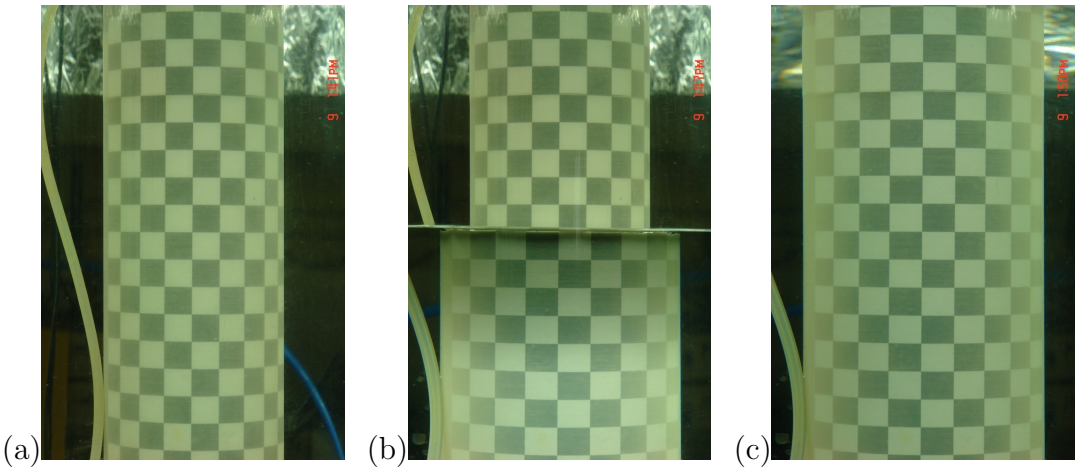

FIGURE 4.1: Photographs of a dummy sample showing refraction effects: (a) empty cell, (b) cell partially filled with water and (c) cell fully filled with water

Due to the cylindrical shape of the sample, the cell wall and the water inside the cell and the different refractive indices of the various media, the optical trajectories from the sample to the imaging device (camera) are quite complicated. Light rays pass through two interfaces: water to cell wall (Poly Methyl Methacrylate, PMMA), and cell wall to air. In the vertical direction, these interfaces are parallel hence the deviation of the light rays is only slight. In the horizontal direction, these interfaces are curved therefore the deviation of the light rays is more pronounced. These deviations of the light rays result in a magnification of the sample image.

To gain a clear illustration of the effects of refraction, a paper with a printed checkerboard pattern (grid spacing 10mm in both directions) was wrapped on the surface of a dummy sample, 70 mm in diameter and more than 160 mm in height, and the sample was photographed from outside the cell (Figure 4.1) when the cell was (a) empty, (b) partially, and (c) fully filled with water. The photographs clearly show that the vertical and horizontal magnifications are not equal; as expected, the sample was magnified much more in the horizontal than in the vertical direction.

To include the effects of refraction in optical measurement of sample deformation in hollow cylinder tests, Saada et al. (1999) photographed a sample with grid imprinted on its surface after it had been placed inside the cell and pressurized. This photograph was taken as the reference. In the horizontal direction, an empirical relationship between a length measured on the sample surface and distance measured on the image plane was established, giving a calibration curve. The

calibration curve was used to obtain real lengths from lengths measured on the image Figure 4.2(a, b). In the vertical direction, all nodes were moved proportionally upwards or downwards depending upon whether they are above or below the camera lens, since the configuration of the sample and the rigidity of the end platens constrains those lines that are initially horizontal to remain horizontal Figure 4.2(c). Similar approaches were adopted by Alshibli & Al-Hamdan (2001) and Kikkawa et al. (2006) to take into account refraction effects and lens distortion effects using an image with a grid of known dimensions imprinted on the surface of the sample.

For the measurement of volume changes in triaxial tests using digital imaging techniques, Macari et al. (1997) developed a 2D correction model using Snell's law of refraction to take into account of the refraction on horizontal plane. The technique was employed by Lin & Penumadu (2006) to study strain localization in hollow cylinder tests and by Sachan & Penumadu (2007) to study strain localization in triaxial tests. In the vertical plane, the correction was applied separately by Macari et al. (1997). Cecinato (2004) took account of refraction in a cylindrical triaxial cell by applying corrections using paraxial approximations (Jenkins & White, 1976). A major limitation of this approach is that it assumes the image scale to be independent of the view point. Also, only a correction for the horizontal distortion was applied i.e. it was assumed that there was no distortion on the vertical direction. To avoid refraction effects, Rechenmacher (2006) and Rechenmacher & Medina-Cetina (2007) carried out triaxial tests under vacuum confinement without use of the conventional confining cell. Therefore, it is evident that to take into account refraction fully, there is a necessity to develop a technique to carry out analysis directly in three dimensions.

This chapter describes a new measurement system for monitoring deforming triaxial samples in a transparent triaxial cell developed to understand the local phenomena occurring at a particulate scale which in fact determine the global response of the sample. A ray tracing technique is used to take account of image distortion due to refraction. A suitable digital image correlation routine is developed to analyse the captured images. The technique is illustrated with reference to a pluviated Leighton Buzzard sand (LBS), tested in drained triaxial compression.

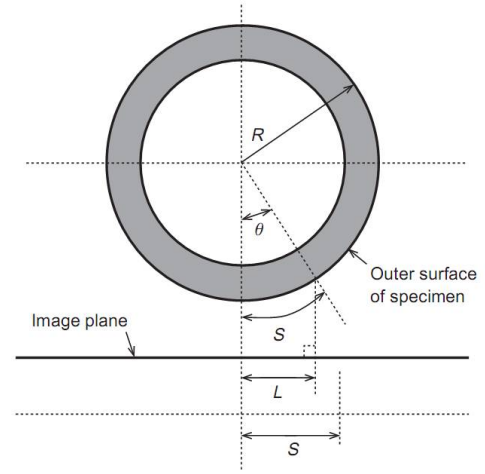

(a)

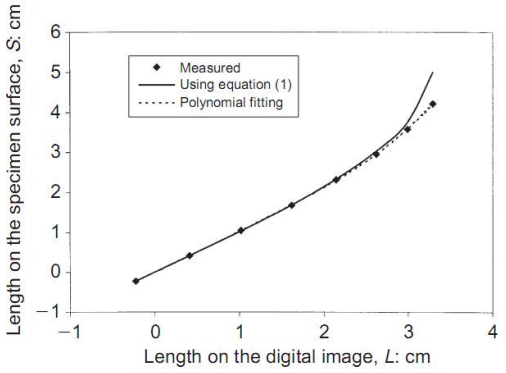

(b)

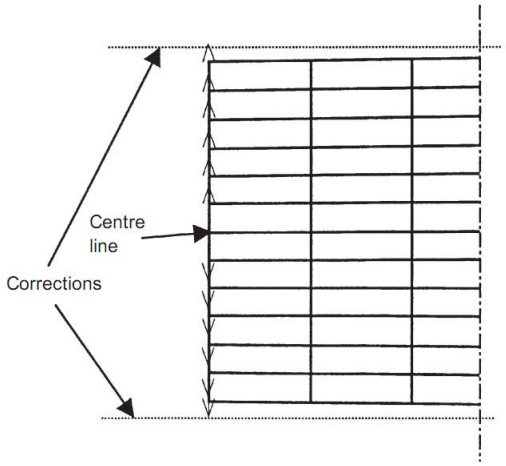

(c)

FIGURE 4.2: (a) Relationship between the length on the image and the length on the sample's surface (b) Relationship between S and L [equation (1) ignoring refraction effects $S = R \arcsin \frac{L}{R}$, Polynomial fitting $S = -0.011156 + 0.977054L + 0.125584L^2 0.085549L^3 + 0.023024L^4$] (c) Vertical corrections (Saada et al., 1999)

4.2 Experimental setup

Three digital cameras (SONY DSC-R1 Cyber shot 10 mega pixels) placed on radii at intervals of 120° viewed on plan outside a transparent triaxial cell were used to capture the images of the deforming samples at various time intervals. Figure 4.3 shows the transparent cell, three digital cameras, light source and light reflection arrangement to illuminate the sample uniformly through out the test.

4.2.1 Camera setup

The cameras were mounted on camera heads which were clamped at the free end of cantilever mounts. The other end of each cantilever was screwed onto the base of the triaxial platform, so that the whole camera system moves up with the cell base during the shearing process. The cameras heights can be adjusted using 10 mm thick steel plates to compensate for variations in sample height and bring the optical axes of the cameras approximately level with the mid-height of sample. The horizontal and vertical rotation adjustment screws allow setting up the camera properly (Figure 4.4). The grid lines which divide the camera display screen into three parts heightwise and widthwise, as shown in Figure 4.5, made setting up the camera easier. Trial images were captured from each camera and the offset distances (from the edge of the sample to the edge of the image) on either side of the sample were checked using Matlab to make them approximately equal.

4.2.2 Camera settings

The aspect ratio of images recorded by the cameras is 3:2 (3888 pixels x 2592 pixels). This provides greater pixel resolution for a sample 70 mm in diameter and 140 to 178 mm in height than the 4:3 ratio more commonly found in digital cameras. As focusing on the sample through the cell wall is difficult in auto focus mode, images were captured in manual focus mode. The aperture was set to a small opening (a larger F-number) decreasing the amount of light admitted and increasing the depth of field. In this mode, the shutter speed is automatically adjusted by the camera to obtain the correct exposure according to the brightness of the object. This setting allows the whole sample to be sharpened on the image. To record a smoother image, images were captured with relatively low ISO

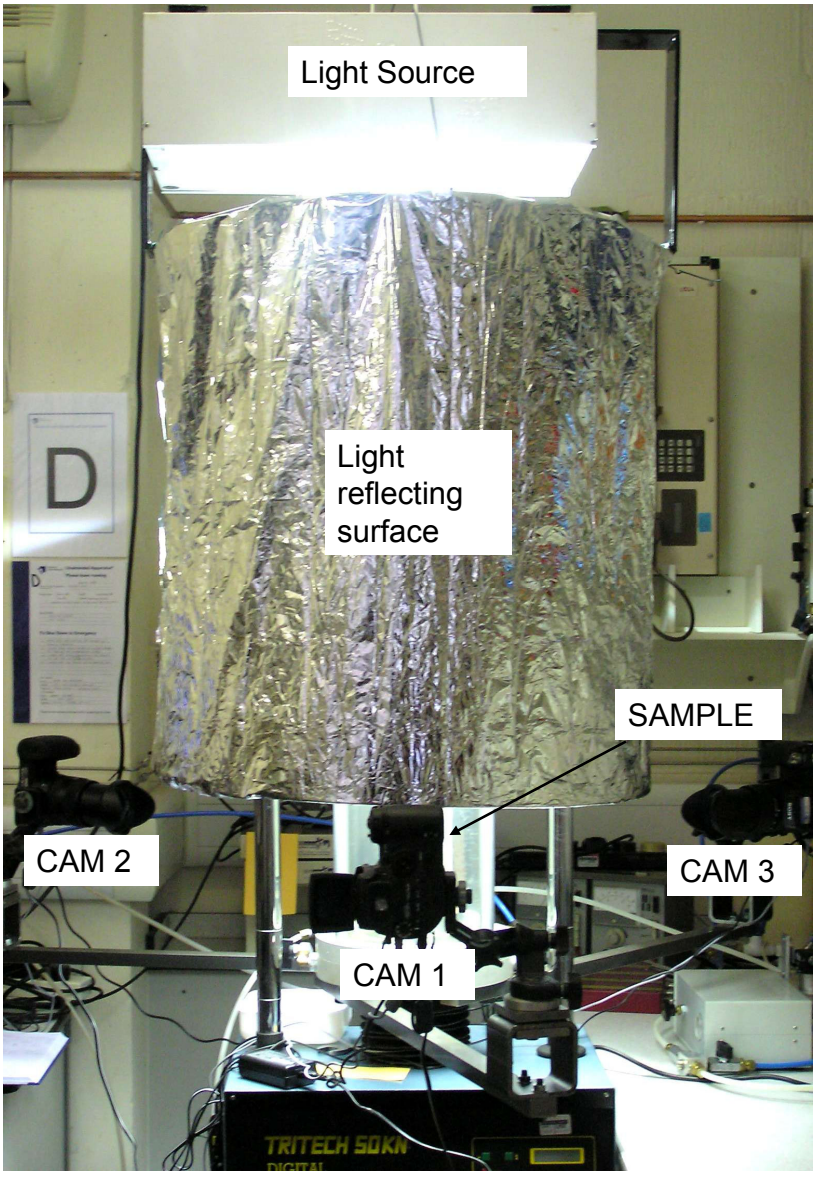

FIGURE 4.3: The transparent triaxial cell, three digital cameras, uniform light source and light reflecting surface

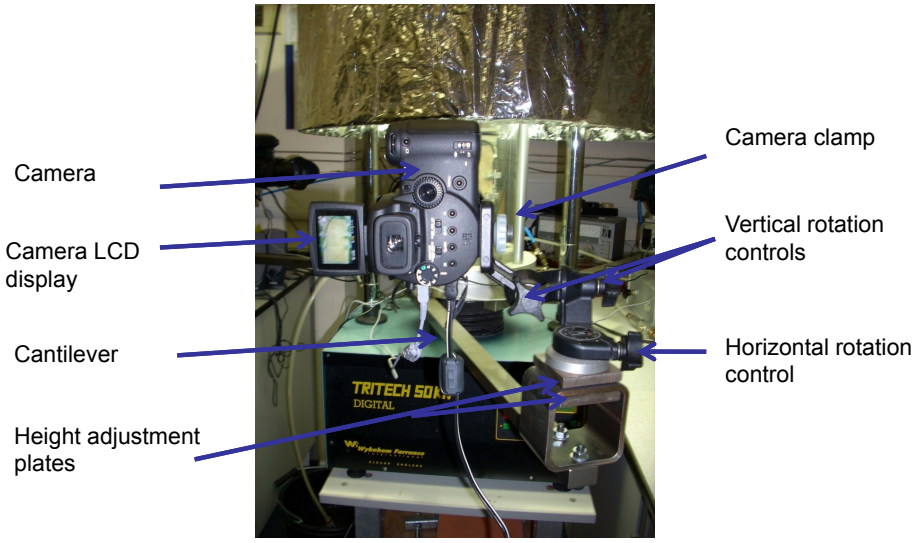

FIGURE 4.4: Camera setup detail

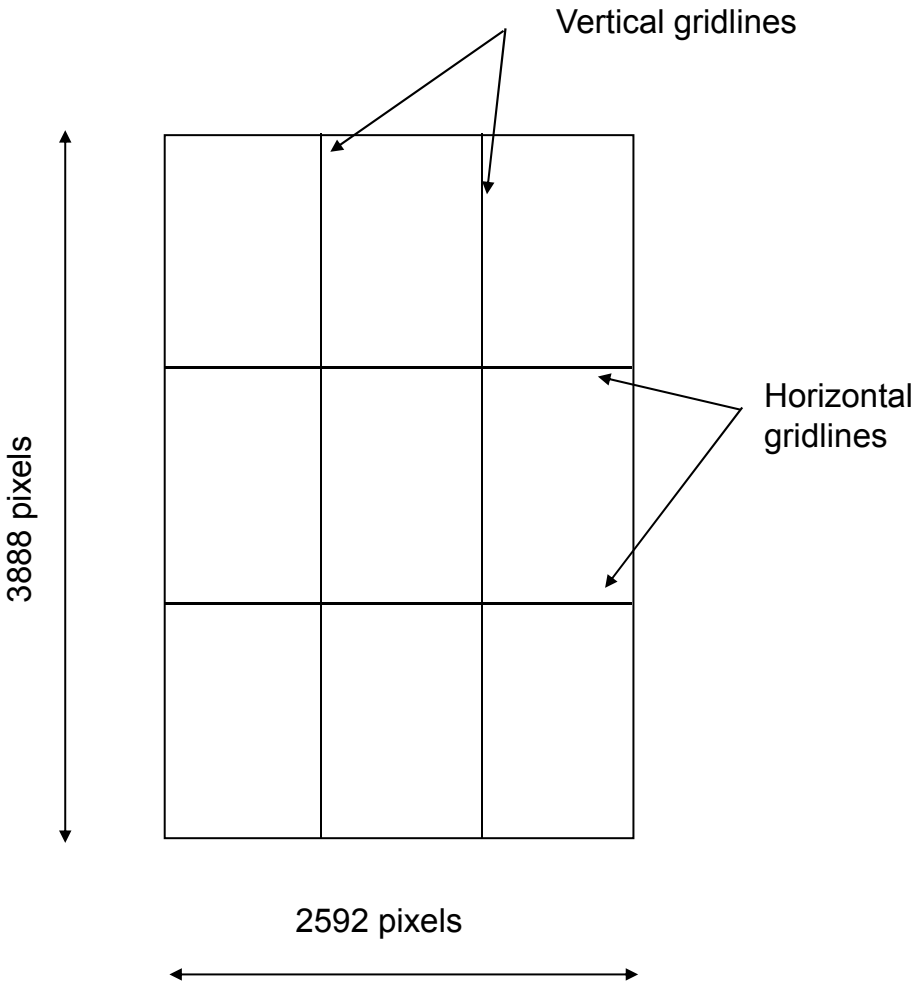

FIGURE 4.5: Camera grid

(International Organization for Standardization) sensitivity (ISO=400). This ISO rating indicates the level of sensitivity of the camera sensor to the light. Images were captured in RAW mode in which the camera records the data captured from the CMOS sensor directly without compression. The file extension is .SR2. A JPEG format image like the one recorded in the normal shooting mode is also recorded at the same time. In this mode, writing data to the memory card takes slightly longer time than in the normal recording mode. Since the strain rate of shearing was kept slow, the time interval between consecutive images is large enough compared with the recording time.

4.2.3 Lighting arrangement

A lighting arrangement was designed to illuminate the sample enabling the capture of clear, high quality images. The light source was fixed to a yoke clamped onto the two vertical posts of the triaxial apparatus frame. It consisted of a 200W white light bulb enclosed in a metal box, with a transparent glass plate on the bottom face and reflective coatings on all the other faces. A curtain of reflective aluminium foil was placed around the triaxial cell from just below the lamp bulb to the mid-height of the sample. This arrangement provided uniform light and illumination of the sample.

4.2.4 Creation of artificial texture on the membrane

The digital image correlation technique relies heavily on the visual texture. It should be distinct enough to contain information (in the form of a group of intensity values) unique to the area of interest. This information will be sought in subsequent images. The natural variation of the texture of sand grains is normally sufficient for this purpose (White et al., 2003; Rechenmacher & Finno, 2004). However, in the present case, the latex membrane absorbed water from the cell and the sample, and after a few hours in contact with water, turned completely opaque (Figure 4.6 (a, b)). Therefore it was not possible to rely on the visual texture of the sand grains. To resolve this problem an artificial texture was produced on the membrane, by spraying it with quick drying black enamel paint. The spraying creates small dots on the membrane surface (Figure 4.6 (c)).

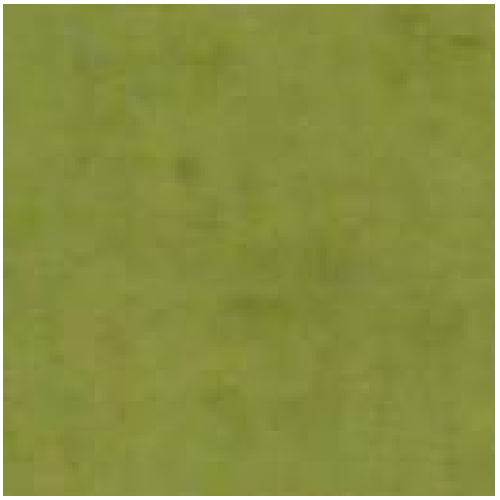

(a)

(b)

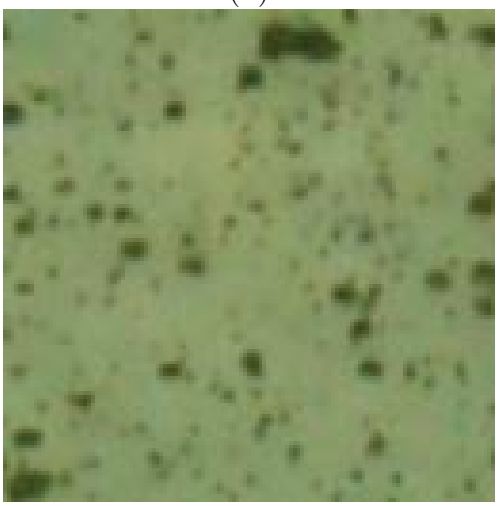

(c)

FIGURE 4.6: Membrane texture: (a) before absorbing water, (b) after absorbing water, (c) after spraying with black enamel paint

4.3 Methodology of the image-based measurement technique

The image-based measurement technique consists of the following steps:

1. Ray trace points of an imaginary plane (assumed in front of the triaxial cell) backwards from the camera focus to the sample surface.
2. Calibrate camera to determine camera parameters (focal length, principal point etc.).
3. Establish measurement points on the sample surface, determine their positions on the imaginary plane by bi-linear interpolation using the ray tracing data and on the image using camera parameters, and determine the scaling factors.
4. Use digital image correlation to determine the movement of measurement points (i.e. displacement components in pixels) between two subsequent images, captured during shear deformation of the sample.
5. Calculate the true displacement components by multiplying the displacement components determined in the step 4 by the scaling factors (for the vertical and horizontal directions) at each measurement point and convert them into millimetres using the camera parameters and the Pinhole camera model.
6. Plot displacement vectors on the sample surface (unwrapped).
7. Post processing of displacement data.

Each step is described in detail in the following sections.

4.4 Ray tracing

This section describes the use of ray tracing technique to account for the effects of refraction. Ray tracing involves tracing the path of each ray of light backwards from the camera focus and through the image point (of the apparent image plane) to the object space.

4.4.1 Refraction model

Figure 4.7(a) shows an isometric view of a transparent triaxial cell filled with water and a sample placed inside the cell. The cell outer and inner walls are represented by Surface 1 and Surface 2. The axes x, y and z originating from O, which is assumed to be the apparent focus of a camera, are also shown. An imaginary plane was assumed to exist in front of the Surface 1. The imaginary plane can also be called the image plane. The x axis passes normal to the imaginary plane at the mid-height of the sample and intersects the longitudinal axis of the sample at C. Only the upper half-portion of the cell and sample are shown. The x axis is the optical axis of the camera and the camera is facing towards the cell at O. The cell is filled with water. The idea of ray tracing is to follow the path of all rays backwards from O through points on the imaginary plane to the sample surface. Their locations on the sample surface must also be found. As an example, in the Figure 4.7 (a) the ray tracing for a typical ray OI is shown. This ray originates from the focus O and passes through point $I(x_i, y_i, z_i)$ on the imaginary plane. It hits Surface 1 at the Point $P(x_1, y_1, z_1)$, Surface 2 at the Point $Q(x_2, y_2, z_2)$, and finally the surface of the sample at the Point $R(x_0, y_0, z_0)$. The deviations of the ray at cell outer wall (i.e. air cell interface) and cell inner wall (i.e. cell water interface) are also shown. The refraction of light at these interfaces is governed by the *Snell's law*. The plan view is shown in Figure 4.7(b). Points I', P', Q', and R' are the projections of Points I, P, Q, and R on the xy plane. N_1 and N_2 are the normals to the Surface 1 and Surface 2 at Point P' and Point Q' respectively. The distance of the camera focus from the cell outer wall and the radii of Surface 1 and Surface 2 are also given.

Although the ray tracing process is conceptually simple, carrying out ray tracing in three-dimensional space is not an easy task. The problem can be simplified by dealing only with the projection of the incident and refracted rays on horizontal and vertical planes at each interface. To illustrate this technique and to find out the refracted ray PQ for the incident ray OP at Point P on the Surface 1 in the Figure 4.7(c), the incident ray OP is projected onto the horizontal plane ($OAP'B$) and the vertical plane ($AP'PH$). The vertical plane ($AP'PH$) is the normal plane to the Surface 1 and passes through the axis of the sample. OP' and AP are the projected horizontal and vertical components. Let PK be the refracted ray (drawn in the opposite direction to its actual path PQ) of the incident ray OP. PK can also be projected on the horizontal and vertical planes. $P'M$ and PJ are

the projected horizontal and vertical components. Now $P'M$ drawn in the opposite direction should pass through $P'Q'$ and PJ drawn in the opposite direction should pass through $P'Q''$. $P'Q'$ is the refracted ray for the incident ray OP' at Point P' on the horizontal plane and $P'Q''$ is the refracted ray for the incident ray AP at Point P on the vertical plane. The Points Q' and Q'' are the projections of Point Q on the horizontal and vertical planes.

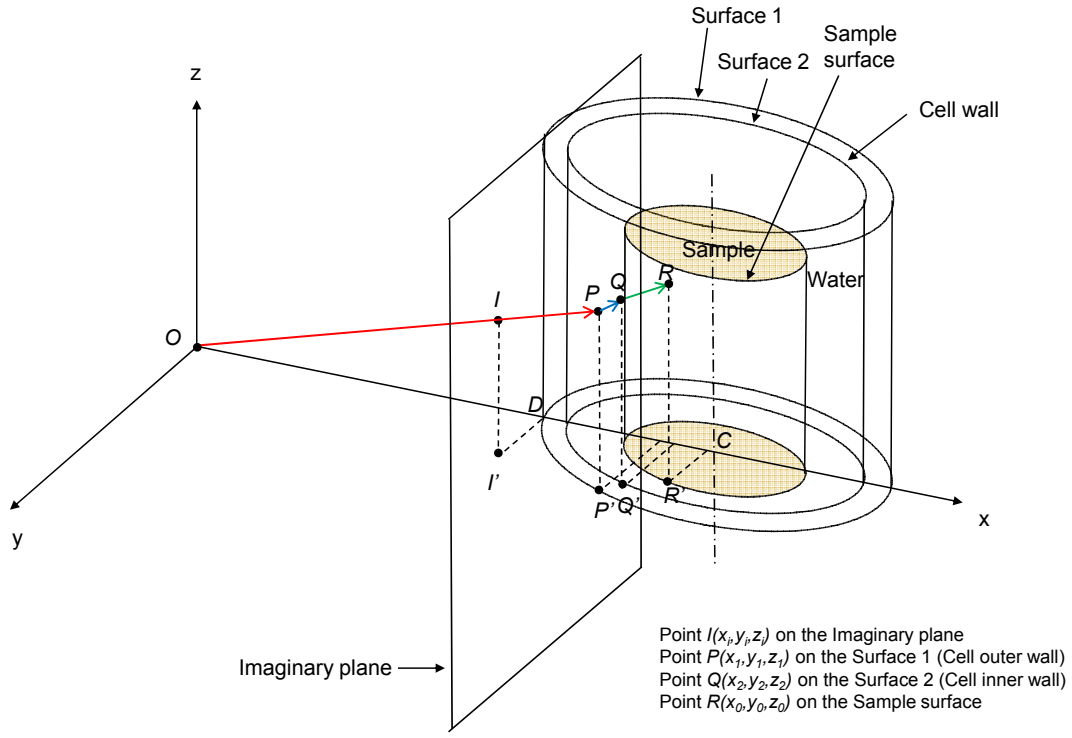

(a)

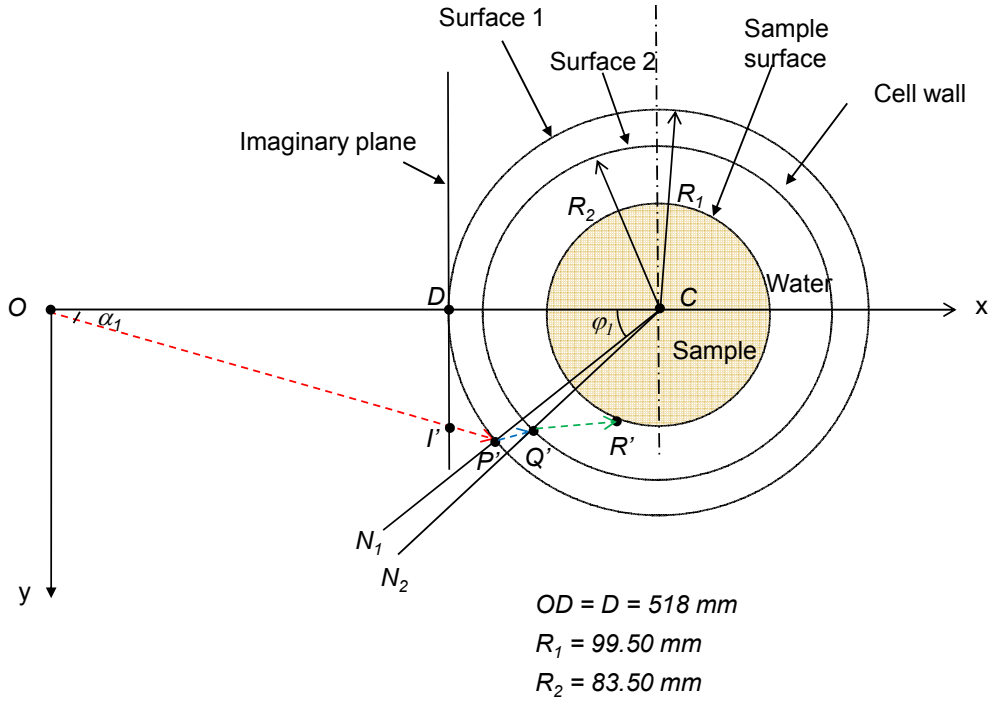

(b)

FIGURE 4.7: Schematic representation of the Ray tracing technique for a ray (a) 3D view (b) Plan view (c) 3D refraction model (To be continued in next page)

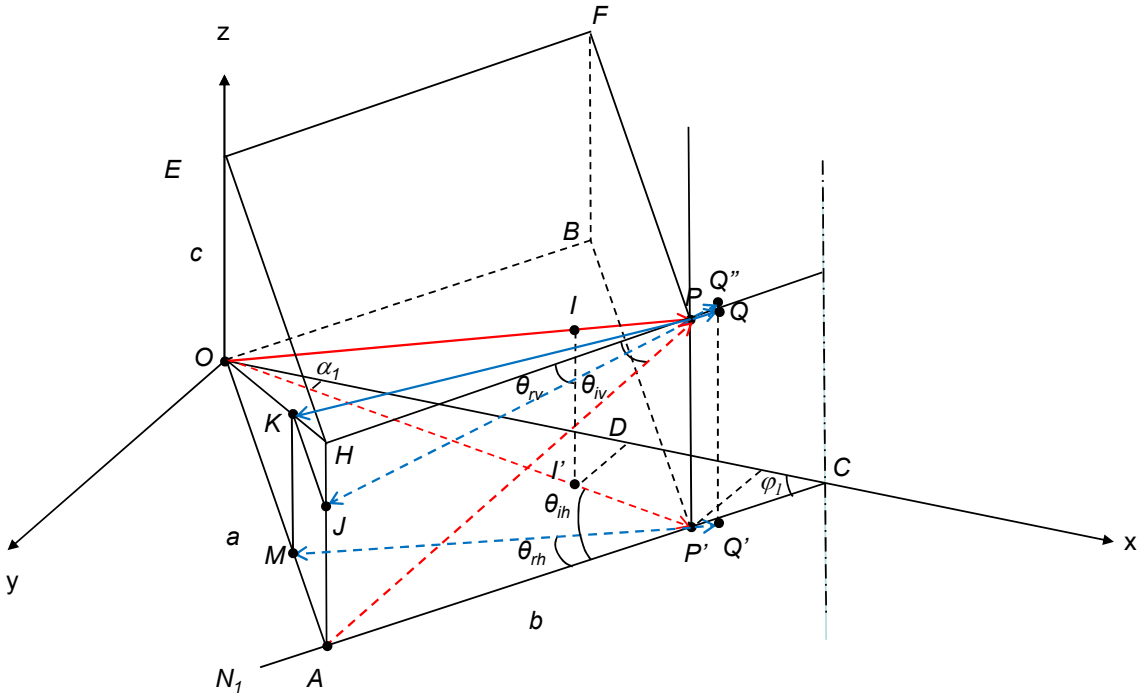

(c) FIGURE 4.7 (Continued from previous page)

Let,

$$\angle OPH = \theta_i \text{ (angle of incidence)},$$
$$\angle HPK = \theta_r \text{ (angle of refraction)},$$
on the horizontal plane $(OAP'B)$ at Point P':
$$\angle OP'A = \theta_{ih} \text{ (angle of incidence)},$$
$$\angle AP'M = \theta_{rh} \text{ (angle of refraction)},$$
on the vertical plane $(AP'PH)$ at Point P
$$\angle APH = \theta_{iv} \text{(angle of incidence) and}$$
$$\angle HPJ = \theta_{rv} \text{ (angle of refraction)}$$

Also let $OA = a$, $AP' = b$, $OE = HA = PP' = c$ and $MA = ka$, where, k is constant. Then by comparing the similar triangles $\triangle HKJ$ and $\triangle OHA$, $HJ = kc$. Now on the vertical plane $(AP'PH)$,

$$\frac{\tan\theta_{rv}}{\tan\theta_{iv}} = \frac{\frac{HJ}{PH}}{\frac{HA}{PH}} = \frac{HJ}{HA} = k \tag{4.1}$$

Therefore,

$$\tan\theta_{rv} = k\tan\theta_{iv} \tag{4.2}$$

Similarly on the horizontal plane $(OAP'B)$,

$$\tan\theta_{rh} = k\tan\theta_{ih} \tag{4.3}$$

Using Snell's law,

$$n_a \sin\theta_i = n_p \sin\theta_r \tag{4.4}$$

Substituting for $\sin\theta_i$ and $\sin\theta_r$ manipulating algebraically, Equation 4.5 is obtained.

$$\frac{1}{k^2} = r^2 + (r^2 - 1)\frac{a^2 + c^2}{b^2} \tag{4.5}$$

where, $r = \frac{n_p}{n_a}$, n_p and n_a are the refractive indices for cell wall and air, respectively.

The values of a, b and c for the ray OP can be calculated from the geometry. The coordinates of point I, (x_i, y_i, z_i), are known. Therefore, on the horizontal plane $(OAP'B)$, the equation of the ray OP' passing through the origin (camera focus) and the point $I'(x_i, y_i)$ can be determined. Solving the equation of this ray and the equation of the Surface 1 on the horizontal plane (i.e. $(x - L)^2 + y^2 = R_1^2$) gives the coordinates (x_1, y_1) of the point of intersection P', where, $L = OC$ is the distance of sample centre from the focus O. Then,

$$\alpha_1 = \tan^{-1}\left(\frac{y_1}{x_1}\right) \tag{4.6}$$

$$\varphi_1 = \sin^{-1}\left(\frac{y_1}{R_1}\right) \tag{4.7}$$

$$\theta_{ih} = \alpha_1 + \psi \tag{4.8}$$

$$a = OP\sin\theta_{ih} \tag{4.9}$$

$$b = OP\cos\theta_{ih} \tag{4.10}$$

On the vertical plane $(AP'PH)$,

$$c = (z_i/x_i) \times x_1 \tag{4.11}$$

$$\theta_{iv} = \tan^{-1}\left(\frac{c}{b}\right) \tag{4.12}$$

Using Equation 4.5, k can be determined.

Next using Equation 4.2 and Equation 4.3, the angles of refractions θ_{rv} and θ_{rh} can be determined.

Let, α'_{rh} be the angle the refracted ray $P'Q'$ makes with the x-axis on the horizontal plane then, $\alpha'_{rh} = \varphi_1 - \theta_{rh}$, from which the slope of the refracted ray $P'Q'$ can be calculated. The equation of the refracted ray $P'Q'$ can then be determined. Solving the simultaneous equations of this ray and Surface 2 (i.e.$(x-L)^2+y^2 = R_2^2$), gives the coordinates (x_2, y_2) of the point of intersection Q'. To locate the point Q, z_2 is needed: $z_2 = c + \overline{P'Q'} \tan\theta_{rv}$.

For incident ray PQ on the Surface 2 at Point Q, the whole process as described above is repeated. After this, the point R at which the refracted ray from Surface 2 strikes the surface of the sample, (x_0, y_0, z_0), can be determined. In the above equations, the indices of refraction of light in the media are taken as $n_a = 1.000$ (air), $n_p = 1.490$ (cell wall) and $n_w = 1.333$ (water) (Jenkins & White, 1976).

4.4.2 Ray tracing algorithm

Using the refraction model and the ray tracing technique described above, all the points on the imaginary plane can be ray traced backwards from the camera focus to find their respective positions in the object space (only the rays those are likely to hit the sample surface are of interest). Figure 4.8 shows the coordinate system adopted for representing points globally, on the imaginary image plane and on the sample surface. Exploiting the symmetry of the problem, points representing only a quarter portion on the imaginary plane were ray traced. A function was developed in Matlab to ray trace the points located at desired intervals on the quarter of the imaginary plane shown onto the sample. For example, to cover 40 mm wide by 80 mm high portion of the imaginary plane at a grid spacing of 0.1 mm, requires 400 × 800 passes through the algorithm.

4.5 Camera calibration

The problem of estimating the value of the *extrinsic and intrinsic parameters* is called *camera calibration* (See Appendix C for details about these parameters, the Pinhole Camera Model, and all the three cameras calibration results). All three digital cameras were calibrated using the Camera Calibration Toolbox for Matlab (Bouguet, 2008). The principal point was assumed to be the image centre and no distortion was assumed on the captured images due to camera lens system. Only

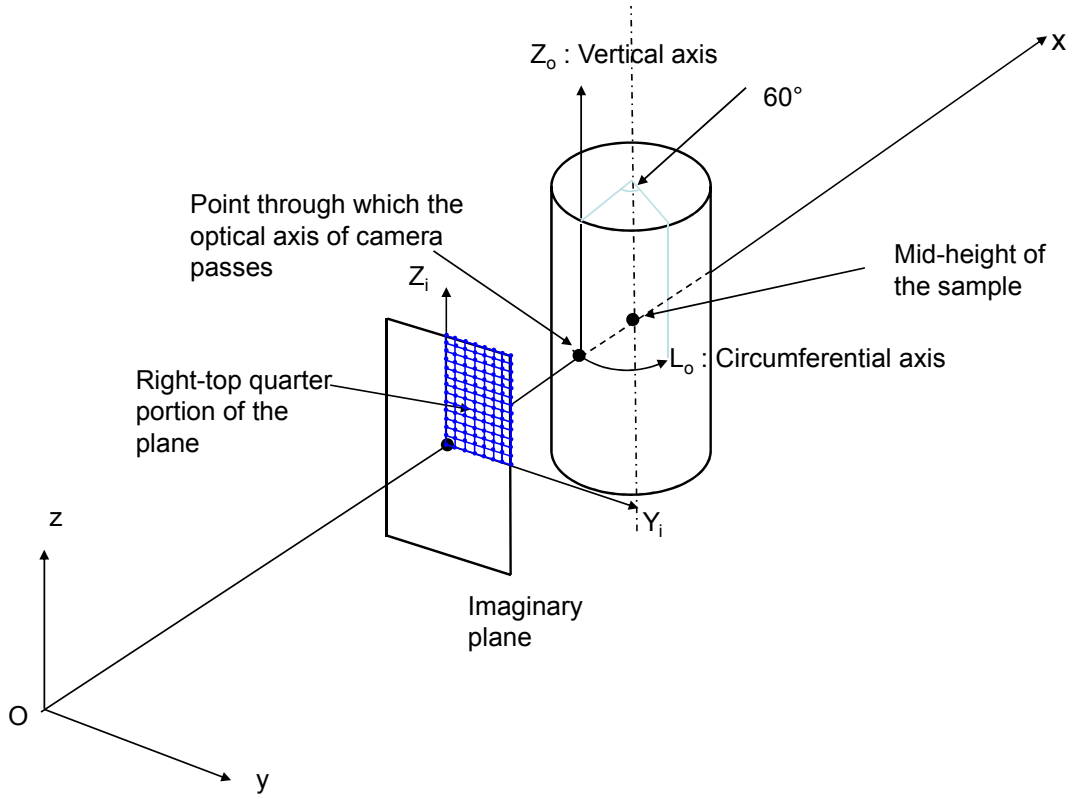

FIGURE 4.8: Coordinate axes, sample and the imaginary plane in front of the triaxial cell

the estimated focal lengths were used to convert the coordinates of points on the imaginary plane or the camera measurement frame (in millimetres unit) to the coordinates (in pixels unit) on the image plane using the Pinhole Camera Model (Trucco & Verri, 1998).

4.6 Measurement points, interpolation algorithm and determination of measurement points on the image

To monitor the deformation of the sample, measurement points are assumed on the surface of the sample at an equal interval on the circumferential axis L_o and on the vertical axis Z_o (Figure 4.8).

To determine the locations of the measurement points on the imaginary plane using the ray trace data, an interpolation algorithm was developed. As shown

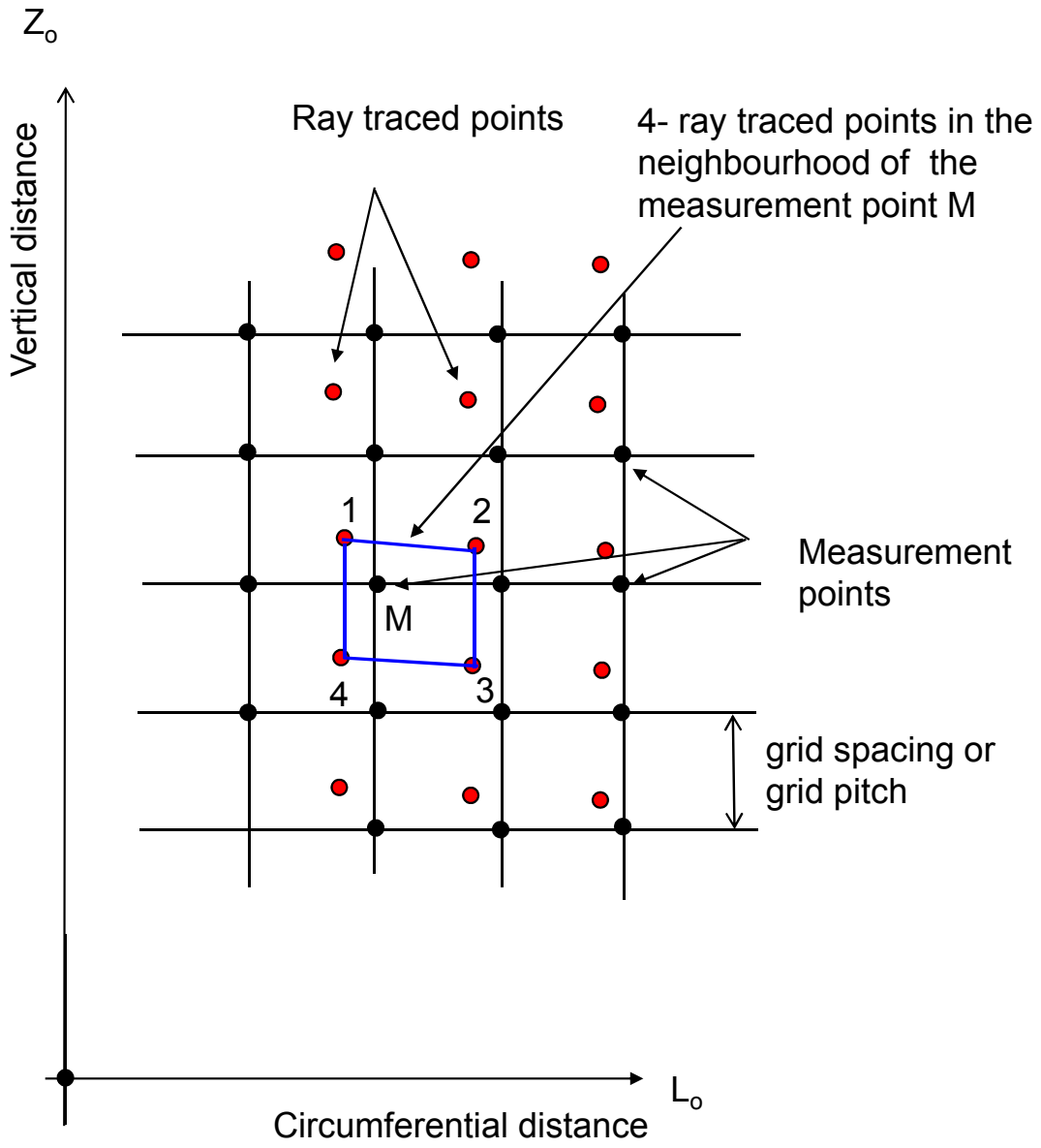

FIGURE 4.9: Measurement points and ray traced points on the surface of the unwrapped sample (Note: only four ray traced points around a measurement point are shown for the illustration purpose)

in Figure 4.9, this algorithm finds four ray traced points on the left and right of and above and below the measurement points (for example, point M), in its close neighbourhood, whose locations on the imaginary plane are already known from the ray tracing process. Based on this information, the locations of the measurement points on the imaginary plane were found by bi-linear interpolation. Using the Pinhole Camera Model (Trucco & Verri, 1998) (See Appendix C), the locations of the measurement points were then determined on the image (or camera plane) from their locations on the imaginary plane.

Figure 4.10 shows the flowchart to determine the pixel coordinates of the measurement points.

4.6.1 Verification of the technique

A dummy sample was wrapped with a grid pattern of equal size in both the horizontal and vertical directions. The size of a square is 10 mm × 10 mm. The sample was placed inside the cell and then filled with water. The photograph of the sample was then captured. The camera settings were kept same as during the calibration process. The locations of the grid points (or the measurement points) were determined on the image by using the technique described above. Figure 4.11 indicates a close match about the axis of the sample but for the points located near the edges a slight difference was observed. To quantify the difference approximately, the location of the grid points (1, 2, 3, 4, 5, and 6) were identified on the image by zooming and compared with the values determined using the technique. The point 1 was taken as centre of the image therefore no difference was found. The difference observed at points 2, 3, 4, were found to be less than 6 pixels. But at points 5 and 6 differences of 23 and 32 pixels (26 pixels ≈ 1 mm), respectively, were found. The difference may be minimised by - a more accurate camera calibration also taking into account any distortions of the image due to the camera lens system and the use of an accurate verification grid.

4.6.2 Determination of scaling factors

The scaling factors, in the circumferential direction (or the horizontal direction for the sample surface unwrapped) and in the vertical direction to take into account the variation of scale within the image, for the horizontal and vertical components of a displacement vector (calculated by using digital image correlation - describe in the next section) at each measurement point depend on the chosen spacing of the measurement points. These factors should be determined, ideally, for an infinitesimal spacing between measurement points. Figure 4.12 shows the plots of scaling factors for vertical components of displacement vectors, Sv, where (L_{co} represents the distance along the circumferential axis L_o and Z represents the distance along the vertical axis Z_o), for 20, 10, 5, 2, and 1 mm grid spacings. As expected, the effect the spacing of the measurement points on the calculated

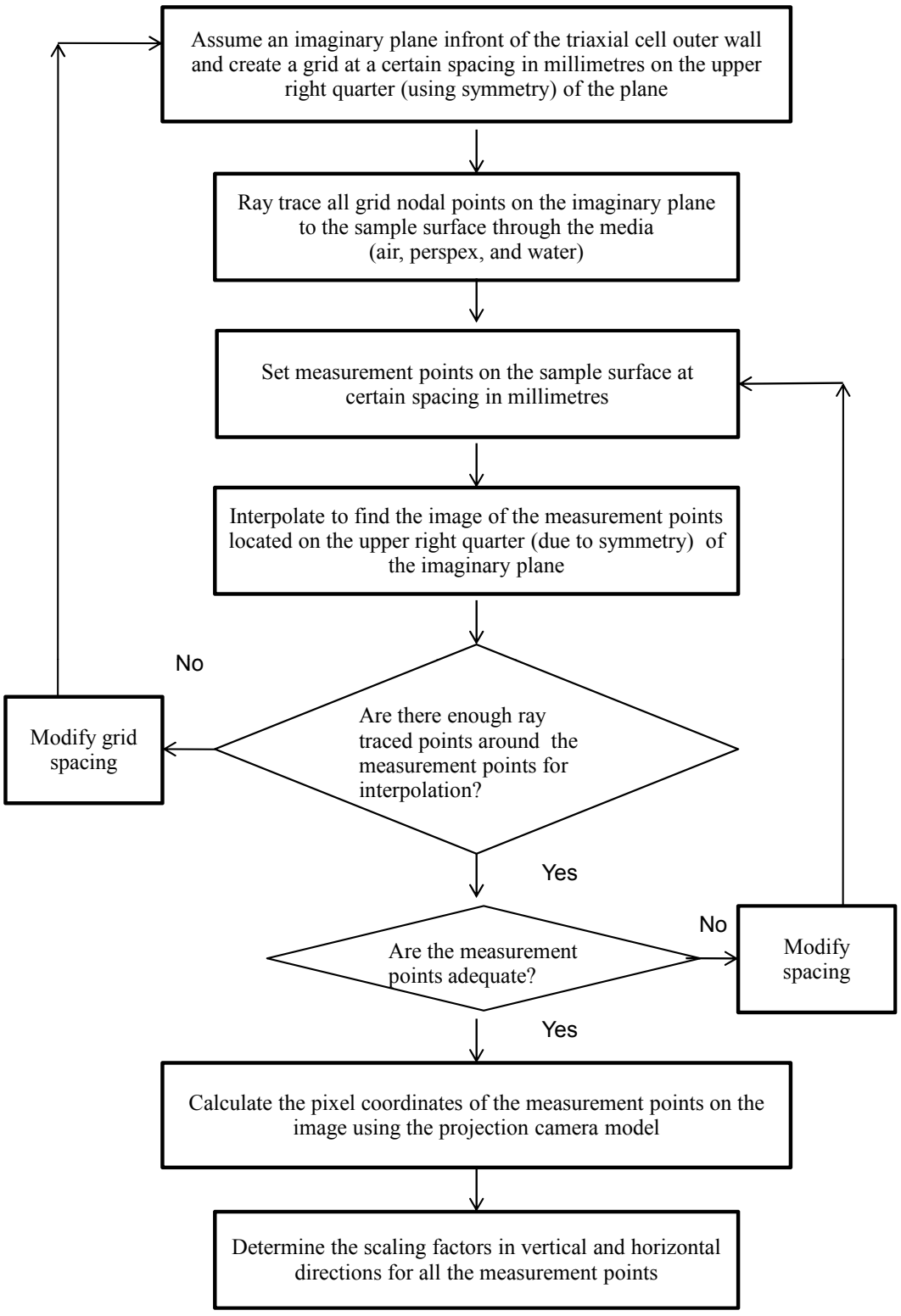

FIGURE 4.10: Flowchart to determine pixel coordinates of the measurement points

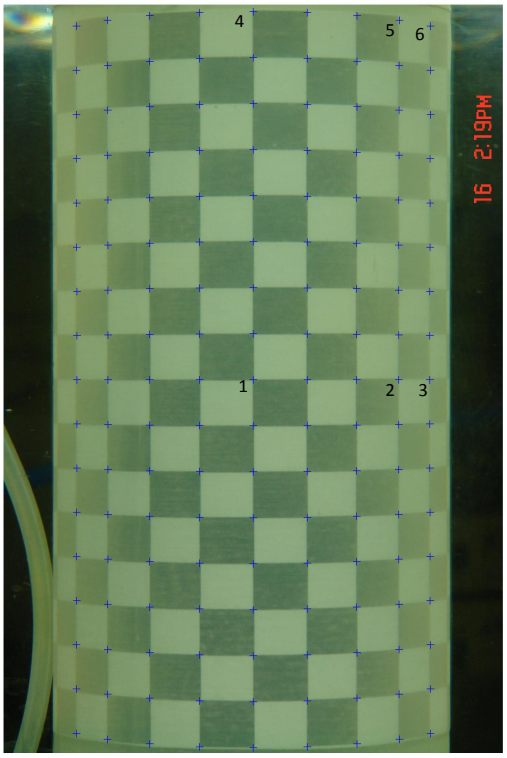

FIGURE 4.11: Verification of ray tracing technique

scaling factors is quite small in the vertical direction. This is because the image distortion in the vertical direction is similarly small. Figure 4.13 shows the plots of scaling factors for horizontal components of displacement vectors, Sh; the effect of the measurement points spacing is clear. However, on reducing the grid spacing, the difference diminishes. The scaling factors are almost identical for 5mm, 2mm and 1mm spacings, up to a circumferential distance of $\pm$ 36.66 mm on the sample surface. With this distance, each camera covers one-third portion of the sample surface (for a sample of diameter 70 mm).

4.7 Digital Image Correlation

4.7.1 Digital image representation

A digital image can be considered as a matrix, each element of which has a value proportional to the light intensity recorded at each pixel of the recording medium

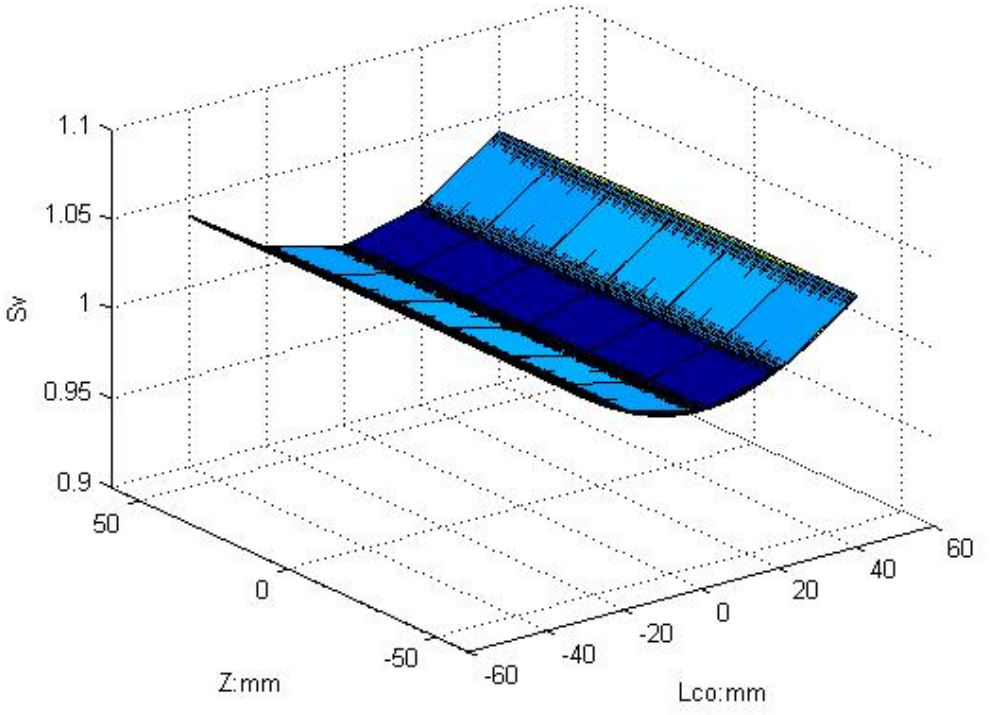

(a)

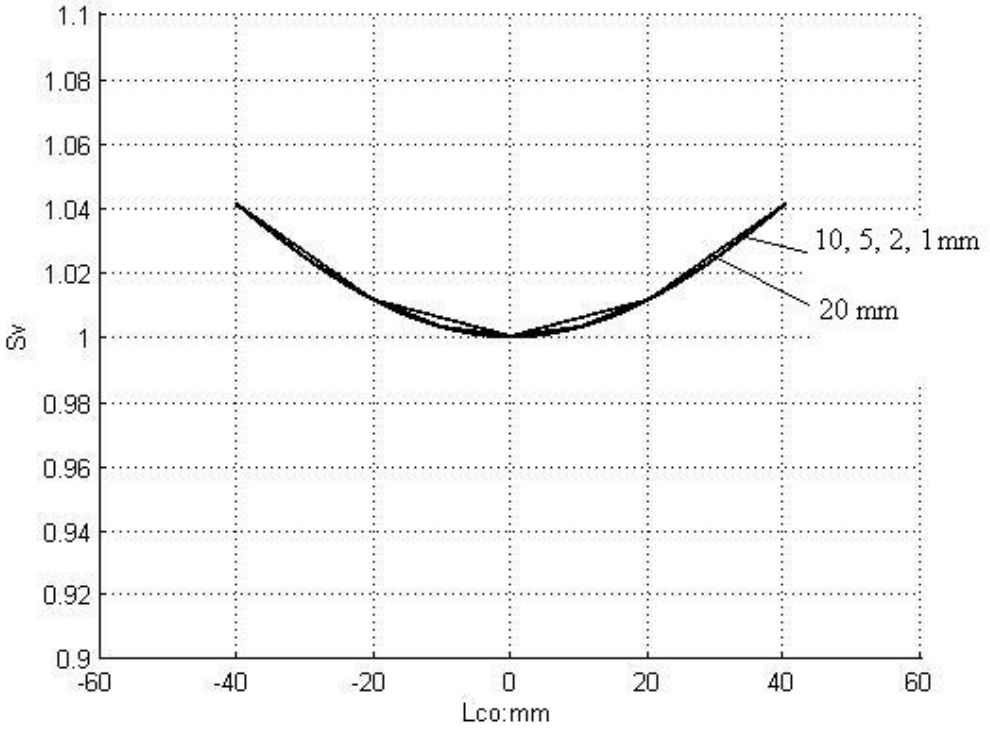

(b)

FIGURE 4.12: Scaling factors surfaces for vertical component of displacement for 20, 10, 5, 2, and 1 mm spacing of measurement points

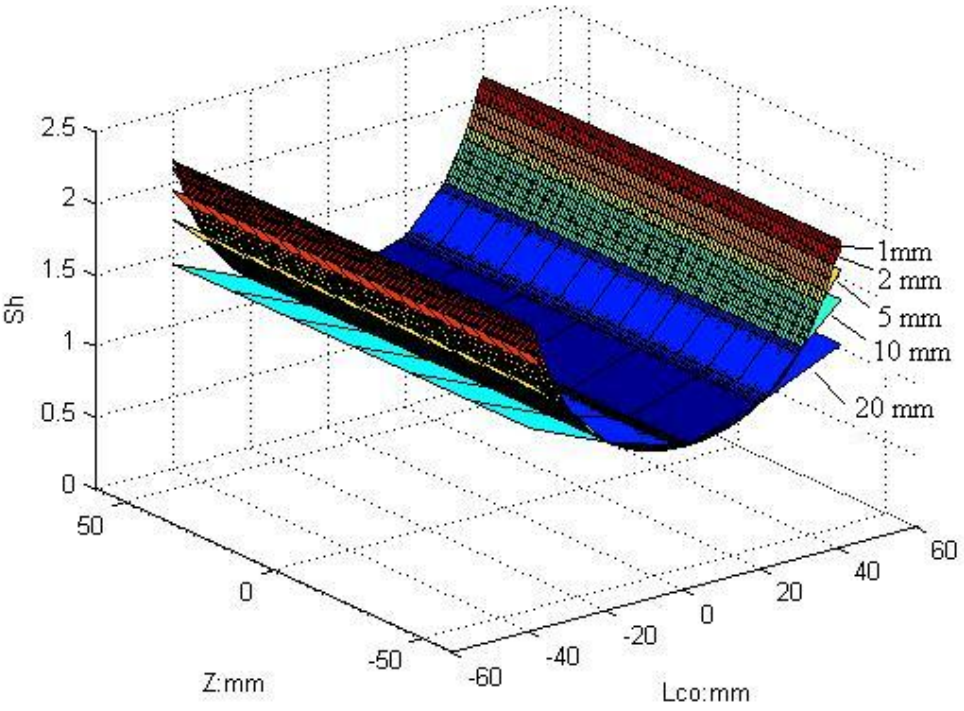

(a)

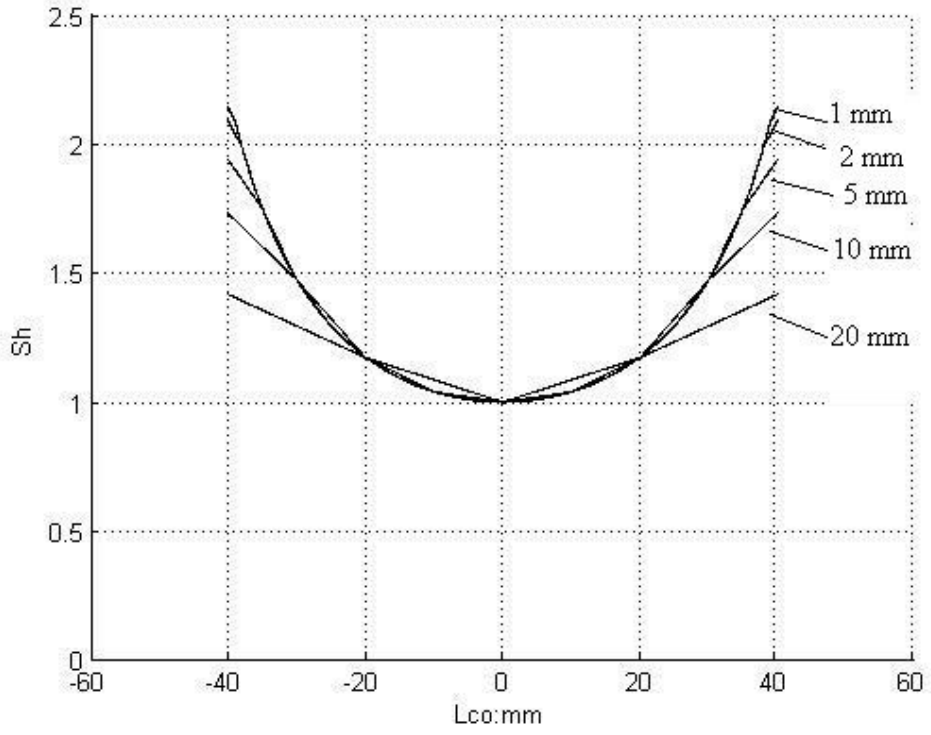

(b)

FIGURE 4.13: Scaling factors surfaces of horizontal component of displacement for 20, 10, 5, 2, and 1 mm spacing of measurement points

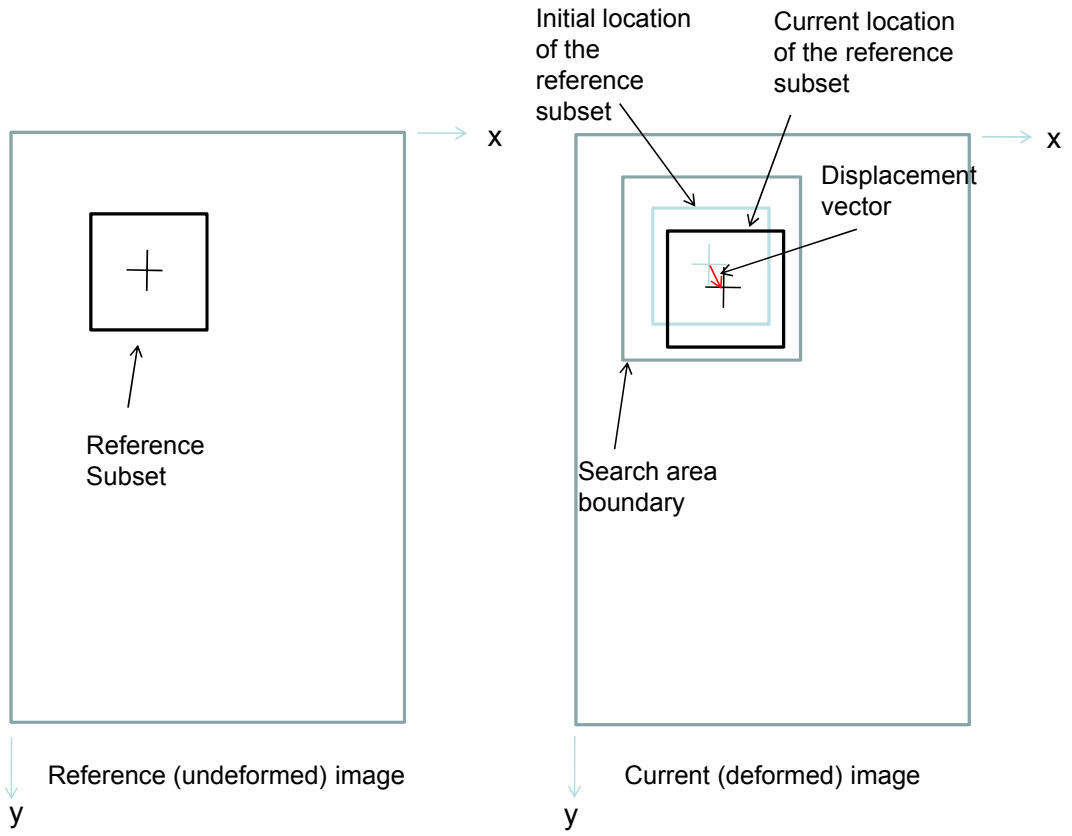

FIGURE 4.14: Digital image correlation principle

(CMOS sensor) of the camera. For example, a color image (RGB representation), contains intensity values for each color channel per pixel. For an 8 bit representation per channel, the intensity values vary from 0 (perfect black) to 255 (perfect white).

4.7.2 Principle of matching

The technique of displacement measurement using image analysis involves capturing images of the sample undergoing shear deformation at various stages of loading. Then the captured images are analysed using a mathematical measure to identify the most similar patterns in the subsequent images. The basic assumption is that the pattern is approximately constant between successive images and the local textural information is unique. Several matching criteria are available (Giachetti, 2000; Tong, 2005). The matching algorithm compares the image subsets in the reference (undeformed) image to the image subsets in the current (deformed) image. For example, an image subset t from the reference image and an image

subset s from the current image, are compared by computing the cross-correlation function $C(u, v)$, given by,

$$C(u,v) = \sum_{x,y} t(x,y) \cdot s(u+x, v+y) \tag{4.13}$$

This cross-correlation function will yield different maximum correlation values for the same degree of matching because the function is not normalized. This makes a comparison of the degree of correlation between the individual interrogation windows impossible. The problem is overcome by using normalized cross-correlation coefficient, Equation 4.14.

$$C_n(u,v) = \frac{\sum_{x,y}\left(t(x,y) - \bar{t}\right) \cdot \left(s(u+x, v+y) - \overline{s_{u,v}}\right)}{\sqrt{\sum_{x,y}\left(t(x,y) - \bar{t}\right)^2}\sqrt{\left(s(u+x, v+y) - \overline{s_{u,v}}\right)^2}} \tag{4.14}$$

where $\bar{t}$ and $\overline{s_{u,v}}$ represent the arithmetic means of the reference and the current image subsets. A Matlab Executable (MEX) interface function implementation of this correlation coefficient, developed by Eaton (2008) was used (in the form of dynamic link library (*.dll*)) of the OpenCV which is open source computer vision library available from *http://SourceForge.net/projects/opencvlibrary*. This function is computationally efficient compared with the built-in function 'normxcorr2' in Matlab. The OpenCV library (written in C/C++) is also optimised for Intel based processors. The function was validated by comparing the result with that obtained by using 'normxcorr2'. In addition, for a small test subsets t (3 rows x 3 columns) and s (6 rows by 6 columns) - the position of t in s is already known, the location of t in s was found by hand calculation of the normalised cross correlation coefficients. The downloaded function also gave the same correlation coefficients and location of peak.

4.7.3 Sub-pixel interpolation

The correlation calculated according to Equation (4.14) is evaluated at single pixel intervals. To estimate the displacement vector to sub-pixel resolution, a bi-cubic interpolation function evaluated at 1/100 th pixel intervals was fitted to the region close to the peak. With added computational cost, this interval may be reduced further to increase the resolution of calculation.

4.7.4 Selection of subset size

To determine a suitable size of subset to input in crosscorrelation analysis, the displacement patterns of 11 vertical points (45, 46,....., 55) located vertically, 5 mm apart, at the centre of the uniformly deforming intact and pluviated samples were compared for different size of subsets: 33, 65, 97, 129, 161, 193, 225, and 257 pixels squares (Figure 4.15 and Figure 4.16). For uniform vertical compression and equally spaced points, the expected profile is a linear variation of vertical displacement. As can be seen, with the increase of subset size, much linear variation of the vertical displacement is evident. Considering the computation cost involved with the size of the subset and the effect of subset size on the reliability of the measurement, 129 pixels square was chosen as the optimal size of the subset for crosscorrelation analysis. Unless stated specifically, this subset size is used in all analysis presented hereafter.

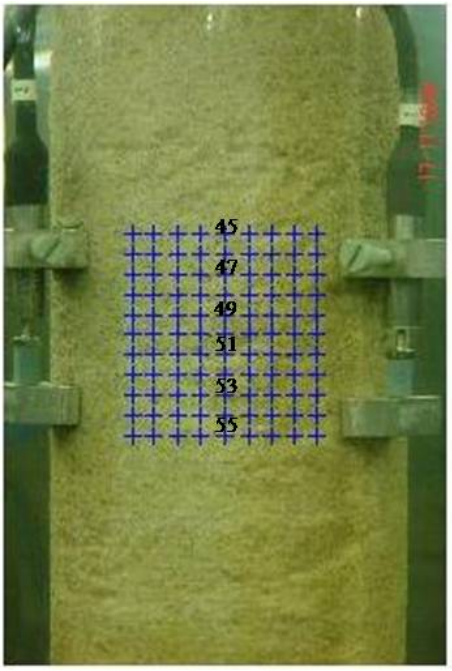

(a)

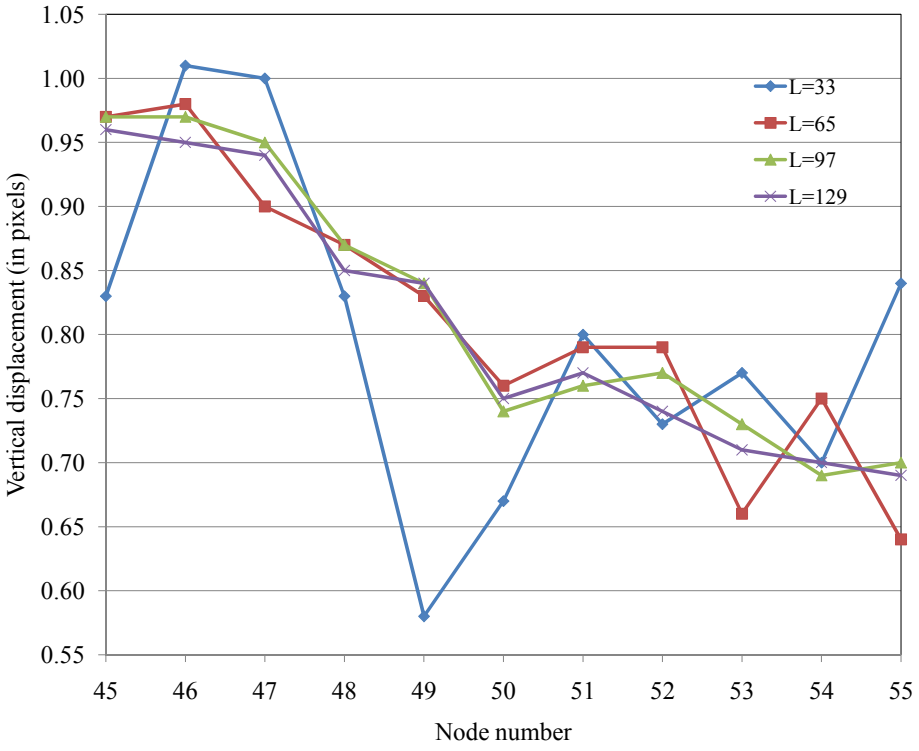

(b)

FIGURE 4.15: (a) Equally spaced vertical points on an intact sample, (b) Vertical displacement during a small deformation step (or strain increment) of the points for a patch size of 33 to 129 pixels and (c) Vertical displacement during a small deformation step (or strain increment) of the points for a patch size of 161 to 257 pixels (To be continued in next page)

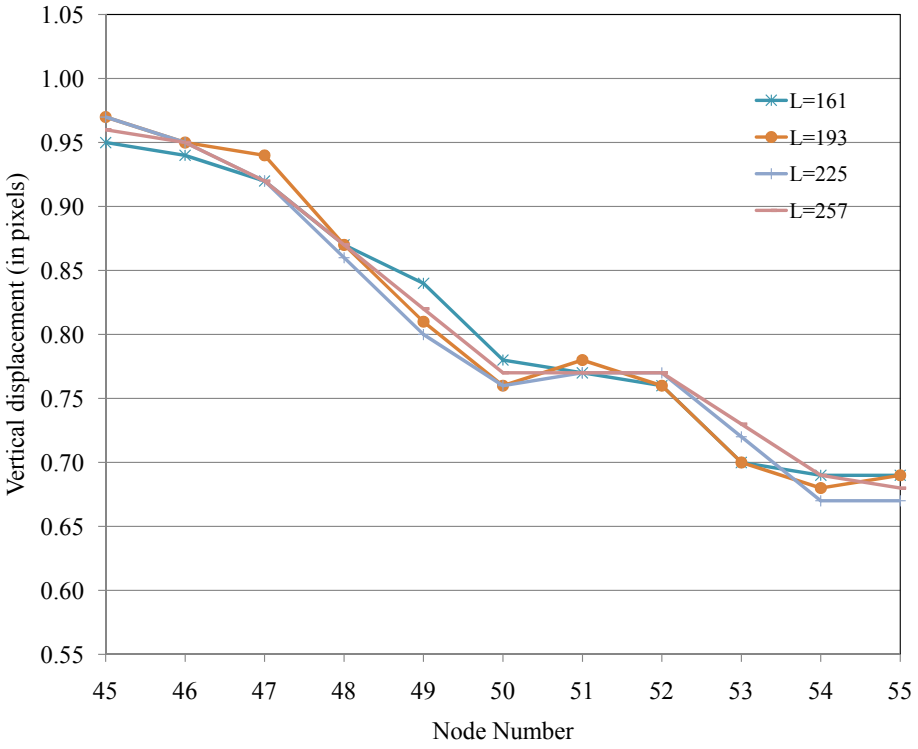

(c)

FIGURE 4.15 (Continued from previous page)

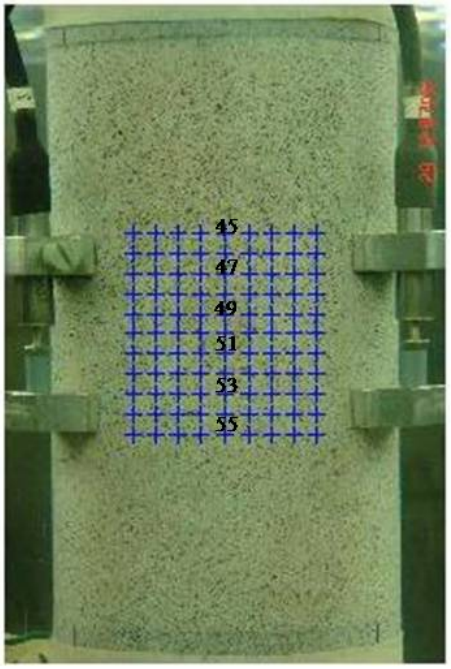

(a)

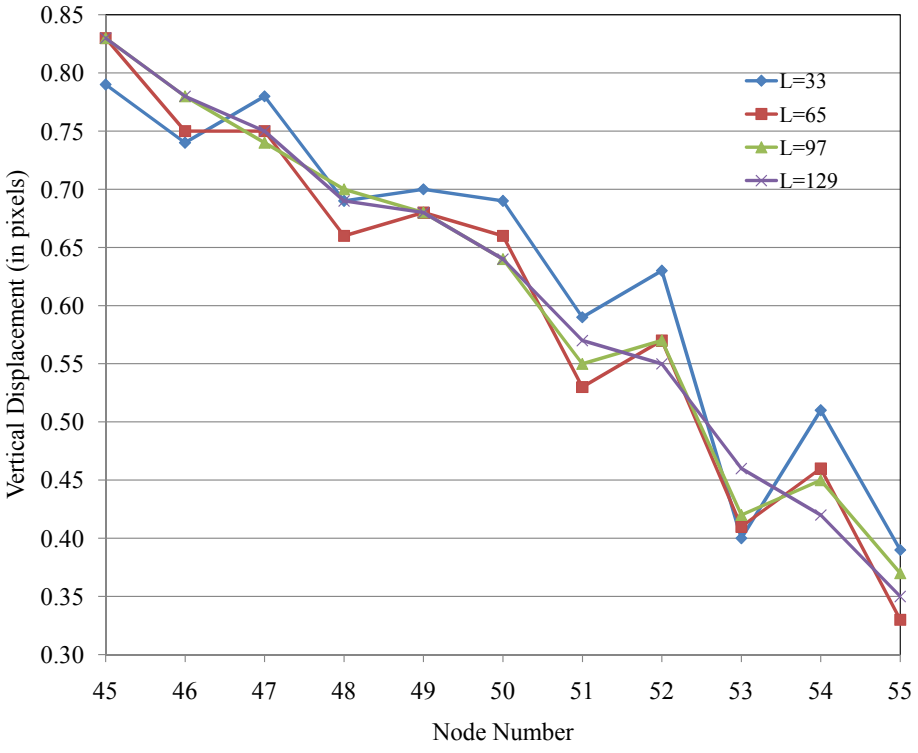

(b)

FIGURE 4.16: (a) Equally spaced vertical points on a pluviated sample, (b) Vertical displacement during a small deformation step (or strain increment) of the points for a patch size of 33 to 129 pixels and (c) Vertical displacement during a small deformation step (or strain increment) of the points for a patch size of 161 to 257 pixels (To be continued in next page)

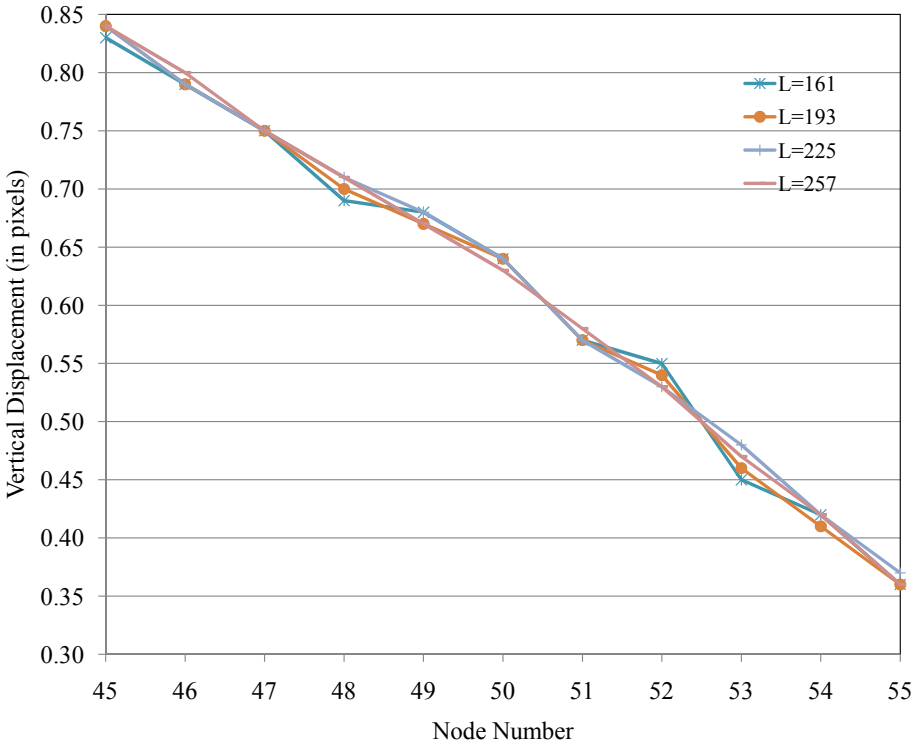

(c)

FIGURE 4.16 (Continued from previous page)

4.7.5 Comparison of image-based measurements and LVDT data

The image analysis system was demonstrated on a drained triaxial compression test, carried out on a pluviated Leighton Buzzard sand at an effective confining pressure of 50 *kPa*. Figure 4.17(a) shows a view of the sample from a camera. The use of three digital cameras and three LVDTs provides a means to compare directly the digital image-based measurements with LVDT data. This comparison was made only on the initial stage of deformation, prior to the peak strength being achieved. Images in JPEG (Joint Photographic Experts Group) format were used.

Vertical displacement components at 54 measurement points (enclosed by the rectangles in the Figure 4.17(a)) were determined using DIC for deformation steps 4-5 to 4-11 Figure 4.17(b)). These measurement points are level with the upper and lower holders supporting the LVDTs. The difference between the average of the top row displacements and the average of the bottom row displacements gives the displacement between the LVDT supports, which was compared with the average

of the two LVDT recordings. The LVDT measurement (in millimeters) was converted into pixels using the Camera Projection Model. As shown in Figure 4.17(c), a good agreement between the LVDT and image-based measurements was found. The LVDTs and image-based measurements were compared in more tests described in chapter 5 and a very close match was found.

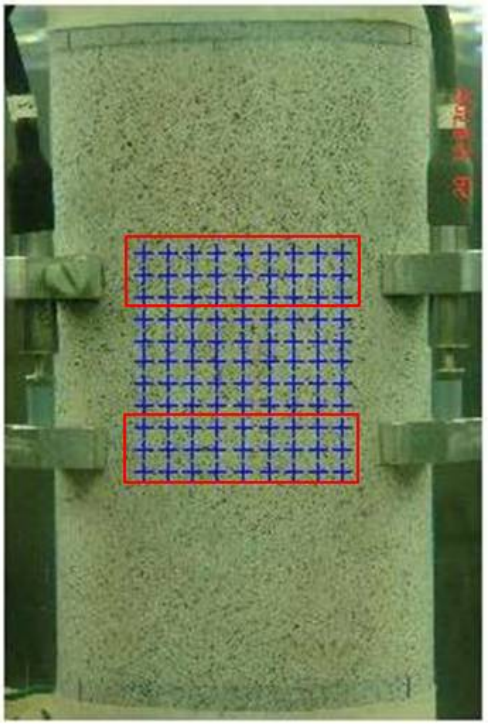

(a)

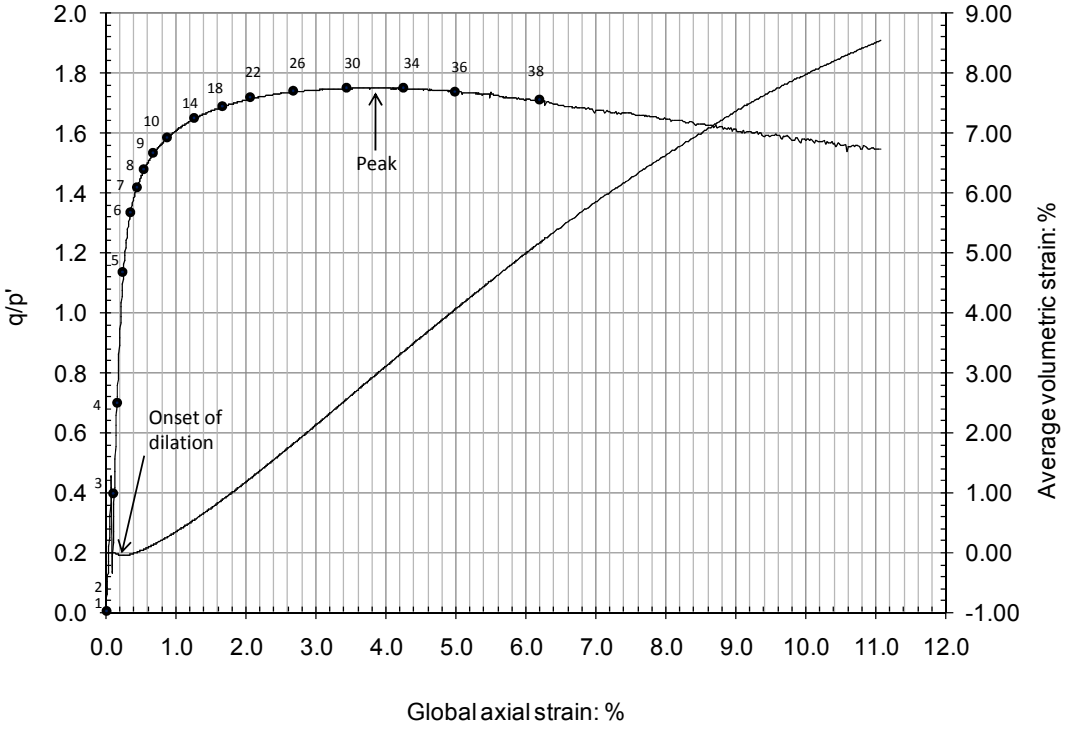

(b)

FIGURE 4.17: (a) Measurement points, (b) Stress ratio, $q/p^{'}$, and average volumetric strain plotted against global axial strain and (c) Deformation measured using LVDT and DIC using different subset sizes (To be continued in next page)

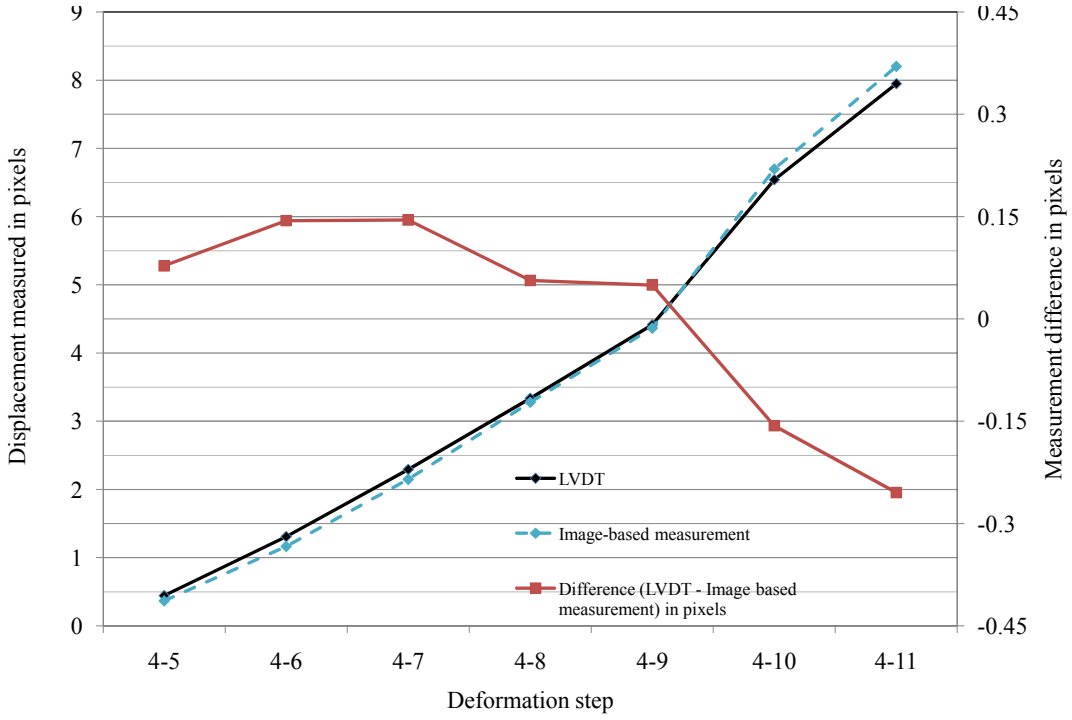

(c)

Figure 4.17 (Continued from previous page)

Figure 4.18 shows a typical grid pattern used for cross-correlation analysis of the sample image. These measurement points are spaced equally (5 mm apart) on the surface of the sample. Measurement points very close to platens, which could give rise to subsets falling partly on the soil (deformable) and partly on the platen (rigid), are avoided.

4.8 Post processing of displacement data

4.8.1 Validation of data and replacement of incorrect data

A few incorrectly determined displacement vectors (so-called *outliers* or *wild vectors*) may occasionally be found by visual inspection of the displacement vectors. Their features are: (i) their magnitude and direction differ considerably from their surrounding neighbours (ii) in most cases, they appear as single incorrect vectors. They are due to noise (such as, reflected bright spots on sample surface of the light reflecting surface) or artefacts and not due to the proper correlation of image subsets. Any subsequent operations (such as strain field calculation) on the

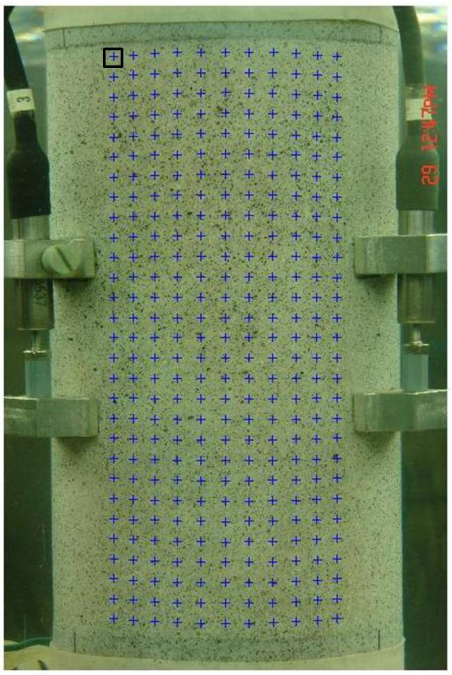

FIGURE 4.18: Typical grid used for cross-correlation analysis

displacement data still including such wild vectors would enhance and smear out these errors locally and could mask data of good quality (Raffel et al., 1998). Any incorrect data present were therefore corrected manually by interpolation.

4.8.2 Calculation of strain fields

During the shearing of a sample, images of the sample were captured in a very close interval (typically at an interval of 0.1 % global axial strain). The captured images were analysed incrementally. The measurement points are chosen closely spaced (typically at a 5 mm grid spacing). The values of the obtained displacement components are small compared with the grid spacing. Therefore, small strain theory is used in the calculation of strain components.

Having determined the displacement components in both the x and y directions at each measurement point, the region was divided into quadrilateral elements. A bilinear quadrilateral and its eight nodal degrees of freedom (d.o.f) are shown in Figure 4.19. For the rectangular four-noded element, shape functions are defined as follows (Cook et al., 2001):

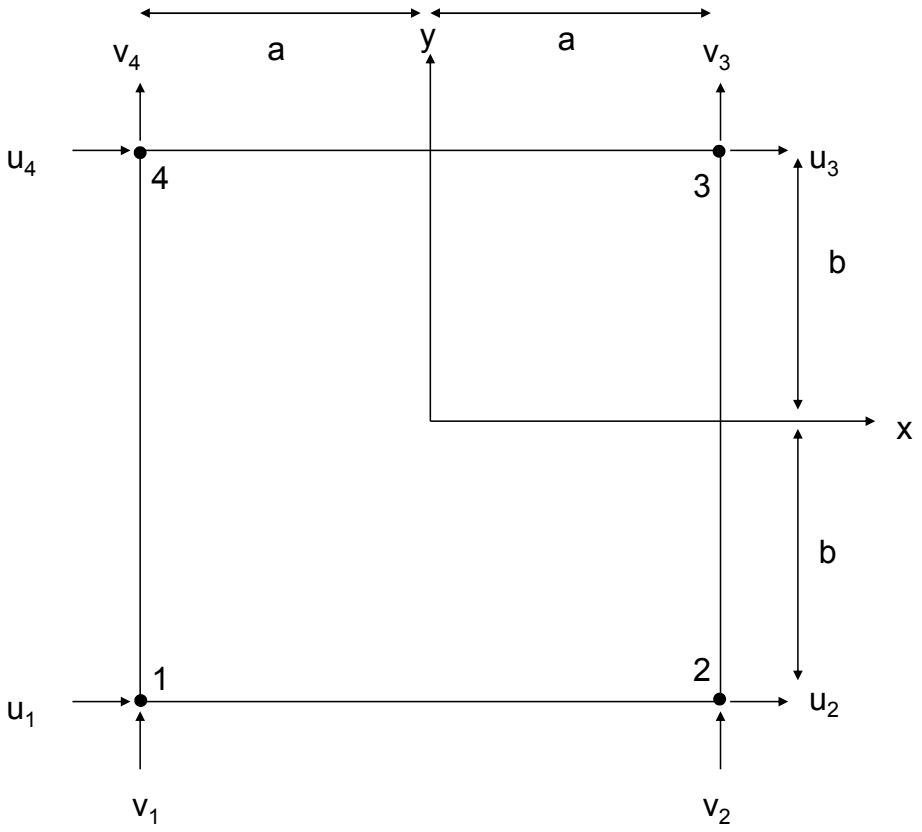

FIGURE 4.19: 4-noded quadrilateral element

$$N_1 = \frac{(a-x)(b-y)}{4ab} \tag{4.15}$$

$$N_2 = \frac{(a+x)(b-y)}{4ab} \tag{4.16}$$

$$N_3 = \frac{(a+x)(b+y)}{4ab} \tag{4.17}$$

$$N_4 = \frac{(a-x)(b+y)}{4ab} \tag{4.18}$$

Let $u_1, v_1, u_2, v_2, u_3, v_3, u_4, v_4$ represent the displacement components (x, y) at the four nodes (1, 2, 3, and 4). Then u and v can be represented by

$$u = u_1N_1 + u_2N_2 + u_3N_3 + u_4N_4 \tag{4.19}$$

$$v = v_1N_1 + v_2N_2 + v_3N_3 + v_4N_4 \tag{4.20}$$

$$\left\{ \begin{array}{c} u \\ v \end{array} \right\} = \left[\begin{array}{cccccccc} N_1 & 0 & N_2 & 0 & N_3 & 0 & N_4 & 0 \\ 0 & N_1 & 0 & N_2 & 0 & N_3 & 0 & N_4 \end{array} \right] \left\{ \begin{array}{cc} u_1 & v_1 \\ u_2 & v_2 \\ u_3 & v_3 \\ u_4 & v_4 \end{array} \right\} \tag{4.21}$$

Following soil mechanics convention, whereby compression is positive, the strain is calculated as

$$\varepsilon = - \left[\begin{array}{cc} \frac{\partial}{\partial x} & 0 \\ 0 & \frac{\partial}{\partial y} \\ \frac{\partial}{\partial y} & \frac{\partial}{\partial x} \end{array} \right] \left\{ \begin{array}{c} u \\ v \end{array} \right\} \tag{4.22}$$

$$\varepsilon = - [B] \, d \tag{4.23}$$

where,

$\varepsilon = \{\varepsilon_x, \varepsilon_y, \gamma_{xy}\}^T$

$$[B] = \frac{1}{4ab} \left[\begin{array}{cccccccc} -(b-y) & 0 & (b-y) & 0 & (b+y) & 0 & -(b+y) & 0 \\ 0 & -(a-x) & 0 & -(a+x) & 0 & (a+x) & 0 & (a-x) \\ -(a-x) & -(b-y) & -(a+x) & (b-y) & (a+x) & (b+y) & (a-x) & -(b+y) \end{array} \right]$$

$d = \{u_1, v_1, u_2, v_2, u_3, v_3, u_4, v_4\}^T$

The principal strains are

$$\varepsilon_1 = \frac{(\varepsilon_x + \varepsilon_y)}{2} + \sqrt{\frac{1}{4} (\varepsilon_x - \varepsilon_y)^2 + \left(\frac{\gamma_{xy}}{2} \right)^2} \tag{4.24}$$

$$\varepsilon_3 = \frac{(\varepsilon_x + \varepsilon_y)}{2} - \sqrt{\frac{1}{4} (\varepsilon_x - \varepsilon_y)^2 + \left(\frac{\gamma_{xy}}{2} \right)^2} \tag{4.25}$$

The maximum shear strain is

$$\gamma_{max} = \varepsilon_1 - \varepsilon_3 \tag{4.26}$$

The volumetric strain is

$$\varepsilon_v = \varepsilon_1 + \varepsilon_3 = \varepsilon_x + \varepsilon_y \tag{4.27}$$

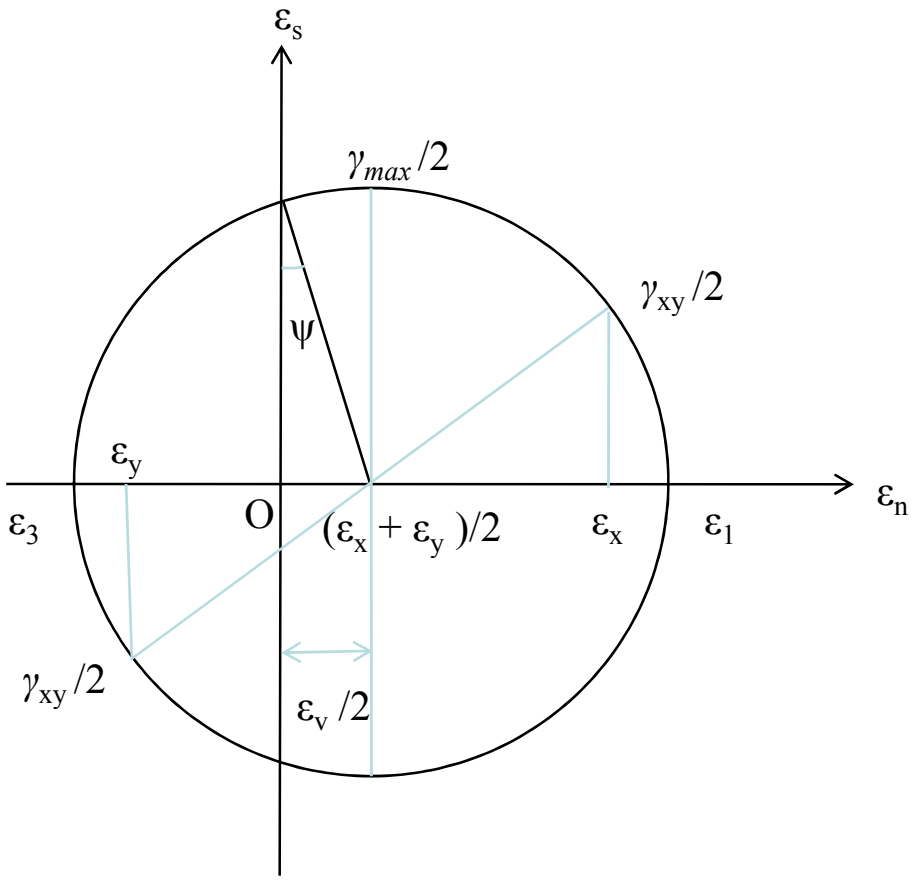

FIGURE 4.20: Mohr's circle representation of maximum shear strain

Figure 4.20 shows the Mohr's circle representation of maximum shear strain and volumetric strain. Typical displacement vectors, horizontal displacement contours, vertical displacement contours, and strain fields (maximum shear strain and volumetric strain) are shown in Figure 4.21, for deformation step 8-9 in Figure 4.17(b). A reference vector is given below the displacement vector plot. A colourbar to the right of each strain field represents strain expressed in %. In the volumetric strain field, a negative value represents dilation. The effect of use of non-lubricated end platens is clearly evident.

4.9 Discussion

Ray tracing was used to determine the image locations of the points located on the imaginary plane on the sample surface. The locations of the images of the measurement points on the imaginary plane were determined by interpolation. The scaling factors in the horizontal and vertical directions were shown to depend

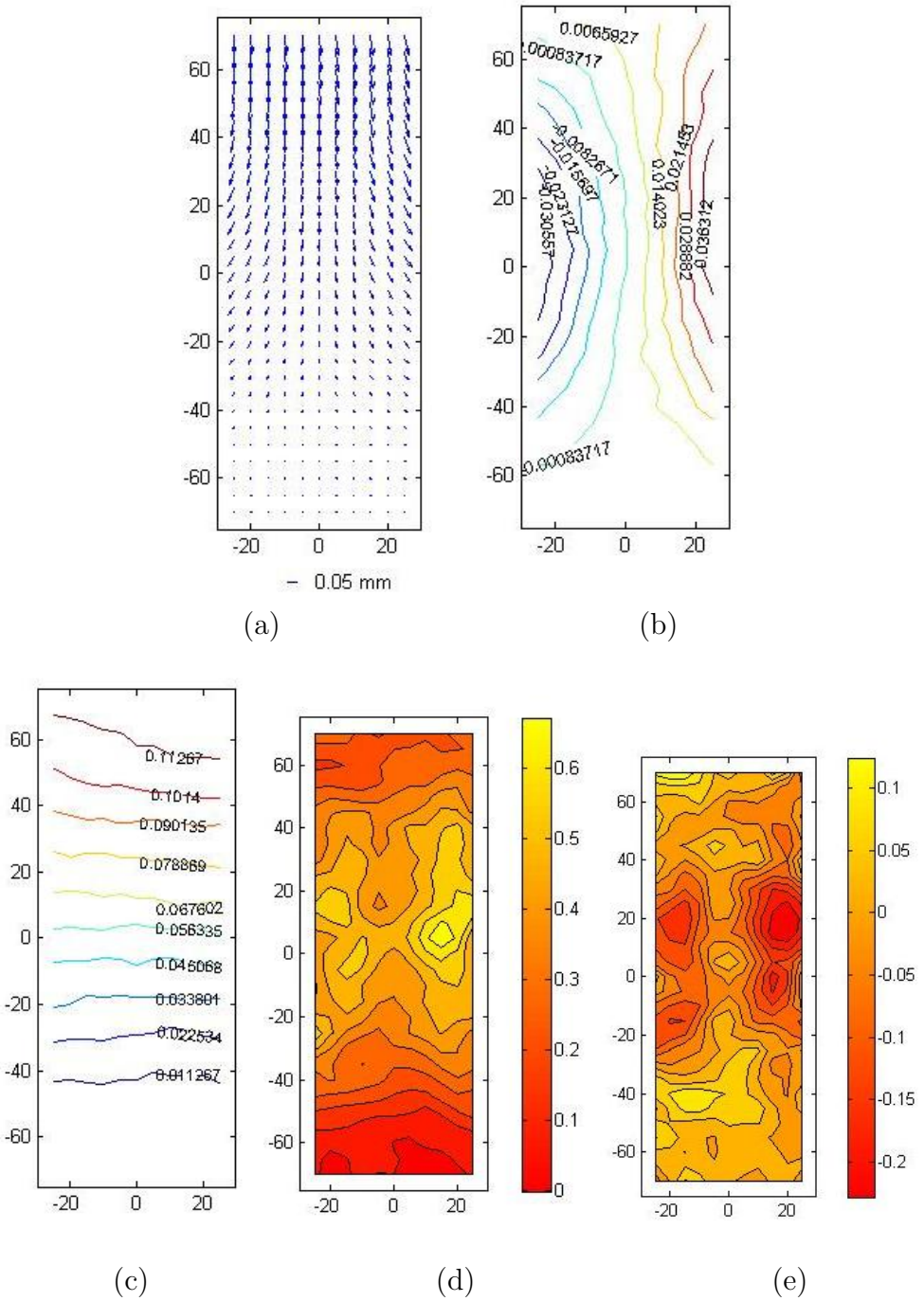

FIGURE 4.21: Typical fields for a deformation step 8-9 in a pluviated sample: (a) displacement vector, (b) horizontal displacement contours, (c) vertical displacement contours,(d) maximum shear strain, and (e) volumetric strain

on the chosen spacing of measurement points. For the spacing of 5 mm used in this study, no significant effect of spacing of measurement points on the scaling factors were found.

Any distortion of image of the sample due to the camera lens system was ignored. Modern cameras justify this approach (Bouguet, 2008). The performance of DIC depends on the quality of texture (Zhang et al., 2005; Lecompte et al., 2006). A random artificial texture was created on the membrane by spraying quick drying black enamel paint; no other methods were attempted. Comprehensive evaluations and quality assessment of different textures will help to identify an appropriate artificial texture for the better performance in image correlation.

The normalised crosscorrelation coefficient has been shown to be reliable and robust by Tong (2005), although it is computationally costly. In the criterion (Equation 4.14), only the displacement components were evaluated and the displacement gradients were not considered. Consideration of displacement gradients will require a robust algorithm for detection of image subsets and is also computationally quite intensive (Bruck et al., 1989). Also, in Equation 4.14, the variation of image scale within the chosen subset was not considered. Since the image analyses were carried out incrementally, the deformation between subsequent images is quite small; it is assumed that the resulting error due to above effects is quite small.

The size of the subset for image correlation was selected on a trial and error basis. The minimum size of a subset is dictated by a requirement that it should contain sufficient textural information to produce a sharp correlation peak with the subsets from the subsequent image(s). A subset of large size, ideally, will contain more information therefore it can be found in subsequent image(s) with more reliability. However, such a subset will be affected more by soil deformation than a small subset. The subset size therefore should also be chosen in accordance with the expected deformations. Furthermore, the computational cost will increase substantially with the size of subset. Recently, Yaofeng & Pang (2007) developed the concept of subset entropy to denote quantitatively the subset image quality for DIC and Pan et al. (2008) developed a theoretical model based on the variance of image noise and the sum of square of subset intensity gradients (SSSIG) which leads to a criterion for choosing a more rigorous subset size for DIC analysis. The implementation these approaches would make the selection of subset size less subjective.

Careful considerations are required when selecting the spacing between measurement points (or grid pitch). A large grid pitch gives an accurate strain field but a limited number of measurement points. A small pitch, however, gives access to larger number of measurement points but the deduced strain field may be noisy.

4.10 Conclusions

DIC was adapted for detailed sample deformation measurements in triaxial tests, using ray tracing to take account of image distortion due to refraction. The following conclusions can be made from this chapter:

1. Using the ray tracing technique, the effects of distortion of the image of the sample due to refraction can be properly taken into account. Digital images taken from outside the cell can be used to develop digital image-based measurement system for triaxial test applications.

2. A close match between LVDTs and the developed image-based system shows that the system can be reliably used to monitor the surface deformation characteristics of triaxial samples.

Chapter 5

Study of deformation of triaxial samples using the image-based measurement system

5.1 Introduction

The triaxial test is one of the most commonly used tests to study the strength and deformation characteristics of geomaterials. Interpretation of the triaxial test is commonly based on the assumption that the soil element deforms uniformly under loading. The strength and deformation parameters are usually derived from overall stress-strain curves without considering the internal shearing deformation mechanism. Geomaterials with post-peak softening behaviour are prone to progressive failure, localisations of deformations, and shear banding (Vardoulakis & Sulem, 1995; Desrues & Viggiani, 2004). The occurrence of such phenomena affects significantly the uniformity of deformation and poses significant difficulties in the interpretation of experimental results (Atkinson, 2000).

The confining stress, boundary conditions, sample imperfections, and sample slenderness ratio all influence the deformation characteristics of samples (Desrues & Viggiani, 2004). With increasing confining pressure, deformation becomes more ductile and the onset of localisation is progressively delayed (Desrues, 1998 (Figure 5.1); Desrues et al., 2007). The use of rigid frictional platens can promote nonuniform deformation (Balla, 1960; Bishop & Green, 1965; Balasubramaniam,

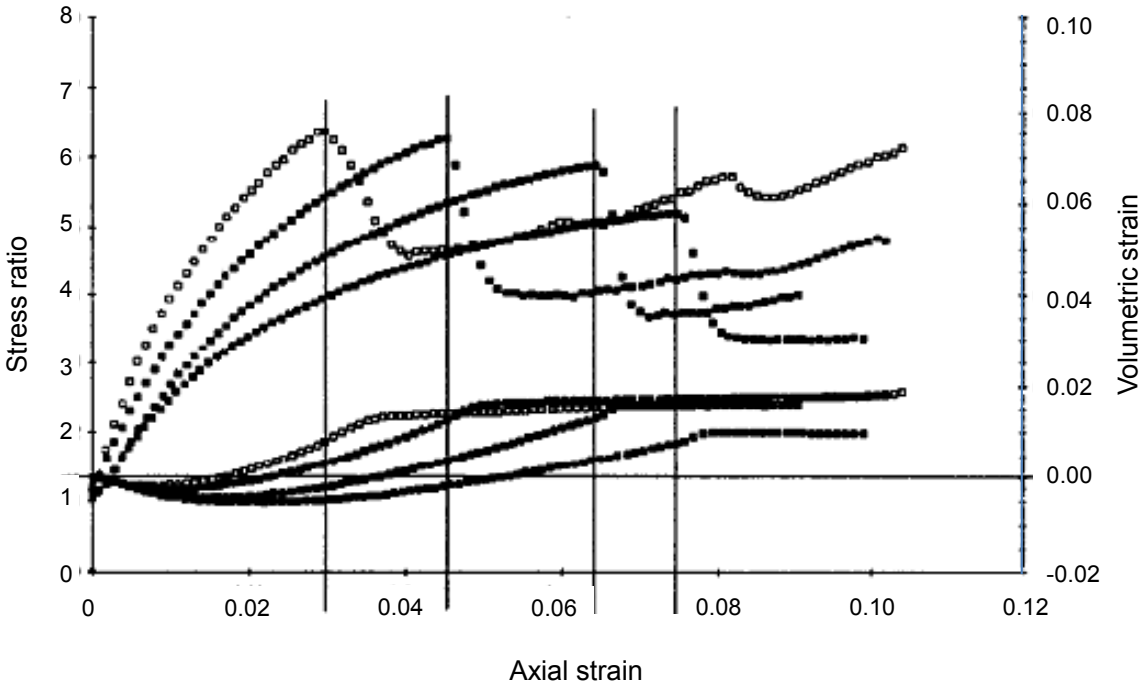

FIGURE 5.1: Influence of lateral pressure on the onset of localisation: the higher the pressure is, later the localised mode appears but it is not suppressed (after Hammad, 1991) redrawn from Desrues (1998)

1976; Cui et al., 2007; Jeremic et al., 2004; Kirkpatrick & Belshaw, 1968;Kikkawa et al., 2006; Liyanapathirana et al., 2005; Peric & Su, 2005; Powrie et al., 2005; Rowe, 1964). In plane strain conditions, samples are more prone to distinct localisation modes than samples tested in triaxial conditions, and are also more likely to exhibit a severe softening response (Alshibli et al., 2003; Alshibli & Akbas, 2007). The tendency of a sample to buckle increases with slenderness but increasing the sample length also provides an opportunity to accommodate any non-uniformity within the sample without it intersecting the boundary platens (Desrues & Viggiani, 2004).

This chapter uses the image-based deformation measurement system developed in chapter 4 to study the surface deformation characteristics of intact samples of Reigate silver sand, tested with frictional end platens at various confining pressures of all less than or equal to 100 kPa or below. To reduce the platen interference on shear band development (as observed in chapter 3 for intact samples with $H_0/D_0 \approx 2$), the height of samples was increased to 178 mm ($H_0/D_0 \approx 2.55$). Of particular interest are the phases of the test corresponding to the initial quasi-homogeneous deformation, the onset of localisation, the evolution of deformation from onset of localisation to formation of a persistent shear band, and the development of a

rigid body movement mechanism outside the shear band. The effects of confining pressure on the above phenomena result in the development of different kinematic mechanisms, and the impacts on global stress-strain relations are studied. The study of the behaviour within the shear band and the difficulties associated with that are discussed. The surface deformation characteristics of a pluviated sample of Leighton Buzzard sand at an effective cell pressure of 50 kPa are also examined for comparison purposes. The results of a Computed Tomography (CT) scan carried out on an intact sample after the test to determine the shear band patterns within it are also presented.

5.2 Description of image analysis approach and presentation of results

The main aim of this chapter is to identify the initiation of non-homogeneity, i.e., the onset of localisation of deformation. During the test, images were taken at intervals of 0.1 % global axial strain. Since the phenomena associated with the localisation process are dynamic in nature, the recorded images were analysed incrementally rather than cumulatively. One of the advantages of incremental analysis is that, since the deformation between the images is minimal, good correlation is always guaranteed in the image crosscorrelation process. The displacement vectors, maximum shear strain fields and volumetric strain fields are presented.

For the sake of completeness and for ease of comparison, the displacement vectors and strain fields for a strain increment (deformation step) obtained by analysing images from all cameras are all presented together. They are presented from left to right in the same order as the cameras are positioned around the sample, in the anticlockwise direction. For a sample approximately 70 mm diameter, to cover the whole sample circumferentially each camera requires to cover 73.33 mm circumferential distance (or ± 36.665 mm). The displacement vectors and strain fields presented may not include the whole sample, especially when the LVDTs are used to monitor the sample deformation in conjunction with the cameras. The horizontal axis of the results represents the distance around the sample circumference measured on each side, and the vertical axis represents the sample height measured from the optical axis of the camera, which in most cases coincides with the mid-height of the sample. The height of the sample varied from 150 mm to

178 mm. Image analysis avoided areas close to the end platens and also any bright reflection spots and the LVDTs cable which obscured the sample surface, as meaningful displacement information would not be obtained. However, attempts were made to cover as much of the sample surface as possible, so as not to omit any crucial spots. Images in JPEG (Joint Photographic Experts Group) format were used.

5.3 Deformation characteristics of an intact sample

5.3.1 Pre-peak deformation

Figure 5.2 shows the stress ratio , q/p', and the average volumetric strain plotted against global axial strain for an intact sample of Reigate silver sand tested at a cell pressure of 50 kPa. The black points on the stress ratio curve represent the instants at which the images were captured. The numbers adjacent to the points are those assigned to the captured images. The image number corresponding to the instant after the sample actually starts to take some load (identified from the load cell reading) was taken as an initial image for starting the image analysis. The displacement vectors and strain field obtained from analysing images 2 and 3 are termed 'step 2-3: displacement vectors and strain field'. Figure 5.3 shows the surface areas of the sample covered in the image analysis.

Figure 5.4(a) shows the displacement vectors for the initial stages of loading, steps 2-3, 3-4, 4-5, and 5-6, respectively. A reference vector is also shown below each vector plot. The reference vector length is based on the median value of the displacement vectors indicated. Initially a small tilting of the sample was observed. This was mainly due to the alignment of the platens with the sample ends on loading. From these displacement vectors, it can be seen that locally each analysis step only consists of very small displacement and therefore deformation. Each step, in the initial stage of deformation, corresponds approximately to 0.1 % of global axial strain.

Figure 5.4(b) shows the corresponding maximum shear strain fields for steps 2-3 to 5-6. The colourbars (on the right of all fields) show the maximum shear

strain (Equation 4.26) values in percentages. Figure 5.4(c) shows the corresponding volumetric strain fields for steps 2-3 to 5-6. The colourbars (on the right of all fields) show the volumetric strain (Equation 4.27) values in percentages. A negative volumetric strain represents dilation. As far as possible, any wild vectors were identified and removed. The strain fields should be judged on the basis of overall behaviour rather than the values at a particular point. For easy distinction the colormap was divided into 10; this does not necessarily mean that each division is at a better resolution than the strain accuracy. For steps 2-3 to 5-6 from the displacement vectors and strain fields presented, it can be concluded that the deformation is generally quasi-homogeneous.

5.3.2 Near-peak deformation

The displacement vectors and strain fields for the steps in the vicinity of the peak stress ratio are presented in Figure 5.5. In step 6-7, a tendency for deformation to localise can be seen but it is not clearly observed. In step 7-8, clear initiation of localisation of deformation can be seen in both the maximum shear strain and volumetric strain fields. This is the step when the onset of dilation was observed but the peak stress ratio was not yet achieved. The evolution of the displacement fields shows how the deformation quickly localised into a persistent shear band. Strain heterogeneity was found to increase steadily with increasing axial strain. A single non-planar shear band was developed in this sample, at an orientation of about 67° to the horizontal. The shear band was partly seen on camera 3 (in the upper right corner), and more fully on cameras 2 and 1.

5.3.3 Post-peak deformation

After the deformation had localised into a shear band, the parts of the sample outside the shear band (above and below) exhibited rigid body deformation. As shown in Figure 5.6(a), the top part of the sample slid past the bottom part, which remained stationary. The ball race arrangement above the top platen made free growth of the shear band possible by the absence of any lateral constraint in the radial direction to the sample from the loading ram. After localisation, the global volumetric measurement becomes physically meaningless. As shown in Figure 5.2(a), the average volumetric strain at the end of the shearing process

was nearly 3 %. With further post-peak deformation, significant distortion of the membrane above the shear band (as evident by the folding of membrane) was observed. At this stage, the application of digital image correlation to study the ongoing deformation in the shear band is quite unreliable as the basic assumption of minimal distortion between images is not valid anymore. By this time, the mechanism of rigid body motion outside the shear band has already been established. Figure 5.7 shows the photographs of the sample taken at the end of the test. The sketches shows the locations of the shear bands identified by playbacking the images.

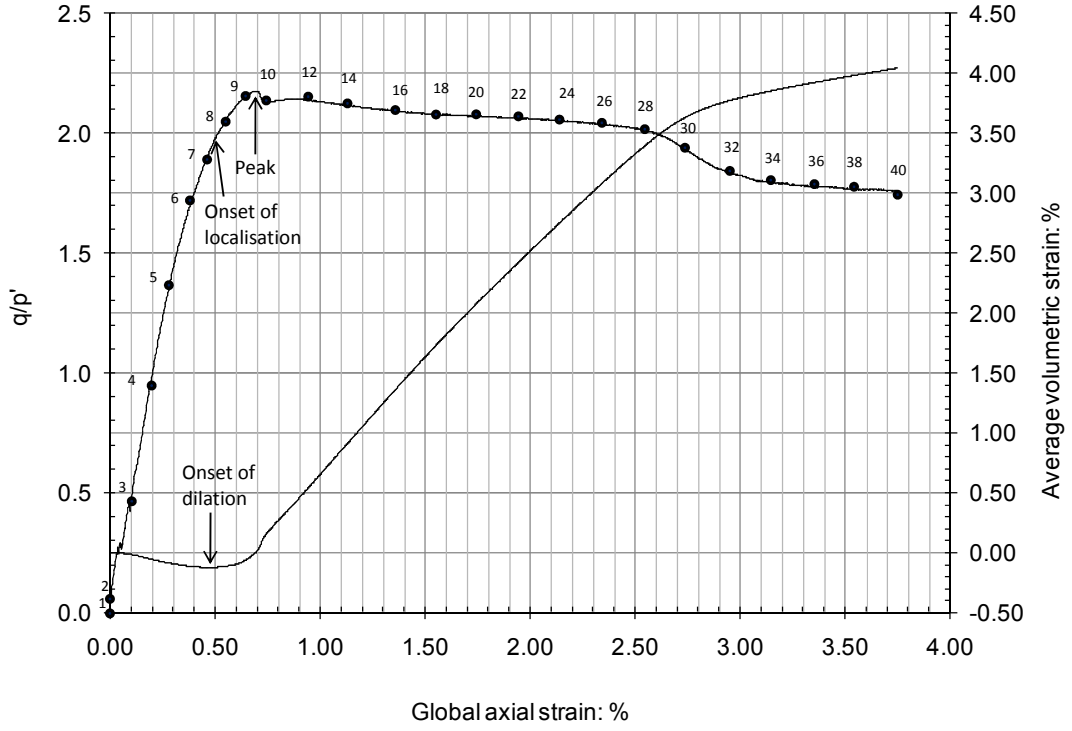

(a)

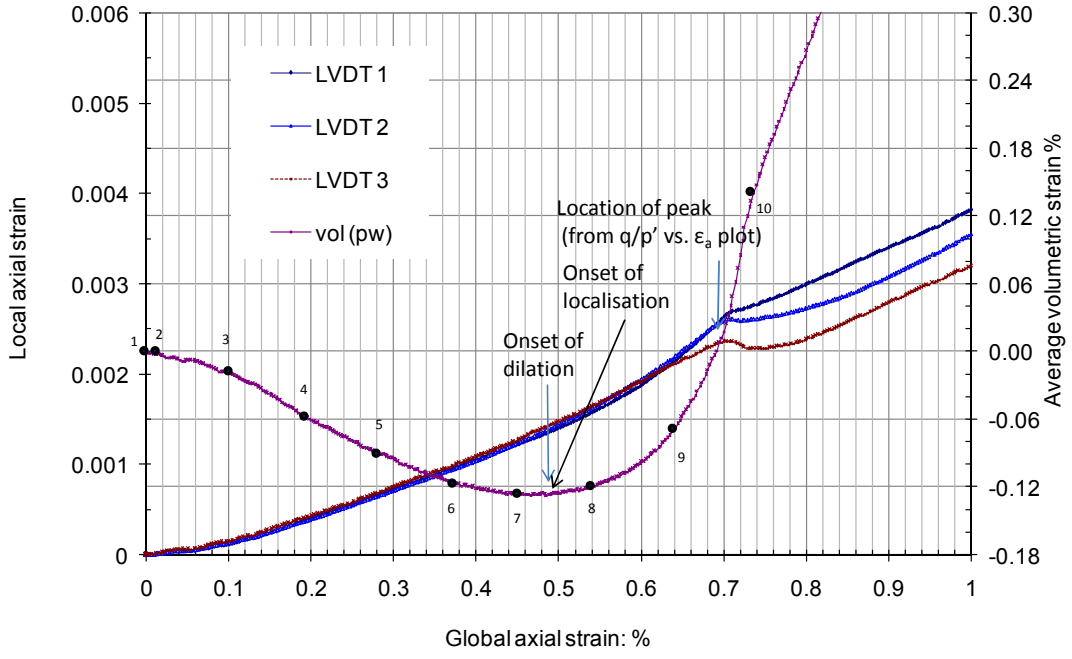

(b)

FIGURE 5.2: (a) Stress ratio, q/p', and average volumetric strain plotted against global axial strain, and (b) local axial strain and average volumetric strain plotted against global axial strain, for an intact RSS sample tested at 50 kPa effective cell pressure

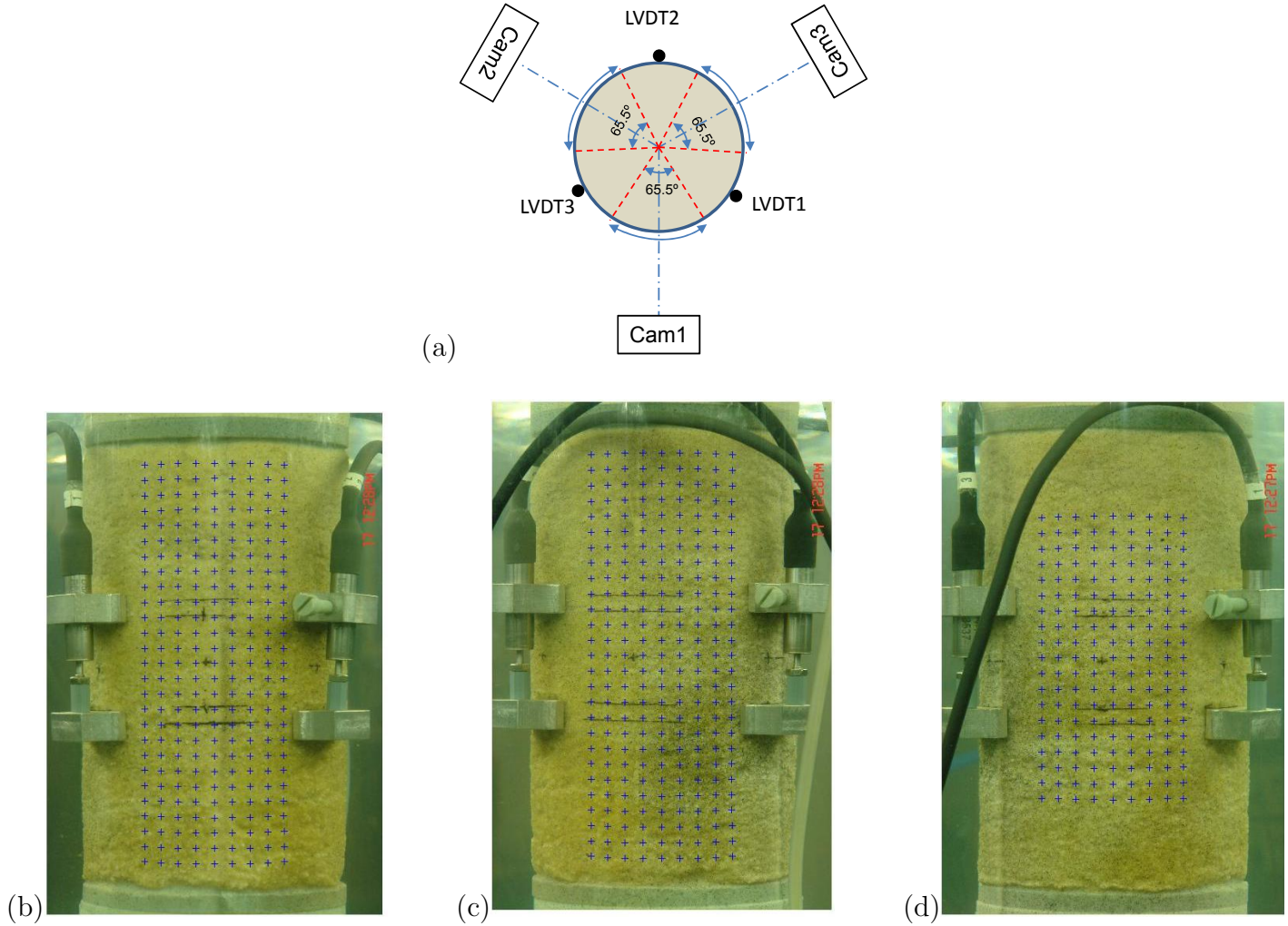

FIGURE 5.3: Cross-sectional view (a), and Measurement points shown in the images (represented by '+' symbols): (b)Cam3 (c) Cam2, and (d) Cam1, for the intact sample tested at 50 kPa

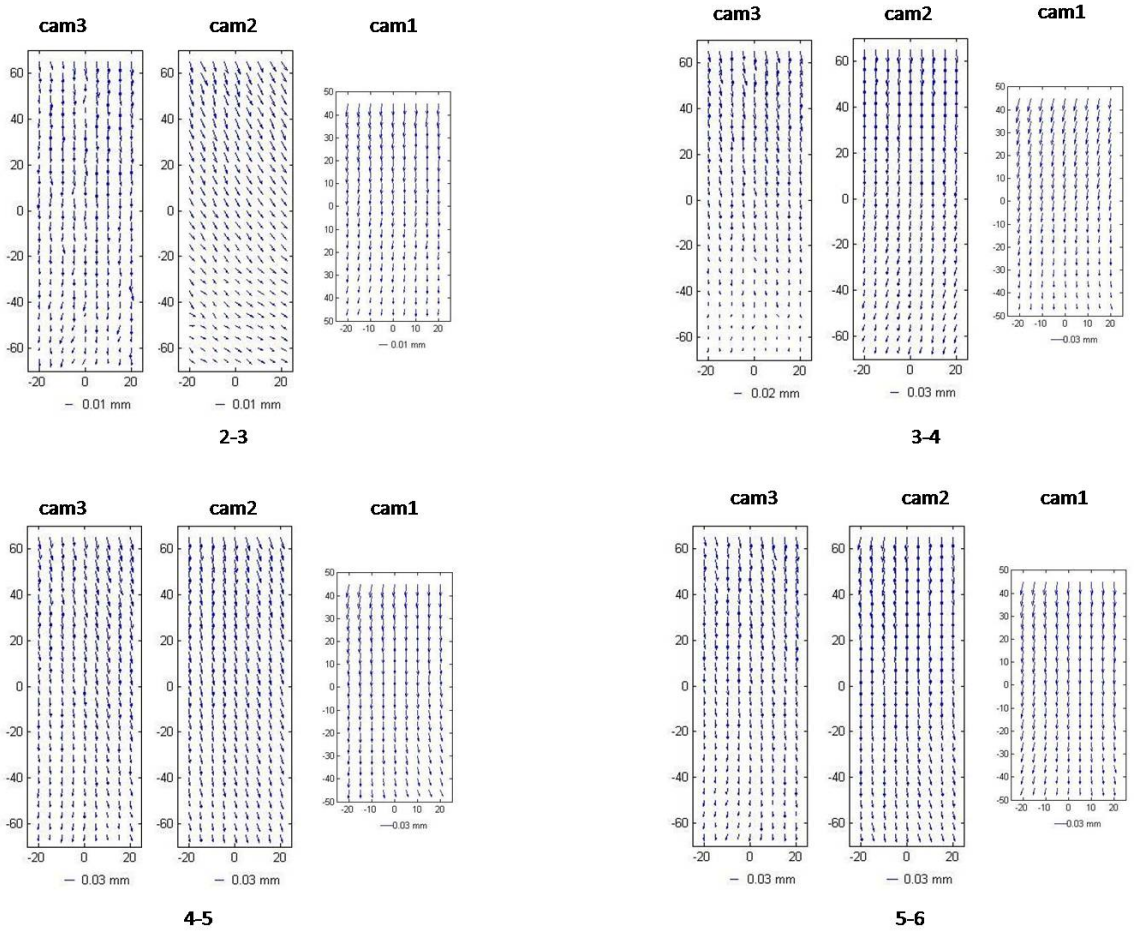

(a)

FIGURE 5.4: (a) Displacement vectors, (b) maximum shear strain fields, and (c) volumetric strain fields - on the pre-peak regime, at steps 2-3, 3-4, 4-5, and 5-6 for IRSS tested at 50 kPa effective cell pressure (To be continued in next pages)

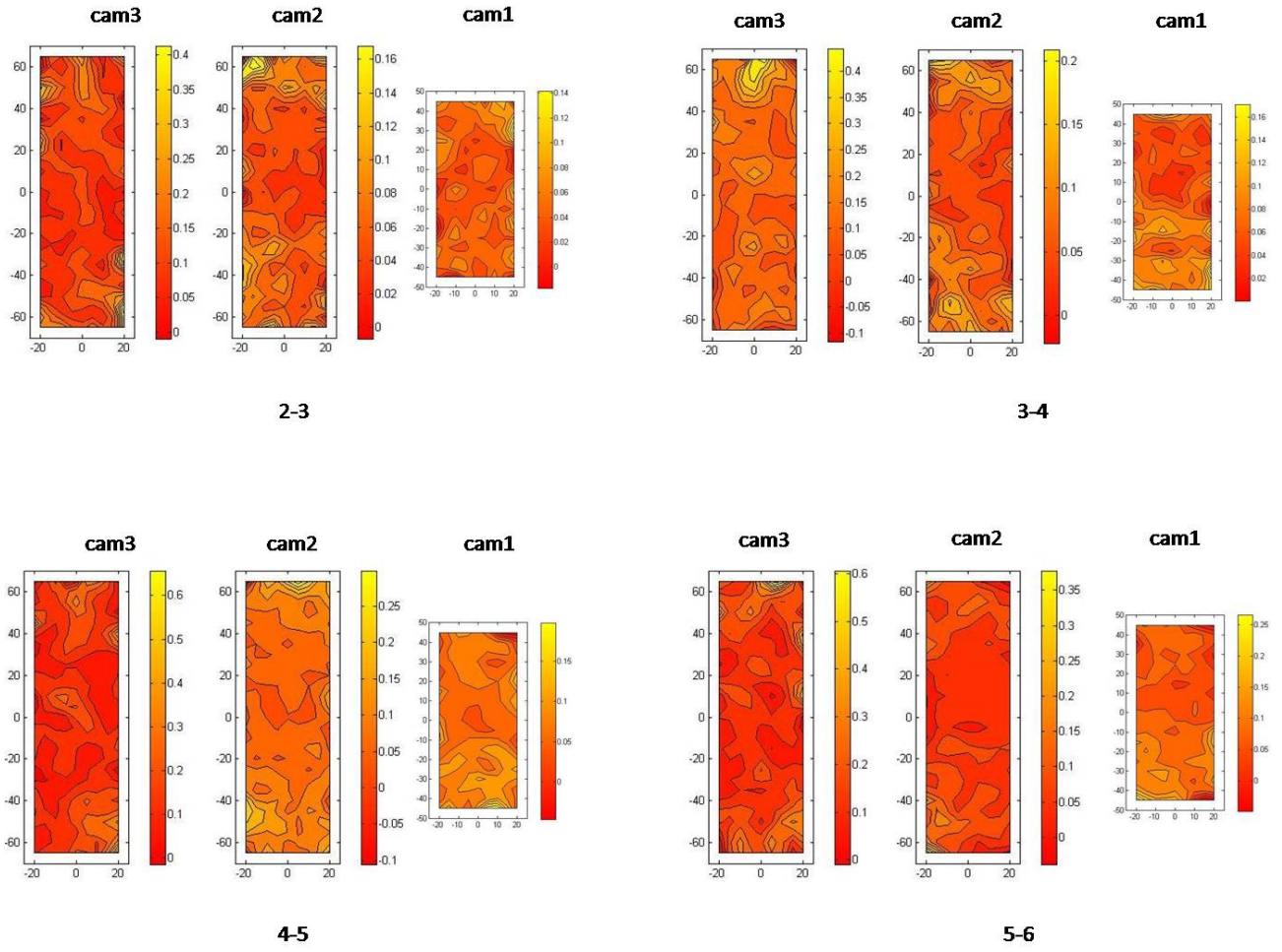

(b)

FIGURE 5.4 (Continued from previous page)

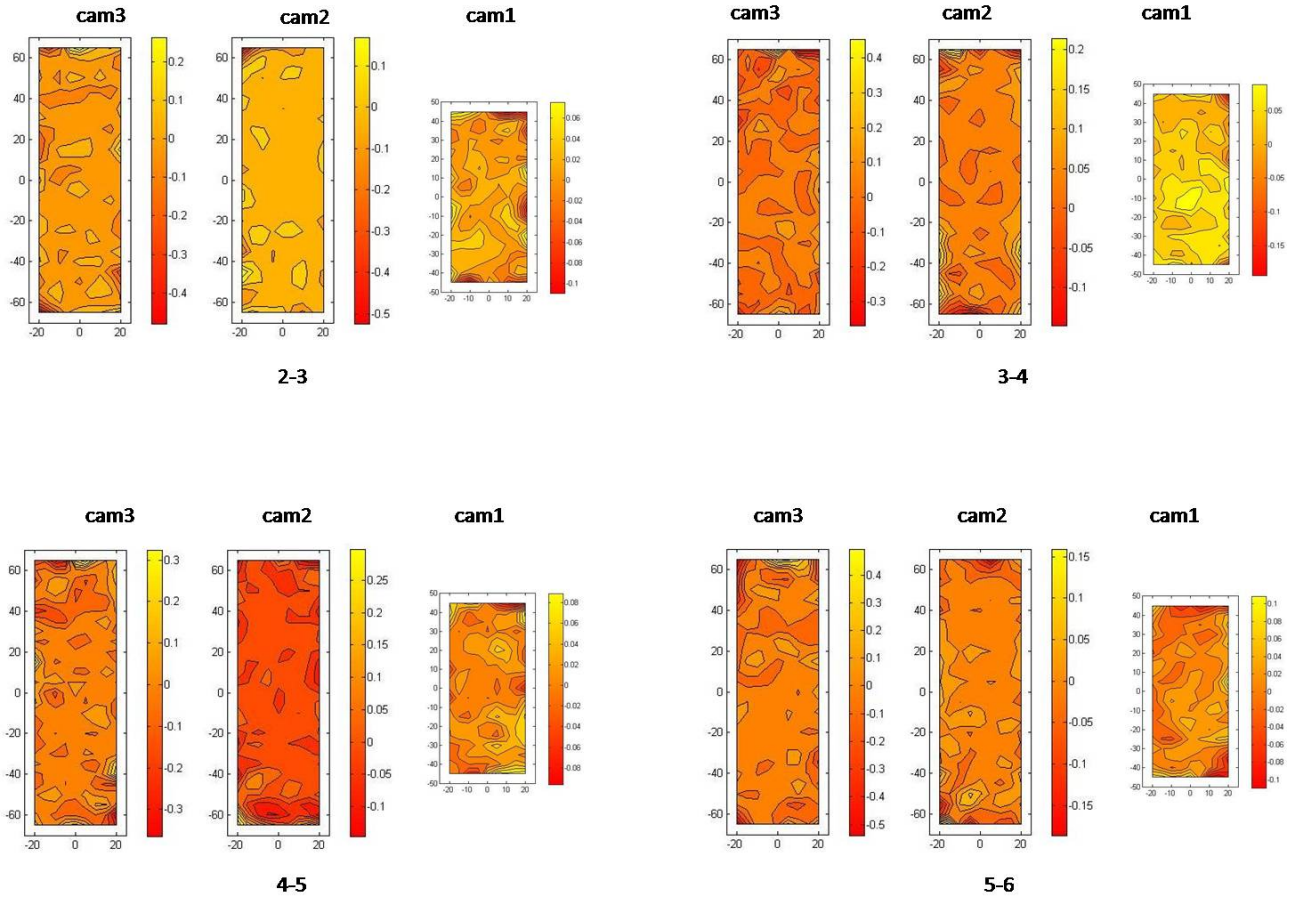

(c)

FIGURE 5.4 (Continued from previous page)

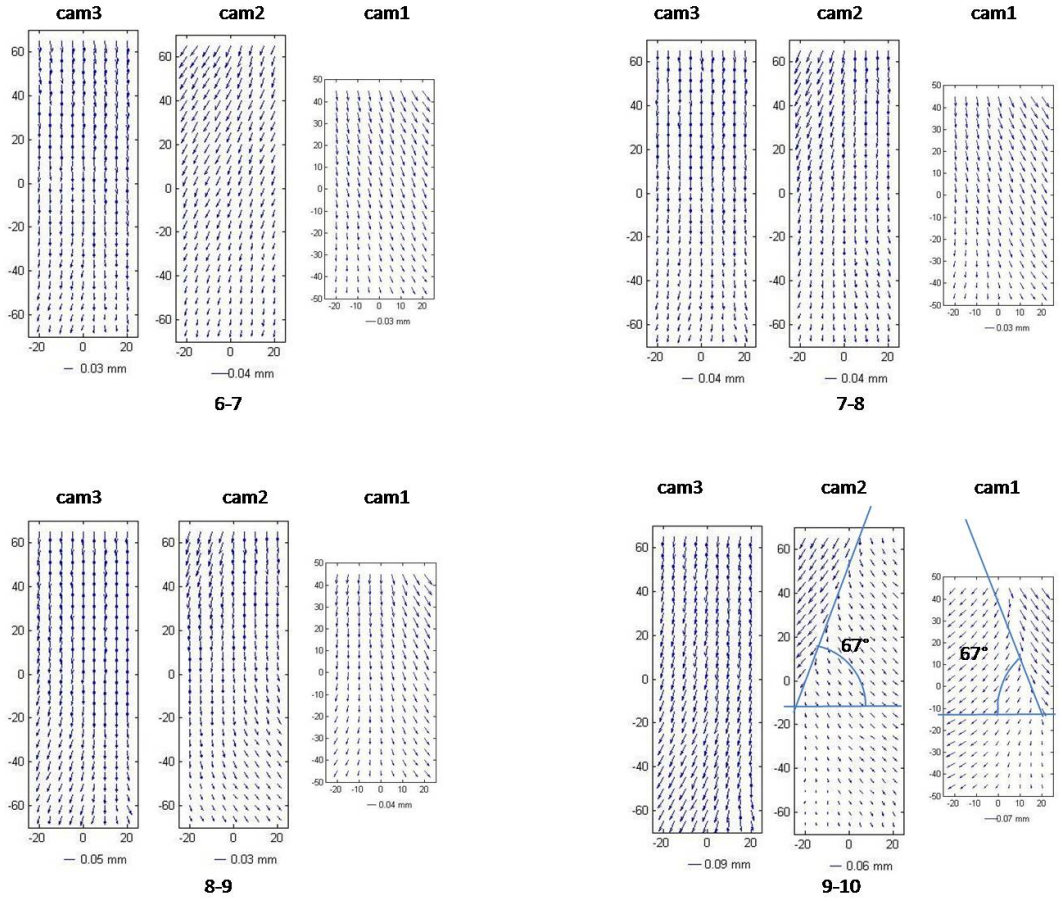

(a)

FIGURE 5.5: (a) Displacement vectors, (b) maximum shear strain fields, and (c) volumetric strain fields - on the near-peak regime, at steps 6-7, 7-8, 8-9, and 9-10 for IRSS tested at 50 kPa effective cell pressure (To be continued in next pages)

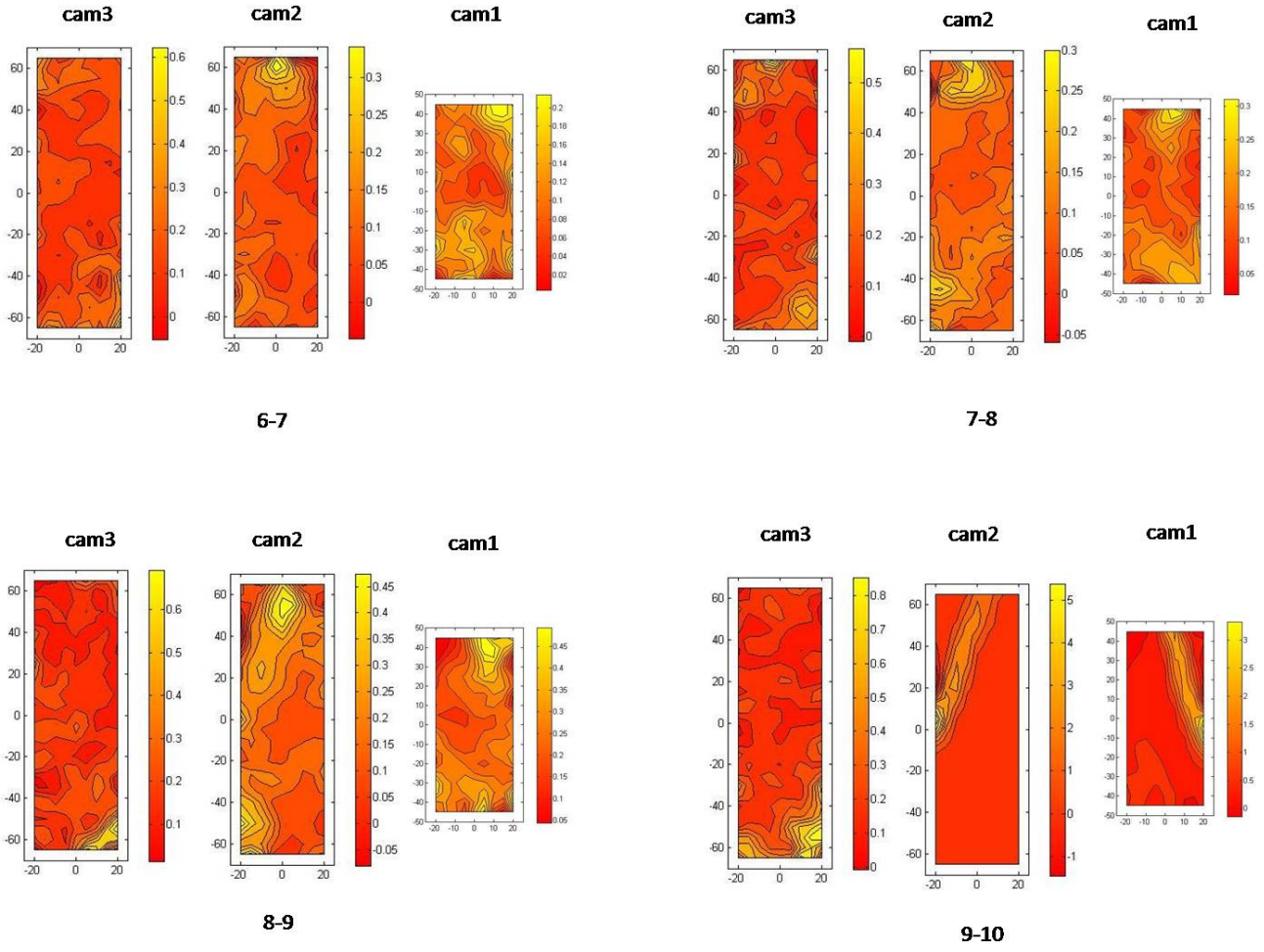

(b)

FIGURE 5.5 (Continued from previous page)

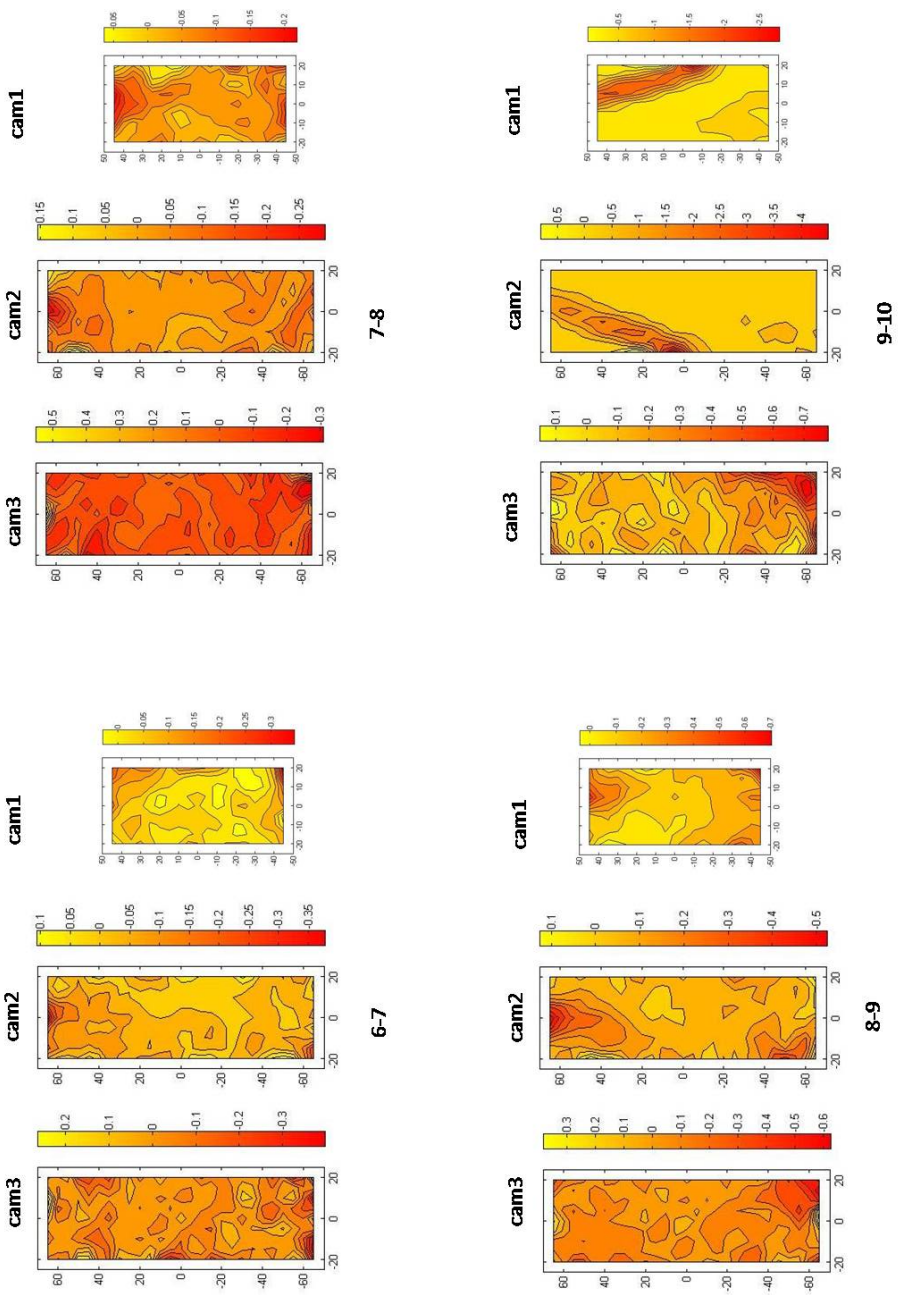

(c)

FIGURE 5.5 (Continued from previous page)

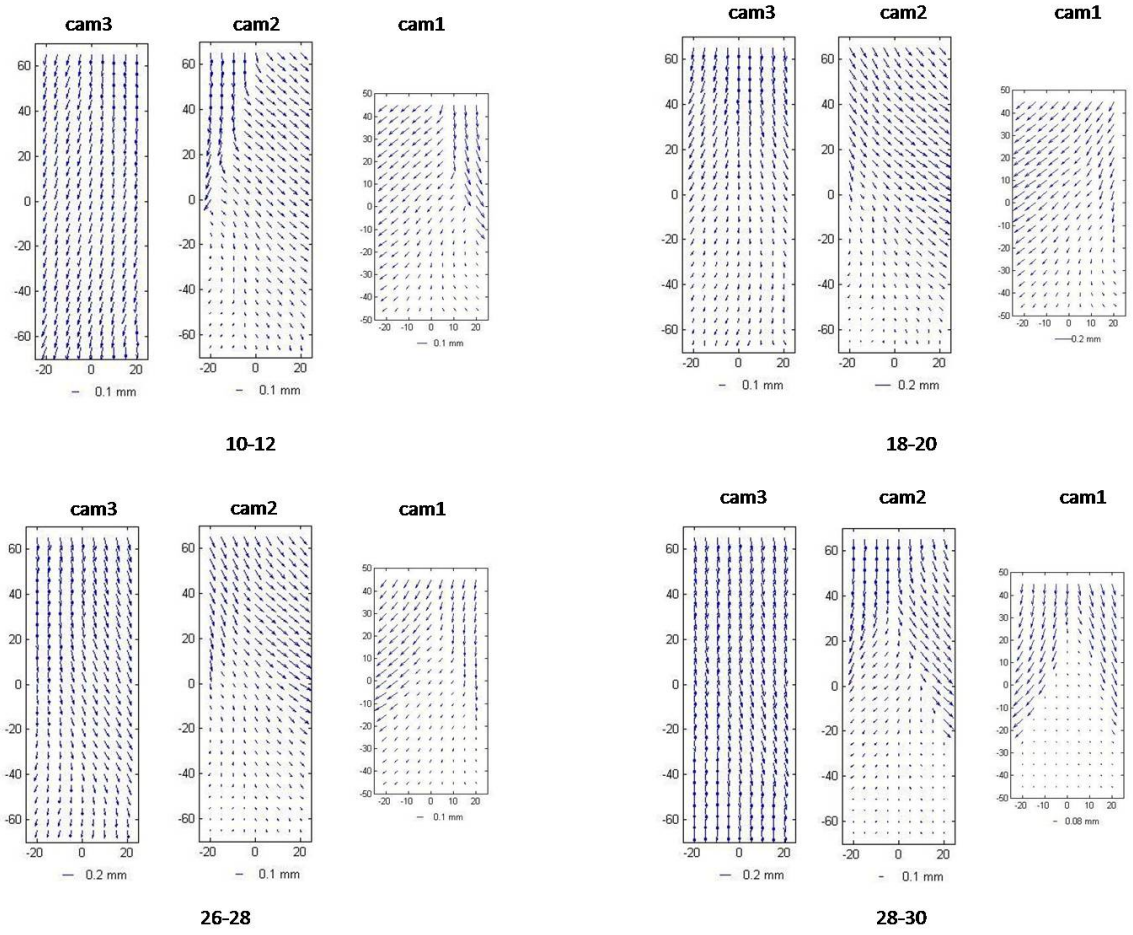

(a)

FIGURE 5.6: (a) Displacement vectors, (b) maximum shear strain fields, and (c) volumetric strain fields - on the post-peak regime, at steps 10-12, 18-20, 26-28, and 28-30 for IRSS tested at 50 kPa effective cell pressure (To be continued in next pages)

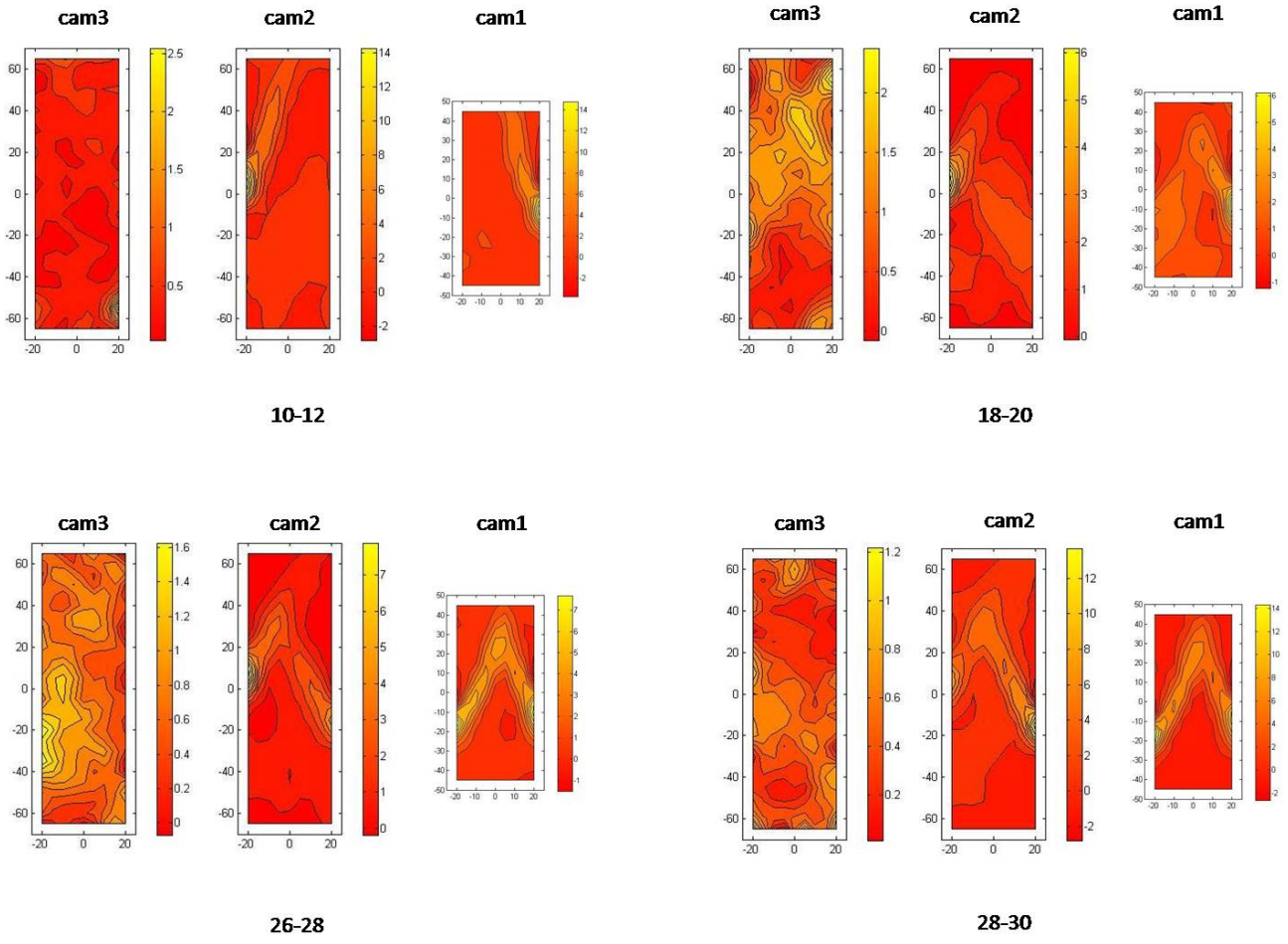

(b)

FIGURE 5.6 (Continued from previous page)

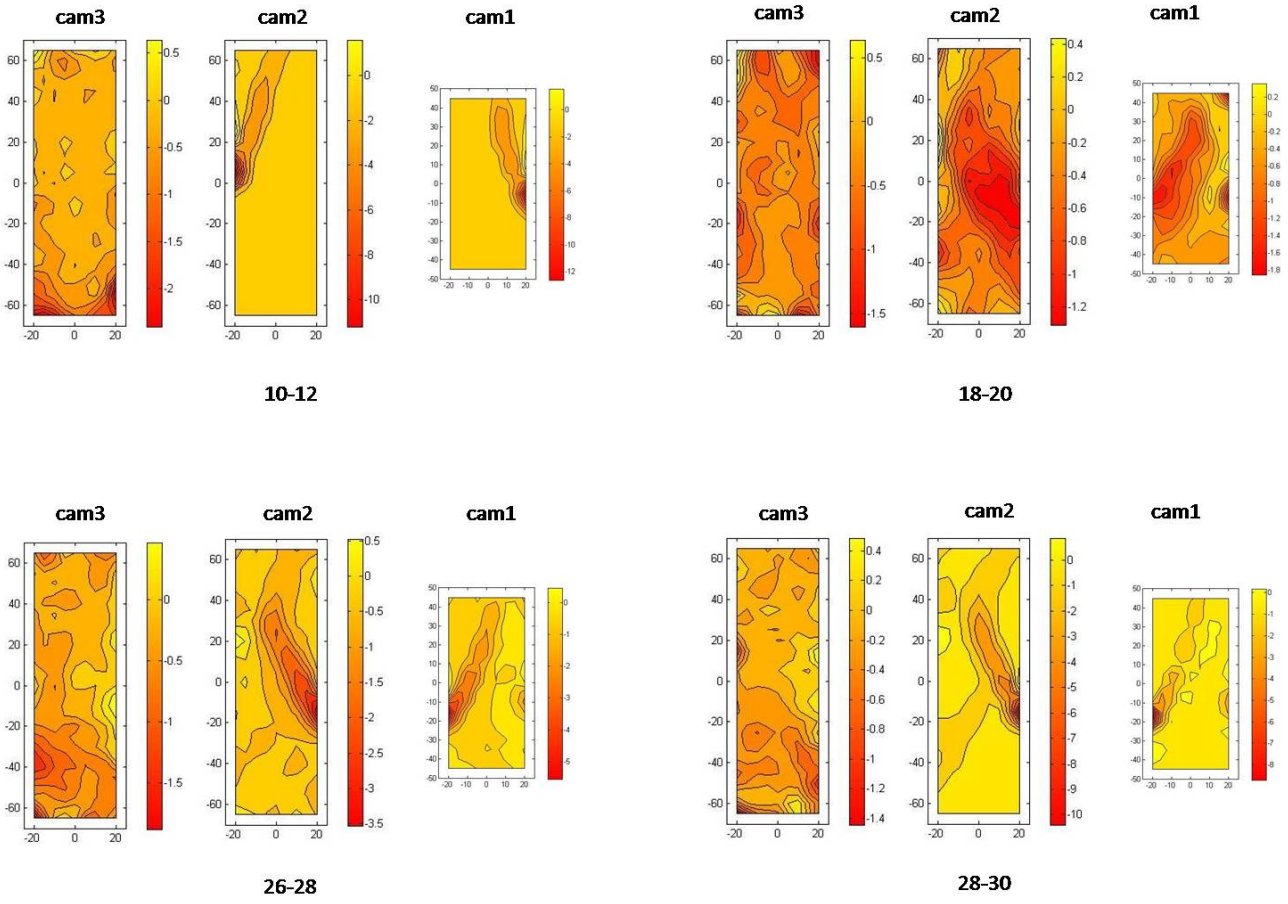

(c)

FIGURE 5.6 (Continued from previous page)

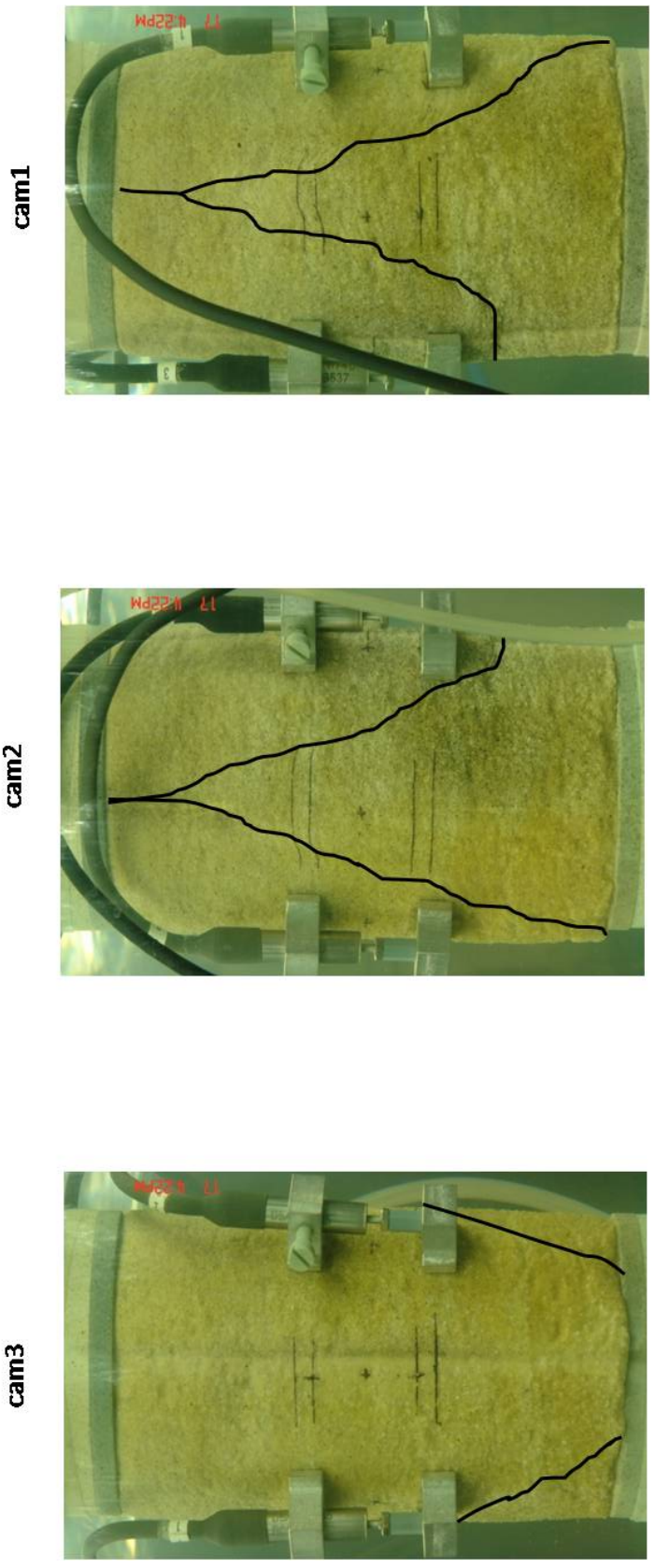

FIGURE 5.7: Photographs of the sample taken at the end of the test. The sketches show the positions of shear bands.

5.4 Deformation characteristics of a shear band

Figure 5.8 shows the stress ratio, q/p', and the average volumetric strain plotted against global axial strain, and local axial strain and average volumetric strain plotted against global axial strain for an intact sample of Reigate silver sand tested at a cell pressure of 50 kPa. This test (Test IRSS-3B) is different test from the one presented in the previous section. There was a slight variation in sample slenderness ratio (cf. Test IRSS-3B and Test IRSS-3A in Table 5.2). Thin-section examination by Cresswell & Powrie (2004) found the thickness of shear bands in Reigate silver sand to be less than a millimetre (involving just 3 to 4 grains). Therefore, to study the deformation characteristics of a shear band, a grid pitch of 5mm is not small enough. Figure 5.9(a) shows the displacement vectors and maximum shear strain field for step 10-11, the deformation step immediately after the peak. The grid pitch is 1.0 mm. Step 14-15, Figure 5.9(b) shows the coalescence of localisations to form a clear shear band. The grid pitch was further reduced to 0.5 mm in the Step 14-15, which ensures that at least some displacement vectors should start within the shear band.

5.5 Effect of confining pressure on deformation characteristics of intact samples

Figure 5.10(a), (b), Figure 5.2 (a), and Figure 5.11(a) show the stress ratio , q/p', and the average volumetric strain plotted against global axial strain for samples of intact RSS tested at cell pressures of 12.5, 25, 50, and 100 kPa. As can be seen, the peak stress ratio was achieved at much larger global axial strains with increasing confining pressure. The post-peak response can be seen to be highly dependent on the applied confining pressure. Figures 5.12, 5.13, 5.14 show the surface areas of the samples covered in the image analysis for 12.5, 25, and 100 kPa tests. For 50 kPa test, it was already presented in Figure 5.3.

5.5.1 Localisation pattern

The displacement vectors and strain fields at the onset of localisation are shown in Figure 5.15, Figure 5.5 (Step 7-8) and Figure 5.16. At 12.5 kPa, the onset of

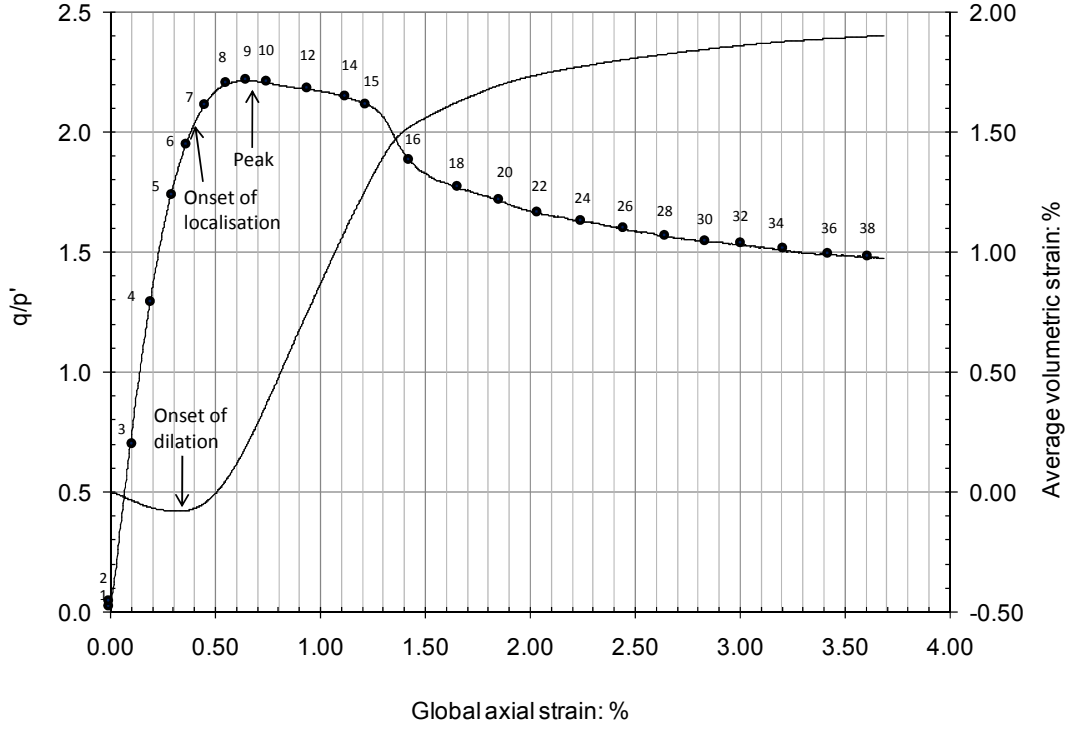

(a)

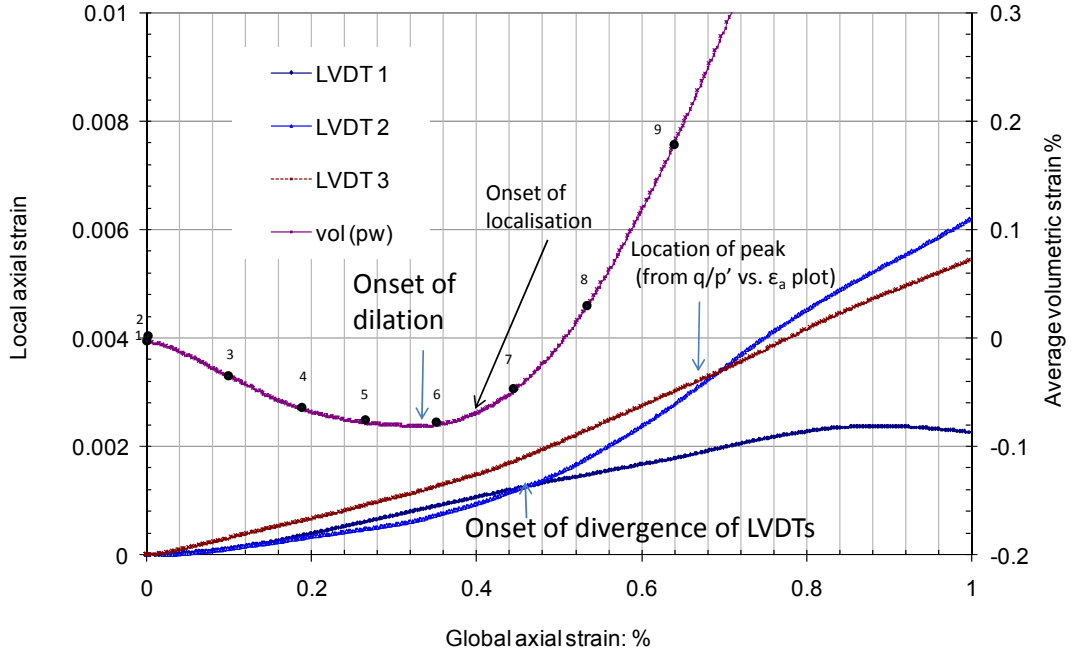

(b)

FIGURE 5.8: (a) Stress ratio, q/p', and average volumetric strain plotted against global axial strain, and (b) local axial strain and average volumetric strain plotted against global axial strain, for an intact RSS sample tested at 50 kPa effective cell pressure

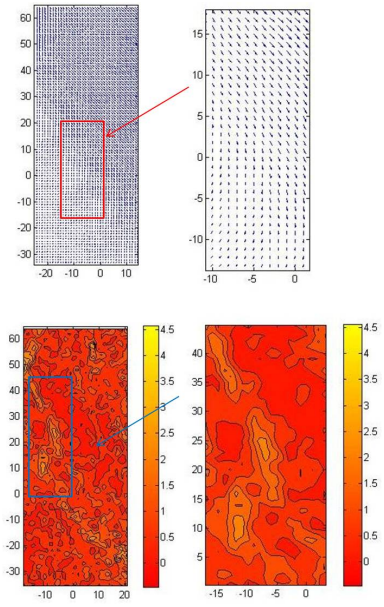

(a) Step 10-11

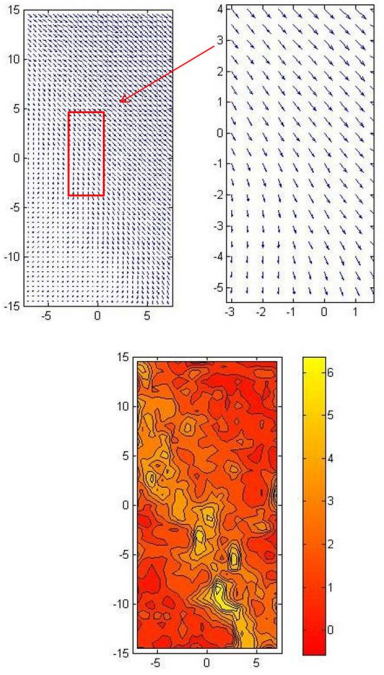

(b) Step 14-15

FIGURE 5.9: Displacement vectors and maximum shear strain fields containing a shear band during the post peak regime while testing an intact sample of RSS at 50 *kPa* effective cell pressure. The grid pitch is (a) 1.0 mm (Step 10-11), and (b) 0.5 mm (Step 14-15).

localisation occurred in step 5-6 (Figure 5.15(a)). At 25 kPa, it is slightly delayed with respect to global axial strain and occurred in step 6-7 (Figure 5.15). This sample contains a pre-existing discontinuity inside the sample (almost horizontally) between the top portion and the middle portion of the sample (i.e. nearer to the top end of the whole sample). It was formed during the sample preparation process. At 50 kPa, it was occurred in step 7-8. At 100 kPa, it is further delayed and was found to occur in step 9-10 (Figure 5.16). A clear tendency of progressive delay of the onset of localisation with increasing global axial strain at the increasing confining pressure is apparent. Furthermore, with the increasing cell pressure, from the strain fields presented a clear change in strain localisation mode from a localised to a more diffused type of pattern can also be identified. Figure 5.19 and Figure 5.19 show the photographs of the samples taken at the end of the test for 12.5 and 25 kPa. In Figure 5.19, reflections of the shear band at the boundaries can be seen. For the test conducted at 50 kPa, the photographs were shown in Figure 5.7. For the test conducted at 100 kPa, since the test was terminated well before the clear formation of shear bands, the locations of the shear bands were not possible to identify from the visual observations of the images. The sketches shown are the locations of the shear bands identified by playbacking the images.

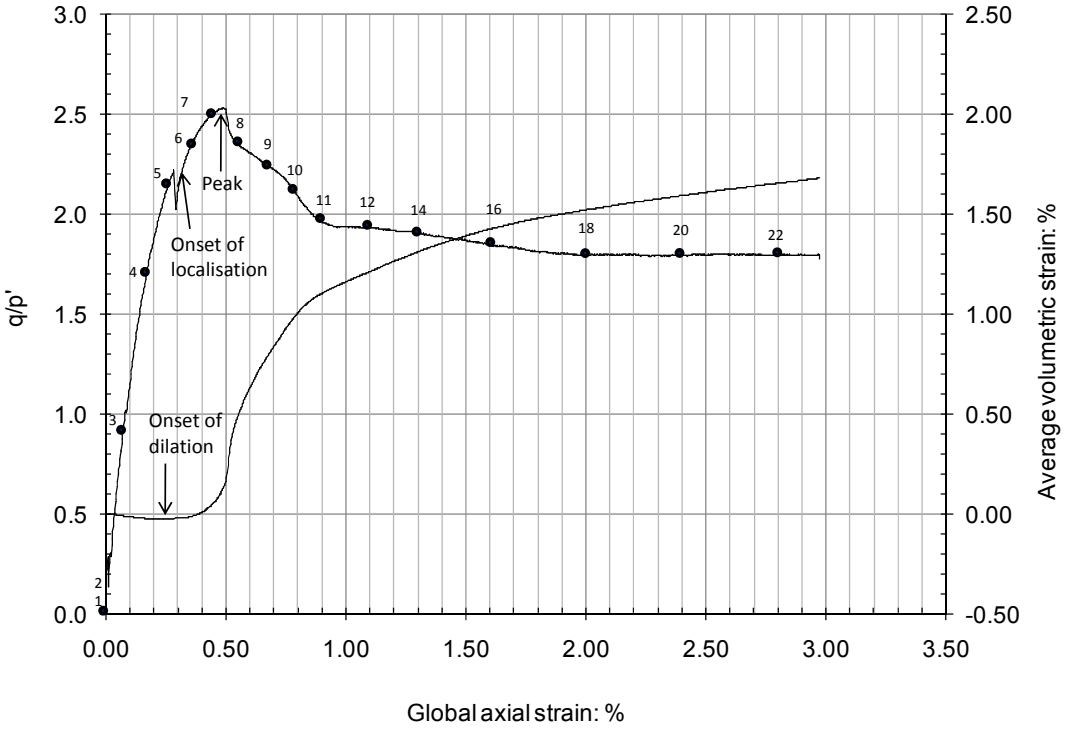

(a)

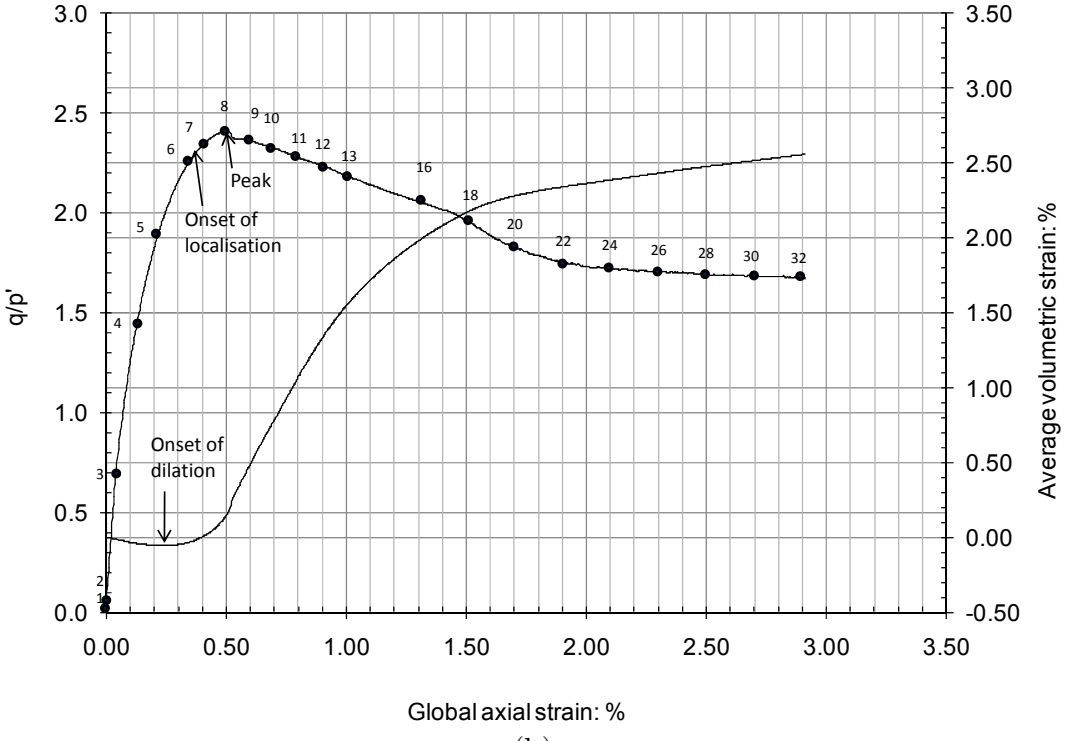

(b)

FIGURE 5.10: (a) Stress ratio, q/p', and average volumetric strain plotted against global axial strain for an intact RSS sample tested at (a) 12.5 kPa, and (b) 25 kPa effective cell pressure

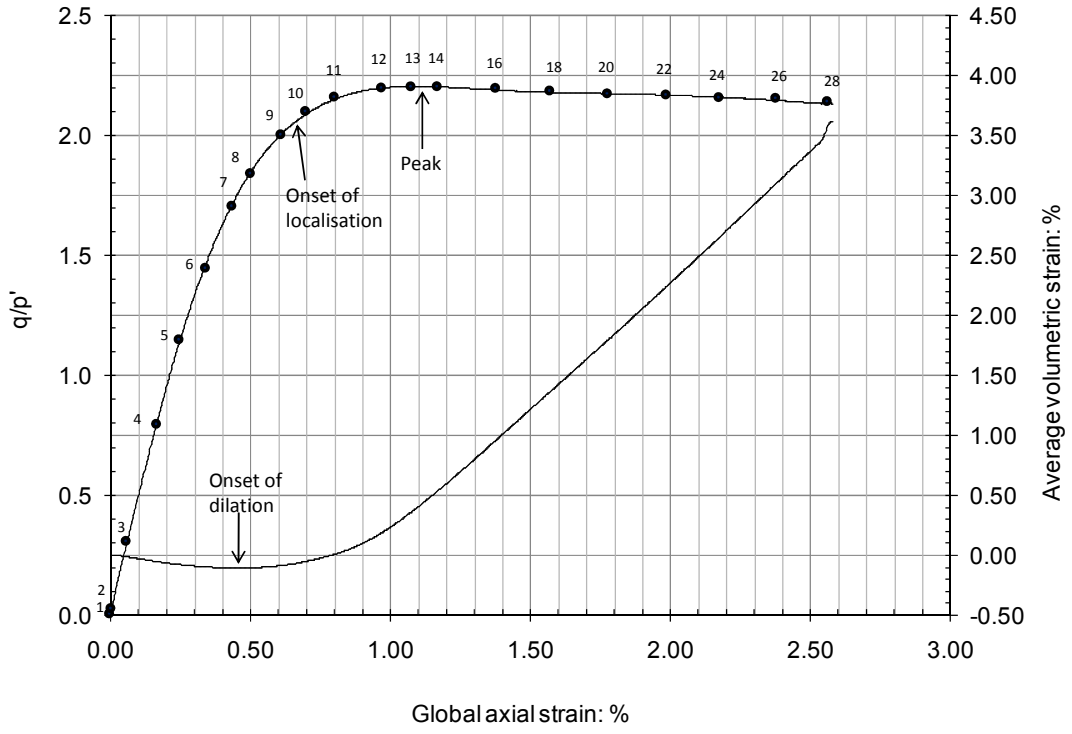

(a)

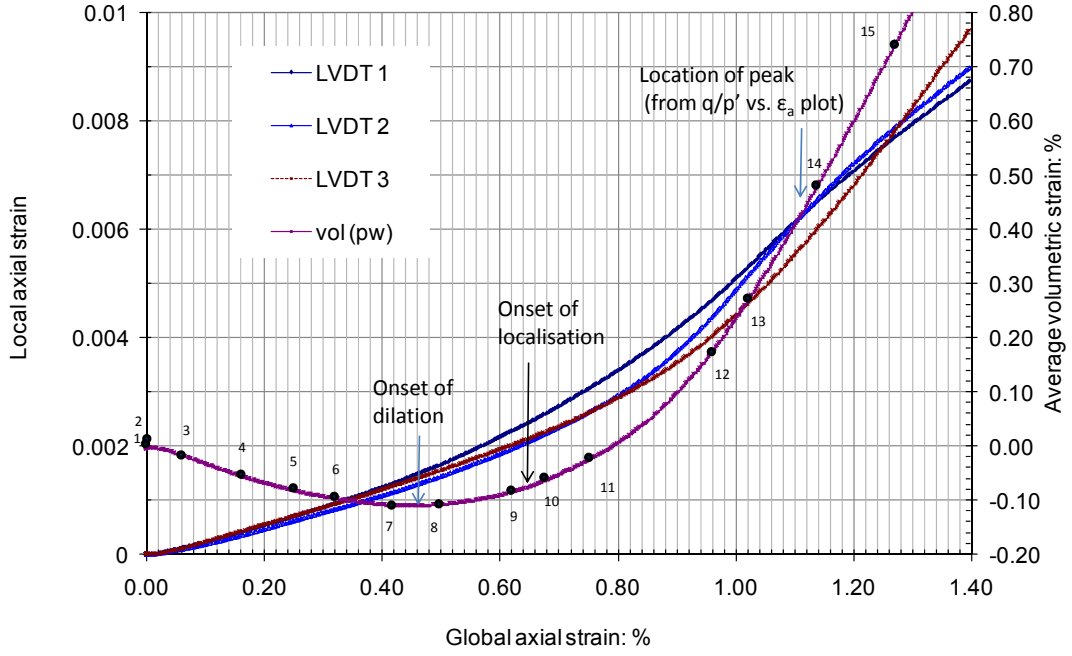

(b)

FIGURE 5.11: (a) Stress ratio, q/p', and average volumetric strain plotted against global axial strain, and (b) local axial strain and average volumetric strain plotted against global axial strain, for an intact RSS sample tested at 100 kPa effective cell pressure

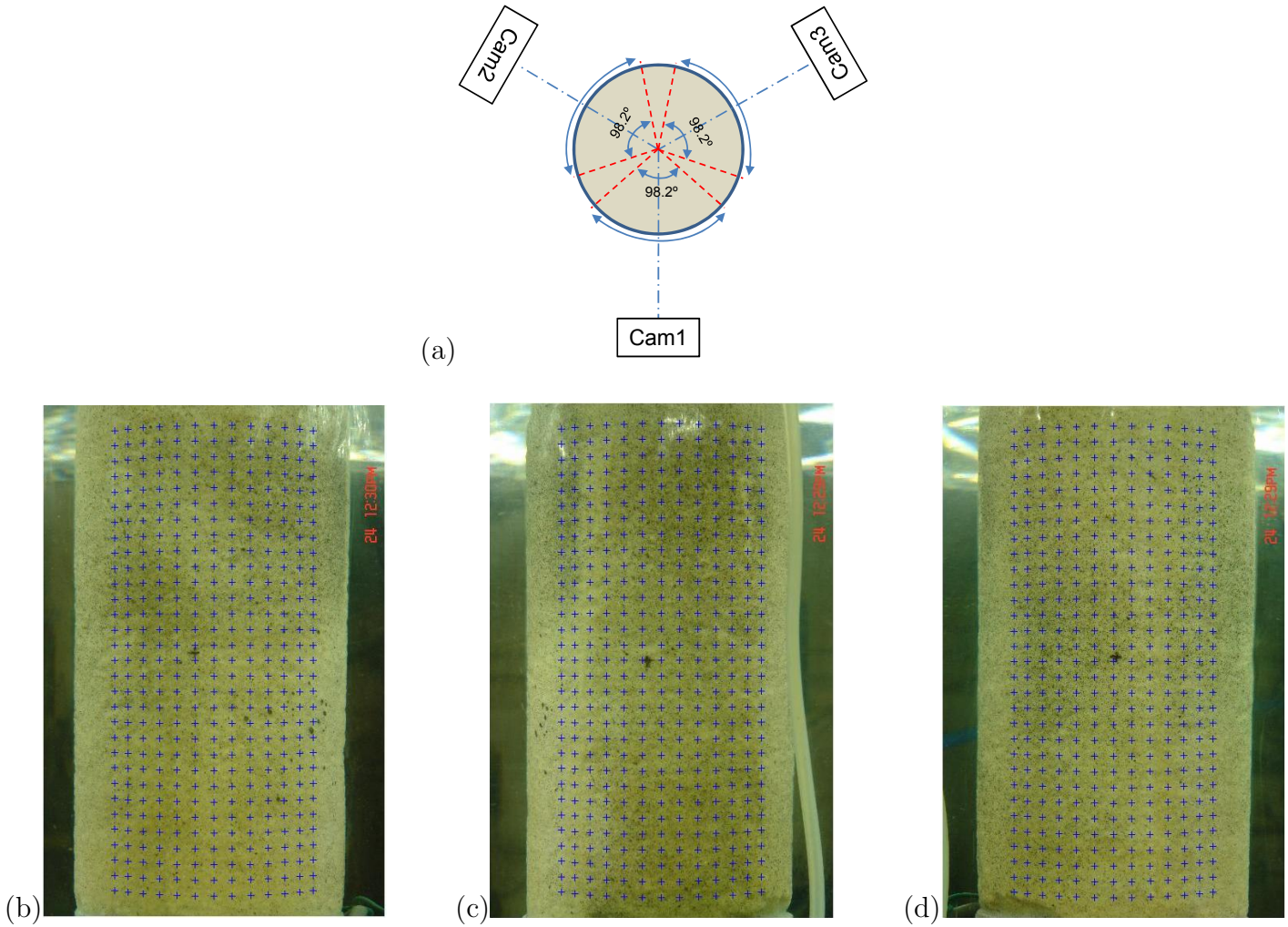

FIGURE 5.12: Cross-sectional view (a), and Measurement points shown in the images (represented by '+' symbols): (b)Cam3 (c) Cam2, and (d) Cam1, for the intact sample tested at 12.5 *kPa*

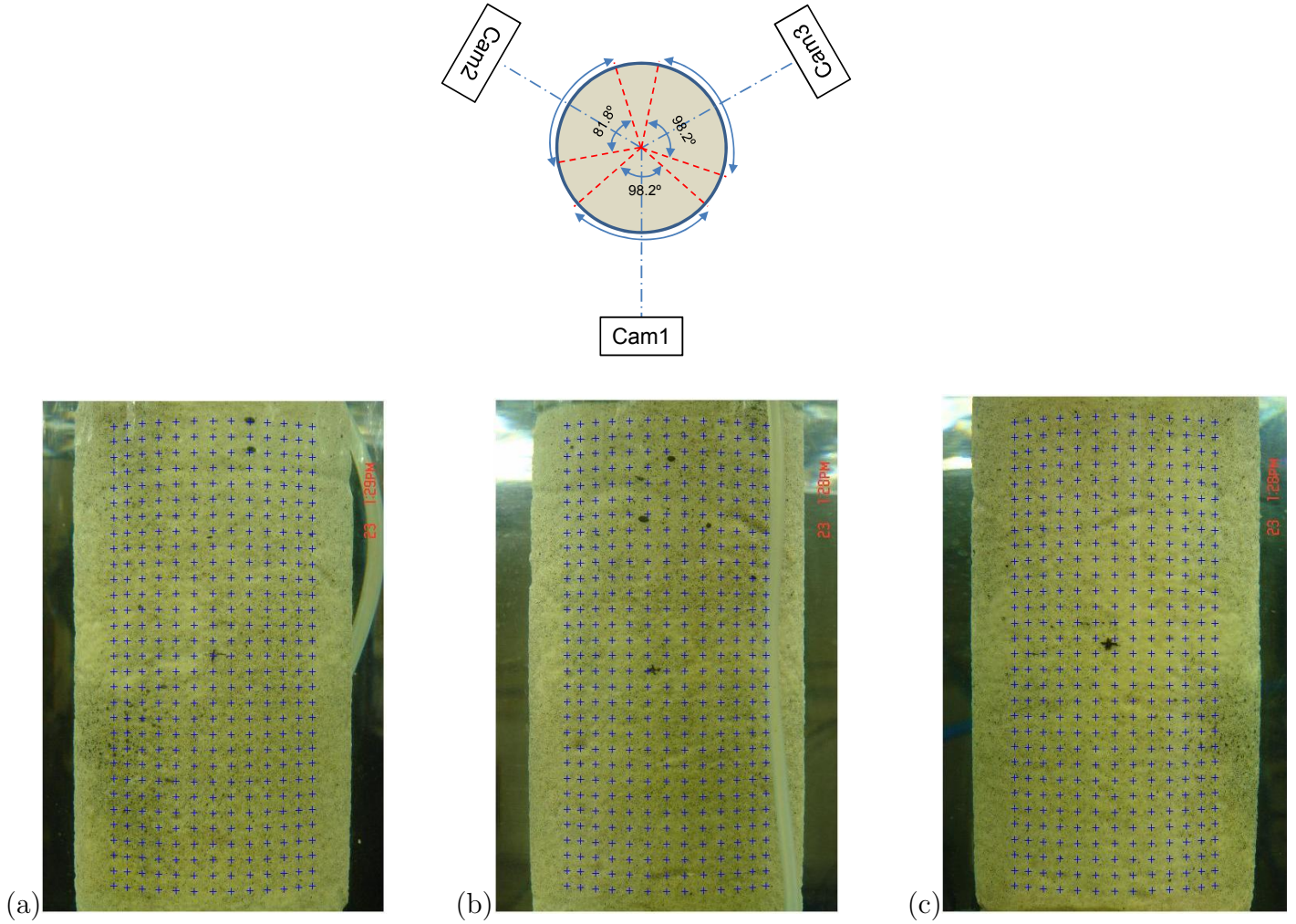

FIGURE 5.13: Cross-sectional view (a), and Measurement points shown in the images (represented by '+' symbols): (b)Cam3 (c) Cam2, and (d) Cam1, for the intact sample tested at 25 kPa

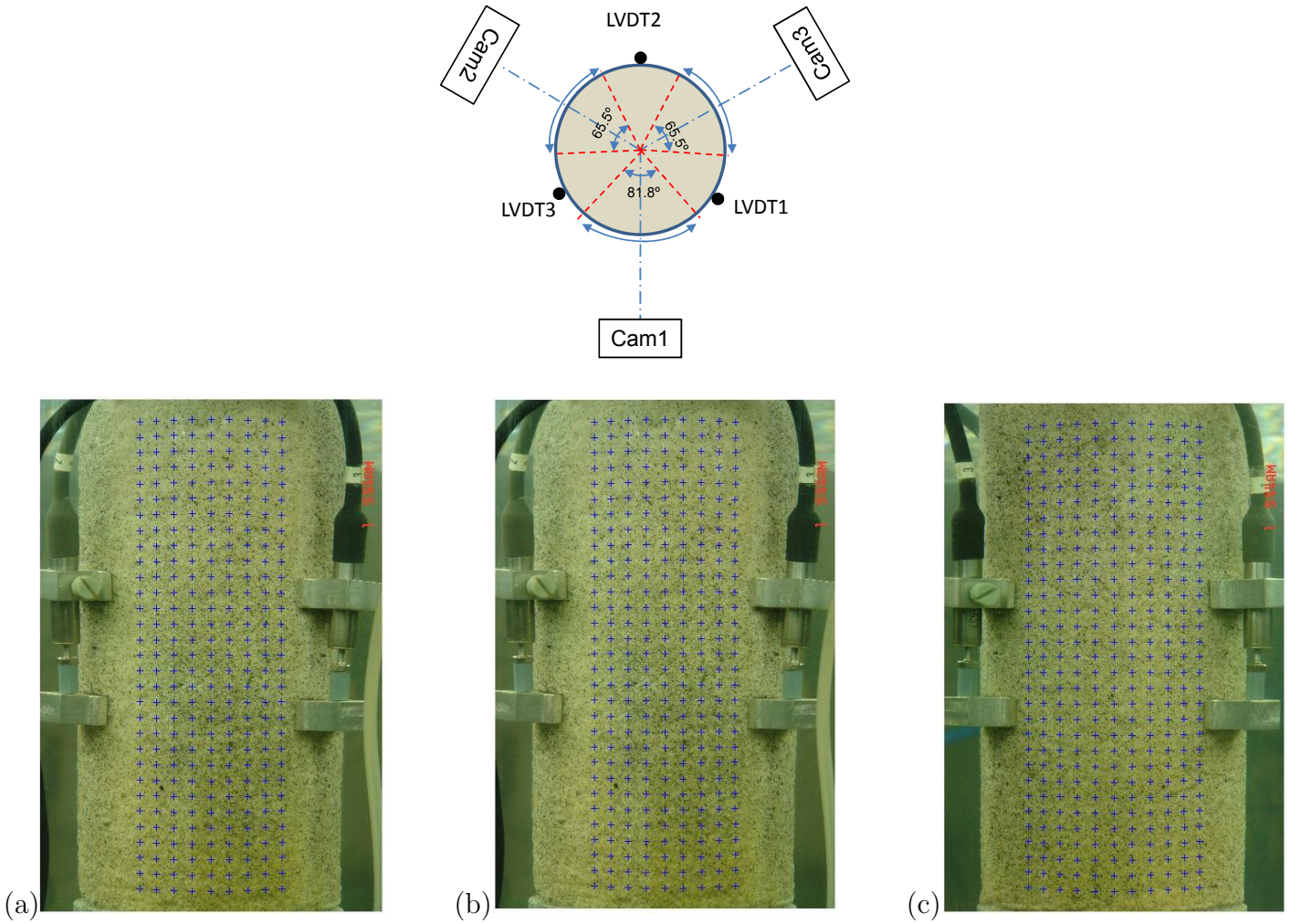

FIGURE 5.14: Cross-sectional view (a), and Measurement points shown in the images (represented by '+' symbols): (b)Cam3 (c) Cam2, and (d) Cam1, for the intact sample tested at 100 kPa

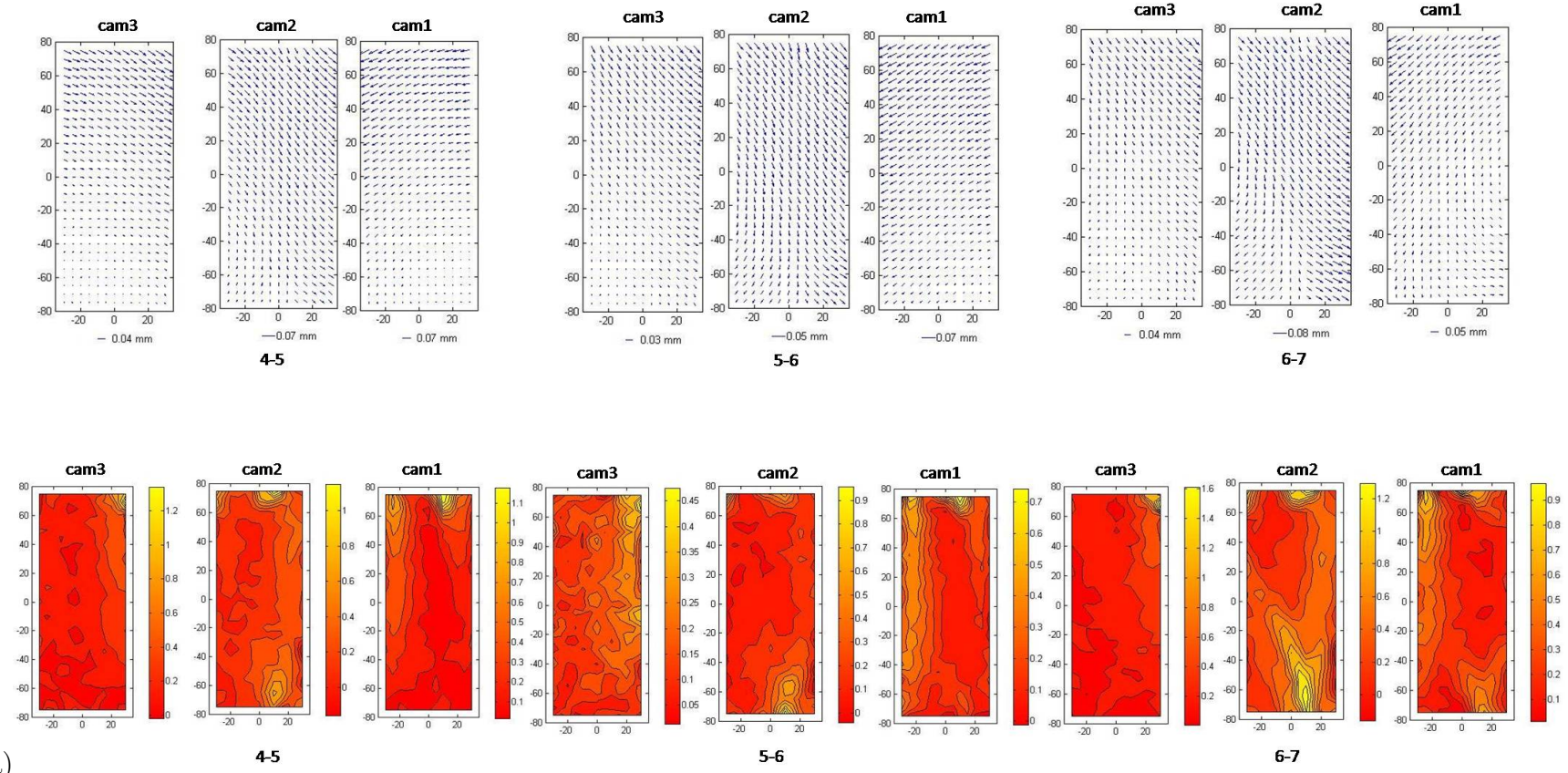

(a)

FIGURE 5.15: (a) Displacement vectors, and maximum shear strain fields around onset of localisation for intact RSS samples tested at (a) 12.5, and (b) 25 *kPa* confining pressures (To be continued in next page)

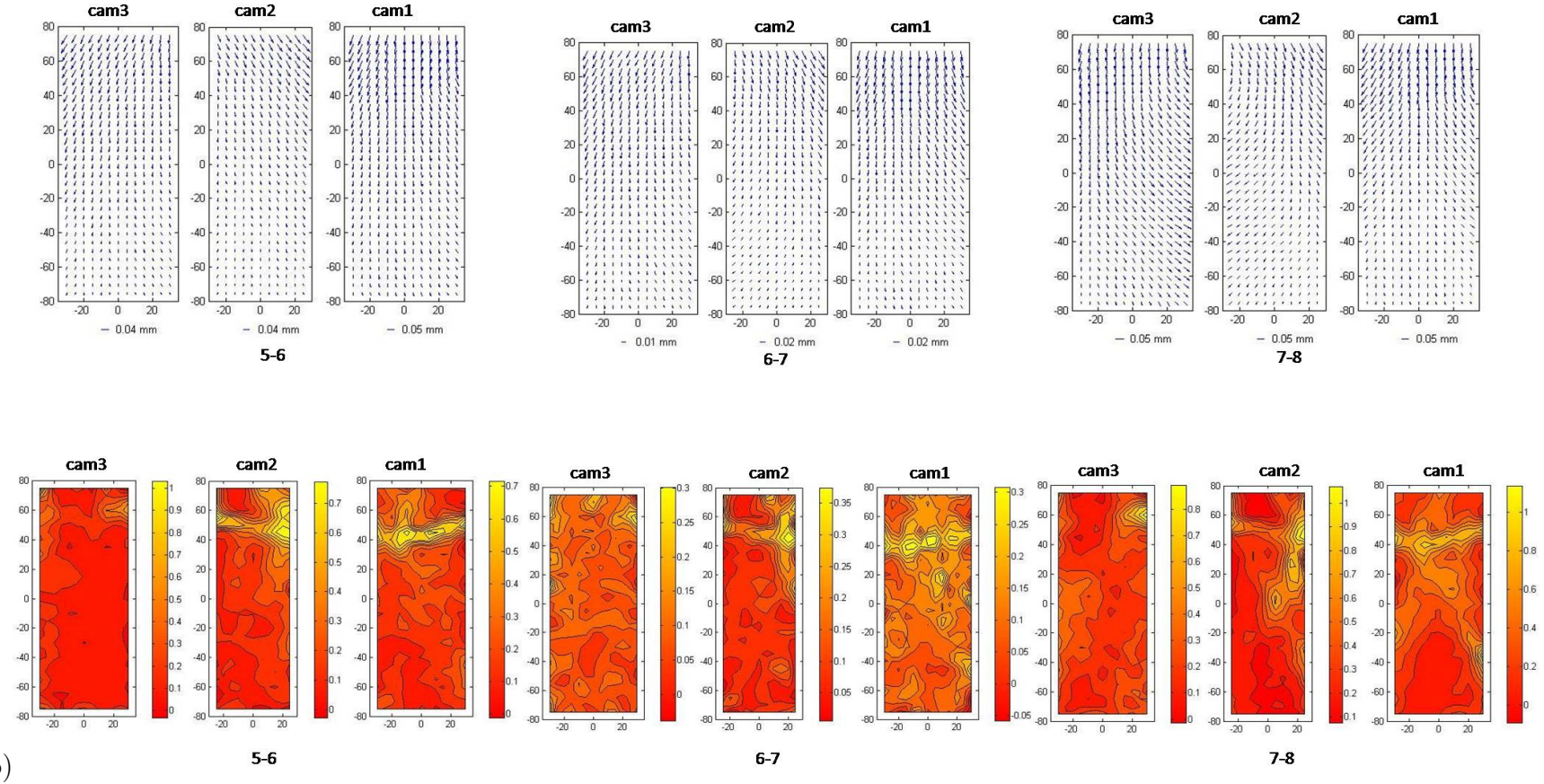

(b)

FIGURE 5.15 (Continued from previous page)

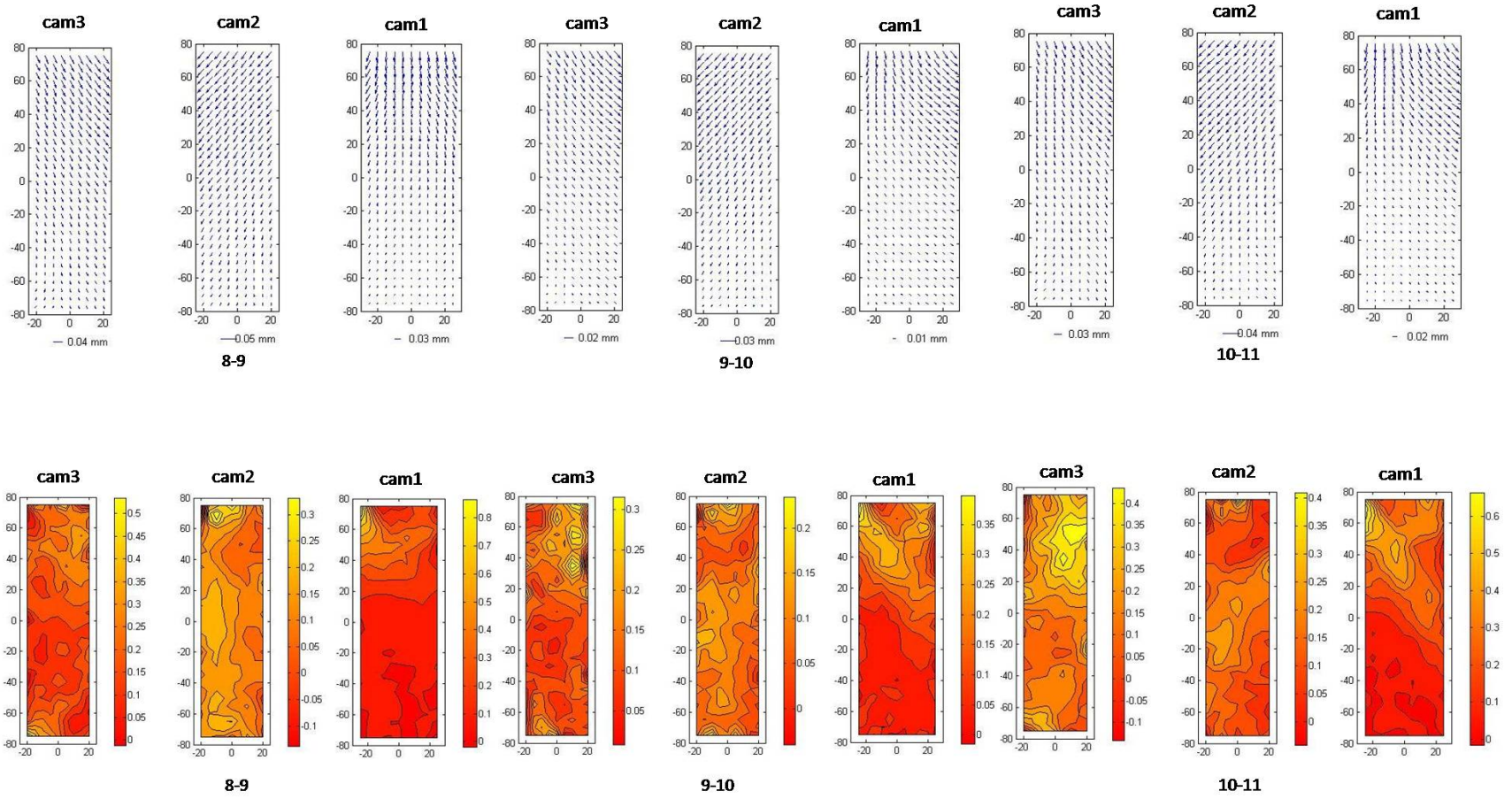

FIGURE 5.16: Displacement vectors, and maximum shear strain fields around onset of localisation for intact RSS samples tested at 100 kPa confining pressure

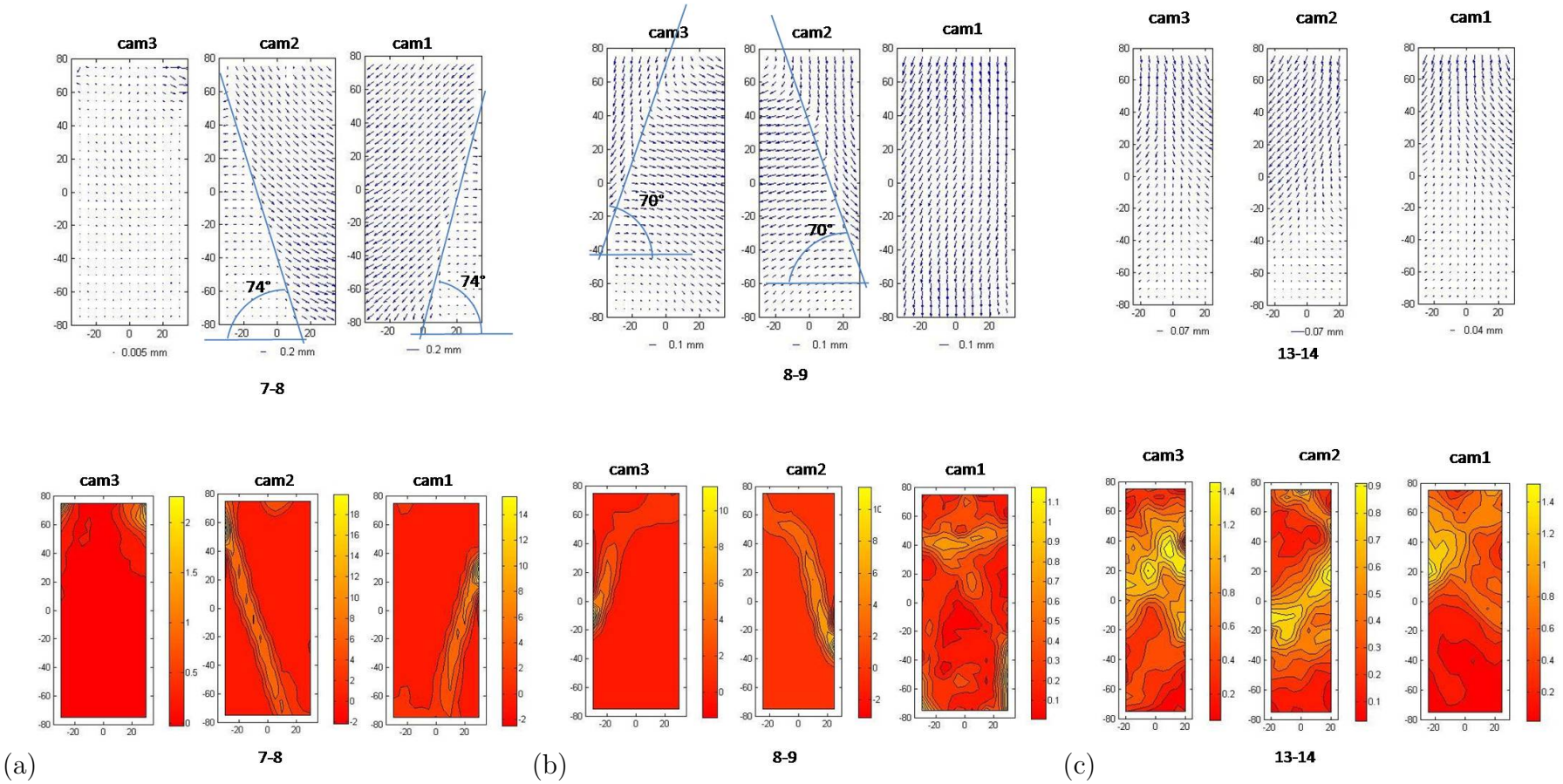

FIGURE 5.17: Displacement vectors, and maximum shear strain fields around peak for intact RSS samples tested at (a) 12.5, (b) 25, and (c) 100 kPa confining pressures

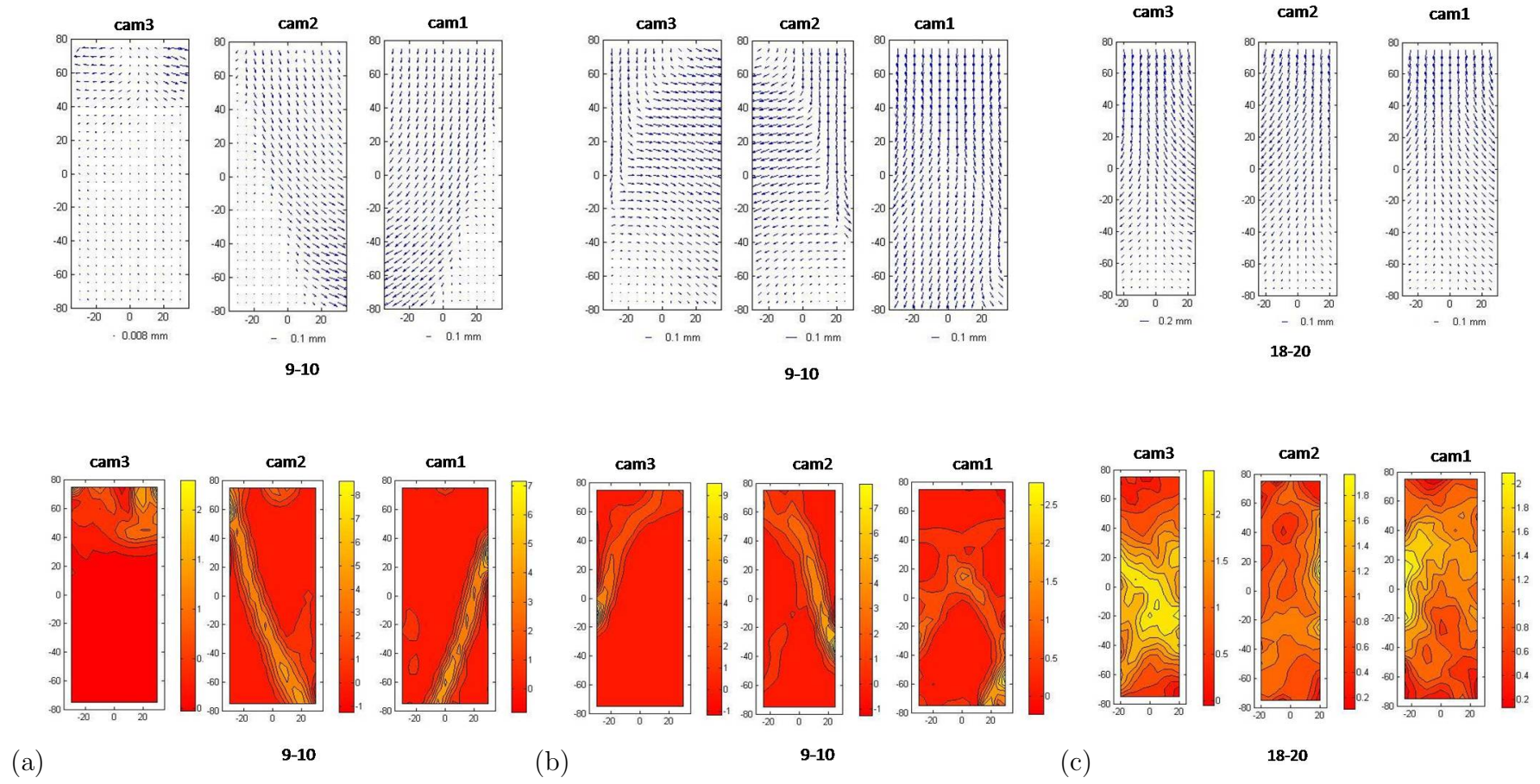

FIGURE 5.18: Displacement vectors, and maximum shear strain fields on the post-peak for intact RSS samples tested at (a) 12.5, (b) 25, and (c) 100 kPa confining pressures

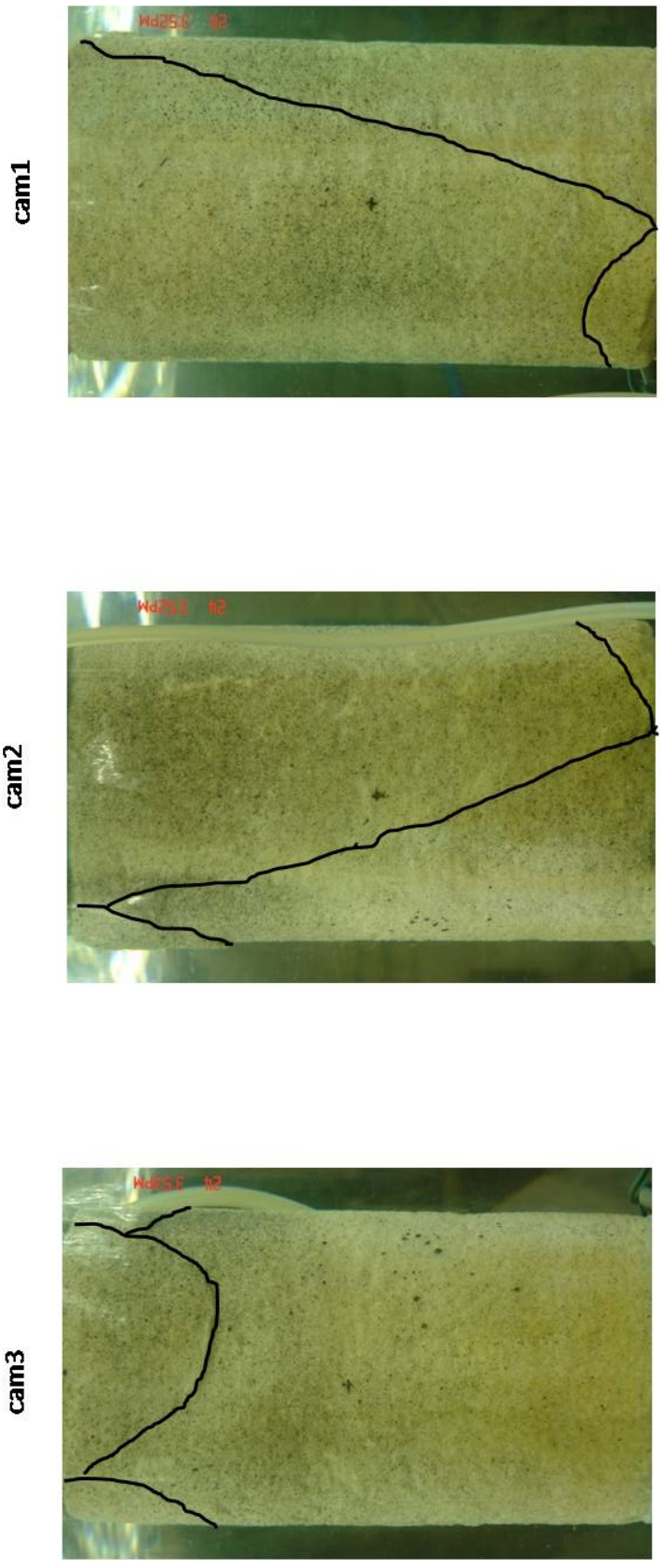

FIGURE 5.19: Photographs of the sample tested at 12.5 kPa taken at the end of the test. The sketches show the positions of shear bands.

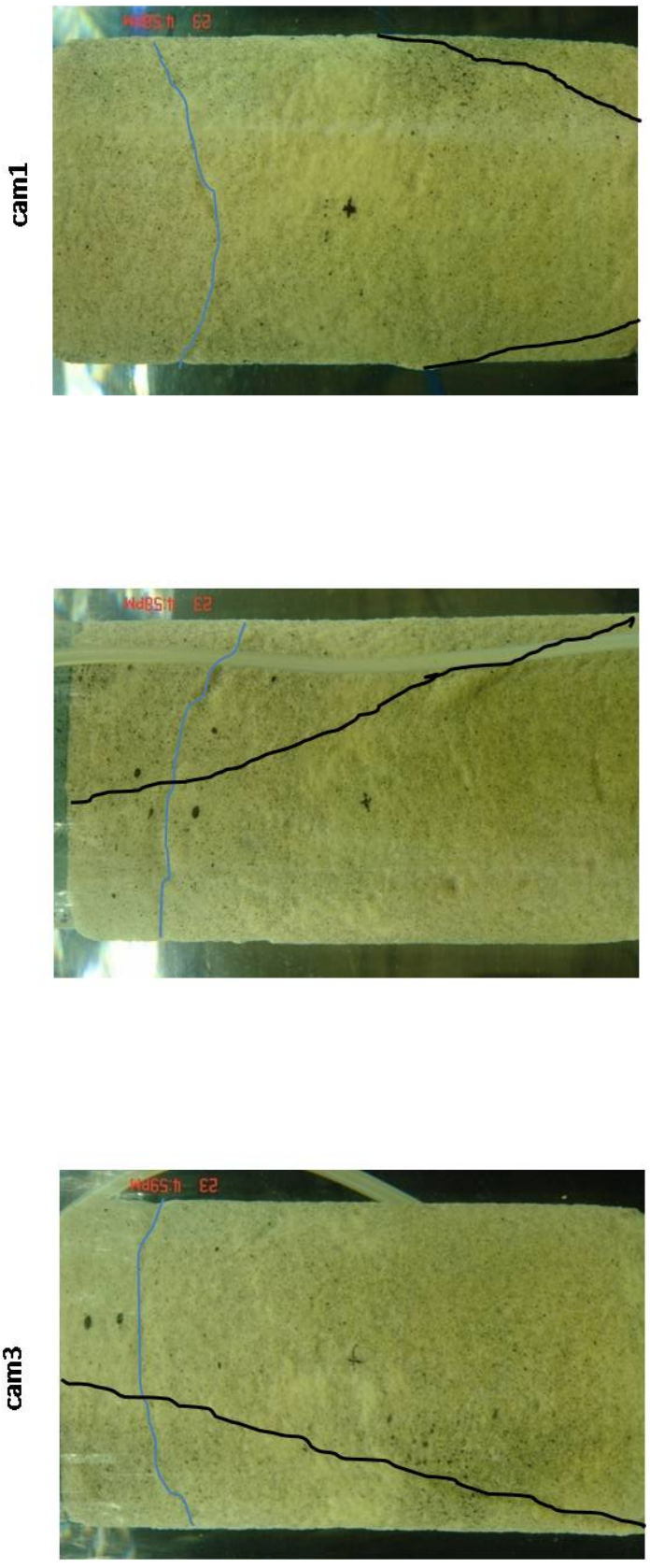

FIGURE 5.20: Photographs of the sample tested at 25 kPa taken at the end of the test. The sketches show the positions of shear bands.

5.5.2 Inclination of the shear band

Table 5.1 summarises the inclination of shear band with respect to the horizontal (i.e. the direction of minor principal stress) observed at different confining pressures. The shear band inclination was found to decrease with increasing of confining pressure. The *Coulomb's solution*, the shear band inclination given by $\theta_C = 45^\circ + \frac{\phi_p^{'}}{2}$ was found to overestimate the shear band angle. The *Roscoe's solution*, the shear band inclination given by $\theta_R = 45^\circ + \frac{\psi}{2}$ (where ψ was calculated using the relation: $\sin\psi = -\frac{\delta\varepsilon_a^p + 2\delta\varepsilon_r^p}{\delta\varepsilon_a^p - \delta\varepsilon_r^p}$ (Houlsby, 1991; Vaid & Sasitharan, 1992)) was found to underestimate the shear band angle. The *Aurthur's solution*, the shear band inclination given by $\theta_A = 45^\circ + \frac{\phi_p^{'} + \psi}{4}$ was found to match the observed shear band inclination.

TABLE 5.1: Inclination of the shear band

Test (Series B2)	Effective Cell pressure (kPa)	θ_B	$\phi_p^{'}$	ψ at $\phi_p^{'}$	$\theta_C = 45° + \frac{\phi_p^{'}}{2}$	$\theta_R = 45° + \frac{\psi}{2}$	$\theta_A = 45° + \frac{\phi_p^{'}+\psi}{4}$
IRRS-1	12.5	74	62.8	45.1	76.4	67.6	72.0
IRRS-2	25	70	59.2	38.5	74.6	64.3	69.4
IRRS-3A	50	67	52.9	33.4	71.5	61.7	66.6
IRRS-3B	50	68	53.9	27.5	72.0	58.8	65.4
IRRS-4	100	65	53.6	28.7	71.8	59.4	65.6

5.6 Deformation characteristics of a pluviated sample

Figure 5.21 shows the stress ratio q/p' and average volumetric strain plotted against global axial strain, and also local axial strain plotted against global axial strain for a pluviated samples of LBS tested at a cell pressure of 50 kPa. Figure 5.22 shows the surface areas of the sample covered in the image analysis. The displacement vectors and strain fields for the initial deformation steps are shown in Figure 5.23 and Figure 5.24. Significant non-axisymmetric behaviour can be seen initially. As deformation increases, the effect of the end restraints became more significant and barreling was observed. The subsequent evolution of strain fields shows that the strain concentrates around the mid-height of the sample (Figure 5.25). While the central part of the sample is experiencing large strains, the upper and lower parts are undergoing very small strains. Figure 5.26 shows the photographs of the sample taken at the end of the test.

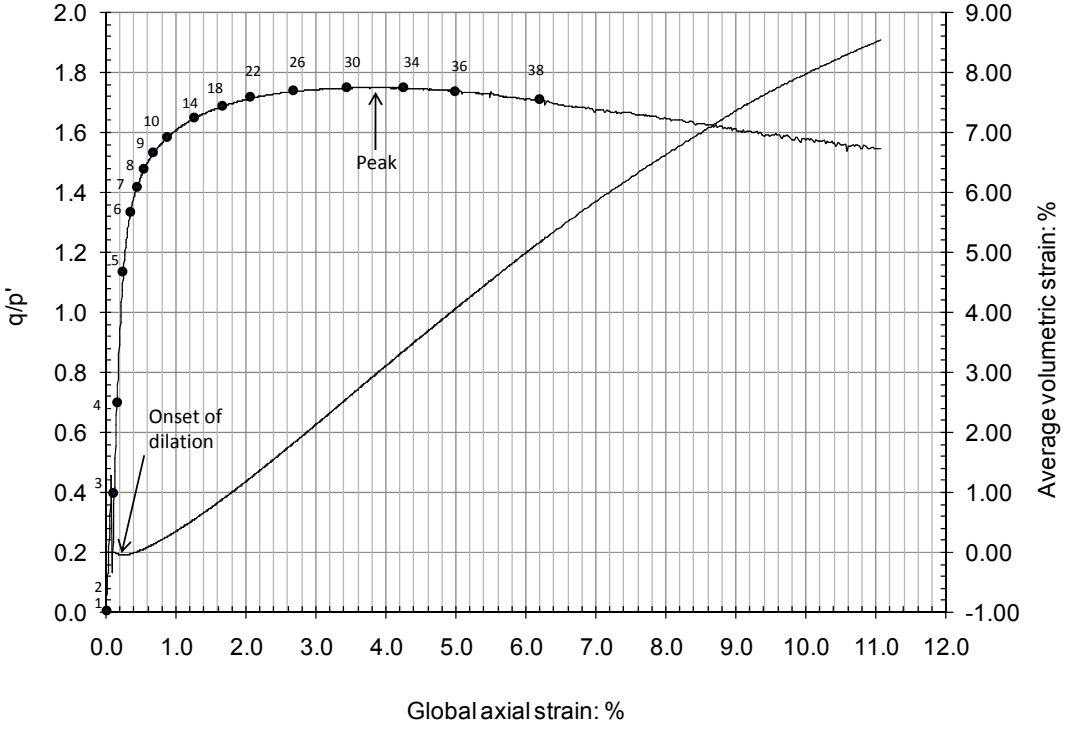

(a)

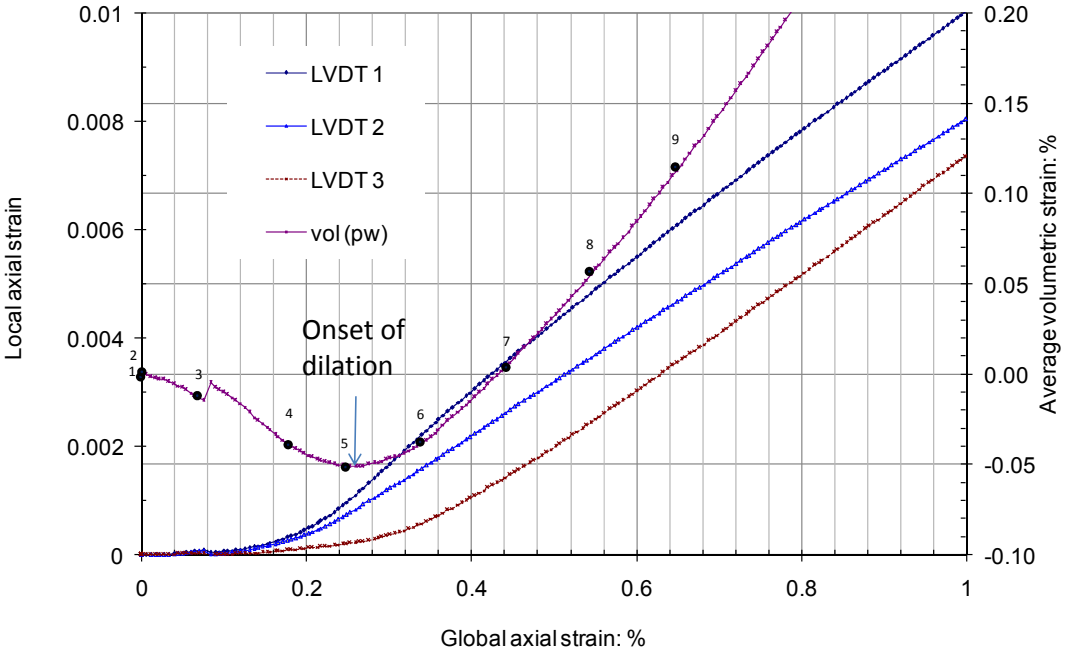

(b)

FIGURE 5.21: (a) Stress ratio, q/p', and average volumetric strain plotted against global axial strain, and (b) local axial strain and average volumetric strain plotted against global axial strain, for a pluviated LBS sample tested at 50 kPa effective cell pressure

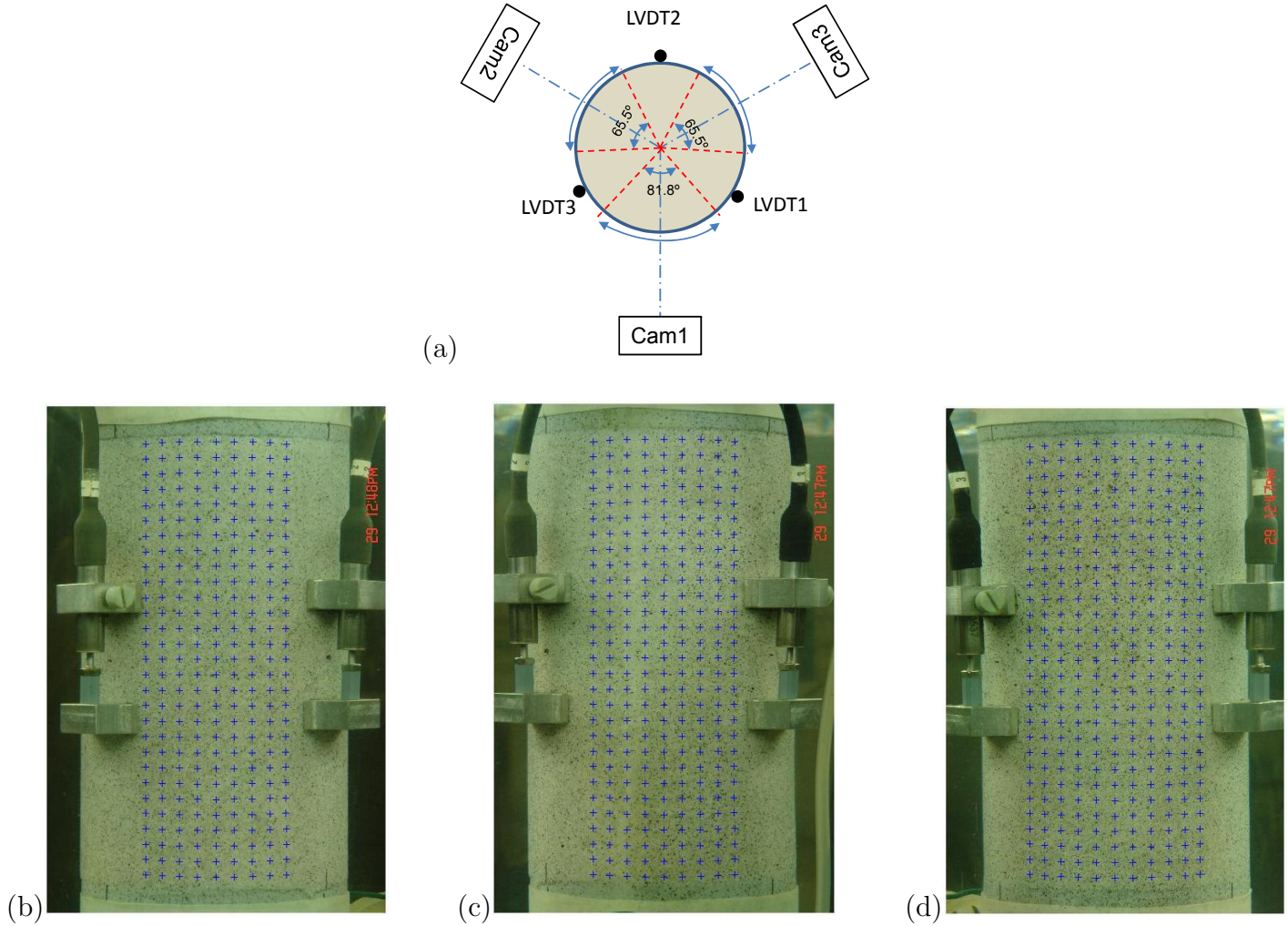

FIGURE 5.22: Cross-sectional view (a), and Measurement points shown in the images (represented by '+' symbols): (b)Cam3 (c) Cam2, and (d) Cam1, for the pluviated LBS sample tested at 50 *kPa* effective cell pressure

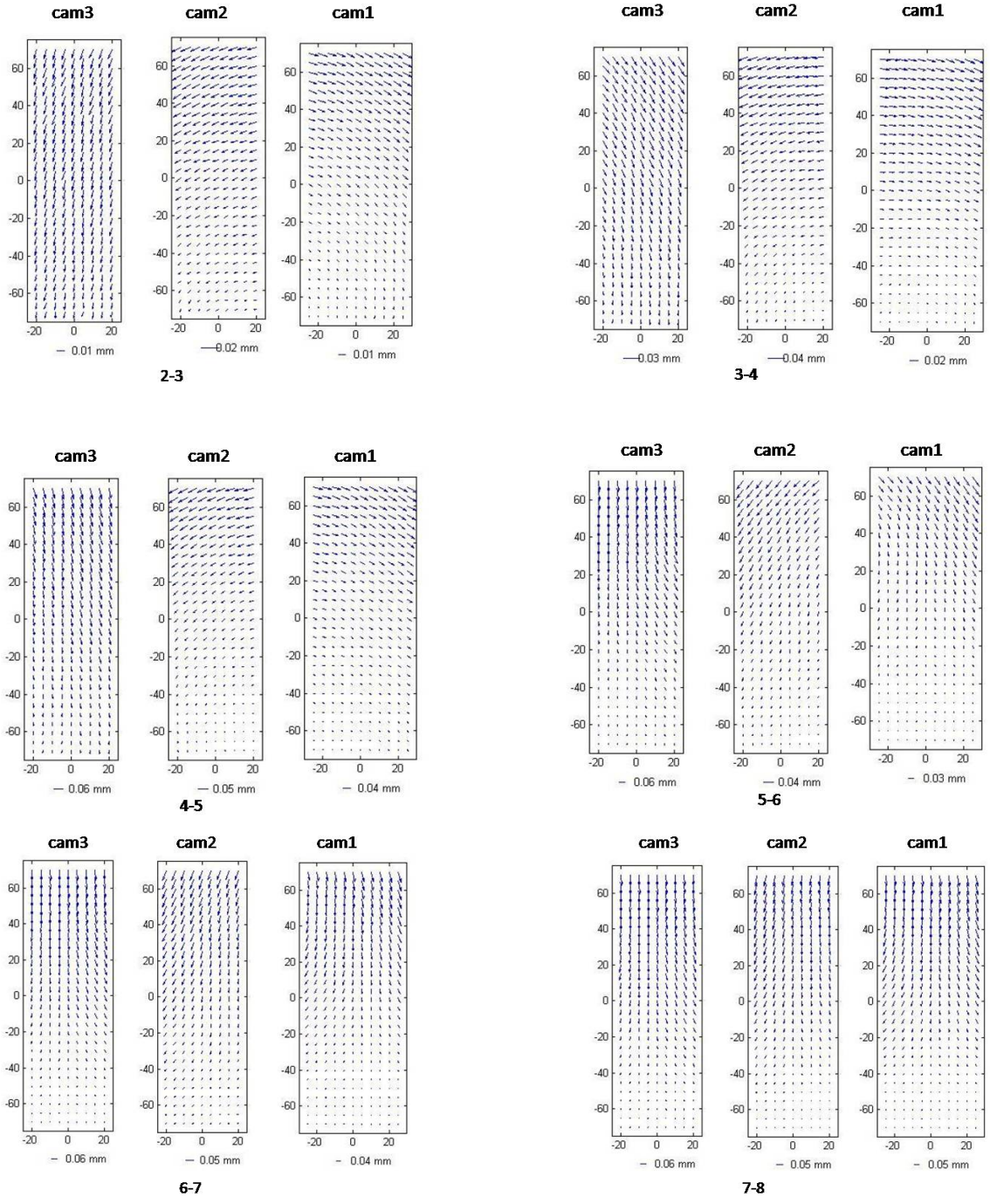

FIGURE 5.23: Displacement fields for pluviated sample of LBS tested at 50 kPa effective cell pressure

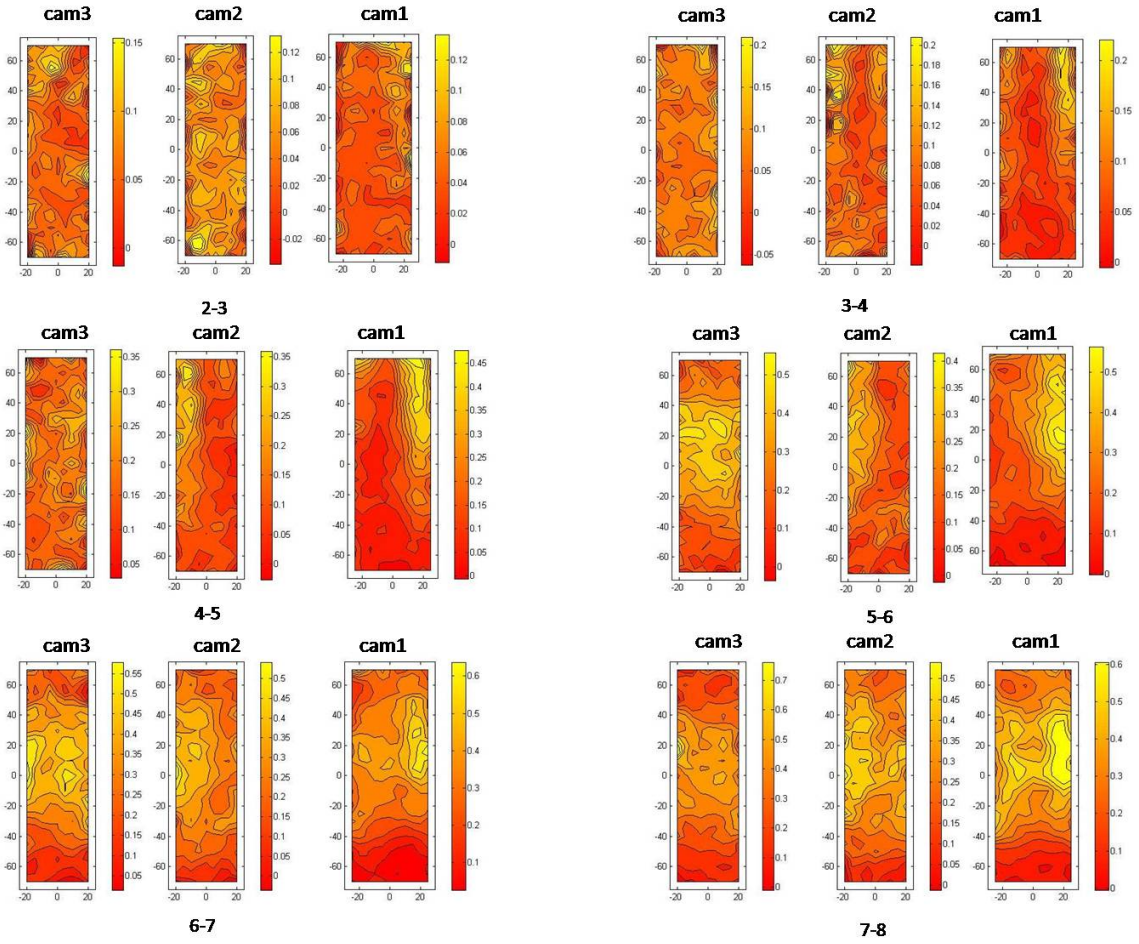

FIGURE 5.24: Strain fields for pluviated sample of LBS tested at 50 *kPa* effective cell pressure

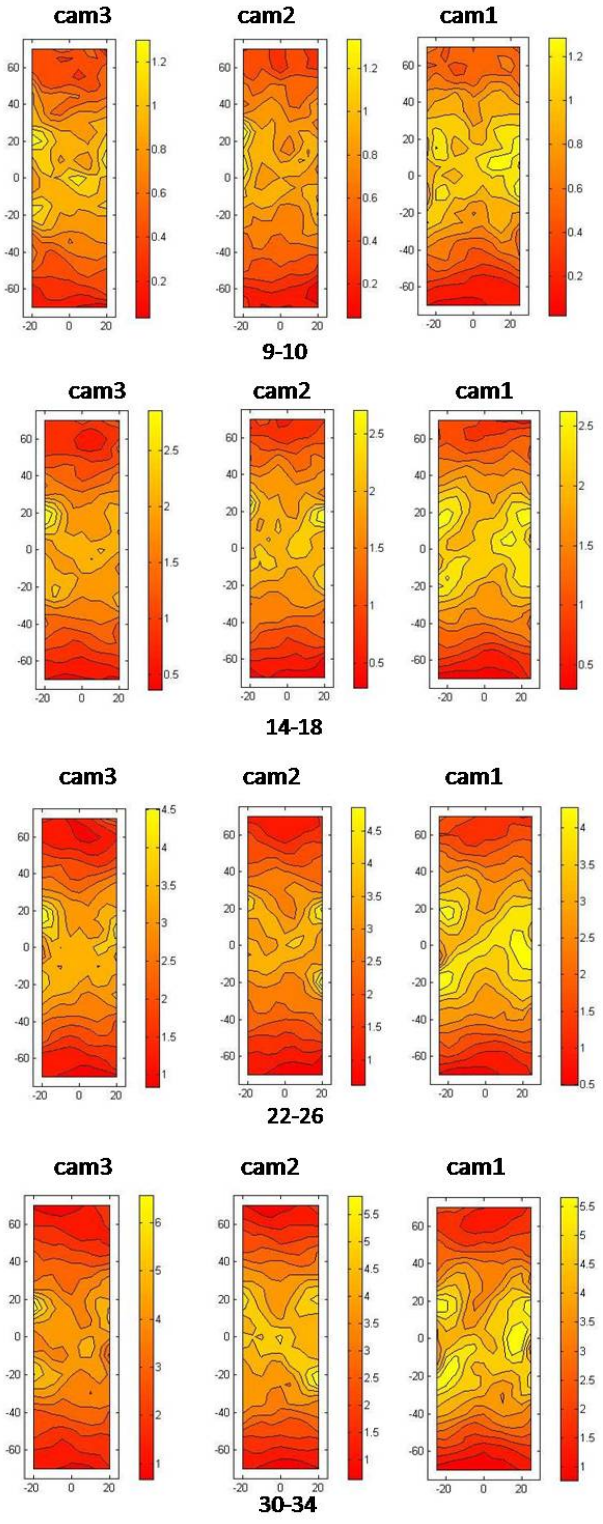

FIGURE 5.25: Strain fields for pluviated sample of LBS tested at 50 kPa effective cell pressure

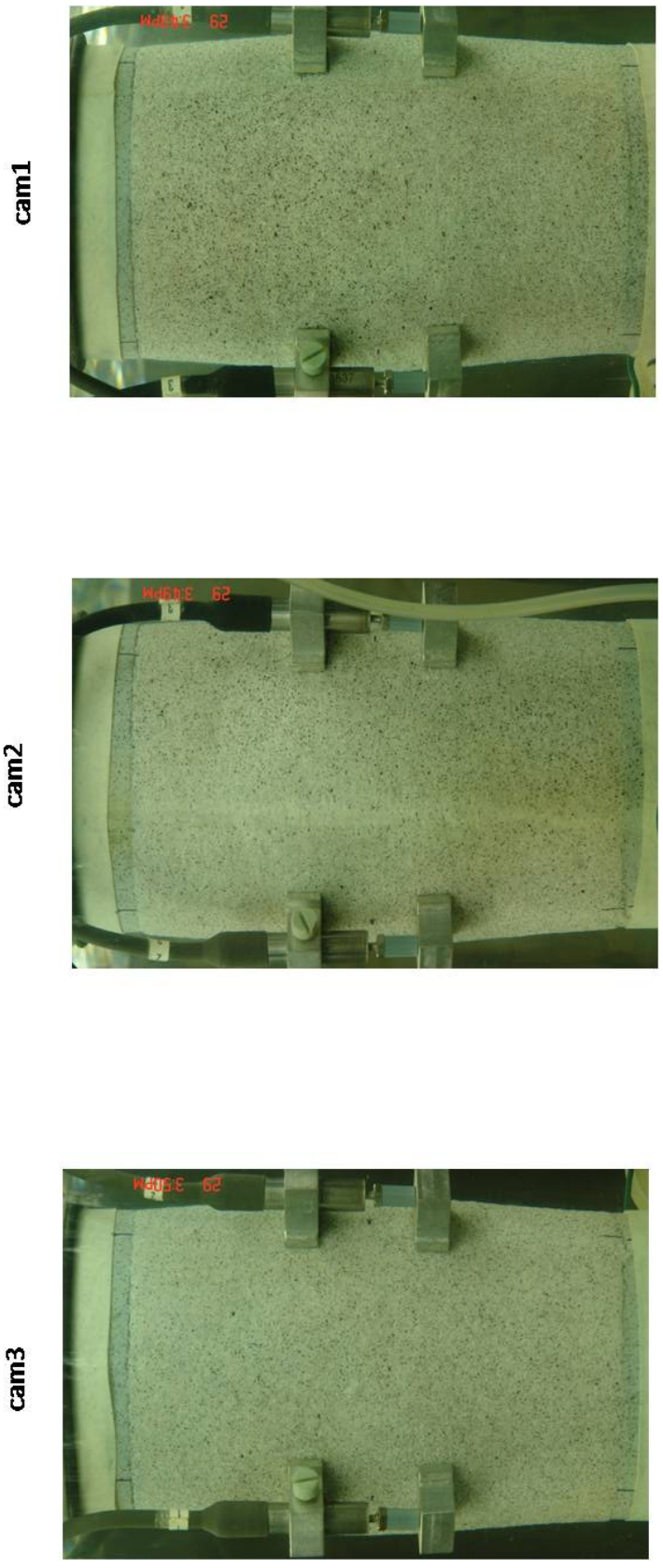

FIGURE 5.26: Photographs of the sample taken at the end of the test.

Table 5.2 summarises the slenderness ratio, maximum stress ratio, onset of dilation, maximum dilatancy rate with respect to global and local axial strain and probable critical state for intact RSS samples and a pluviated LBS sample, the displacement and strain fields of which are presented in this chapter.

TABLE 5.2: Slenderness ratio, maximum stress ratio, onset of dilation, maximum dilatancy rate and critical state for intact RSS and pluviated LBS samples

Test	Effective cell pressure	$\frac{H_0}{D_0}$	At $(q/p^{'})_{max}$						At onset of dilation			At d_{max}			At critical state
Series B2	kPa		η	Global axial strain: %	Av. local axial strain:%	Vol. change, dilation +ve		d	η	Global axial strain: %	Av. local axial strain:%	η	Global axial strain: %	Av. local axial strain:%	η
Intact RSS						mm^3	%								
IRSS-1	12.5	2.49	2.53	0.49	-	863	0.13	1.24	2.10	0.25	-	2.40	0.52	-	1.79
IRSS-2	25	2.49	2.40	0.50	-	1116	0.16	1.05	2.03	0.25	-	2.36	0.53	-	1.67
IRSS-3A	50	2.13	2.17	0.69	0.25	-	-	0.90	1.87	0.45	0.12	2.13	0.73	0.25	1.75
IRSS-3B	50	2.55	2.21	0.66	0.26	1439	0.20	0.73	1.90	0.34	0.09	2.19	0.83	0.38	1.47
IRSS-4	100	2.51	2.20	1.11	0.61	2744	0.43	0.76	1.77	0.46	0.14	2.13	2.54	1.97	-
Pluviated LBS															
PLBS-1	50	2.13	1.74	3.64	3.50	15797	2.75	0.49	1.20	0.27	0.08	1.74	3.36	3.23	1.52

5.7 CT examination of a sheared sample

The image-based system described in chapter 4 provided information about the evolution of deformation and the shear band patterns evident on the surface of a sample. To reveal the shear band patterns inside the the intact sample tested at 50 *kPa* cell pressure, (image analysis results presented in the section 5.3, Test IRSS-3A (Series B2)), CT analysis of the sample was carried out after the test (see Appendix D for a brief description of the CT technology and equipment).

5.7.1 Impregnation of a tested sample

To preserve the grain structure, the sample was impregnated with 4 % Polyvinyl Acetate (PVA) solution using the method of Cresswell & Powrie (2004). This was done when the sample was inside the cell with the cell pressure on, so as to maintain a similar effective stress throughout the process. Once the sample had been impregnated, the cell pressure was turned off and the sample removed from the cell. Figure 5.27(a) shows the PVA impregnation process. The PVA solution was flushed through the sample from the bottom to the top. The cell pressure was kept at about 50 *kPa*. About 2 litre of PVA solution was passed through the sample. The next step was to dry the sample (Figure 5.27(b)). To speed up the drying process, the top end of the sample was exposed to the air and the bottom end of the sample to a small vacuum (-5 to -10 *kPa*).

The sample was monitored continuously during the impregnation and drying process using the image-based system described in the previous chapter.

Figure 5.28 shows the variation of cell pressure and pore pressure during the impregnation process. Readings from a load cell, an external displacement transducer, and a local LVDT are shown in the Figure 5.29 (only one LVDT reading is presented because the other two LVDTs were already out of range). Slight extension of the sample was observed during the process. Images of the sample were taken with a camera; the image analysis result for the images taken at the beginning and end of the impregnation process is shown in Figure 5.30. As can be seen, no significant movements and deformation were observed during the PVA impregnation process.

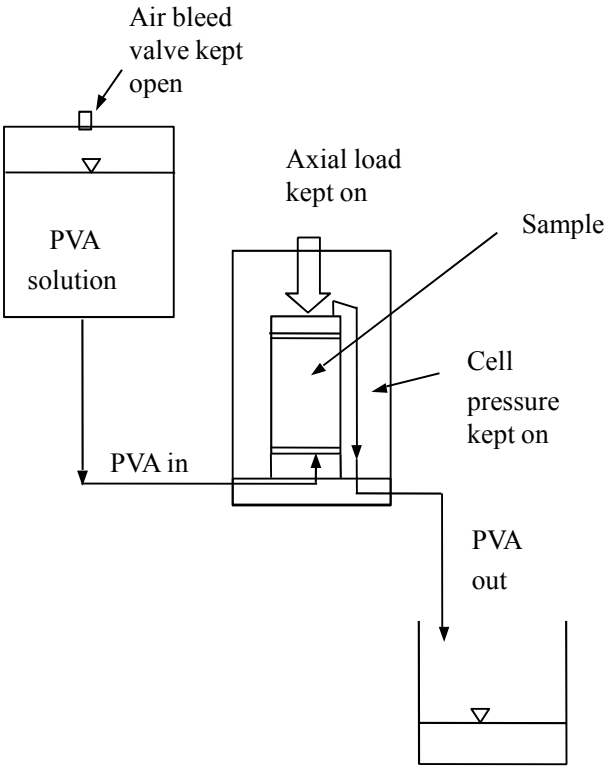

(a)

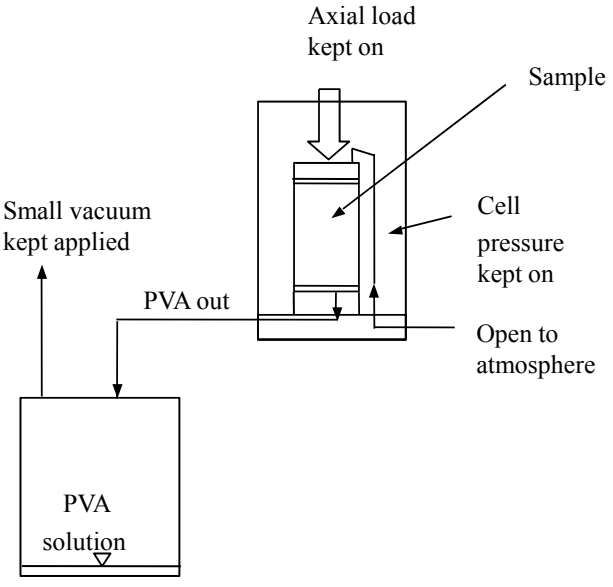

(b)

FIGURE 5.27: PVA Impregnation process

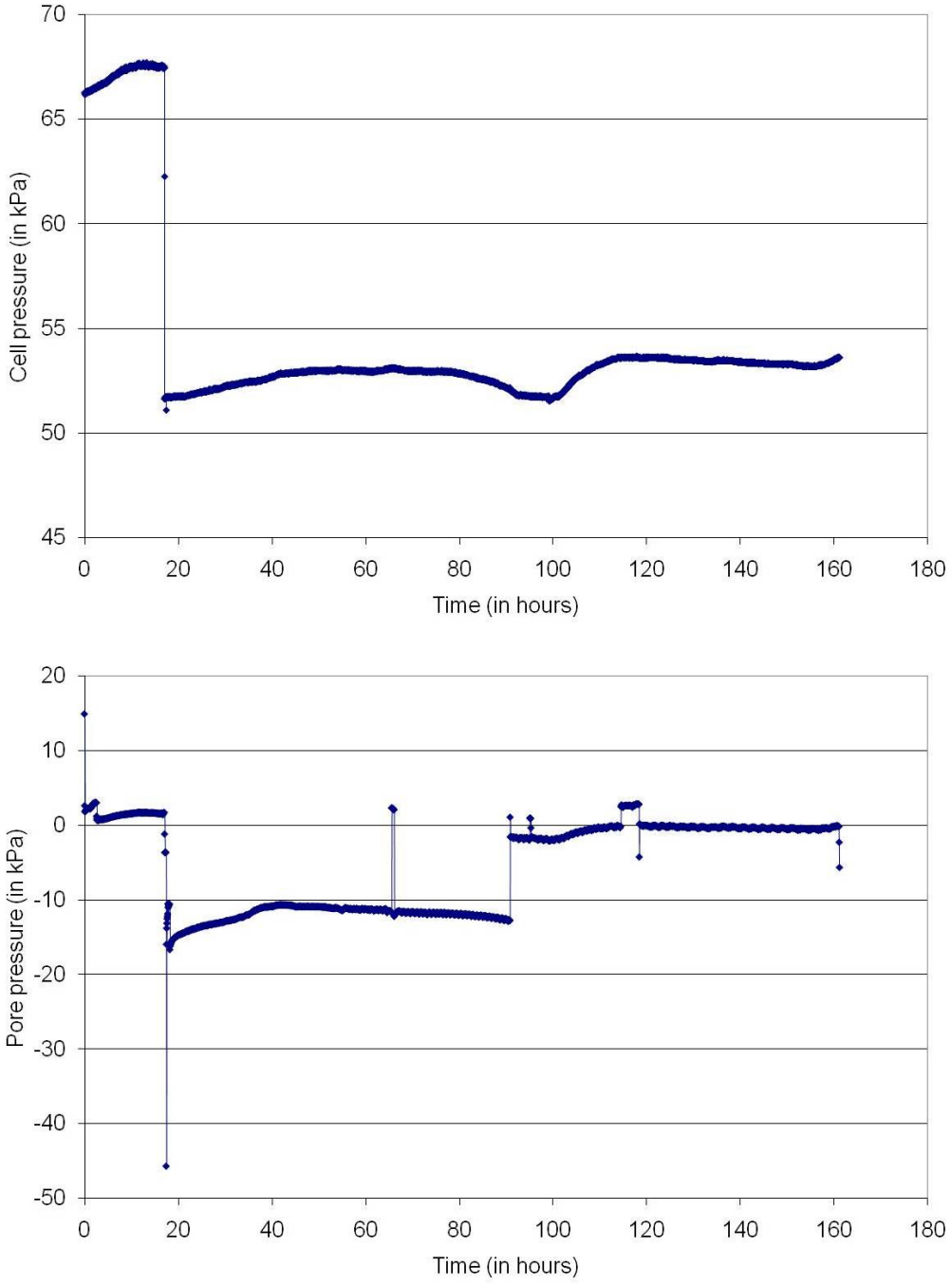

FIGURE 5.28: Cell pressure and pore pressure variation during the impregnation process

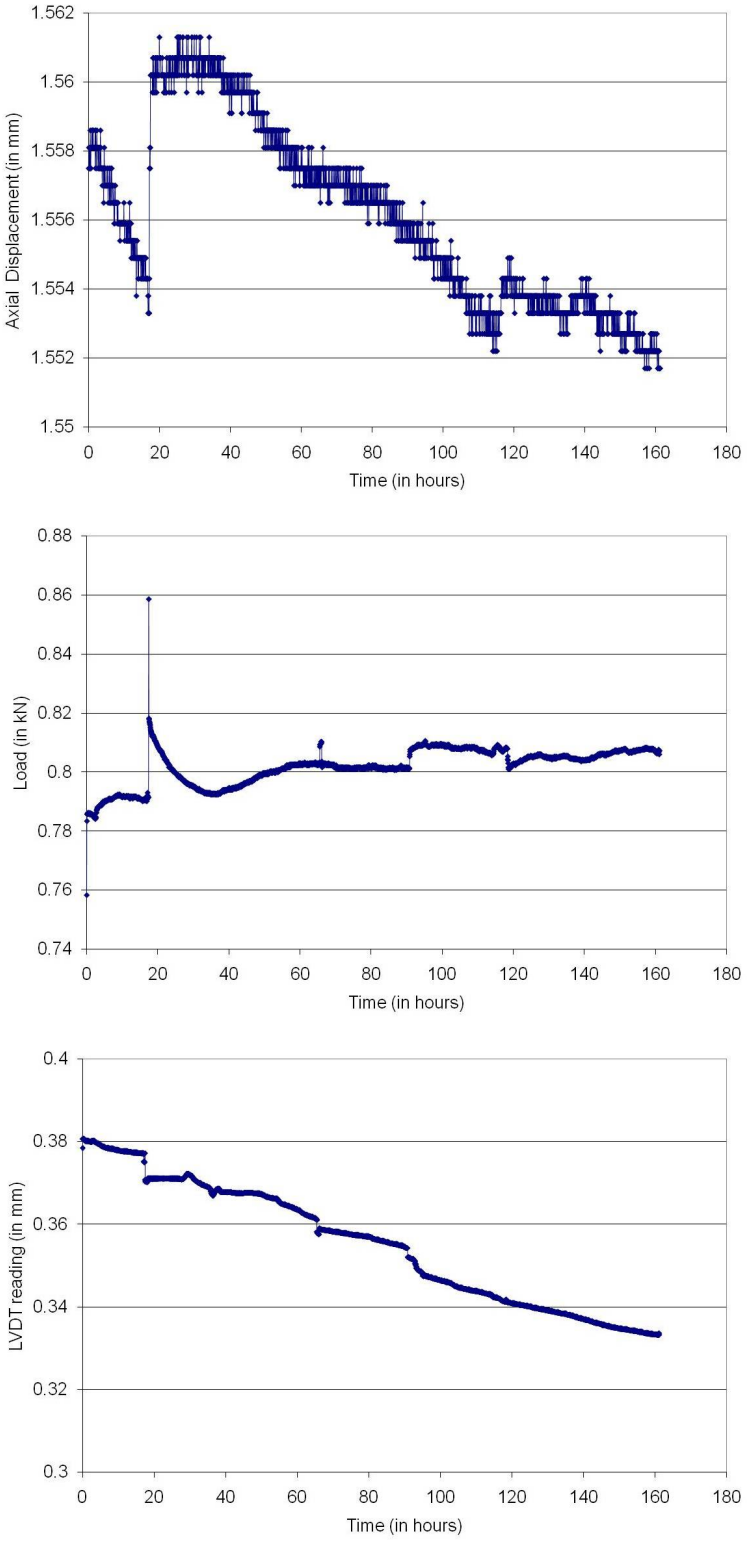

FIGURE 5.29: Axial displacement, load cell and a LVDT recording variation during the impregnation process

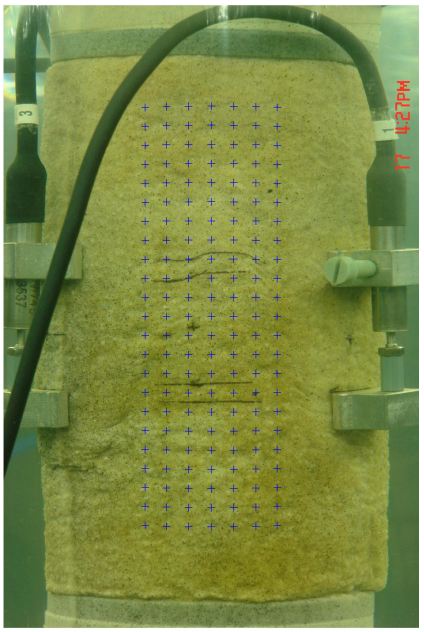

(a)

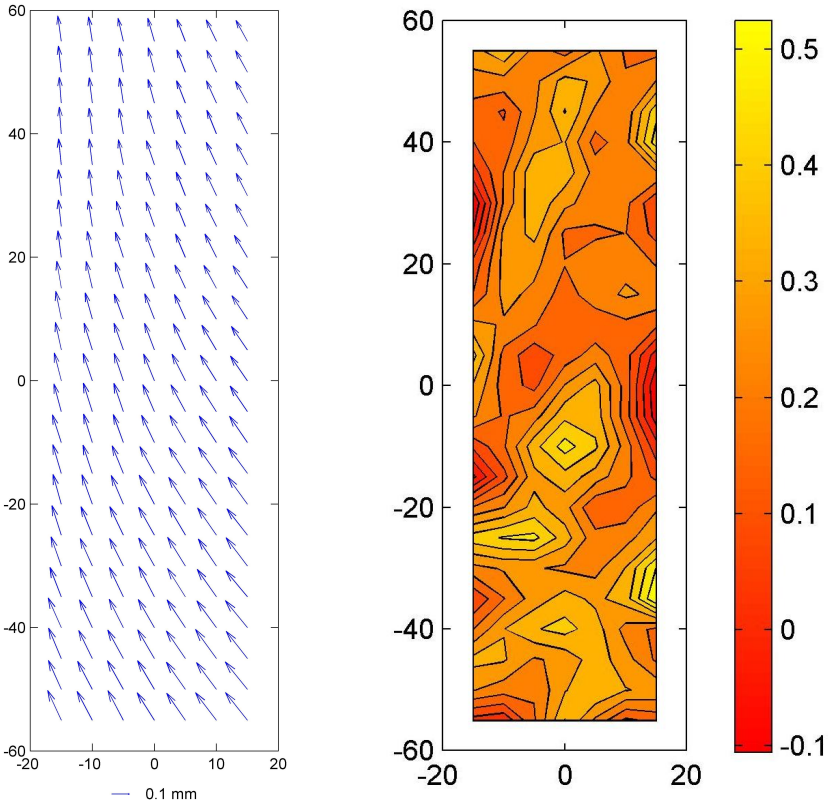

(b) (c)

FIGURE 5.30: (a) Measurement points; (b) Displacement field and (c) Maximum shear strain field during the impregnation process

5.7.2 CT Results

Due to a limitation on sample height of 100 mm in the CT scanner, the top and bottom of the impregnated sample were scanned separately. Figure 5.31 and Figure 5.32 show the CT images of the top and bottom portions of the sample. There is some overlap, containing the middle portion of the sample between these images. The test was terminated at a global axial strain of 3.82 % (Figure 5.2). Since the diameter of the sample is 70 mm diameter, it is not possible to identify individual sand grains. However, shear bands developed in the sample are visible from the intensity variation due to the density change between the shear bands and their surroundings. Darker regions within the CT image represent the less dense material on the shear bands. The shear bands locations and geometry observed from the CT images are in agreement with the results of image analysis presented in Figure 5.6.

There is no clear evidence of any density variation outside the shear band, nor of the effect of end restraints. The trace of the shear band is not perfectly straight, which means that the localisation is not perfectly planar. The orientation of shear band can be calculated using these CT results, but the thickness of the shear band is difficult to estimate. It is difficult to guess the initial localisations patterns based on these results as the scan was done at the end of the test. An in situ testing facility would be required to examine the order of localisation patterns as they developed.

5.8 Discussion

The digital image-based technique described in chapter 4 was used to study the deformation characteristics of intact RSS samples at cell pressures of 100 kPa or below. The initial deformation, the onset of localisation, near-peak and post-peak deformation were characterised.

Initial deformation of the samples was found to be quasi-homogeneous. This stage corresponds to micro-slips and deformation between sand grains. Localisation was found to initiate by prior smooth heterogeneities. Such a localisation process was also observed by Desrues (1998) and he described it as “ a kind of condensation

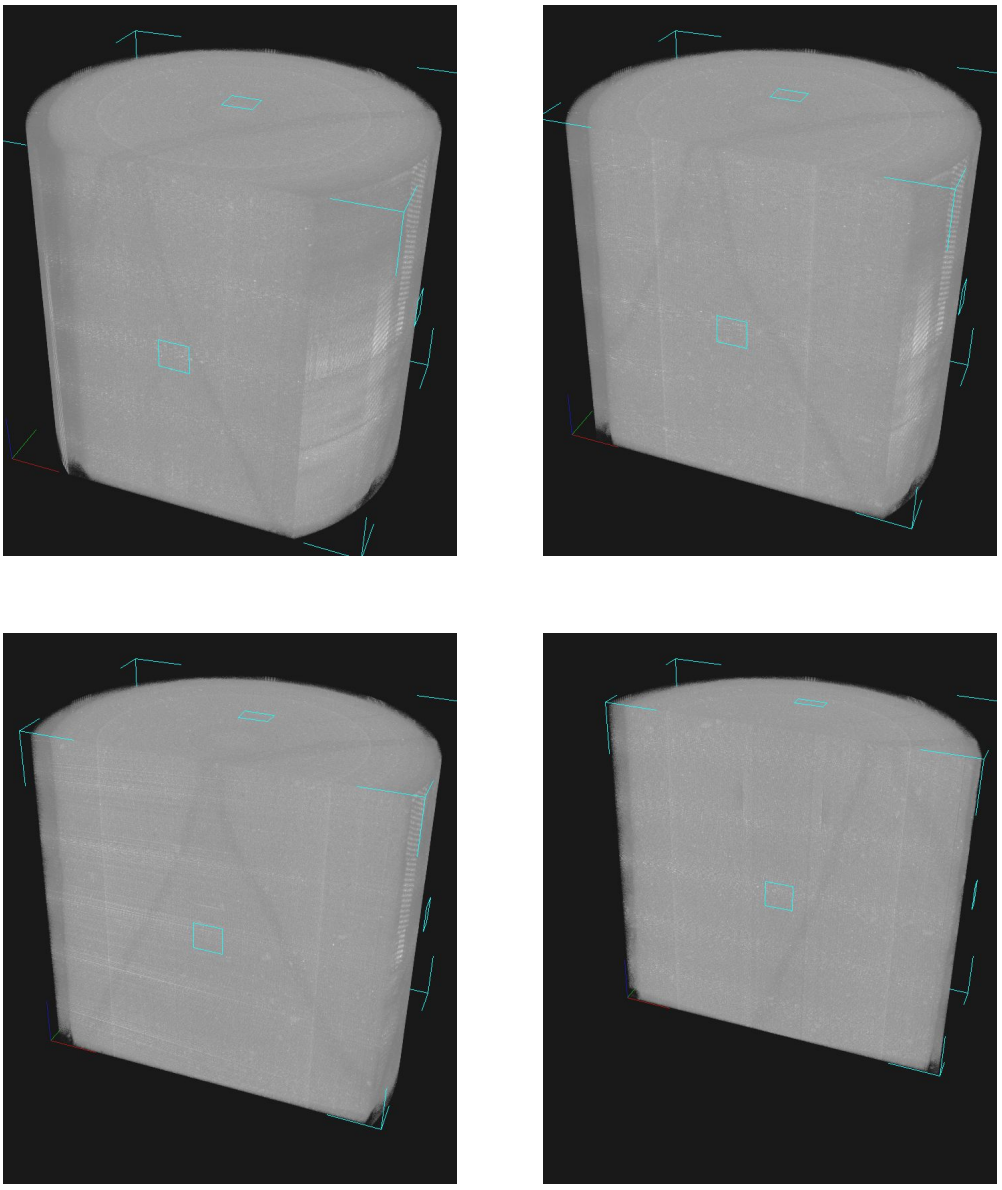

FIGURE 5.31: CT images showing sections of the top portion of the sample

of the heterogeneities ". A progressive delay in the onset of localisation with increasing confining pressure was observed.

Strain localisation was found to initiate prior to the mobilisation of peak stress ratio. The instant of onset of localisation identified from the study of strain fields did not coincide with the divergence of the local LVDT traces. It was found to occur earlier. The onset of localisation coincided closely with the onset of dilation. This observation is in contrast with that by Cresswell & Powrie (2004); they reported the divergence of the displacements measured by the local strain LVDTs

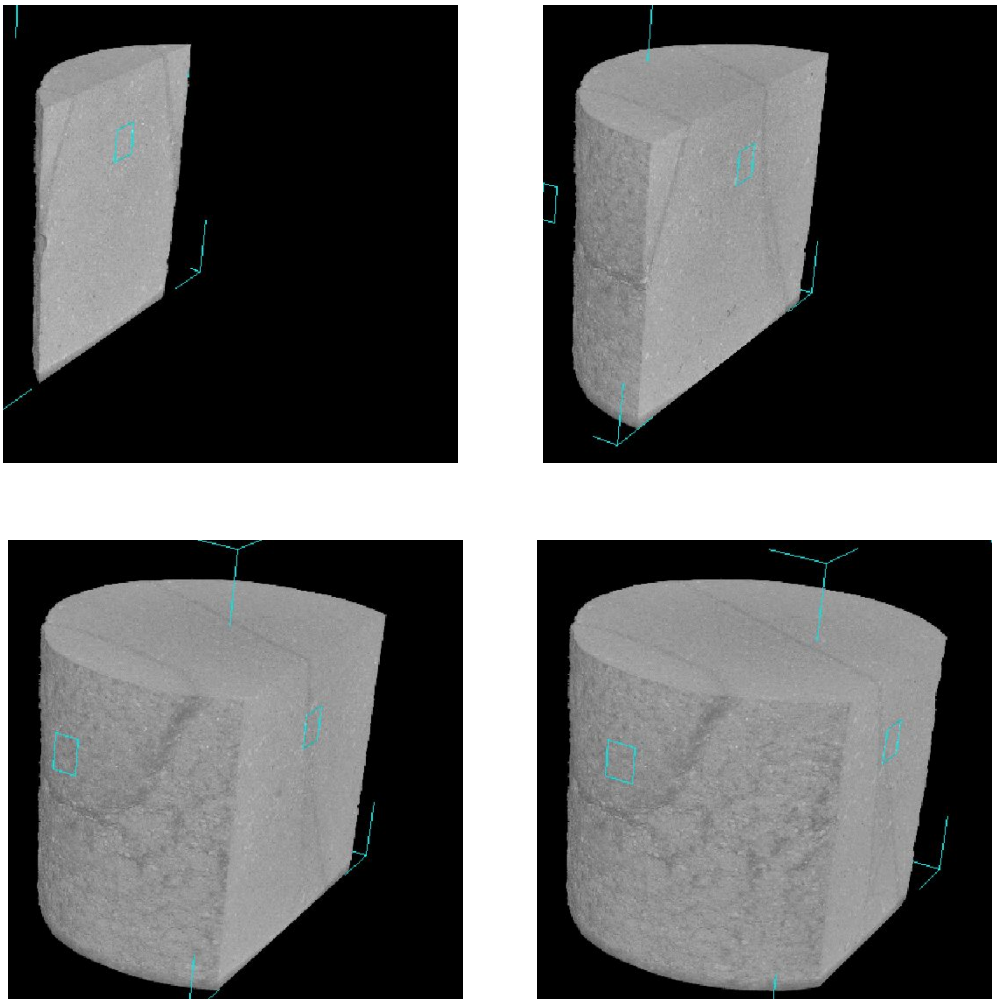

FIGURE 5.32: CT images showing sections of the bottom portion of the sample

coincided closely with the onset of dilation, and considered it as an indication of the initiation of localisation.

The achievement of peak stress ratios was found to occur at progressively greater global axial strain with increasing confining pressures. The peak strengths were achieved immediately after onset of localisations at 12.5 and 25 kPa confining pressures. Well marked peaks in stress-strain curves were observed in both cases. At 50 and 100 kPa confining pressures, however, the achievement of peak strengths were further delayed after the onset of localisations. This can be attributed to the different localisation patterns observed in the near-peak regime. At 12.5 and 25 kPa, relatively well-defined localisation patterns were observed. The well marked peaks, therefore, can be considered as the signature of an established strain localisation system over the samples. This suggests that the localisation patterns and their evolution in the near-peak regime determine the strength and strain at peak

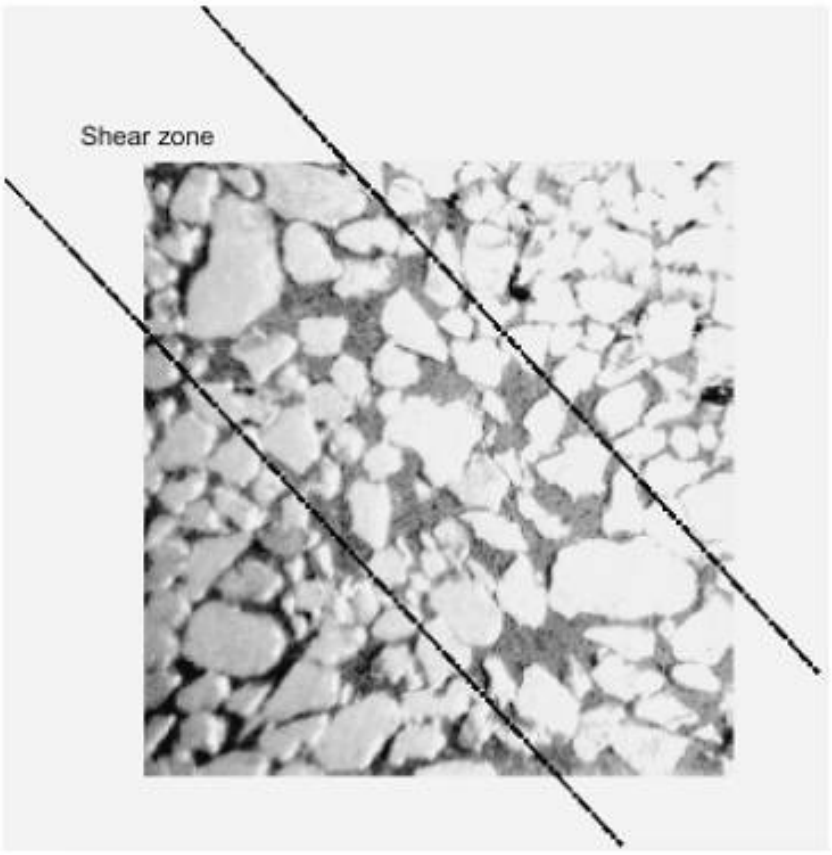

FIGURE 5.33: Thin section of the shear zone showing macrovoids (Cresswell & Powrie, 2004)

and, therefore, the period of strain-hardening (i.e. of increasing stress ratio, q/p'). The above observations are consistent with the through-out-the-sample disruption and formation of proto-shear planes in samples taken to ultimate strength at high cell pressures observed in thin-sections examinations by Cresswell & Powrie (2004).

In the post-peak regime, strain-softening (i.e. of decreasing stress ratio, q/p') rate was found to depend on the formation, distribution, and propagation of shear bands. At 12.5 and 25 kPa, the marked strain-softening response in the post-peak regime were due to the continuous localised growth of shear bands. At 50 and 100 kPa, a more diffused localisation pattern was observed, thus giving a gentle strain-softening response.

The achievement of constant strength at constant dilation rate at large strain is

regarded as a critical state (Roscoe et al., 1958). CT, thin sections and SEM investigation of shear bands by Alshibli & Hasan (2008), Cresswell & Powrie (2004), Desrues & Viggiani (2004), Oda & Kazama (1998) and Wong (2001) concluded that the sheared material inside the shear band does approach a limiting value. In the intact samples, the achievement of such a state with respect to global axial strain were found to be delayed with the increase of confining pressure.

The intact samples tested in chapter 3 were relatively short, $H_0/D_0 \approx 2$, therefore the shear band was found to intercept the platens. The intact samples tested in this chapter were of relatively high slenderness ratios, $H_0/D_0 \approx 2.50$ (except one sample tested at 50 kPa (Test IRSS-3A), in which case $H_0/D_0 \approx 2.15$). The adequate length of the samples provided enough room for shear band to develop without intercepting both the top and bottom platens, except at 12.5 kPa in which test reflections of the shear band on the top and bottom platens were observed (Figure 5.19). A single shear band was observed at the end of in the tests conducted at 25 kPa (Test IRSS-2)(Figure 5.20) at 50 kPa (Test IRSS-3B), but at different orientations with respect to the horizontal and the shear band intersected the free boundary sides of the cylindrical sample. Surprisingly, conjugate shear bands were observed in the another test conducted at 50 kPa (Test IRSS-3A) (Figure 5.7). Despite the increase of the slenderness ratios, different strengths were mobilised at critical states in the intact samples of RSS (Table 5.2). Also, the critical state strengths were significantly higher than the reconstituted samples (cf. Table 5.2 and Table 3.1). They are also much higher than those estimated from a probable critical angle (assuming $\phi'_{cv} = 31$ degrees and using $\sin\phi'_{cv} = 3M/(6+M)$; M is approximately 1.24 and the same value M was observed by (Cresswell & Powrie, 2004) for the pluviated RSS samples). Cresswell & Powrie (2004) also reported two different values of M for intact and pluviated samples of RSS (M (intact) = 1.41, M (pluviated) =1.24). The difference was found to be much larger in this study, which is possibly due to the low confining pressure involved, that promotes more nonuniform deformation of the sample.

To better understand the strengths mobilised at critical states in the intact and pluviated samples, the effects of the development of different kinematically admissible deformation mechanisms on the post-peak regime are required to be considered. Figure 5.34 shows the stress ratio, q/p', as a function of orientation for single and conical shear bands, from limit equilibrium condition assuming the

value of ϕ'_{cv} as 31°. As can be seen, the mobilised stress ratio is highly dependent on the orientation of the shear band. Wong (1999) have considered additional kinematically admissible modes (Figure 5.35 (a)) and demonstrated that the strengths mobilised can be even much higher than the true critical state value (Figure 5.35 (b, c)). Furthermore, any complex localisation mechanism developing within a sample (for example that illustrated by Desrues et al. (1996) using CT, Figure 5.36) may requires additional consideration. Although such a mechanism was not clearly evident from the surface deformation measurements of the intact and pluviated samples and the CT analysis of the intact sample, it could be of relevance to test carried out at higher pressures and in the pluviated samples. At low effective stresses, the change in cross-section area due to formation of a shear band and the additional restraint provided by the rubber membrane could have a significant effect on the mobilised strength (Chandler, 1966), therefore required to be considered for accurate analysis. The effects of nonlubricated end platens also require consideration.

5.9 Conclusions

The image-based measurement technique was used to study deformation characteristics of intact and pluviated samples. It is now possible to characterise complex progressive failure mechanisms. In this way, from the results and discussion presented in this chapter, the following conclusions can be made:

1. The initial deformation of samples before the onset of localisation is quasi-homogeneous.

2. The onset of localisation occurs before the achievement of peak stress ratio but near the onset of dilation. Therefore, localisation is a pre-peak phenomenon. Strain localisation in the hardening regime limits the peak strength.

3. From the onset of localisation to the clear formation of a shear band, localisation characteristics were found to depend on the applied confining pressure. At low confining pressure, the initial localisation was found to concentrate immediately to form a clear shear band. At increased confining pressures,

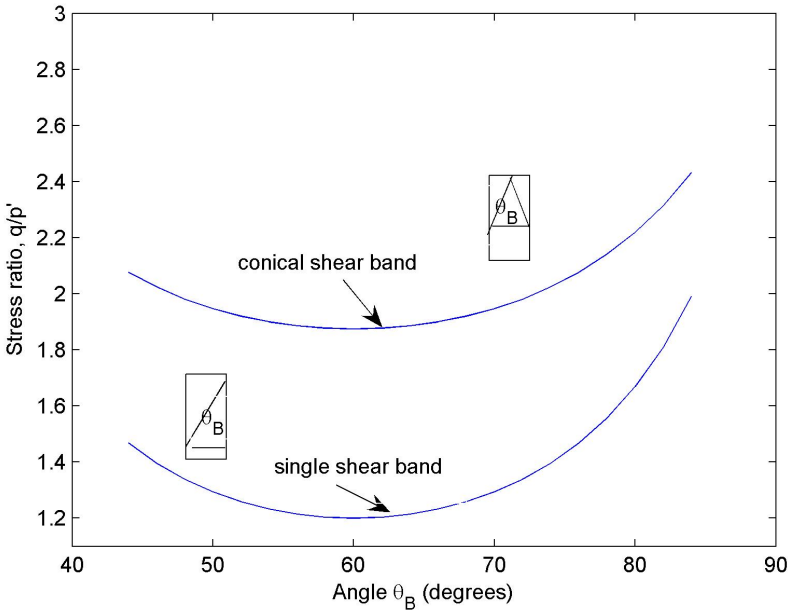

From limit equilibrium condition:
For single shear band, $\frac{\sigma_1}{\sigma_3} = \frac{1+\tan\phi'_{cv}\tan\theta_B}{1-\tan\phi'_{cv}\cot\theta_B}$
For conical shear band, $\frac{\sigma_1}{\sigma_3} = \frac{2\tan\theta_B}{\tan(\theta_B-\phi'_{cv})}$
and $\frac{q}{p'}$ calculated using $\frac{q}{p'} = \frac{3(\frac{\sigma_1}{\sigma_3}-1)}{\frac{\sigma_1}{\sigma_3}+2}$ and the value of ϕ'_{cv} is taken as 31°.

FIGURE 5.34: The stress ratio, q/p', as a function of orientation for single and conical shear bands (inspired by (Wong, 1999))

localisation does not concentrate immediately into a shear band. The localisation zones spread out to wider area of the sample during the shearing process before the deformation localises into a clear shear band. This explains the transition of deformation characteristics from ductile to brittle response with decreasing confining pressure.

4. Different critical state strengths for intact and pluviated samples are due to the deformation characteristics which resulted into different kinematically admissible deformation mechanisms.

5. The image-based measurement system was used to monitor the impregnation process of the sample and to confirm that any disturbance in the soil structure during this process was minimal.

6. In the context of the rapid development of advanced constitutive models for geomaterials in recent years, the displacement and strain fields presented

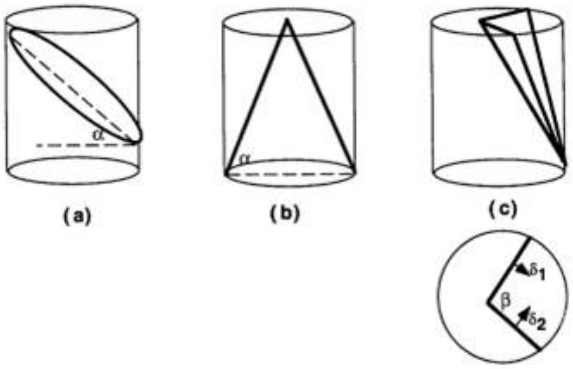

(a)

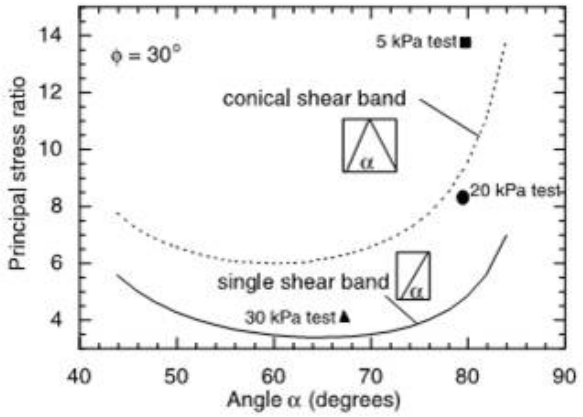

(b)

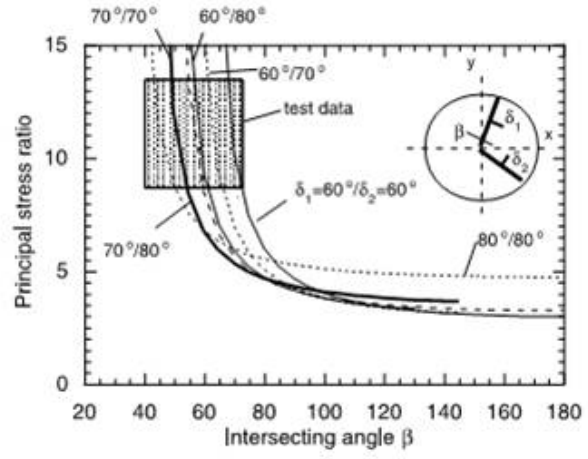

(c)

FIGURE 5.35: (a) Kinematically admissible modes, (b) Principal stress ratio as a function of orientation for single and conical shear bands, and (c) Principal stress ratio as function of wedge configuration for a multiple shear band (Wong, 1999)

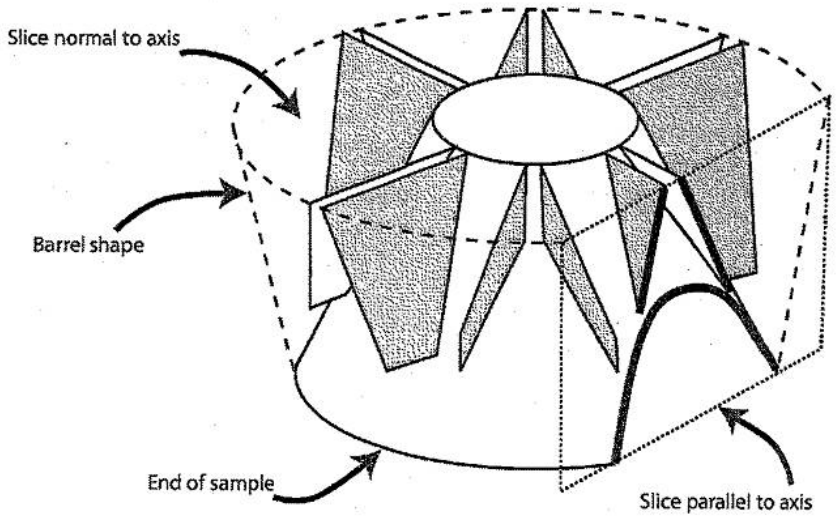

FIGURE 5.36: Schematic representation of geometry developed in triaxial axisymmetric test as inferred from tomodensitometry study. Diagram show radial paired features and conical feature. These features intersect the top surface of the specimen as paired radial lines and their intersection on vertical surfaces sliced parallel to the axis is shown on the right-hand side. (Desrues et al., 1996)

herein will motivate the development of new calibration procedures, and will also be useful to verify the physical basis of such constitutive models.

Chapter 6

Conclusions and future work

6.1 Introduction

This research has investigated the strength and deformation characteristics of intact and pluviated samples of Reigate silver sand in conventional triaxial compression at effective cell pressures from 12.5 to 100 kPa. New insights were gained regarding the influence of fabric structure on the strength and deformation characteristics at low effective stresses. Chapter 3 focused particularly on understanding the small strain behaviour. LVDTs were used to characterise the initial deformation. The difficulty associated with identifying the onset of localisation by relying on the visual evidence of the divergence of LVDTs was highlighted. The shortcomings of the LVDTs in characterising localised deformation and post-peak deformation were highlighted. To understand the local phenomena occurring at a particulate scale (such as localisation and shear banding) that determine the global response, a new digital image-based deformation measurement system was developed (chapter 4). The effects of refraction were properly taken into account using a ray tracing technique. A digital image correlation routine was developed to analyse the images and characterise the associated deformation. With this development, it is possible to determine accurately onset of localisation and study the deformation in the post-peak regime. Chapter 5 combines the study of localisation and dilation. The role and significance of dilation with respect to the development of localisation in samples were studied. In this chapter (chapter 6), the major results, findings and conclusions are summarised and recommendations for further work are made.

6.2 New techniques developed and specific issues addressed on this study

Using the ray tracing technique, the effects of image distortion due to refraction was properly taken into account and an image-based deformation measurement system for triaxial test was developed. A very close match between LVDTs and the image-based system proves that the system can be reliably used to monitor the surface deformation characteristics of triaxial samples.

A comprehensive study of dilation and localisation together, which was not possible until now with conventional triaxial test using LVDTs for local strain measurement, was made using the technique developed. The role and significance of dilation in the context of deformation localisation were identified. The applied confining pressure was found to have a significant influence on the initiation and growth of the localisation and on the overall volumetric behaviour of the sample.

New imaging and lighting systems were designed. Arrangements were made to accommodate the cameras and lighting system within the transparent triaxial cell and the loading frame. Furthermore, the use of LVDTs for local axial strain measurement made it possible to compare the LVDT data with the image-based measurement.

In order to conduct triaxial tests at low effective stresses, development of a reliable low pressure application system is vital. The hunting effect was a major problem to resolve. The mechanisms of operation of the cell and pore pressure application equipment required changes to be made to eliminate this effect. The pore pressure was controlled by a GDS advanced pressure volume controller and the cell pressure was applied with an air-water pressure interface system by controlling the air pressure inside the air-bladder. These modifications minimised the hunting effect when two standard GDS pressure/volume controllers were used.

The successful block sampling in the sand quarry and the safe transportation of the sand blocks to laboratory, before sample preparation and strength testing, are the crucial to laboratory testing of intact samples of locked sands. The ease of block sampling and transporting were found to depend on the moisture conditions in the field. Sampling and transporting of sand blocks were found quite difficult in conditions that were too wet or too dry. The rather wet English weather mostly favours the former condition, at least from the experience gained from

this research. Some improvement of the method of Cresswell (2001) was made to enable sampling even in wet field conditions with the use of elasticated tubular bandage. It was found to make the sampling and transportation of the blocks easier, even in wet conditions.

6.3 Comparison of main results with previous work

At low effective stresses, intact samples were found to sustain stress ratios close to peak at the onset of dilation. It highlights the significant effect of the interlocked fabric on the strength deformation behaviour. Test results confirm the results of Cresswell & Powrie (2004).

The test results presented showed that the divergence of LVDTs occurs after the onset of dilation and near the peak. Cresswell & Powrie (2004) observed that the divergence of displacements measured by the local strain LVDTs coincided closely with the onset of dilation. This point was considered as the initiation of localisation. The localisation was found to initiate in this research after the onset of dilation but before the peak strengths was achieved.

The initial deformations of the samples were found to be quasi-homogeneous. This stage corresponds to micro-slips and deformation between sand grains. Localisation was found to initiate by prior smooth heterogeneities. Such a localisation process was also observed by Desrues (1998) and he described it as " a kind of condensation of the heterogeneities ". The progressive delay of onset of localisation with confining pressure was observed.

Different strengths for intact and pluviated samples at the end of shearing, i.e. at possible critical state, were reported by Cresswell & Powrie (2004). They did not identify the effect of different kinematically admissible mechanisms and the difference was mainly attributed to the inability of the triaxial test to reach the true critical state based on the volume change behaviour, as the condition of no volume change was not achieved.

6.4 New findings about soil mechanics and behaviour

At very low strain in the intact samples, as the shear modulus decreases gradually the sample exhibits compression. Compression continues slowly accompanied by a reduction in stiffness, but an acceleration of the rate of compression is associated with a recovery of stiffness back to its initial value. The dip in shear modulus observed at very low strain is linked to the compression of the sample. An obvious yield point can be defined at which (a) the sample stiffness starts to reduce dramatically and (b) dilation starts.

In the intact samples, the peak stress achieved does not correspond to the instant at which the dilation rate is a maximum. Until the onset of dilation, significant contribution is made by the interlocked structure on the mobilised strength, and starts to fall thereafter. From the onset of dilation to the achievement of peak strength, dilation plays an important role in additional strength mobilisation. During this regime, although the dilation makes the contribution of interlocked fabric weaker, the work required to overcome the resistant against it mobilises some additional strength. In the pluviated samples, however, the peak strength corresponds to the instant at which maximum dilation rate is achieved by the samples as in conventional soil mechanics.

The friction angle and rate of dilation at peak were found to depend on stress level. The onset of localisation occurs before the achievement of peak stress ratio but near the onset of dilation. Therefore, localisation is a pre-peak phenomenon. Strain localisation in the hardening regime limits the peak strength.

From the onset of localisation to the clear formation of a shear band, localisation characteristics were found to depend on the applied confining pressure. At low confining pressure, the initial localisation was found to concentrate immediately to form a clear shear band. At increased confining pressures, localisation does not concentrate immediately into a shear band. The localisation zones spread out to wider area of the sample during the shearing process before the deformation localises into a clear shear band. This explains the transition of deformation characteristics from ductile to brittle response with decreasing confining pressure.

Different strengths at the inferred critical state for intact and pluviated samples are due to different post-peak deformation characteristics produced on the triaxial

sample due to the boundary conditions and the soil behaviour. The intact samples failed into with the formation of a single shear bands. The pluviated samples were found to barrel, although clear shear bands were visible at the end of tests at least in the pluviated samples of RSS. The possible different kinematically admissible deformation mechanisms should be taken into account to determine the strengths at the critical state from the triaxial test data.

6.5 Recommendations for future work

The following recommendations for future work are made:

1. The results presented highlight the significant contribution of interlocked fabric on the mobilisation of high peak strength and stiffness. The development of new engineering design models (design methods) are necessary to include the contribution of the interlocked fabric and to exploit the high peak strength and stiffness of this material in design.

2. In this study, SEM examination of the sand particles provided information about the shape and surface textural characteristics. Earlier thin section and CT slice examination provided contact characteristics in 2D. To understand properly the stress-strain behaviour of intact and pluviated samples of Reigate silver sand and to identify the different mechanisms mobilised, it is very important to characterise the microstructure of the samples prior to loading and the evolution of microstructures upon shearing. There is clearly scope to use CT data to study the soil microstructure and characterise it in 3D. 3D characterisation can also provide important information required to represent sand particles more realistically in particle level simulation studies.

3. This work has laid the foundations for the development of nondestructive methods, using ray tracing to resolve the long outstanding problem of refraction in triaxial test. It is now possible to identify the initiation of the localised deformation more precisely than ever before and track its evolution using the digital image-based technique. This work should stimulate further experimental studies that attempt to study strain localisation and related phenomenon in a more comprehensive manner.

4. The image-based measurement technique developed in this study may be useful to provide valuable information about sample behaviour for calibration of constitutive models. Based on the observed displacement and strain fields, instead of the current practice of a more global approach mainly based on boundary measurement or measurement made at only limited points on the surface of the sample using local instrumentation, such an approach will represent the real material behaviour.

Appendix A

Calibration of Transducers

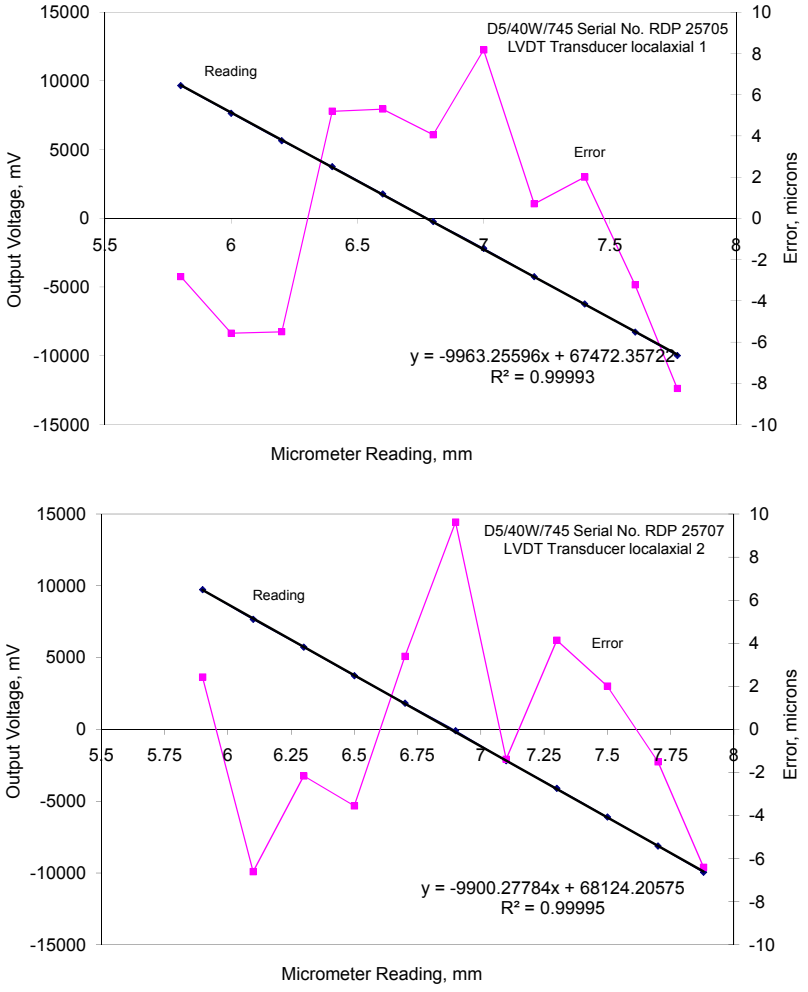

FIGURE A.1: Calibration results of the local axial LVDTs 1 and 2

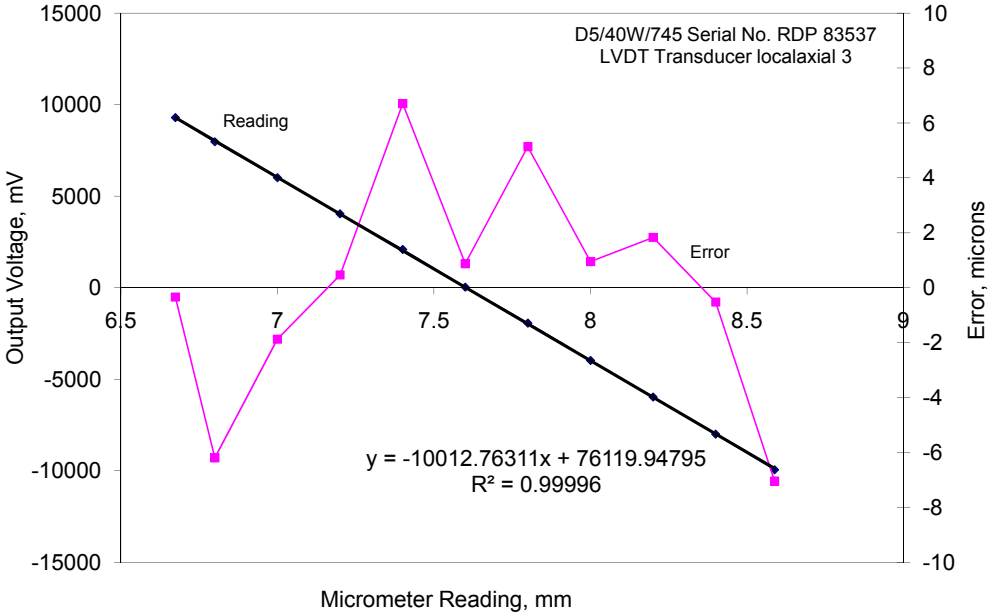

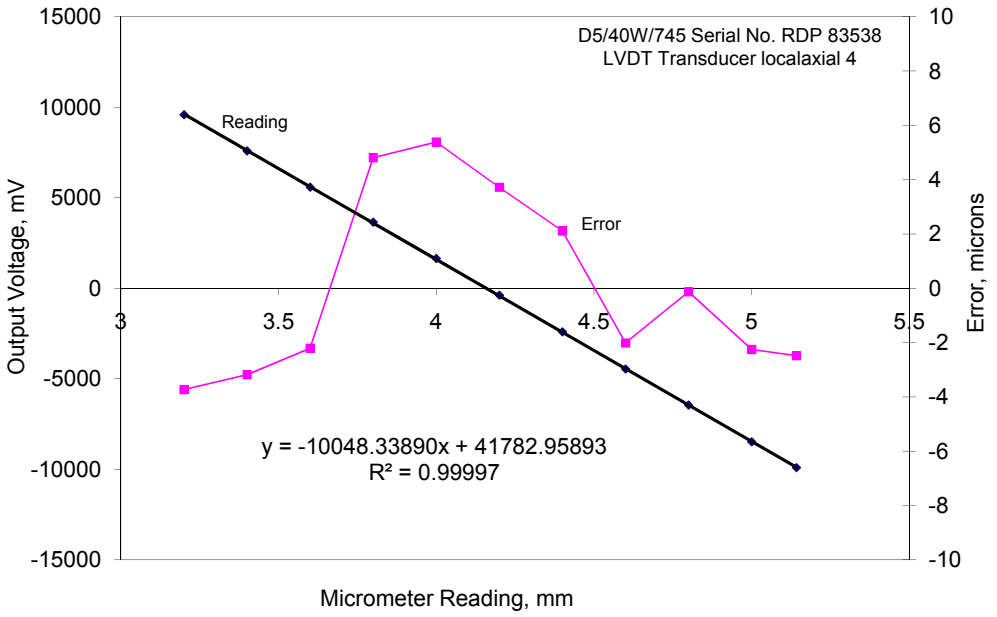

FIGURE A.2: Calibration results of the local axial LVDTs 3 and 4

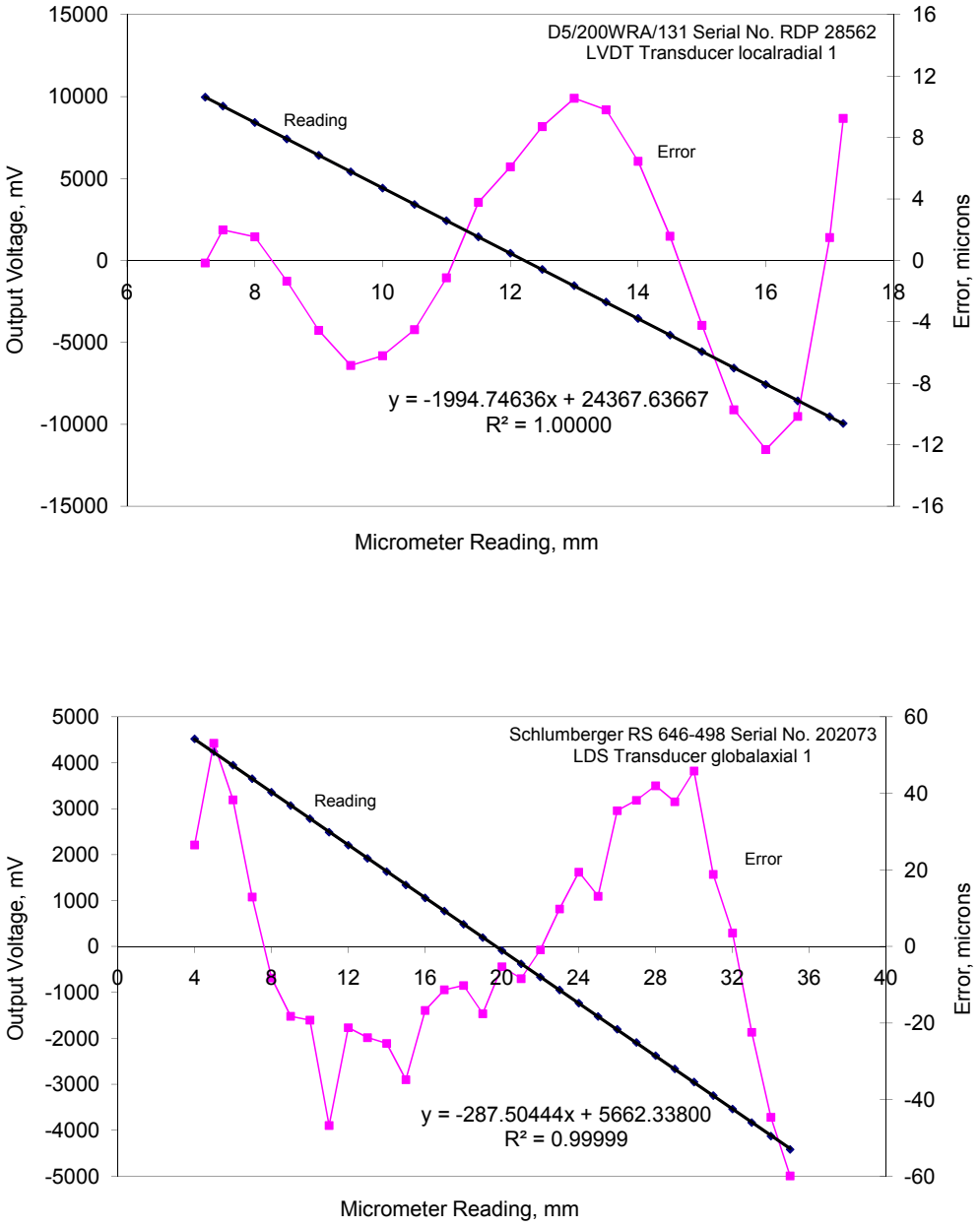

FIGURE A.3: Calibration results of the radial LVDT and external LDS

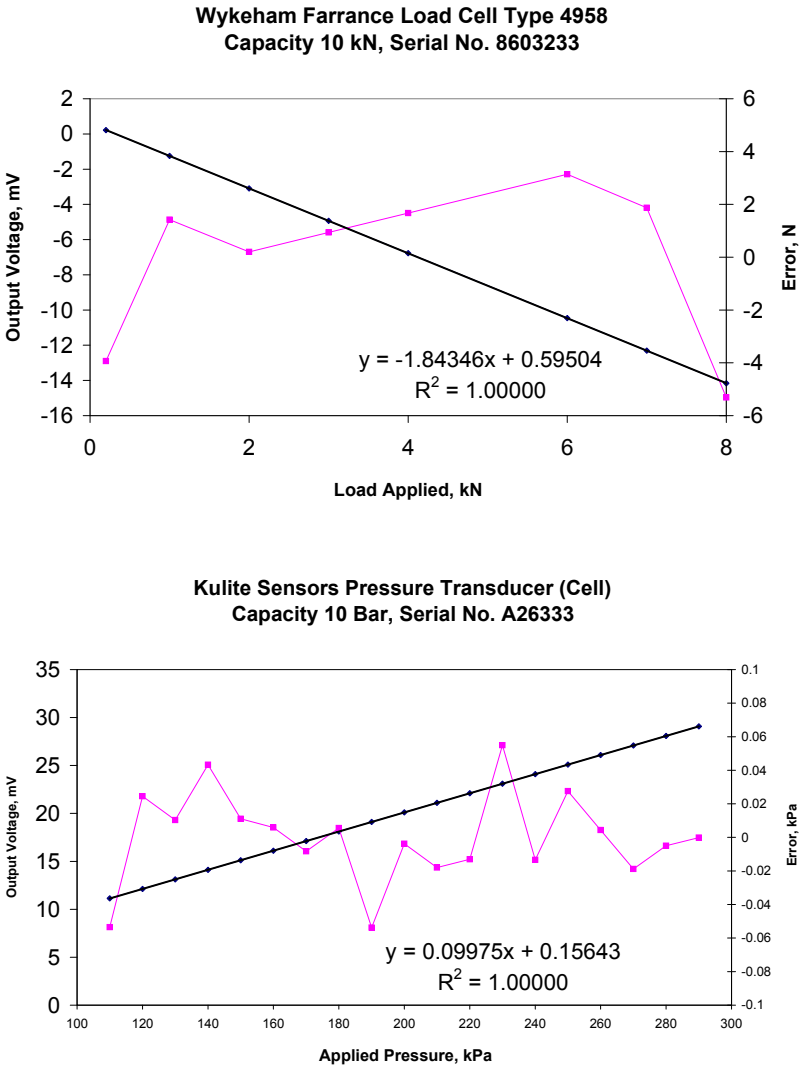

FIGURE A.4: Calibration result of the load cell and cell pressure transducer

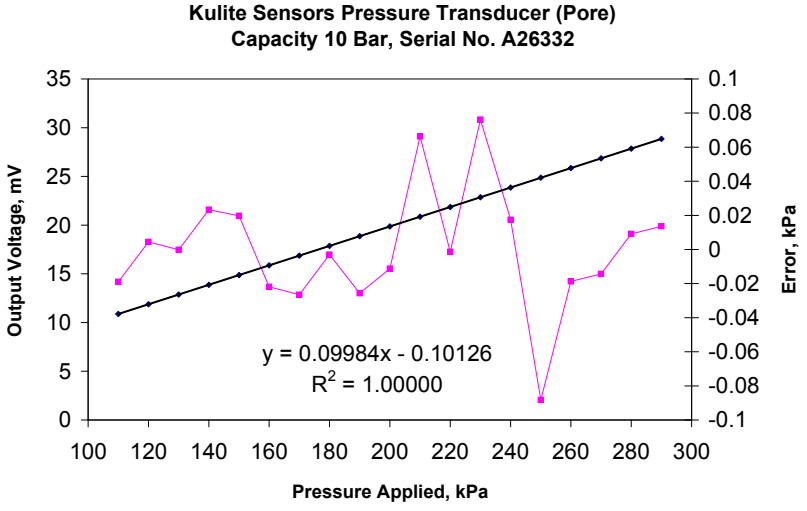

FIGURE A.5: Calibration result of the pore pressure transducer

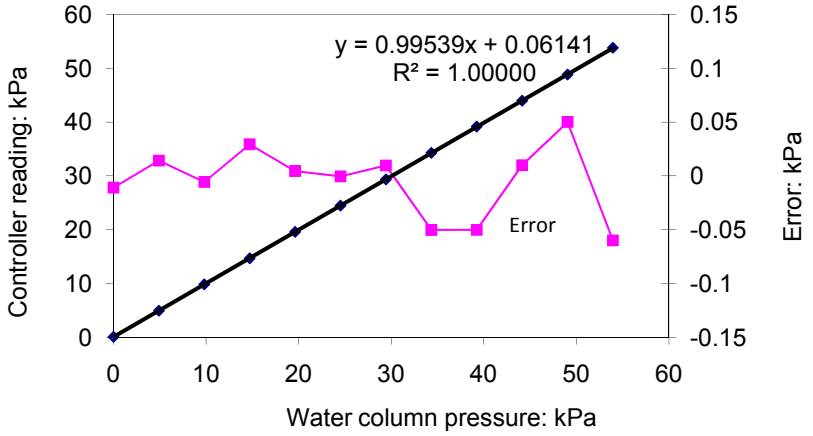

FIGURE A.6: Comparison of Advanced GDS pressure/volume controller against water columns of various heights

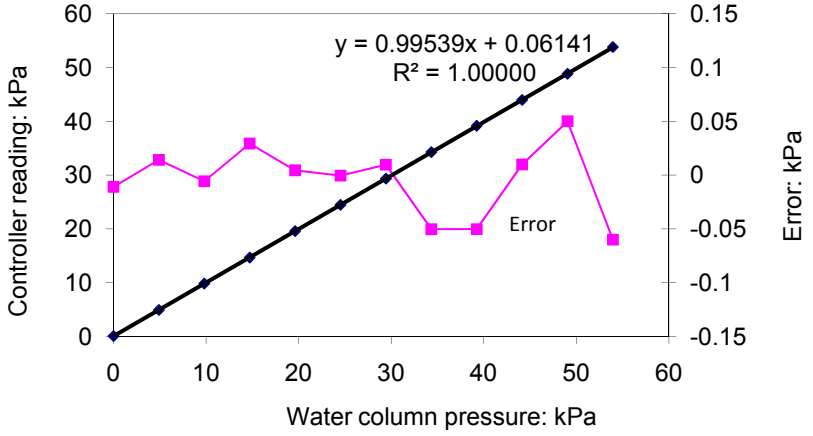

FIGURE A.7: Comparison of Advanced GDS pressure/volume controller against water columns of various heights

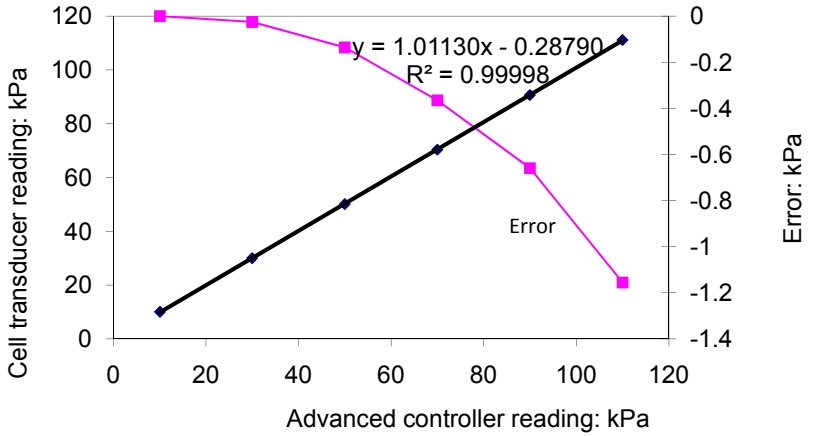

FIGURE A.8: Comparison of cell pressure transducer reading against Advanced GDS pressure/volume controller

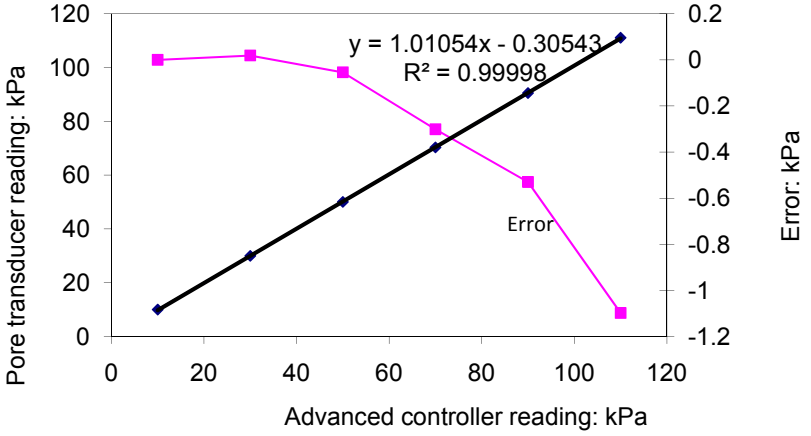

FIGURE A.9: Comparison of pore pressure transducer reading against Advanced GDS pressure/volume controller

TABLE A.1: Transducers and calibration results

S. No.	Transducer	Measurement	Company	Serial No.	Design Range	Calibration Range	Sensitivity
1	Load cell	Axial load (internal)	WF	8603233	10 kN	0 to 5 kN	0.542546 kN/mV
2	Pressure transducer	Pore pressure	KULITE	A26332	1000 kPa	110 to 290 kPa	10.01562 kPa/mV
3	Pressure transducer	Cell pressure	KULITE	A26333	1000 kPa	110 to 290 kPa	10.02522 kPa/mV
4	LVDT1	Axial displacement (internal)	RDP	25705	± 1 mm	± 1.00 mm	0.0001 mm/mV
5	LVDT2	Axial displacement (internal)	RDP	25707	± 1mm	± 1.01 mm	0.000101 mm/mV
6	LVDT3	Axial displacement (internal)	RDP	83537	± 1mm	± 1.00 mm	0.0001 mm/mV
7	LVDT4	Axial displacement (internal)	RDP	83538	± 1mm	± 1.00 mm	0.0001 mm/mV
8	LVDT5	Radial displacement (internal)	RDP	28562	± 5 mm	± 5.01 mm	0.000501 mm/mV
9	LDS	Axial displacement (external)	RS	646-498	± 25 mm	± 15.00 mm	0.003478 mm/mV

Appendix B

Laser Diffraction Technology

When a particle passes through a light beam, light rays are scattered in all directions. The scattering angle is inversely proportional to the particle size. But the scattering intensity is directly proportional to the particle size. The single particle scattering patterns consisting of alternate high and low intensities is illustrated on the Figure B.1.

The Laser Diffraction equipment as shown in Figure B.2 consists of a laser source, sample presentation system (flow cell, sample dispersion unit), a series of detectors for measuring the scattered patterns, and a computer with customed software installed to control the instrument, recording, and calculating the volumetric particle size distribution.

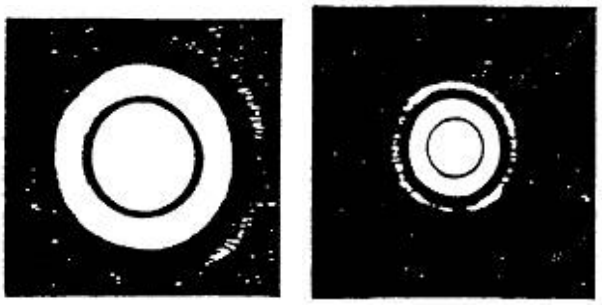

(a) (b)

FIGURE B.1: Scattering pattern for two spherical particles. The particle generating pattern (a) is twice as small as the one generating pattern (b) (after BS ISO 13320-1 (1999))

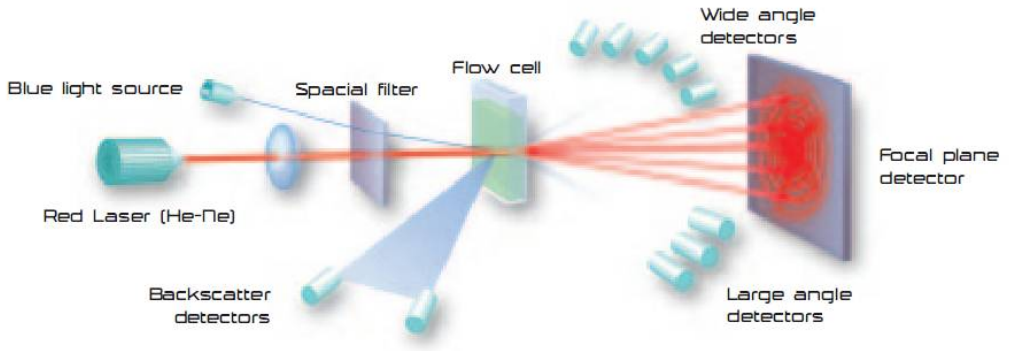

FIGURE B.2: Schematic of a Laser diffraction apparatus (Malvern Instruments Ltd.)

The scattering pattern of an ensemble of particles is assumed to be identical to the sum of individual scattering patterns of all particles (BS ISO 13320-1, 1999). The angular intensity of scattered light is measured by a series of detectors. The collected intensity patterns data is used to compare with an equivalent light scattering pattern of the particles being measured predicted by using Mie Theory. Mie theory requires the input of the refractive indicies of the particles, and the dispersent (water), and the absorption of the particles. The use of this theory enables the measurement of wider range of particles. Measurement range of particles using the laser diffraction technology is from 0.02 μm to 2000 μm.

The Laser Diffraction technique determines the spherical equivalent size, relating to the volume, of the particle that gives the similar scattering pattern of the actual particle. On the other hand, in sieve analysis, size is usually related to the second largest dimension of the particle. Due to different particle properties measured by the two techniques, significant difference can be found for non-spherical particles. For spherical or semi-spherical particles, both techniques yields same results. In general, Laser Diffraction reports a larger particle size compared to sieving (Malvern, 2009).

Appendix C

Calibration of Cameras

C.1 The perspective projection or pinhole camera model

The purpose of a camera model is to establish a link between the position of scene points with that of their corresponding image points. The most common geometric model of a camera is the perspective or pinhole model (Figure C.1). It consists of an image plane, and a 3-D point O, the centre or focus of projection. The distance between the image plane and O is the focal length, f. The line through O and perpendicular to the plane is the optical axis, and o, the intersection between the plane and the optical axis, is named the principal point or the image centre. As shown in Figure C.1, p, the image of point P, is the point at which the straight line through P and O intersects the image plane. Consider the 3-D reference frame in which O is the origin and the image plane is orthogonal to X axis, and let $P = [X, Y, Z]^T$ and $p = [x, y, z]^T$. This reference frame is called the camera reference frame. In the camera frame, we have

$$y = f\frac{Y}{X} \tag{C.1}$$

$$z = f\frac{Z}{X} \tag{C.2}$$

C.2 Camera parameters

The extrinsic parameters define the location and orientation of the camera reference frame with respect to a some other known reference frame known as world reference frame. The intrinsic parameters link the pixel coordinates of an image point with the corresponding coordinates in the camera reference frame. The detail description of these parameters and mathematical relationships for the perspective camera model is given by Trucco & Verri (1998) which are briefly summarised below.

C.2.1 Extrinsic parameters

The camera reference frame has been introduced for the purpose of writing the fundamental equations for the perspective projection (Equations C.1 and C.2) in a simple form. However, the camera reference frame is often unknown, and a common problem is determining the location and orientation of the camera frame with respect to some known reference frame, using only image information. The extrinsic parameters are defined as any set of geometric parameters that identify uniquely the transformation between the unknown camera reference frame and the world reference frame.

$$\mathbf{P}_c = R(\mathbf{P}_w - \mathbf{T}) \tag{C.3}$$

$\mathbf{P}_c$ and $\mathbf{P}_w$ are the vectors representing the coordinates of a point with respect to the camera reference frame and the world reference frame. The camera extrinsic parameters are the translation vector $\mathbf{T}$, and the rotation matrix R which specify the transformation between the camera and the world reference frame.

C.2.2 Intrinsic parameters

These are parameters required to characterise the optical, geometric and digital characteristics of the viewing camera. For a pinhole camera model, we need three sets of intrinsic parameters, specifying respectively

- the perspective projection, for which the only parameter is the focal length f
- the transformation between the camera frame coordinates and pixel coordinates
- the geometric distortion by the optics

To find the second set of intrinsic parameters, we must link the coordinates (y_{im}, z_{im}) of an image point in pixel units with the coordinates (y, z) of the same point in the camera reference frame. The coordinates (y_{im}, z_{im}) can be thought of as coordinates of a new reference frame, sometimes called image reference frame.

Neglecting any geometric distortions possibly introduced by the optics and in the assumption that the CCD (or CMOS) array is made of a rectangular grid of photosensitive elements, we have

$$y = -\left(y_{im} - o_y\right) s_y \tag{C.4}$$

$$z = -\left(z_{im} - o_z\right) s_z \tag{C.5}$$

with (o_y, o_z) the coordinates in pixel of the image centre (the principal point) and s_y and s_z the effective size of pixel (in millimetres) in the horizontal and vertical direction respectively.

Therefore, the current set of intrinsic parameters is f, o_y, o_z, s_y, s_z.

In several cases, the optics introduce image distortions that become evident at the periphery of the image, or even elsewhere using optics with large fields of view. Fortunately, these distortions can be modelled rather accurately as simple radial distortions,

$$y = y_d \left(1 + k_1 r^2 + k_2 r^4\right)$$

$$z = z_d \left(1 + k_1 r^2 + k_2 r^4\right)$$

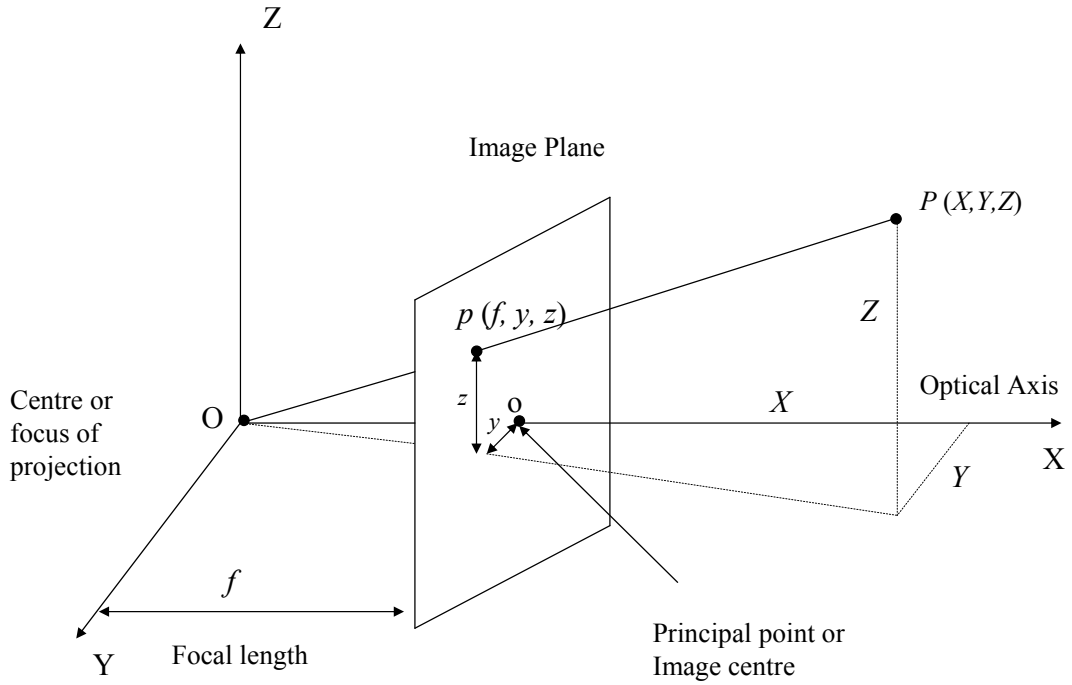

FIGURE C.1: The pinhole camera model

where (y_d, z_d) are the coordinates of the distorted points and $r^2 = y_d^2 + z_d^2$. k_1 and k_2 are further intrinsic parameters.

As an example, the extrinsic parameters (camera-centered) determined from calibration of camera 1 is shown in Figure C.3. The intrinsic parameters for all three cameras are shown in Table C.1.

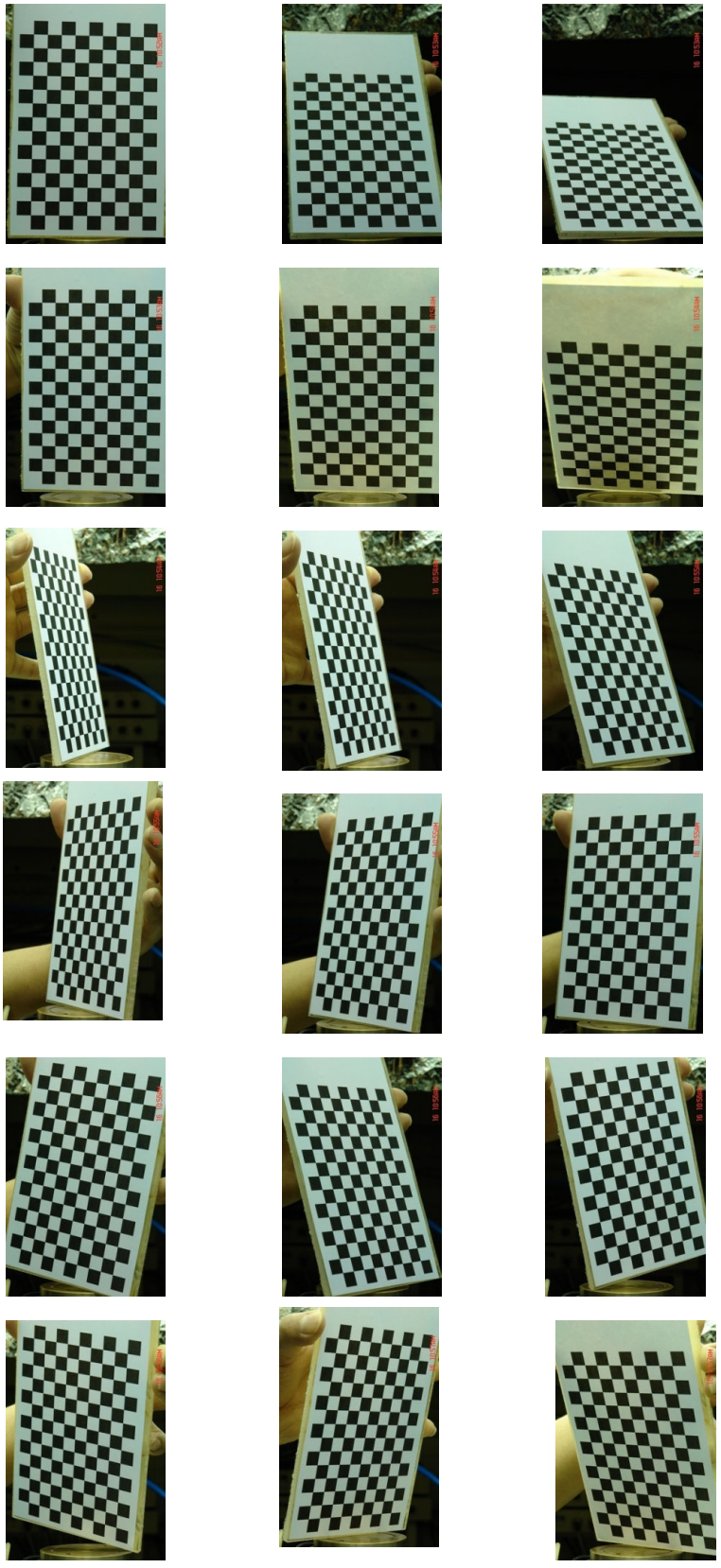

FIGURE C.2: Photographs of a planar checkerboard (used as a calibration pattern) at different orientations. The camera was kept stationary and only the planar checkboard was moved. The size of a square is 10 mm $\times$ 10 mm.

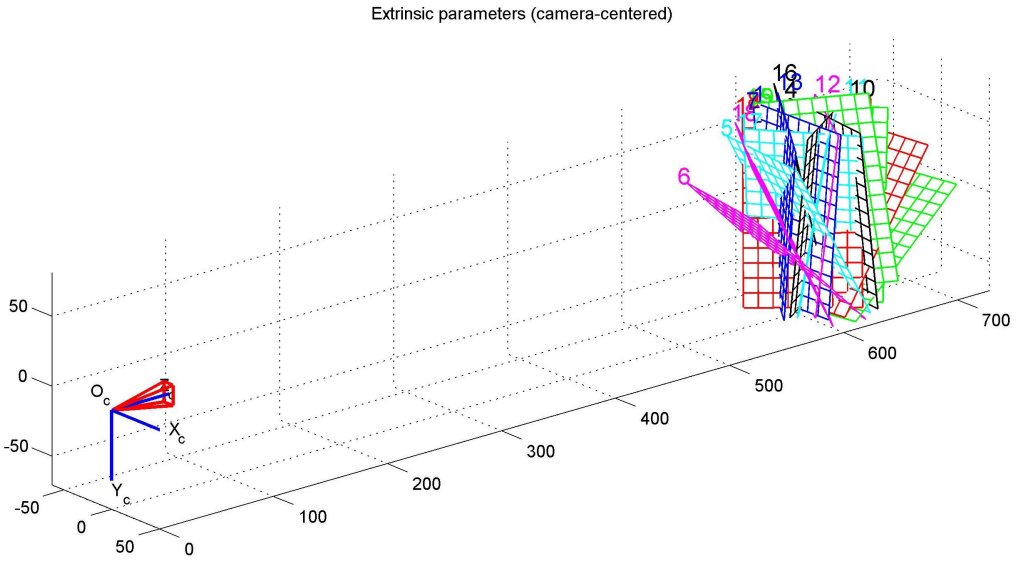

FIGURE C.3: Extrinsic parameters (camera-centered) determined from calibration for camera 1: camera and different calibration planes

TABLE C.1: Intrinsic Parameters for Cameras

Parameter	Camera 1	Camera 2	Camera 3
Focal lengths			
$fc(1) = f \times s_y$	13436.53704±17.76714	13471.39502±64.31095	13374.51982±41.14377
$fc(2) = f \times s_z$	13424.92560±17.73571	13519.12527±62.08957	13451.17891±43.40745
Principal point			
$cc(1) = o_y$	1419.2680456±26.80456	1840.23971±90.13016	1473.06456±66.84987
$cc(2) = o_z$	1969.50259±31.83947	2247.38091±136.33227	2310.13888±109.87805
Skew alpha			
	0.00000±0.00000	0.00000±0.00000	0.00000±0.00000
Distortion			
$kc(1) = k_1$	0.00000±0.00000	0.00000±0.00000	0.00000±0.00000
$kc(2) = k_2$	0.00000±0.00000	0.00000±0.00000	0.00000±0.00000
$kc(3)$	0.00000±0.00000	0.00000±0.00000	0.00000±0.00000
$kc(4)$	0.00000±0.00000	0.00000±0.00000	0.00000±0.00000
$kc(5)$	0.00000± 0.00000	0.00000± 0.00000	0.00000± 0.00000
Pixel error			
$err(1)$	0.69568	1.60964	1.69816
$err(2)$	0.42363	1.32028	1.14796

Appendix D

Computed Tomography Technology

Computed Tomography (CT) is a powerful nondestructive, radiographic technique which can provide three-dimensional spatial information of local density distribution inside the object. It is being used increasingly to probe the internal structure of objects in many fields of engineering. Since it can easily reveal the density variation, it is quite popular to study the homogeneity of deformation of a sand sample during actual test (by developing an in situ testing facility (Razavi, 2006)) or soil sample after test.

A beam of X-rays is passed through the object and collected in a detector. The object is rotated such that the beam probes the object from different angles. The collected data of the object at several angles give a measurement of the attenuation of an X-ray beam through the object. The attenuation is physically proportional to the electron density inside the body, which is itself proportional to mass density if the material is chemically homogeneous. The attenuation information collected is then used by a computer program based on a *Filtered Back Projection* algorithm to reconstruct the internal structure of the object.

Filtered Back Projection: A set of 1D projections of the attenuation through a slice of the sample is measured for different angular positions. The 2D slices are reconstructed by a mathematical algorithm. From several adjacent slices, the 3D specimen can be reconstructed to visualize 2D projection on any plane, in particular on a plane parallel to the axis.

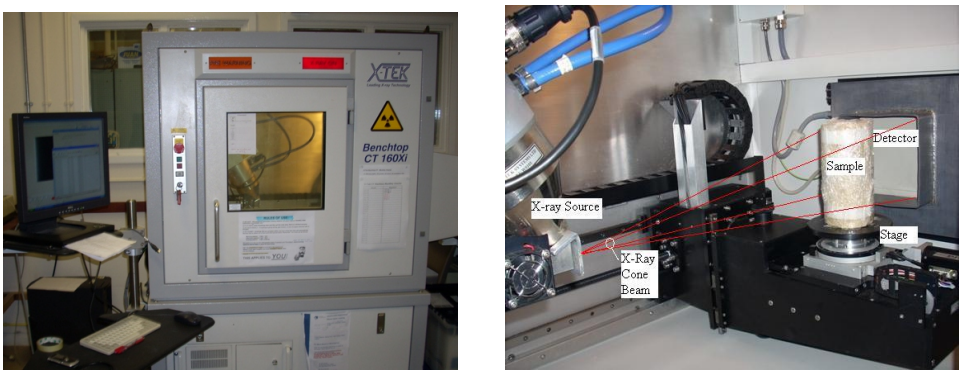

(a) (b)

FIGURE D.1: (a) Computed Tomography (CT) apparatus (b) X-ray source, sample, stage, and detector

The machine used in this research was an X-TEK Benchtop CT 160Xi, in the School of Engineering Sciences at the University of Southampton. Figure D.1 shows the equipment with the sample on the stage. Table D.1 gives the details about the detector size, resolution and approximate pixel resolution obtained; beam parameters, target materials and filter material used depending on the sample size; number of projections; control, reconstruction and visualisation softwares used.

TABLE D.1: CT details

Description	70 mm sample	9 mm sample
CMOS flat panel detector (100 mm × 100 mm)	1248 × 1248 pixels	1248 × 1248 pixels
Approx. resolution (1000th of width of the object imaged)	70 μm	9 μm
Target material	Tungsten	Molybdenum
Beam energy	158 kV	99 kV
Beam intensity	271 μA	78 μA
Filter	Copper (thickness: 1 mm)	-
Number of projections	1831	3601
CT scan software	Inspect-X control	Inspect-X control
Reconstruction software	CT-Pro v.1.0. (X-TEK Systems Ltd., Herts, UK)	CT-Pro v.1.0. (X-TEK Systems Ltd., Herts, UK)
Visualisation software	Volume Graphics GmbH, Heidelberg, Germany	Volume Graphics GmbH, Heidelberg, Germany

References

Abdelaziz, T. S., Martin, C. D., & Chalaturnyk, R. J. (2008). Characterization of locked sand from Northeastern Alberta. *Geotechnical Testing Journal*, *31*(6), 1–10.

Alshibli, K. A., & Akbas, I. S. (2007). Strain localization in clay: plane strain versus triaxial loading conditions. *Getech Geol Eng*, *25*, 45–55.

Alshibli, K. A., & Al-Hamdan, M. Z. (2001). Estimating volume change of triaxial soil specimens from planar images. *Computer-Aided Civil and Infrastructure Engineering*, *16*(6), 415–421.

Alshibli, K. A., Batiste, S. N., & Sture, S. (2003). Strain localization in sand: plane strain versus triaxial compression. *Journal of Geotechnical and Geoenvironmental Engineering*, *129*(6), 483–494.

Alshibli, K. A., & Hasan, A. (2008). Spatial variation of void ratio and shear band thickness in sand using X-ray computed tomography. *Geotechnique*, *58*(4), 249–257.

Atkinson, J. H. (2000). Non-linear soil stiffness in routine design. *Geotechnique*, *50*(5), 487–508.

Balasubramaniam, A. S. (1976). Local strains and displacement patterns in triaxial specimens of a saturated clay. *Soils and Foundations*, *16*(1), 101–114.

Balla, A. (1960). Stress conditions in triaxial compression. *Journal of Soil Mechanics and Foundations Division, Proceedings of the ASCE*, *86*(SM 6), 57–84.

Barton, M. E. (1993). Cohesive sands: the natural transition from sands to sandstones. *Geotechnical engineering of hard soils-soft rocks (eds A. Anagnostopoulos, F. Schlosser, N. Kalteziotis, R. Frank)*, *1*, 367–374.

Barton, M. E., Palmer, S. N., & Wong, Y. L. (1986). A geotechnical investigation of two Hampshire Tertiary sand beds; are they locked sands? *Quarterly Journal of Engineering Geology & Hydrogeology*, *19*(4), 399–412.

Been, K., & Jefferies, M. G. (1985). The state parameter for sands. *Geotechnique*, *35*(2), 99–112.

Been, K., Jefferies, M. G., & Hackey, J. (1991). The critical state of sands. *Geotechnique*, *41*(3), 365–381.

Besuelle, P., Desrues, J., & Raynaud, S. (2000). Experimental characterisation of the localisation phenomenon inside a Vosges sandstone in a triaxial cell. *International Journal of Rock Mechanics and Mining Sciences*, *37*(8), 1223–1237.

Bishop, A. W. (1973). The influence of an undrained change in stress on the pore pressure in porous media of low compressibility. *Geotechnique*, *23*(3), 435–442.

Bishop, A. W., & Green, G. E. (1965). The influence of end restraint on the compression strength of a cohesionless soil. *Geotechnique*, *15*(3), 243–266.

Bishop, A. W., & Henkel, D. J. (1962). *The Measurement of Soil Properties in the Triaxial Test*. Edward Arnold Ltd., London, 2nd ed.

Black, D. K., & Lee, K. L. (1973). Saturating laboratory samples by back pressure. *Proceedings of the American Society of Civil Engineers: Journal of the Soil Mechanics and Foundations Division*, *SM1, January*, 75–93.

Bolton, M. D. (1986). Strength and dilatancy of sands. *Geotechnique*, *36*(1), 65–78.

Bolton, M. D. (1991). *A Guide to Soil Mechanics*. Chung Hwa Book Company, Hong Kong.

Bouguet, J. (2008). Camera Calibration Toolbox for Matlab. (Last accessed: 14 October 2008).
URL `http://www.vision.caltech.edu/bouguetj/calib_doc/`

Bruck, H. A., McNeill, S. R., Sutton, M. A., & Peters, W. H. (1989). Digital image correlation using Newton-Raphson Method of partial differential correction. *Experimental Mechanics*, (pp. 261–267).

BS ISO 13320-1 (1999). Particle size analysis- Laser diffraction methods- Part 1: General principles. British Standards Institution, London.

Bui, M. T. (2009). *Influence of some particle characteristics on the small strain response of granular materials*. Ph.D. thesis, University of Southampton.

Burland, J. B. (1990). On the compressibility and shear strength of natural clays. *Geotechnique*, *40*(3), 329–378.

Cecinato, F. (2004). Soil deformation measurement using Particle Image Velocimetry on triaxial tests. Tech. rep., University of Southampton.

Chandler, R. J. (1966). The measurement of residual strength in triaxial compression. *Geotechnique*, *16*(3), 181–186.

Clough, G. W., Rad, N. S., Bachus, R. C., & Sitar, N. (1981). Cemented sands under static loading. *Journal of the Soil Mechanics and Foundations Division*, *107*(6), 799–817.

Cook, R. D., Malkus, D. S., Plesha, M. E., & Witt, R. J. (2001). *Concepts and Applications of Finite Element Analysis*. John Wiley & Sons, 4th ed.

Coop, M. R., & Atkinson, J. H. (1993). The mechanics of cemented carbonate sands. *Geotechnique*, *43*(1), 53–67.

Cornforth, D. H. (1964). Some experiments on the influence of strain conditions on the strength of sand. *Geotechnique*, (pp. 143–167).

Cresswell, A. W. (1999). *Sampling and strength testing of an unbonded locked sand*. Ph.D. thesis, University of Southampton.

Cresswell, A. W. (2001). Block sampling and test sample preparation of locked sands. *Geotechnique*, *51*(6), 567–570.

Cresswell, A. W., & Barton, M. E. (2003). Direct shear tests on an uncemented, and a very slightly cemented, locked sand. *Quarterly Journal of Engineering Geology & Hydrogeology*, *36*(2), 119–132.

Cresswell, A. W., Barton, M. E., & Brown, R. (1999). Determining the maximum density of sands by pluviation. *Geotechnical Testing Journal*, *22*(4), 324–328.

Cresswell, A. W., & Powrie, W. (2004). Triaxial tests on an unbonded locked sand. *Geotechnique*, *54*(2), 107–115.

Cuccovillo, T., & Coop, M. R. (1997). Yielding and pre-failure deformation of structured sands. *Geotechnique*, *47*(3), 491–508.

Cuccovillo, T., & Coop, M. R. (1999). On the mechanics of structured sands. *Geotechnique*, *49*(6), 741–760.

Cui, L., O'Sullivan, C., & O'Neil, S. (2007). An analysis of the triaxial apparatus using a mixed boundary three-dimensional discrete element model. *Geotechnique*, *57*(10), 831–844.

Desrues, J. (1998). Localization patterns in ductile and brittle geomaterials. *Material Instabilities in Solids*, (pp. 137–158).

Desrues, J., Besuelle, P., & Lewis, H. (2007). Strain localization in geomaterials. *Geological Society, London, Special Publications*, *289*(1), 47–73.

Desrues, J., Chambon, R., Mokni, M., & Mazerolle, F. (1996). Void ratio evolution inside shear bands in triaxial sand specimens studied by computed tomography. *Geotechnique*, *46*(3), 529–46.

Desrues, J., & Viggiani, G. (2004). Strain localization in sand: an overview of the experimental results obtained in Grenoble using stereophotogrammetry. *International Journal for Numerical and Analytical Methods in Geomechanics*, *28*(4), 279–321.

Dusseault, M. B., & Morgenstern, N. R. (1979). Locked sands. *Quarterly Journal of Engineering Geology & Hydrogeology*, *12*(2), 117–131.

Eaton, D. (2008). How to do normalized cross-correlation fast. (Last accessed: 14 October 2008).
URL `http://www.cs.ubc.ca/~deaton/remarks_ncc.html`

Finno, R. J., & Rechenmacher, A. L. (2003). Effects of consolidation history on critical state of sand. *Journal of Geotechnical and Geoenvironmental Engineering*, *129*(4), 350–360.

Frydman, S., Talesnick, M., Nawatha, H., & Schwartz, K. (2007). Stress-dilation of undisturbed sand samples in drained and undrained triaxial shear. *Soils and Foundations*, *47*(1), 27–32.

Fukushima, S., & Tatsuoka, F. (1984). Strength and deformation characteristics of saturated sand at extremely low pressures. *Soils and Foundations*, *24*(4), 30–48.

Georgiannou, V. N., & Burland, J. B. (2006). A laboratory study of slip surface formation in an intact natural stiff clay. *Geotechnique*, *56*(8), 551–559.

Giachetti, A. (2000). Matching techniques to compute image motion. *Image and Vision Computing*, *18*, 247–260.

Guo, P. J., & Su, X. (2007). Shear strength, interparticle locking, and dilatancy of granular materials. *Canadian Geotechnical Journal*, *44*, 579–591.

Hardin, B. O. (1985). Crushing of soil particles. *Journal of Geotechnical Engineering*, *111*(10), 1177–1192.

Henkel, D. J., & Gilbert, G. D. (1952). The effect of the rubber membrane on the measured triaxial compression strength of clay samples. *Geotechnique*, *3*(1), 20–29.

Houlsby, G. T. (1991). How the dilatancy of soils affects their behaviour? *In Proceedings of the 10th European Conference on Soil Mechanics and Foundation Engineering, Florence, Italy*, (pp. 1189–1202).

Jenkins, F. A., & White, H. E. (1976). *Fundamentals of Optics, 4th edition*. McGraw-Hill, New York.

Jeremic, B., Yang, Z., & Sture, S. (2004). Numerical assessment of the influence of end conditions on constitutive behavior of geomaterials. *Journal of Engineering Mechanics*, *130*(6), 741–745.

Kavvadas, M., & Amorosi, A. (2000). A constitutive model for structured soils. *Geotechnique*, *50*(3), 263–273.

Kikkawa, N., Nakata, Y., Hyodo, M., & Murata, H. (2006). Three-dimensional measurement of local strain using digital stereo photogrammetry in the triaxial test. In *Geomechanics and Geotechnics of Particulate Media - Hyodo, Murata & Nakata (eds.)*, (pp. 61–67). Taylor & Francis Group, London.

Kirkpatrick, W. M., & Belshaw, D. J. (1968). On the interpretation of the triaxial test. *Geotechnique*, *18*, 336–350.

Lade, P. V., & Boer, R. D. (1997). The concept of effective stress for soil, concrete and rock. *Geotechnique*, *47*(1), 61–78.

Lancelot, L., Shahrour, I., & Al Mahmoud, M. (2003). Experimental study of sand behaviour at low stresses. In *Deformation characteristics of Geomaterials, Di Benedetto et al.(eds.)*, (pp. 655–662). Swets and Zeitlinger, Lisse.

Lancelot, L., Shahrour, I., & Al Mahmoud, M. (2006). Failure and dilatancy properties of sand at relatively low stresses. *Journal of Engineering Mechanics*, *132*(12), 1396–1399.

Lecompte, D., Smits, A., Bossuyt, S., Sol, H., Vantomme, J., Hemelrijck, D. V., & Habraken, A. M. (2006). Quality assessment of speckle patterns for digital image correlation. *Optics and Lasers in Engineering*, *44*, 1132–1145.

Leroueil, S., & Vaughan, P. R. (1990). General and congruent effects of structure in natural soils and weak rocks. *Geotechnique*, *40*(3), 467–488.

Lin, H., & Penumadu, D. (2006). Strain localization in combined axial-torsion testing on kaolin clay. *Journal of Engineering Mechanics*, *132*(5), 555–564.

Liyanapathirana, D. S., Carter, J. P., & Airey, D. W. (2005). Numerical modeling of nonhomogeneous behavior of structured soils during triaxial tests. *International Journal of Geomechanics*, *5*(1), 10–23.

Macari, E. J., Parken, J. K., & Costes, N. C. (1997). Measurement of volume changes in triaxial tests using digital imaging techniques. *Geotechnical Testing Journal*, *20*(1), 103–109.

Malandraki, V., & Toll, D. (2000). Drained probing triaxial tests on a weakly bonded artificial soil. *Geotechnique*, *50*(2), 141–151.

Malvern (2009). Comparing Laser Diffraction and Sieve Results (Last accessed: 19 January 2009), Malvern Instruments Ltd.
URL `http://www.malvern.com/LabEng/technology/laser_diffraction/sieve_results.htm`

Mooney, M. A., Finno, R. J., & Viggiani, G. (1998). A unique critical state for sand? *Journal of Geotechnical and Geoenvironmental Engineering*, *124*(11), 1100–1108.

Muir Wood, D. (1984). On stress parameters. *Geotechnique*, *34*(2), 282–287.

Muir Wood, D. (1990). *Soil Behaviour and Critical State Soil Mechanics*. Cambridge University Press.

Newland, P. L., & Allely, B. H. (1957). Volume changes in drained triaxial tests on granular materials. *Geotechnique*, *7*(1), 17–34.

Oda, M., & Kazama, H. (1998). Microstructure of shear bands and its relation to the mechanisms of dilatancy and failure of dense granular soils. *Geotechnique*, *48*(4), 465–481.

Pan, B., Xie, H., Wang, Z., Qian, K., & Wang, Z. (2008). Study on subset size selection in digital image correlation for speckle patterns. *Optics Express*, *16*(10), 7037–7048.

Peric, D., & Su, S. (2005). Influence of the end friction on the response of triaxial and plane strain clay samples. In *Proceedings of the International Conference on Soil Mechanics and Geotechnical Engineering*. Netherlands: A.A. BALKEMA.

Ponce, V., & Bell, J. (1971). Shear strength of sand at extremely low pressures. *Journal of the Soil Mechanics and Foundations Division*, *97*(4), 625–638.

Powrie, W. (2004). *Soil Mechanics: Concepts and Applications*. Spon Press, 2nd ed.

Powrie, W., Ni, Q., Harkness, R. M., & Zhang, X. (2005). Numerical modelling of plane strain tests on sands using a particulate approach. *Geotechnique*, *55*(4), 297–306.

Raffel, M., Willert, C. E., & Kompenhans, J. (1998). *Particle Image Velocimetry: A Practical Guide*. Springer.

Razavi, M. R. (2006). *Characterization of microstructure and internal displacement field of sand using X-Ray Computed Tomography*. Ph.D. thesis, Washington State University.

Rechenmacher, A., & Finno, R. (2004). Digital image correlation to evaluate shear banding in dilative sands. *Geotechnical Testing Journal*, *27*(1), 1–10.

Rechenmacher, A. L. (2006). Grain-scale processes governing shear band initiation and evolution in sands. *Journal of Mechanics and Physics of Solids*, *54*(1), 22–45.

Rechenmacher, A. L., & Medina-Cetina, Z. (2007). Calibration of soil constitutive models with spatially varying parameters. *Journal of Geotechnical and Geoenvironmental Engineering*, *133*(12), 1567–1576.

Richards, N., & Barton, M. E. (1999). The Folkestone Bed sands: microfabric and strength. *Quarterly Journal of Engineering Geology*, *32*, 21–44.

Roscoe, K. H., Schofield, A. N., & Wroth, C. P. (1958). On the yielding of soils. *Geotechnique*, *8*(1), 22–53.

Rowe, P. W. (1962). The stress-dilatancy relation for static equilibrium of an assembly of particles in contact. *Proc. R. Soc. Lond. A*, *269*(1339), 500–527.

Rowe, P. W. (1964). Importance of free ends in triaxial testing. *Journal of Soil Mechanics and Foundation Engineering, Proceedings of the ASCE*, *SM1*, 1–27.

Saada, A. S., Liang, L., Figueroa, J. L., & Cope, C. T. (1999). Bifurcation and shear band propagation in sands. *Geotechnique*, *49*(3), 367–385.

Sachan, A., & Penumadu, D. (2007). Strain localization in solid cylindrical clay specimens using digital image analysis (DIA) technique. *Soils and Foundations*, *47*(1), 67–78.

Schanz, T., & Vermeer, P. A. (1996). Angles of friction and dilatancy of sand. *Geotechnique*, *46*(1), 145–151.

Schofield, A., & Wroth, C. P. (1968). *Critical State Soil Mechanics*. McGraw-Hill New York.

Shuttle, D. A. (2006). Can the effect of sand fabric on plastic hardening be determined using a self-bored pressuremeter? *Canadian Geotechnical Journal*, *43*, 659–673.

Sture, S., Costes, N. C., Batiste, S. N., Lankton, M. R., Alshibli, K. A., Jeremic, B., Swanson, R. A., & Frank, M. (1998). Mechanics of granular materials at low effective stresses. *Journal of Aerospace Engineering*, *11*(3), 67–72.

Taylor, D. (1948). *Fundamentals of Soil Mechanics*. John Wiley & Sons, New York.

Tong, W. (2005). An evaluation of digital image correlation criteria for strain mapping applications. *Strain*, *41*, 167–175.

Trucco, E., & Verri, A. (1998). *Introductory Techniques for 3-D Computer Vision*. Prentice Hall, Upper Saddle River, New Jersey.

Vaid, Y. P., & Sasitharan, S. (1992). The strength and dilatancy of sand. *Canadian Geotechnical Journal*, *29*, 522–526.

Vardoulakis, I., & Sulem, J. (1995). *Bifurcation Analysis in Geomechanics*. Taylor & Francis Group.

White, D. J., Take, W. A., & Bolton, M. D. (2003). Soil deformation measurement using particle image velocimetry (PIV) and photogrammetry. *Geotechnique*, *53*(7), 619–631.

Wong, R. C. K. (1999). Mobilized strength components of Athabasca oil sand in triaxial compression. *Canadian Geotechnical Journal*, *36*(4), 718–735.

Wong, R. C. K. (2001). Strength of two structured soils in triaxial compression. *International Journal for Numerical and Analytical Methods in Geomechanics*, *25*, 131–153.

Yaofeng, S., & Pang, J. H. L. (2007). Study of optimal subset size in digital image correlation of speckle pattern images. *Optics and Laser in Engineering*, *45*, 967–974.

Zhang, Y. D., Tan, T. S., & Leung, C. F. (2005). Application of particle imaging velocimetry (PIV) in centrifuge testing of uniform clay. *International Journal of Physical Modelling in Geotechnics*, *5*(1), 15–26.